Coventry University

DOCTOR OF PHILOSOPHY

Non-invasive damage detection and classification of the bond beneath thin overlays in rigid pavements. A pilot study

Khan, Adil Idrees

Award date:
2021

Awarding institution:
Coventry University

Link to publication

Non-Invasive Damage Detection and Classification of the Bond beneath Thin Overlays in Rigid Pavements. A Pilot Study

By

Adil Idrees Khan

PhD

July 2020

Coventry University

Non-Invasive Damage Detection and Classification of the Bond beneath Thin Overlays in Rigid Pavements. A Pilot Study

By

Adil Idrees Khan

July 2020

A thesis submitted in partial fulfilment of the University's requirements

for the Degree of Doctor of Philosophy

Certificate of Ethical Approval

Applicant:

Adil Idrees Khan

Project Title:

Non-Invasive Damage Detection and Classification of the Bond beneath Thin Overlays
in Rigid pavements. A pilot Study.

This is to certify that the above named applicant has completed the Coventry
University Ethical Approval process and their project has been confirmed and
approved as Low Risk

Date of approval:

01 March 2019

Project Reference Number:

P88705

An Executive Abstract

Separation (debonding) of the top, thin course is a common mode of failure in modern road and pavement construction and rehabilitation. Freeze-thaw environmental cycles, exacerbated by repeated and wide-ranging traffic loads, cause expansion and pushing of the top layer up from its base. Repeated traffic loads break this layer and, if no remediate action is taken, the latter disintegrates into loose fragments (chippings, grit) revealing a pothole. These chippings have no cohesion with the lower layer whatsoever, reducing friction and skid resistance, affecting vehicle handling, stability and compromising safety. Often, loose chippings are caught between the tread patterns of vehicle tyres and then catapulted onto other vehicles, or bikers. It is clear that this can result in loss of concentration at best, but can also become exceptionally dangerous, often leading to very serious consequences. All this comes at a time when Government and local authorities around the globe promote and support sustainable and environmentally friendly transport means.

A relevant research project started over three years ago at the School of Energy, Construction and Environment, Coventry University, under the title: Non-invasive Damage Detection and Classification of the Bond beneath Thin Overlays in Rigid Pavements. This project is the first of a series and is regarded as a pilot study.

A critical literature review has shown that a number of non-destructive testing and evaluation NDT&E techniques have been deployed for the detection and evaluation of the flaw bond beneath thin overlays in pavements. However, no technique has been accepted universally that can both '*identify*' and '*quantify*' the flaw-bond reliably.

In essence, this project endeavours to develop a ''new''- NDT&E method and demonstrate, how the combination of two initially incompatible non-destructive testing and evaluation (NDT&E) techniques, such as Infrared Thermography (IRT) and Impact Hammer Testing (IHT) can team up to provide an accurate and reliable account of the problem and evaluate and predict the degree of substandard bond. These two methods

have never been used together for the purpose of assessing debonding in pavement structures. However, prior to that the suitability of both methods to large scale pavement testing had to be tested and several modifications and improvements had to be considered.

Both NDT&E techniques (IRT and IHT), were explored thoroughly, by conducting laboratory scaled experiments on a number of purposely designed concrete slabs (robust and flawed), while replicating overlays and support/boundary conditions in real life. Practical tests were accompanied by corresponding numerical studies. Some tests (IRT) were also carried outside the laboratory, to benefit from the real environmental conditions and calibrate the numerical models accordingly.

The designed concrete specimens with deliberate implanted voids/delaminations, were assessed '*qualitatively* and *quantitatively*' by the IRT and IHT techniques. Finally, both techniques were integrated together with some aid from finite element analysis and the guidelines for a new 'NDT&E method' emerged. Conclusively, the developed procedures were demonstrated, envisioning its real time implementations.

It was found that as the defects became deeper (>30mm) and thinner (<3mm), the assessment through IRT became more complex, and IHT was called-in, to evaluate those dubious areas. Briefly, in this new 'NDT&E method', a special '*three-way*' system analogous to traffic lights (Green, Amber, Red) was proposed and demonstrated (through a case study) to classify the flaw-bond, where each colour was associated with the severity of the defects (delamination/voids). Red, represented '*severe delamination*', necessitating a quick remedial action, Green showed a sound, or '*flawless*' region with no defects, whereas, 'Amber' was used for the *'uncertain regions'*, impossible to classify with IRT, and therefore, handed over to IHT for further investigation. The latter, with the help of numerical modelling was able to classify those uncertain regions with acceptable accuracy (error below 3%).

Conclusively, both techniques showed promising results in detecting and classifying the flaw-bond non-destructively. However, some limitations emerged during the research and these are reported at the end of the thesis. Recommendations for further research are also reported, based on these limitations, together with the need for full-size long stretch road testing before the method gains acceptance as a NDT&E technique, for the evaluation of flaw bond beneath thin road courses. At the end, a possible implementation scenario is also presented, demonstrating the full-scale implementation of the method proposed.

Acknowledgments

Table of Contents

List of Abbreviations

AAPTP	Airport Asphalt Pavement Technology Programme
AC	Asphalt Concrete
A/D	Analogue to Digital
AI	Artificial Intelligence
ALARM	Annual Local Authority Road Maintenance
ANN	Artificial Neural Network
ASTM	American Society for Testing and Materials
BS EN	British Standards European Norms
BST	British Standard Time
CAD	Computer Aided Design
CBR	California Bearing Ratio
COMAC	Coordinate Modal Assurance Criterion
DFT	Discrete Fourier Transform
DLAC	Damage Location Assurance Criteria
DSP	Digital Signal Processing
DOF	Degree of Freedom
EFS	Elastic Foundation Stiffness
EMA	Experimental Modal Analysis
FBD	Flaw-Bond Detect-o-meter
FE	Finite Element
FEA	Finite Element Analysis
FEM	Finite Element Method
FFT	Fast Fourier Transform
FT	Fourier Transform
FHWA	Federal Highway Administration
FOV	Field of View
FPA	Focal Plane Array
FRF	Frequency Response Function
FWD	Falling Weight Deflectometer
GPR	Ground Penetrating Radar
GPS	Global Positioning System
HFS	High Frequency Sweep
HMA	Hot Mix Asphalt
IAEA	International Atomic Energy Agency
IE	Impact Echo
IH	Impact Hammer
IHT	Impact Hammer Test
IR	InfraRed
IRT	Infrared Thermography
LWD	Light Weight Deflectometer
MA	Modal Analysis
MAC	Modal Assurance Criteria
MDOF	Multi Degree of Freedom System

NCE	New Civil Engineer
NDT	Non-Destructive Testing
NDT&E	Non-Destructive Testing and Evaluation
NN	Neural Networks
NRMCA	National Ready Mixed Concrete Association
OWT	Offshore Wind Turbine
PCG	Preconditioned Conjugate Gradient
PSD	Power Spectral Density
PSPA	Portable Seismic Pavement Analyser
RC	Reinforced Concrete
ROI	Region of Interest
SASW	Spectral Analysis of Surface Waves
SDOF	Single Degree of Freedom System
SG	Stiffness Gauge
USW	Ultrasonic Surface Waves

Nomenclature

α	Thermal diffusivity (m^2s^{-1})
c	Specific heat capacity ($Jkg^{-1}k^{-1}$)
C	Damping Matrix
D	Delamination
[D]	Diagonal Matrix
ΔT	Thermal Contrast (dimensionless)
ε	Emission Coefficient or Emissivity
E	Thermal Emission of a real body (Wm^{-2})
E_s	Thermal Emission of a black body (Wm^{-2})
{F}	Global applied Load Vector
$F(\omega)$	Input excitation signal in frequency domain
f	Undamped Natural Frequency (Hz)
$f(t)$	External Force
h	Convection heat-transfer coefficient
$H(\omega)$	Frequency Response Function
k	Thermal conductivity ($Wm^{-1}k^{-1}$)
[L]	Lower Triangular Matrix
[L']	Inverse of Lower Triangular Matrix
M	Mass Matrix
K	Stiffness Matrix
k_N	Normal contact stiffness (Force.length^{-3})
ρ	Density (kgm^{-3})
ρc	Volumetric heat capacity ($Jm^{-3}K^{-1}$)
q_x	Heat transfer rate (W)
$\dot{q}$	Energy generated per unit volume (Wm^{-3})
r	Reflectivity

τ	Time in s
t	Time in s
T	Temperature in °C
$T_d(t)$	Surface temperature of the defected area at any measured time, t.
$T_d(t_0)$	Initial Surface temperature of the defected area.
$T_s(t)$	Surface temperature of sound or reference area at time t.
$T_s(t_0)$	Initial surface temperature of the sound or reference area.
T_w	Temperature of the heated wall (°C)
$T\infty$	Temperature of the air (°C)
τ	Transmissivity
$\{u\}$	Global vector of Nodal displacement
$[U]$	Upper Triangular Matrix
μ_N	Normal penetration (mm)
V	Void
ω	Excitation (input) frequency
ω_d	Damped angular Natural Frequency (rad/s)
ω_n	Undamped angular Natural Frequency (rad/s)
$\bar{\omega}_r^2$	Squared undamped Natural Frequency
$X(\omega)$	Output response signal in frequency domain
$x(t)$	Displacement Vector
$\ddot{x}(t)$	Acceleration Vector
σ_N	Normal Contact Pressure (Nmm^{-2})
$\{\psi\}_r$	Mode Shape
ξ	Damping Ratio

List of Figures

List of Tables

Chapter 1 - Introduction

1.1   Introduction

This project addresses the serious problem of delamination of thin surface courses and overlays in roads and airfield pavements. It endeavours to demonstrate, how the combination of two different and apparently dissimilar techniques, can provide an accurate and reliable account of the damage (delamination), and evaluate the degree of substandard bond between the top (thin) layer and the underlying pavement.

In essence, it utilises existing wisdom from two well established but unrelated technologies:

1. Infrared Thermography; being used successfully and efficiently, in the detection of the heat losses in buildings and structures.
2. Impact Hammer Testing; chiefly used for the exposure and evaluation of damage in a variety of applications such as automotive engineering, aeronautical engineering, naval structures and so on.

1.2   Overview, Motivation and Justification of the Research Study

Pavement infrastructure around the world faces a deterioration problem of unprecedented magnitude. The structural integrity of roads and pavements around the world is seriously compromised by the following two factors: Harsh environmental conditions and repeated traffic loadings, thus, making roads and airport pavements more susceptible than ever. Significant numbers of pavement infrastructures are old, and therefore, susceptible to any unexpected failure, which can have a serious impact on the country's economy and prosperity. It's not feasible due to economic and sustainable (environmental) reasons, to replace all the aged structures with the new ones. Therefore, structural health monitoring and integrity assessment, are two very important factors in

ensuring the reliability of structures including pavement systems, hence, contribute to public safety (Dackermann 2010). Proper and accurate/thorough inspection of the existing pavements, can help in detecting the deficiencies, where, proper evaluation can help in revealing the degree of damage, or the remaining life of the bond. Then, a decision can be made, whether the structure under investigations needs immediate or future replacement or its integrity and robustness can be improved, in order to ensure durability, safety and riding quality.

Road and pavement infrastructure around the globe is a priority in terms of economic prosperity and a more sustainable future. In the UK, and the rest of the world, the major challenge is not only the average age of infrastructure increasing, but also the loading requirements are becoming more demanding. So, the national 'pool' of roads and airfields requiring intervention due to deterioration and lack of strengthening, is growing rapidly. To cope with this situation, in which the intervention due to deterioration has become a necessity, prioritising their maintenance is very important. This can be done after evaluating the damage and the remaining life of the structure.

Essentially, the construction, maintenance and operation of the trunk road network consumes vast quantities of resources. The Highways England, responsible for the maintenance of approximately 6920km (4300miles) of roads and pavements, spent £43k per lane mile on road maintenance alone in 2011-12 (Highways Agency 2012). Similarly, the UK government has pledged £6bn over six years, to help councils maintain local roads, with a £578M reward, to those demonstrating efficiencies (Highways Agency 2012). It is understood that a major element of these maintenances relates to resurfacing the wearing course of the highways and roads, as a result of delamination of the thin surfacings used.

Thin surfacing systems, were introduced into the United Kingdom in 1991. They represent one of the most significant developments in asphalt and concrete in recent years. They are thin layers, usually between 40-50mm, provide good surface texture, and contribute significantly to the reduction of spray, traffic noise and accidents.

However, several problems associated with thin surfacings have become recurrent, one of them is debonding or delamination. This is evident not only on roads but also on bridge decks and airport pavements. With time, delamination will continue to breed. Freeze-thaw cycles and the impact of traffic add to its growth.

In United Kingdom, an extensive initial investigation of wearing course slippage was conducted in the mid-1970s (Kennedy 1978, Kennedy and Lister 1980 and Pell 1980), and the causes of delamination have been investigated by many researchers (Delatte et al. 1998, Granju 2001, Kennedy 1978, Kennedy and Lister 1980, Nawy and Ukadike 1983, Peattie 1979, Saucier and Pigeon 1991, Shahin et al. 1986, Uzan et al. 1978 and Walraven 2007). However, no supplementary research has followed, and with the introduction of thin surfacing the problem remains serious. As the role of the top surface is that of a wearing course that could be replaced once worn-out, no significant attention to detection and evaluation of the bond with the underlying layer was given. However, this slippage or delamination problem of thin overlays is very frequent, and once they start wearing out the phenomenon is rapid, and even the initially sound areas get effected, leading to further damage. This will eventually increase the maintenance cost, labour and repair time. Therefore, it is the need of the hour to carry out a research study, in which, an earliest possible detection of the delamination and its classification will be a prime focus. This will eventually help in repairing the damage section before it spreads out, where, severe debonded sections will be sorted out first and so on and so forth. This well-timed evaluation of the delamination will also help in prioritising budgets, especially in these crucial times, when there is already a maintenance backlog of over10 years (ALARM 2019).

To determine the structural condition of a pavement structure, including that of the interfaces, two main approaches of can be employed: Destructive and Non-Destructive Testing (NDT). A destructive approach can produce accurate results, but it is obvious that it damages the pavement, it is time consuming, costly and causes traffic problems. Alternatively, the NDT approach is preferred over its counterpart, as it is fast, non-invasive and relatively less costly, but the main disadvantages, so far, are its limited

accuracy and high complexity, and requiring experience and expertise, to handle Non-destructive testing (NDT) equipment and especially, to interpret the results (Rens et al. 2005).

Nevertheless, it is widely established that in-situ NDT techniques have become an integral part of the road, pavement and bridge management repair process for selecting proper rehabilitation and reconstruction strategies (Rens et al. 2005, Scott et al. 2003 and Tawfiq et al. 2002). Several research studies have been carried out, however, no established NDT method, or programme exists for the reliable detection of delaminations below thin surfacings and overlays to date.

In the realm of civil engineering, the existing NDT methods for the detection and evaluation of damages, are generally based upon monitoring the continuous variation of stresses, or electromagnetic waves within the structure. In brief, two avenues of approach are available for non-destructive detection of delaminations at present:

1. The first, Involves the propagation, reflection, or interference of mechanical energy (stress waves).
2. The second, Involves electromagnetic energy, such as the Ground Penetrating Radar (GPR) or Infrared Thermography (IRT).

The spectral analysis of surface waves (SASW) as applied in the case of portable seismic pavement analyser (PSPA), seems to be only suitable for depths more than 100mm from the surface (Armitage et al. 2000 and Kruntcheva et al. 2000a, 2000b). Similarly, based on ultrasonic stress-waves propagating and reflecting through the test object, the impact echo method can determine the thickness of concrete's slabs, plates, hollow cylinders and beams. However, it cannot give information on the state of interface on either side of the layer below the test point. According to Davis et al. (1996), continuous calibration is required, and it is more effective in finding defects in Hot Mixed Asphalt layers, over 200mm thick. Other stress wave methods like the falling weight deflectometer (FWD) and light weight deflectometer (LWD), are chiefly

used for estimating the layer stiffnesses and their dynamic moduli through back-calculation algorithms (Al Hakim et al. 1997, 1998, 2000, Gomba 2004, Hammons et al. 2005 and Karadelis and Huges 1998). Generally, these techniques are suitable for layers more than 100mm thick in concrete pavements, and can reflect the bonding condition to an approximation but have uncertainties with the thin surface overlays (Nazarian et al. 2010 and Paul et al. 2007).

Regarding electromagnetic energy, IRT and GPR have been used together on a number of occasions in the civil engineering industry for different applications – concrete structures (Weil and Rowe 1998) and airport pavements. Several researchers (Moropoulou et al. 2001, Weil and Haefner 1989 and Weil and Rowe 1998) have shown that bridges, highway and airport pavements, tested with both, infrared scanner and radar, have disclosed a variety of debonding problems. However, the output from GPR show variations due to the presence of moisture content in the structure, which leads to misinterpretations and the need to repeated calibration. In addition, the strong reflections from the present rebars in the structure, tends to subside the small (0.3m wide) and near surface delaminated areas, hence, makes it vulnerable for the GPR to detect delamination closer to the top thin surfaces (Baright 1999, Evans et al. 2008 and Sultan and Washer 2018).

In UK, IRT is commonly used for the assessment of thermal insulation, moisture ingress, surface cooling, and dampness for all new, non-domestic buildings, mainly for qualitative assessments (BS EN 13187:1999).

IRT has been applied to non-destructive testing of delaminations of concrete and masonry bridges before (Hiasa et al. 2016, Watase et al. 2015 and Rehman et al. 2016), even with low ambient temperatures of $0.2^{o}C$-$0.3^{o}C$, experienced in northern Europe, to identify areas of delamination in a concrete bridge deck, closer to the surface (Clark et al. 2003).

IRT is a fast NDT technique, and at present, the available high speed IR-cameras can scan at a higher rate of 100Hz (FLIR Systems Inc. 2016), hence, able to cover long stretch of roads in no time. Second, the temperature resolution (smallest temperature difference that can be measured) of the high speed IR-cameras is as low as 0.02^{o}C, this easily fulfils the requirement, set by ASTM D4788-03:2013, in which the least difference to be classed as delamination must be of 0.5^{o}C, irrespective of the delamination size.

In general, these are high-priced cameras (£150k-200k) that could be mounted on a vehicle (for surveying roads, etc.), but the trade-off is the less labour cost in contrast to its counterpart destructive testing techniques. However, the overall IR-technique is not explored to a great extent in analysing the results qualitatively and/or quantitatively. Also, the IRT has limitations, while detecting the deeper defects (40-50mm) or the thin defects (3-1mm). Therefore, it needs exhaustive improvements in its approach, results interpretation and mode of applications, in order to use it for the detection and assessment of delamination (1-3mm thick) beneath thin overlays (40-50mm deep) in real pavements.

On the other hand, Impact hammer testing (stress waves method) has been used for the last few years, chiefly for the exposure, and evaluation of defects in engines and structures (Huang et al. 1997 and Storck et al. 2001). This method has shown some promising results within the scope of NDT&E. However, its application in pavement structures has been extremely limited . The essence of this technique is to monitor changes in the vibrational response of the structure, as a function of some defect. Due to the close relation between the vibrational response and the structure's natural frequencies, stiffness, damping and geometrical properties, this technique, combined with the appropriate operational procedures, and interpretation and processing of the data recorded, can provide promising results to detect and evaluate the delamination under thin overlays.

Conclusively, and prior to this investigation, IHT has the potential to give accurate and detailed results, whereas, IRT is a quick method in locating and providing an overall, initial account of the defects. These two methods will be investigated together, and after they undergo thorough improvement procedures, they will be integrated in a structural assessment and evaluation programme.

In essence, the first prime method, IRT, will be employed for a quick scan of the road surface, to identify potential delaminated areas and provide a partial quantification of the problem. In brief, this would be carried out by mounting a high resolution IR camera (or two) on a specially built vehicle (fully equipped with onboard computer and other accessories), that would scan the road surface and record the thermal images at a max speed of 10kph, followed by a special safety vehicle with flashing large yellow arrow to repel traffic from the particular lane and without the need for coning the road. This is considered to be fast road data collection. These recorded thermal images would be then transmitted to the on-board computer, where the first identification and classification of the delamination would take place.

However, if classification is not possible at all or even if it is partially quantified with the IRT, for such uncertain cases of delaminations, the complimentary IHT technique would take over. This IHT would be a modified version of light weight deflectometer (LWD), which will be fully controlled by the on-board computer by its designated (interface) software, so that the operator does not have to step out of the vehicle. In short, the modified IHT will be performed on the uncertain delamination regions, to provide an additional qualitative and quantitative assessment, and evaluation of the problem, that has not been classified by the IRT. This operation is expected to be relatively slow, and can vary from 2-3 minutes (one impact needed only) to several minutes, if more tests are necessary. However, it is anticipated that the recall of this complimentary IHT technique would not always be the case and in payback accuracy is the reward.

It is important to mention here that carrying out a full-scale operation (validation) on concrete roads, or bridge decks, combining IRT and IHT is not in the scope of this research. However, the guidelines will be set and envisioning of a ''New''-NDT&E method would be proposed (Details in Chapter 06 and 07).

1.3   Aim and Objectives of the Study

Based on the initial and preliminary evidence given above, the aim and objectives of the research were formed as follows:

1.3.1 Aim

The central aim of the research is to examine the feasibility of using/utilising two existing but incompatible NDT techniques (infrared thermography and impact hammer testing), to detect and assess flaw bond conditions beneath thin concrete overlays in rigid pavements.

1.3.2 Objectives

There are a number of benefits associated with these non-invasive methods, reported elsewhere in this research. However, a serious drawback and so far, compromise, is accuracy compared with their counterparts. Bearing the latter in mind the following four main objectives were set, as follows:

1. Selection and justification of the IRT and IHT as two complementary techniques for the detection and classification of the bond beneath thin overlays in pavements. Contrast the above (IRT+IHT) with similar NDT techniques.
2. Review the efficiency and reliability of both, IRT+IHT, as used for the evaluation of the bond under shallow overlays in concrete roads and airfields. Contrast the above (IRT+IHT) with similar NDT techniques.

3. Review and demonstrate effective and improved mechanics of IRT testing, as suited for pavement delamination, and use the method for fast initial surveillance of flaw bond detection and assessment in thin concrete overlays.

4. Review and demonstrate effective and improved applicability of IHT, borrowing existing technology from automotive and aerospace disciplines, and use the latter to suit civil engineering realm.

5. Perform extensive (mainly) quantitative analysis and processing of results collected. Review and discuss all findings, and suggest an integrated (IRT+IHT) and automated technique for the detection, and classification of bond quality under thin overlays in concrete pavements.

6. The use of FEA as a powerful supplementary tool, for aiding each NDT technique. This implies, of course, that if FE-models are validated, they can complement with the experimental shortcomings. If so, they can also replace the extensive lab work, as it should be much easier to carry out different tests using a FEA code than changing the real system every time.

1.4 Outline of Thesis

Based on the above it was decided to divide the research work into 7 chapters. The outline of which is as follows:

Chapter 1 provides an overview, motivation and the research justification. This includes a brief discussion on the definition of problem, stresses the significance of the structural health monitoring of the pavement structures around the globe. Moreover, it justifies briefly, the preference of NDT approach over its counterpart, and the broad classification of the NDT techniques, concisely highlighting their advantages and limitations for assessing the particular problem of delamination in thin overlays. Infrared thermography (IRT) together with impact hammer testing (IHT), are the two initially non-compatible NDT techniques, proposed for this feasibility study, in order to detect and assess the flaw bond beneath thin concrete overlays. The aim and main

objectives, as well as a brief outline of thesis are presented in the same chapter. Finally, the novelty and contribution of this research is highlighted at the end.

A Gantt chart to facilitate the management of the research itself is also developed (Figure 1-2).

Chapter 2 is associated with the first objective and presents the important global literature review. This includes briefly, the common types of distresses encountered in rigid pavements, the specific problem of delamination and its potential causes. However, the main theme of this chapter is the critical review of several popular NDT methods including IRT and IHT, used for detecting delamination and providing an account of the condition of the bond. A justification for adopting the aforementioned IRT and IHT methods, is also given, based on their advantages, limitations and room for improvements.

Chapter 3 presents the general methodology, justifying the method of collecting data adopted, centred around the hypothesis and referring to research questions. This chapter also presents a synoptic flow chart at the end portraying the global methodology together to detect and assess the flaw bond by incorporating IRT and IHT in a systematic way, in addition to respective IRT and IHT procedures summary.

Chapter 4 covers all the laboratory based tests, carried out via IRT on the designed concrete slabs together with their FE-models. The latter is deemed to be necessary, because, FE-models can replace time consuming and costly laboratory tests. They can be used as a prediction tool, and provide that essential confidence, complimenting each other. The first section covers the working principles behind IRT, followed by the requirements, tips and precautions of practically carrying out IRT testing in the real life. Further, it includes the theoretical background of thermal analysis, giving an insight to the adopted NDT technique, by explaining the physics and mathematics involved, and their use for the particular applications. The second section, the main substance of this chapter, includes the configuration of the laboratory IRT tests, on the designed concrete

slabs, the recording of thermograms, post processing analysis and extensive discussion. These laboratory scaled tests, are supplemented by finite element modelling. The FE-models are verified and calibrated, by adopting the similar input boundary conditions, recorded during the real time experiments. Finally, a comparison is made between the experimental and FE results, and some initial inferences are made.

Chapter 5 presents an extensive laboratory testing regime on carefully designed concrete slabs via IHT. The first section of the chapter, presents in detail, the working principle behind experimental modal analysis (EMA), followed by the basic governing equations of FE-modal analysis. The second section, covers all the tests carried out with the IHT on the casted slabs, including the ones, tested previously with IR-camera (IRT). All the experimental tests are accompanied by their corresponding FE-models, and the results are compared in order to ascertain the reliability and validity of these FE-models.

Chapter 6 is a crucial chapter. It attempts to combine the two initially non-compatible NDT techniques (IRT and IHT) into one, capable of making prediction, related to the bond condition at interface, and shallow depth under the surface of a concrete slab. This chapter discusses the development of a '*New-NDT&E method',* for the flaw bond detection and assessment. That includes the whole procedure, envisioning the feasibility of using them together remotely, in a real-life scenario by introducing elements of automation in the new proposed methodology.

Chapter 7 is important as it provides the key findings from the combined results obtained from IRT and IHT tests, principal limitations and recommendations for future works. This chapter includes author's opinions, comments plus criticism, as well as advantages and drawbacks of the employed NDT&E techniques, as they were deployed. A proposed implementation scenario is also presented at the end, in order to demonstrate the real time implementation of the proposed method, for the detection and classification of the flaw bond (delamination) beneath thin overlays.

A thesis Synopsis, in a form of business chart, is shown in Figure 1-1.
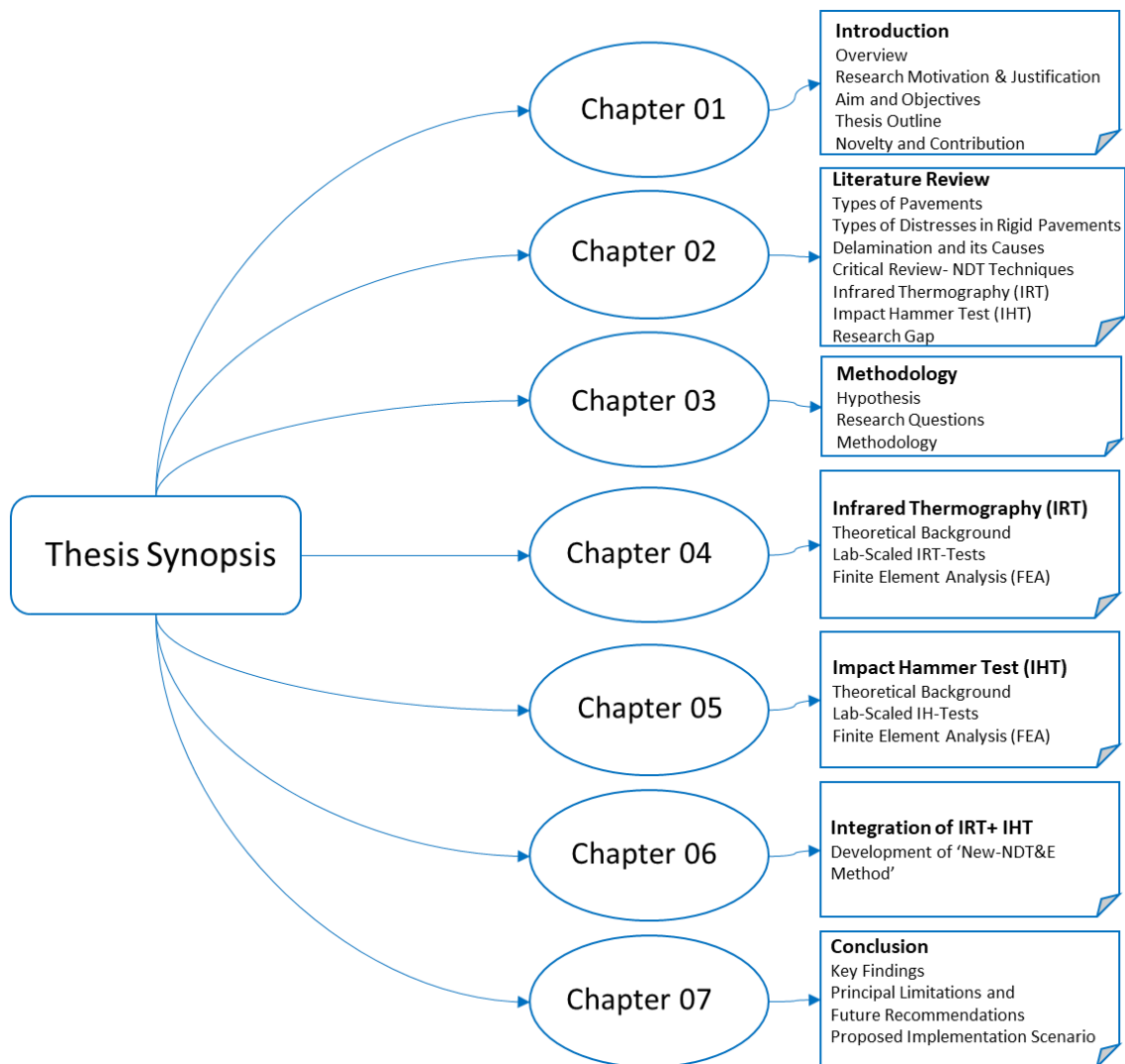
Figure 1-1: Thesis Outline-Synoptic Chart.

1.5 Novelty and Contribution

The novelty and contribution of this thesis lies in unveiling the potential combined usage of initially non-compatible NDT techniques (IRT and IHT) for the very first time, for detecting and evaluating delaminations beneath thin overlays in rigid pavements (roads, airfields and bridge decks).

This in further, relates to the improvements of each selected NDT technique (IRT & IHT), and setting a base, or guidelines for a ''new'', integrated-NDT&E Method, where

the second technique complements the first. In fact, the selection and justification of the aforementioned techniques were first carried out, while contrasting them with other potentially effective NDT techniques (Chapter 02-Literature Review) and the benefits and drawbacks of each of them were considered, and weighted against some basic criteria such as feasibility, ease and speed of operation and future development.

It is also important to mention that since this is a pilot study, all the work was carried out under normal laboratory conditions, backed, and enhanced, of course, by corresponding and suitable FEA. Full-scaled testing (field tests-validation) were not performed (not in the scope).

However, to keep "boundary conditions" as close as possible to real, some tests (IRT) were also carried out outside the laboratory, using ambient settings. The advantage with the latter is that experimentation under the direct sunlight and specifically the direction of the sunrays (position of the sun relative to the test specimens) was possible. Some useful data were collected and corresponding observations were made. This has also made a certain contribution to the novelty and originality of the research.

Each technique (IRT & IHT) was explored separately, before setting the guidelines for the combined/integrated NDT&E Method. The main and promising contributions after improvements are highlighted below:

1.   In contrast to its qualitative nature, IRT (passive) was also used as a quantitative technique, where the defects were detected, and a first assessment regarding the severity of defects (voids/delaminations) was made with the help of thermograms and unique thermal contrast values. These unique thermal contrast values, along with their time of occurrence and the respective thermograms for each defect, helped in quantifying and classifying the delamination/void itself.

In addition, it was shown how by utilising the 'standard thermal contrast' in passive thermography, helped improving the efficiency of the whole method, where all the

defects (voids/delaminations) could be evaluated within 100s - 300s (2-5 mins approx.) by their unique thermal contrast (ΔT) peak values. This quantification approach was a significant improvement in the 'Passive thermography' method, as it helped interpreting the results beyond the typical coloured images (thermograms). The latter was initially only confined to 'Active thermography'.

2.   FEA was introduced for complementing the experimental IRT results and their interpretation. This is also relatively new in passive IRT, but it helped in improving the reliability of the NDT method. It also helped in the assessment of the defects providing a decent accuracy (average error <10% approx.). As mentioned earlier, some tests were also conducted outside the laboratory, taking into account the real environmental conditions and calibrating the numerical models accordingly. It was found that the best time for carrying out IRT tests in a day (noon time), and with a suitable wind speed (<10kph). Optimum conditions were also suggested based on the experimental tests results.

3.   The defects (voids/delaminations) of minimal thicknesses (5mm, 3mm, 2.5mm and 1mm) at depths of 10mm, 20mm, 30mm and 40mm from the concrete surface, were assessed (qualitatively + quantitatively) for the very first time through the IRT (passive) method. Each thickness of voids represented the severity of damage or the stages of delaminations (Initial, Intermediate and Severe). It was inferred that as the depth of the defect (void/delamination) was increased (>30mm) from the concrete surface and the thickness of the defect was reduced (<3mm), the accuracy of IRT method was becoming uncertain, leading to complex interpretations of the results. This also highlighted the limitations of IRT technique. In order to cope with these limitations, the supplementary method, IHT, was introduced, and the final assessment/evaluation of the defects (delaminations/voids) were carried out, accompanied by corresponding numerical modelling with an acceptable accuracy (error below 3%).

4.   Finally, some guidelines and a detailed procedure for a combined ''NEW''-NDT method was proposed and illustrated with the help of flowcharts etc, where the two

initially non-compatible techniques (IRT & IHT) were deployed together, and complementing each other, for the detection and assessment of delamination beneath thin overlays in real pavements.

It is important to mention here that all the laboratory investigation was carried out using very small specimens and samples (concrete slabs, void, etc). This made the detection and classification work significantly more difficult/complex than dealing with full-scale roads and delaminations.

It is therefore not unreasonable to conclude that the method would perform more accurately on actual size roads with actual size delaminations.

PHD STUDENT: ADIL IDREES KHAN **ID:** 6194617
DIRECTOR OF STUDIES: DR JOHN KARADELIS
SUPERVISORS: DR. ADEGKE OLUBANWO AND DR. LUIGI SIMEONE
PROJECT TITLE: NON INVASIVE DAMAGE DETECTION AND CLASSIFICATION OF THE BOND BENEATH THIN OVERLAYS IN RIGID PAVEMENTS. A PILOT STUDY

2016-2020	ID	Year	2016	2017	2018	2019	2020
		Month	Oct Nov Dec	Jan Feb Mar Apr May Jun Jul Aug Sep Oct Nov Dec	Jan Feb Mar Apr May Jun Jul Aug Sep Oct Nov Dec	Jan Feb Mar Apr May Jun Jul Aug Sep Oct Nov Dec	Jan Feb Mar Apr May Jun Jul

PHASE I

Critical Literature Review + Methogology
Justification of Selecting IRT and IHT
Finding Research Gaps in IRT & IHT
Room for Improvements shortlisted for IRT & IHT
Methodology

Phase-I: LITERATURE REVIEW + METHO

ID	Task	
1	Introduction	INTRODUCTION
2	Literature Review	LITERATURE REVIEW
3	Methodology (Hypothesis & Research Questions, Global Methodology)	METHODOLOGY
5	Preparing for Phase 1 - PRP, Write up of 5000 words of Literature Review, Phase 1-Progressive Review Panel (PRP).	PRP-1 ◆

PHASE II

1) Preliminary Testing + Preliminary FEA. 2) Reviewing & demonstrating effective & improved mechanics of IRT testing. 3)Reviewing the efficiency and applicability of IHT

Phase-II: Pre-IRT & IHT (EXP + FEA)

ID	Task	
6	Uncovering IRT	
	1) Desiging of a Single Concrete Slab with Flaws (Voids). 2)Preliminary Test via 'active' and 'passive thermography' for familiarisation. 3) Preliminary FEA (Thermal Analysis)	UNCOVERING 'IRT'
7	Uncovering IHT	
	1) Designing Preliminary platform for IHT testing in labortary. 2)Casting Single and Double Concrete Slabs (No Bonding). 3)Testing with small impact hammer and analysing the results. 4)Preliminary FEA (Modal Analysis)	UNCOVERING 'IHT'
8	Preparing for Phase 2 - PRP, Write up of IHT whole development, updated literature review, Phase 2 - Progress Review Panel (PRP).	PRP-2 ◆

PHASE III

1) Optimizae and Integrate (IRT+IHT). 2) Casting of Single and Double Concrete Slabs (Flawed+Sound). 3) Designing & Replicating real time support conditions (Subgrade). 4) IH-Testing via small & medium sized hammer + FEA. 5) IRT-Testing of similar slabs outside the Civil. Engr. Lab + FEA. 6) Development of a "NEW"-NDT&E METHOD & Proposed Implementation Scenario on the integrated use of IRT &IHT.

Notes:

1. CHRISTMAS AND EASTER TIMES HAVE BEEN ALLOWED FOR
2. ANNUAL LEAVE HAS NOT BEEN ENTERED IN THE PLAN
3. MILESTONES SIGNIFY A COMPLETED PART OF THE RESEARCH AT A SPECIFIC TIME ◆

Phase-III: INTEGRATING IRT + IHT

ID	Task	
9	Essential Tests IHT + FEA	ESSENTIAL TESTS 'IHT'
10	Essential Tests IRT + FEA	ESSESNTIAL TESTS 'IRT'
11	Integrating IRT + IHT, Development of 'New NDT&E Method'	Integrating IRT + IHT
12	Preparing for Phase 3 - PRP, First Draft Thesis, Phase 3 - Progress Review Panel (PRP).	PRP-3 ◆

PHASE IV

Thesis Write Up, Literature Review Updates, Final Touches

Phase-IV: THESIS WRITE UP

ID	Task	
13	Conclusions, Principal Limitations & Future Recommendations	CONCLUSIONS
14	Thesis writing up.	THESIS COMPILATION
15	Submitting Final Thesis and preparing for Viva.	SUBMISSION ◆

Figure 1-2: Gantt Chart for this Research Study.

Chapter 2 - Literature Review

2.1 Introduction

The literature review for this research study is divided into nine sections, as summarised in Figure 2-1.

CH 02: Literature Review

Figure 2-1: Synoptic Plan for Literature Review.

2.2 Types of Pavements

Based on their structural performance, pavements can be classified broadly into two, flexible and rigid pavements (Mathew and Rao 2007). The road pavements development (pavement is the technical term used for roads and not the one being used commonly for sidewalks) has been occurring across the world in different countries with slight biases, hence, with different terminologies.

Flexible pavements are generally a mixture of aggregates, filler, and asphaltic or bituminous material, placed on a bed of granular compacted layers of materials with appropriate quality over the subgrade (Nicholls 1998 and The Constructor-Civil Engineering Home 2015). According to Lenz and Russel (2011), true flexible pavement is the one, that yields 'elastically' to traffic loading.

However, this research is primarily focussing on concrete overlays, i.e. rigid pavements, therefore, the details of flexible pavements are not part of this literature.

2.3 Rigid Pavements

By definition rigid pavements are the type of pavements that provide high flexural strength or high bending resistance, and it distributes loads to the foundation over a comparatively large area (Civil Engg Dictionary 2014, Mathew and Rao 2007 and WebFinance Inc 2017). Cement Concrete is the essence of rigid pavements and according to Jeuffroy and Sauterey (1996), concrete denotes a mixture of materials, mainly gravel and sand, which is agglomerated by cement, hydraulic binder and after being mixed with water, it sets and imparts considerable hardness to the mixture. According to Mathew and Rao (2007), rigid pavements behave like a plate placed on a viscous medium. The load is distributed by the slab action and wheel load is transmitted to a wider area (Figure 2-2).
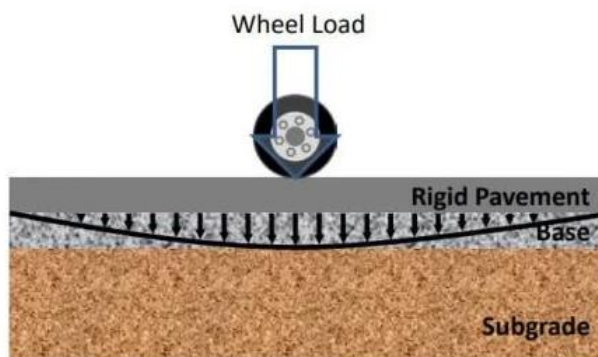
Figure 2-2: Load Distribution in rigid pavements (The Construction-Civil Engineering Home 2015).

2.3.1 Composition of Rigid pavements

Portland cement concrete is the prime structural element in the rigid pavements (The Construction-Civil Engineering Home 2015). In concrete pavements, the concrete slab generally is placed on the compacted sub-base or treated subbase, which is further supported by the compacted sub-grade. The purpose of the sub-base is to provide support uniformity and the sub-surface drainage (Figure 2-3).
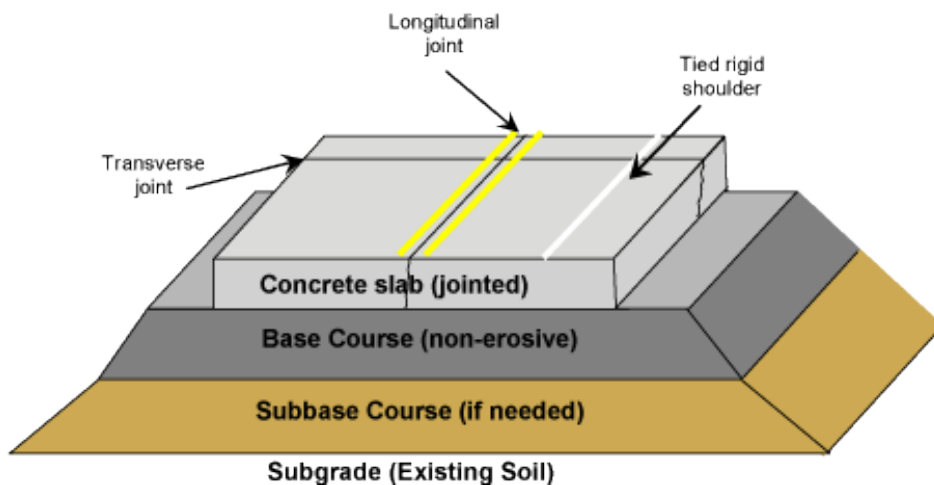
Figure 2-3: Concrete pavement layering system (The Construction-Civil Engineering Home 2015).

Briefly, the concrete pavements are consisted of the following layers, as illustrated in Figure 2-3.

a. **Concrete Slab (Surface layer or Overlay):** Surface layer provides the structural support, skid resistance and also prevents water seeping down into sub-base. It is also known as the overlay and is generally 40-50 mm thick (The Construction-Civil Engineering Home 2015).

b. **Base Course:** It provides uniform support to the pavement slab. It also intends to control frost action, provides sub-surface drainage, provides stable platform for the rigid pavements and also prevents mud-pumping of fine-grained soils (Figure 2-3).

c. **Stabilized Sub-base:** The sub-base is, generally constructed in the rigid pavements, where the weight of the vehicles is brought into account like in runways or aircraft parking lots (Figure 2-3).

d. **Subgrade:** It is the compacted soil foundation layer in the pavement system. Principally they are subjected to lower stresses as compared to the surface and sub-base course. Subgrade soil vary from place to place and the interrelationship of texture, moisture content, density and strength of subgrade material is complex. Similarly, the ability of soil to resist shear and deformation varies with the density and moisture content (The Construction-Civil Engineering Home 2015).

2.4 Types of Distresses in Rigid Pavements, Common Mechanisms of Failure

Pavements under transient loading, with faulty design and low quality material, faces various types of distresses, which eventually leads to their failure. Few typically encountered distresses in concrete pavements are as follow:

2.4.1 Cracking in Concrete Pavements

According to Delatte (2008), cracks can be formed in concrete pavements by one time loading or by a repeated fatigue loading. The Constructor-Civil Engineering Home (2017) and Huang (2006) describes cracking in concrete pavements results due to the stresses caused by contraction, expansion or due to curling, warping of the pavements. Overloading, improper cutting of joints and insufficient or loss of subgrade support could be the other possible causes of cracking in concrete pavements. The various types of cracks that can occur are as follows:

a. **Longitudinal and Transverse Cracks:** According to Miller et al. (2003), longitudinal cracks are parallel to the centre line (Figure 2-4) of the pavement.

Huang (2006) suggests, these cracks are formed by repeated fatigue loading, loss of foundation support, improper longitudinal joints design and curling or warping stresses. According to Delatte (2008) if these cracks are not along the wheel path, their effect on the performance can be considered insignificant. If longitudinal joints are not provided, these cracks can be seen at the crowns of crowned pavements (Rollings 2011).

Transverse Cracks are defined to be the perpendicular cracks (Figure 2-4) to the centreline (Miller et al. 2003). Huang (2006) has noted that, 'Transverse cracks are usually formed due to repeated heavy loading, temperature gradient, moisture gradient and dry shrinkage'. Yu et al. (1998) found out that the higher risk of these cracks in the longer joint spacing are in drier climates due to the fact of the high temperature gradient.

Figure 2-4: Longitudinal cracking (L) and Transverse cracking (R) in concrete pavements (FHWA 2003).

b. **Corner Breaks:** Corner breaks occur at the corner of concrete slabs (Figure 2-5). Usually a triangular concrete piece from 0.3m to half the width of the slab, breaks off from the edge (Miller et al. 2003). These occur more likely in longer slabs, and when heavy vehicles travels across them, the edges warp or curl upwards, therefore, leaving unsupported at the edge, which eventually breaks off (Delatte 2008).

Figure 2-5: Corner Breaks in concrete pavement (FHWA 2003).

c. **Durability ('D') Cracking:** Durability or 'D' cracking occurs more likely near joints (Figure 2-6), and is manifested as 'closely spaced crescent shaped hairline cracking pattern' (Miller et al. 2003). Yoder and Witczak (1975) found out that the phenomenon is regional, and is caused by the inability of concrete to withstand severe climatic conditions or due to use of non-durable material. The cracks are mostly dark than the sound areas. According to Huang (2006), freeze-thaw expansion is the cause of these cracks in some types of coarse aggregate. Mindess et al. (2003) noted that there is a critical size of coarse aggregates, below which they are not susceptible to fracture.

Figure 2-6: D-cracking in concrete pavement (Desta 2014).

d. **Joint Seal Damage:** Joint seals are used in order to prevent water seepage and incompressible materials to accumulate into the joints. These materials can lead to stress concentrations at the joints by preventing the slab to expansion during hot weather, and therefore, may leads to buckling, shattering or spalling (Delatte 2008).

Typical joint seal failure includes extrusion (coming out of seal from the joints), adhesive failure (bonding loss), complete loss of sealant (Figure 2-7), foreign material intrusion or weed growth (Miller et al. 2003).

Figure 2-7: Medium level of joint seal damage (FHWA 2003).

e. **Shattered Slab:** The shattered slabs are defined by The Constructor-Civil Engineering Home (2017), as slabs, in which the intersecting cracks breaks the whole slab into four or more pieces (Figure 2-8). This may be caused by overloading or inadequate support. Usually it is the combination of the two.

Figure 2-8: Shattered Slab (The Constructor-Civil Engineering Home 2017).

2.4.2 Water Bleeding and Pumping

These types of distresses (Figure 2-9) refer to 'seeping or ejecting of water beneath the slab surface through cracks' (Delatte 2008). Sometimes, it could be detectable from the fine material deposits, near the pavement surface, that have been eroded or pumped from the support layers, and therefore, stains the surface (Miller et al. 2003). Yoder and Witczak (1975), found out, and gave an excellent discussion on pumping, saying, active pumping just happens after the rainfall, and was first noticed when the pavements were directly built on the plastic clay soils. Compression of the soil due to heavy loadings, led to the creation of the voids spacing under the pavement, therefore, making a way out for the water to be stored here, which further under the traffic loading and with pump-able material like high plasticity clay, was then pumped out. This phenomenon may be gradual, and couldn't be noticed until years after construction. According to Huang (2004), when pumping takes place, the material under the slab must be saturated, the traffic loading must be frequent, and the material should be erodible.

Figure 2-9: Water bleeding in concrete pavement (FHWA 2003).

2.4.3 Contaminants

Rubber deposits from the vehicles tires on the pavement surface, reduces the skid resistance or desired friction characteristic of the pavement surface (Figure 2-10). Similarly, contaminants like oil spills and other similar, also lower the skid resistance of the pavements (The Constructor-Civil Engineering Home 2017).

Figure 2-10: Contaminants in concrete pavement (The Constructor-Civil Engineering Home 2017).

2.5   The Delamination Problem in Concrete Overlays and Its Causes

Delamination in concrete overlays occurs quite frequently. This problem leads to further distresses in the pavement infrastructures.

According to the following references (Maintenance Technical Advisory Guide 2003, Miller et al. 2003, Patel 2010 and Virginia Department of Transportation 2012), delamination is the separation, in the pavement, due to poor adhesion between the surface and underlying layers (Figure 2-11). Usually in delamination, a clear separation of top from the layer below is observed, and as a result of poor bonding and adhesion, slippage cracking may occur (Miller et al. 2003). A report published by NRMCA (2000), found that in most of the delaminated concrete slabs (trowelled concrete surfaces), the top (30 to 50mm) is densified, primarily due to improper or premature finishing, which is further separated by a thin layer of water or air. The size of delaminations may range from several square inches to several square feet. Traffic and freezing, further exacerbates the problem and may break the surface into large sheets (NRMCA 2000).
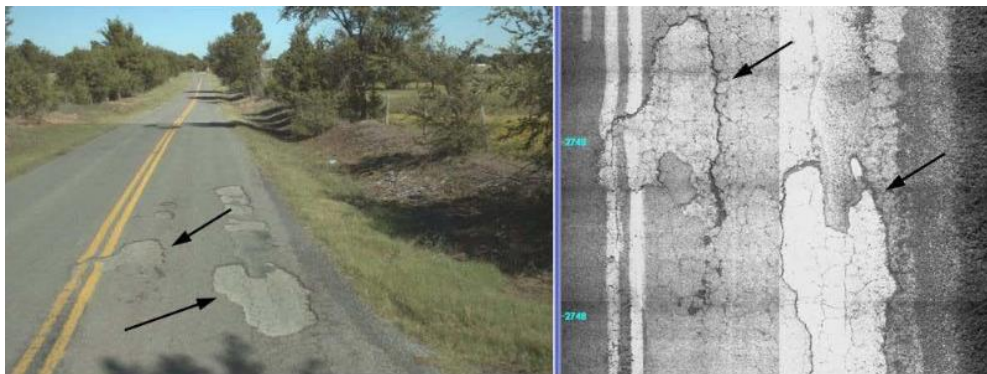
Figure 2-11: Delamination in pavements (Virginia Department of Transportation 2012).

One of the main purposes of the interface, is to prevent the relative lateral and longitudinal movements, transferring the horizontal shear stress among the various layers. The likely causes of the poor bonding between interlayers and their effects on

the multi-layered pavements, especially in thin (40mm-50mm) concrete or asphalt overlay pavements have been studied in several research projects. Although, the real causes of the poor bonding are still in research, and no definite causes have been determined yet. However, there are still some important factors that are being identified with time, and they play a significant role in enhancing the risk of slippage failure due to debonding in pavement layers. These are as follows:

- Base Course Material: According to Kennedy (1978) and Peattie (1979) , if the base course is made up of material, specifically, dry bound granular material, and if laid down in unfavourable conditions like rainy weather, improper moisture content, the pavement is more prone to slippage failure.

- Improper Compaction of Base/Sub-base/Subgrade Course: According to Al Hakim et al. (2000), Khweir et al. (2003) and Nicholas (1979), the low compaction of the base course/sub-base course or subgrade course will cause low stiffness of these layers, which eventually leads to material degradation at the interface. This further results in weak zones at the interface, and becomes vulnerable to the water damage, and therefore, increasing the risk of loss of cohesion.

- Temperature during Pavement Construction: According to the following references (Al Hakim et al. 2000, Kennedy and Lister 1979, Nicholas 1979 and Peattie 1979) the temperature gradient between the wearing course and the binder course, has to be given significant consideration, while laying the wearing course. As in cold weather, the underneath layer is having low temperature, and if the hot wearing course (overlay) is laid over it, will result in reasonable poor bonding between the two. Therefore, a high risk of developing a slip at interface will occur due to insufficient interlayer resistance.

- Contamination at the Interface: Al Hakim et al. (2000) and Khweir et al. (2003) reported that, this type of contamination happens usually during the construction (dust or oil spillage from the construction traffic). This can also result in poor interlayer bonding.

- Wet freezing and Thaw cycles Conditions: Through the cracks, the water seeps down through the surface. During the wet freezing season and due to thaw-cycles, the water freezes, and expands, therefore, pushing the layer upward. Furthermore, with the continuous heavy vehicles loading, the problem exacerbates and spreads out to the other sound interface as well, and thus causing delamination drastically, which is not apparent in the start, but later on brings drastic change in the pavement structure leading to damages like slippage, delamination, and potholes etc. (Raab and Partl 2010).

2.6   Critical Review of Non-Destructive Testing (NDT) Techniques

In parallel to the findings on slippage failure (Delatte et al. 1998, Granju 2001, Kennedy 1978, Kennedy and Lister 1980, Nawy and Ukadike 1983, Peattie 1979, Saucier and Pigeon 1991, Shahin et al. 1986, Uzan et al. 1978 and Walraven 2007), several investigations have been carried out through various NDT techniques, for detecting and evaluating delaminations, at the interfaces of concrete or asphalt overlays. Some techniques seemed promising, and some had feasibility issues with the detection of particular problem of thin overlays delamination. However, a brief critical review of all the possible contenders (NDT techniques) for using them in detecting and evaluating delamination, under thin overlays (40-50mm) in pavements, has been carried out and reported in this section. This is followed by a summary, and finally the selection of the NDT techniques, which are going to be used in this research study for detecting and evaluating the delamination.

NDT techniques that are mainly used for the pavement evaluation, can be classified, based on their working principles into the following categories (Table 2-1).

Table 2-1: NDT Techniques for Pavement Evaluation.

NDT Techniques for Pavement Evaluation	
Stress Waves based Techniques	**Electromagnetic waves based Techniques**
• Impact Echo (IE)	• Ground Penetrating Radar (GPR)
• Ultrasonic Surface Waves (USW)	• Infrared Thermography (IRT)
• Stiffness Gauge (SG)	
• Falling Weight Deflectometer (FWD)	
• Light Weight Deflectometer (LWD)	
• Impact Hammer Test (IHT)	

2.6.1 The Impact Echo Method (IE)

This method was introduced in 1980 by Carino and Sansalone (Please refer Carino et al. 1986, for comprehensive discussion). The detection of defect is based on the reflection of the impact-generated stress (sound) waves from the internal flaw, after being propagated through the test specimen by means of a mechanical impact. The reflection of the impact-generated stress (sound) wave occurs at the interface of the separating materials with different densities and elastic properties, and is received at the surface by a transducer, acting as a receiver. By measuring the speed of the stress wave, the distance of the reflecting boundary is determined and compared with the calibrated measurements (Abramo 2011, Carino 2001, Sansalone and Carino 1986 and Zhang et al. 2016). Researchers (Abramo 2011, Azari et al. 2014, Chaudhary 2013, Davis et al. 1996, Garbacz et al. 2017, Hoegh et al. 2011, Mazzeo et al. 2012, Sansalone and Carino 1986 and Zhang et al. 2016) have shown that impact echo method is generally used for detecting the defects (voids, delaminations) but has almost no capability of full condition assessment i.e. classifying the defect and its severity, in the concrete pavements. In addition, it was noticed that the heterogeneous nature of concrete (presence of binder aggregates interfaces, air voids, porosity, and reinforcing steel etc.)

resulted in multitudes of echoes, that not only obscured from real defects, but also led to lots of calibration and complex interpretation. According to Lin and Sansalone (1996), the impact echo method could be used for evaluating the bond quality between overlay and base in concrete pavements, but it is not possible to determine the bond strength. According to Abramo (2011), the IE method has the ability to show the defect depth in the concrete pavements. However, it is a complex procedure to classify those material characteristics that produce the reflections. For example, the IE method cannot differentiate a response that happens due to air voids, reinforced steel or large aggregate and is sensitive to the size of the slab, hence, more fine-tuning calibration is required. Similarly, according to Armitage et al. (2000), the IE method is more effective in finding the delamination in hot mix asphalt (HMA) layer that is more than 200 mm deep. Celaya (2011) found out that the IE method has limitations in dealing with coarser mixes, and is not feasible in detecting delamination under thin top layer in HMA (40-50mm) with reliability. Furthermore, complex interpretation of the obtained graphs is another issue that requires, frequent calibrations and an experienced operator with thorough understanding of the structure. One main limitation of this technique is to know the defect prior to inspection, which makes it time consuming, as it is a localised testing, therefore, it is generally used as a supplementary technique with other NDT techniques like infrared thermography or ground penetrating radar (Abramo 2011).

2.6.2 The Ultrasonic Surface Waves (USW)

Another popular method used for the delamination detection in the concrete pavements is the ultrasonic surface waves (USW) technique. In ultrasonic testing, high frequencies (greater than 20,000Hz) are generally used, to detect shallow defects like delamination in the rigid pavements (IAEA 2002). A transducer is used to produce sound waves that travel through the material, and are reflected from any anomaly present within the material, which is then received at the surface by the receiving transducer, similar to the IE method. Further analysis of the signals received, gives information regarding the media they have passed through (Hoegh 2012). Generally the USW method is used for estimating the elastic modulus of the material (Carino et al. 1986 and Gucunski et al.

2000). Research carried out by Azari et al. (2014), on the sensitivity of combined techniques, (ultrasonic surface waves and impact echo) in concrete pavements assessment, demonstrated the efficiency of IE and USW in detecting the delamination and voids, ranging from shallow depths (50 mm) to higher depth of (200 mm). The delaminated area was observed with the low frequency peak, and the closer the delamination was to the surface, the lower the frequency peak was observed. High frequency peaks were observed for deeper defects. The results were analysed in PSPA (Portable Seismic Pavement Analyser). Frequency response was used for the IE results analysis, where dispersion curves were used for USW results analyses, in order to find the apparent moduli at different points due to discontinuity. The IE method was quite sensitive to the size and thickness of the slab. It was observed that the reflected waves may interfere with the ongoing signals due to reflection from the lateral boundaries, and therefore, an error in the measurement could be seen in the IE frequency response. Unlike IE, USW results were not affected significantly with the size of the slabs, but with the depth only. The combined method of IE and USW could be made accurate, with more and more calibration, as the exact cause of the wave reflection is hard to determine directly. The error was observed due to the lateral boundaries reflection but the way to overcome it and optimize the procedure was not reported. Similarly, in USW, more points have to be tested and calibrated, as each delay in the wave could not be necessarily associated with the delamination, and there are other factors too that could be the reason for delay. For instance, discontinuity within the material. Overall strength of the material could be predicted through USW, however, the information about the defect's presence, their numbers, sizes, depth, locations, are hard to obtain from this technique. According to Celaya (2011), the modulus of two similar layers bonded together is more or less constant, where, in debonding the modulus will significantly decrease at the interface. This variation in the elastic modulus could be utilised, if calibrated appropriately, to indicate the delamination. However, the depth of debonding, severity of delamination, its size and its exact location, is hard to find through this method alone.

2.6.3 The Stiffness Gauge (SG)

The stiffness gauge imparts energy in the structure, within the range of 100 to 200Hz and it is optimized for low stiffness geo-materials (Celaya 2011). So neither the force, nor the frequency range is compatible for the delamination detection in the rigid or flexible pavements. A study by (Lepert et al. 1992) has shown that this method may not be very efficient in finding the debonding between the interfaces, even in controlled experimental study test specimens. And to the date, no clear report or study has been done on flexible or rigid pavements delamination or sub-surface defects.

2.6.4 Falling Weight Deflectometer (FWD)

The falling weight deflectometer (FWD) is a well-known NDT technique, used widely by the civil engineers in the evaluation of the pavements, including quantification of the joints condition in the concrete pavements, also detecting deterioration in cement treated layers beneath the overlay (Karadelis 1999). This method is based on the surface deflection formed, when a falling weight falls on a plate, already rested on the pavement surface. It simulates the wheel loading on the surface, and the deflection sensors (geophones, force balance seismometers) mounted radially from the load plate centre measure the deformation response in the pavement. This is further analysed, to calculate the stiffness related parameters like the elastic moduli. Various studies have been carried out to find the feasibility for evaluating the delamination in the flexible and rigid pavements. High deflections can indicate poor bonding between asphalt layers (Karadelis and Hughes 1998 and Nazarian et al. 2010).

Lepert et al. (1992) summarized some of the earlier studies based on deflection principle, that the deflection based measurement devices like deflection graphs and FWD, are not suitable for interface debonding assessment in pavement layers. However, recent studies have shown some potential in this technique to detect delamination in flexible pavements (Al Hakim et al. 1997, 1998, 2000, Gomba 2004 and Hammons et al. 2005). These studies have included new 'backcalculation' algorithms to estimate

reasonably the interface stiffness, reflecting the interface bonding condition (Al Hakim et al. 1997, 1998, 2000). Estimating the slippage susceptibility between the interface layers, and calculating the interface stiffness through back calculation algorithms, gives some good approximation of the bonding condition (Gomba 2004 and Hammons et al. 2005). But according to Al Hakim et al. (1997) and Armitage et al. (2000), these approaches have problems, such as uncertainty and difficulty for assessing the bonding conditions between thin layers.

A report structured by Heitzman et al. (2013), summarises that Nazarian et al. (2010) have found out the uncertainty in the 'backcalculation' of moduli in thin overlays. A research carried out by Nazarian et al. (2010), along with Airport Asphalt Pavement Technology Programme (AAPTP), evaluated the FWD on the controlled section of asphalt pavement to assess the delamination. A specified controlled pavement was designed with around 8in of asphalt placed in three lifts, along with deliberate debondings at various depths and levels. A FWD specified with 305mm diameter load plate along with seven geophones at 305mm intervals were used. About 6000lb equivalent load was applied on the specified locations in the asphalt section. The following conclusions were drawn on the basis of experimental study:

- The FWD could be used for detecting the presence of fully debonded area at shallow depths and the partial debonded area with less certainty.
- Due to the temperature susceptibility of HMA, it was observed FWD was more effective in cool weather, which showed some uncertainty in the hot weather.
- There was a concern with the FWD false positive reading in estimation of moduli due to temperature dependent asphalt elastic moduli, especially it was observed in hot weather.

This method as mentioned and in the author's remarks, is a good NDT technique for delamination detection but no rigorous results have been reported for the size, shape, depth of delaminations under thin surfacings pavements. Data obtained from the NDT testing is used for the back calculation of pavement layers moduli through the Artificial

Intelligence (AI) based techniques. Up to date, several AI based techniques have been proposed (Gopalakrishnan and Papadopoulos 2011), but not a single technique can be used with full confidence as they only yield a predictive value, and therefore, further calibration or validity is still required on the credibility and accuracy of the information.

2.6.5 Light Weight Deflectometer (LWD)

Light weight deflectometer (LWD) also known as 'light falling weight deflectometer', is a light drop weight tester and a hand portable device (Elhakim et al. 2014). This method was developed in particular to measure the soil in situ dynamic modulus, in order to check the subsoil degree of compaction (Elhakim et al. 2014). According to Celaya (2011), the light weight deflectometer (LWD) is unsuitable for delamination detection for the thin overlays, due to the fact that generally the impulse duration is long and is not feasible for shallow defects. Moreover, after an extensive literature review, there are no clear cases found, where LWD is used for detecting or evaluating delamination in thin overlays.

2.6.6 Impact Hammer Test Method (IHT)

The basic working principle behind the impact hammer test, or the impulse response method, is imparting the impulse loading to the structure, whose vertical dynamic response is measured through the accelerometers (Sangiorgi et al. 2003). The dynamic response is then evaluated, and is mainly represented by natural frequencies, mode shapes and damping ratios, also known as the modal parameters (Ewins 2000). This analysis is known as Modal Analysis (Please refer Ewins *(2000)* for more details). In principle, IHT method is quite similar to the LWD, but it works in relatively higher frequency range, i.e. 0-several Hz (Celaya 2011). Kruntcheva et al. (2005) found out that the debonding conditions can be classified by the variations in the dynamic responses of the structure. Similarly, according to research study carried out by Özen et al. (2013), it was observed that IHT method showed promising results in detecting delamination in the asphalt layers. Likewise, another research conducted by Sangiorgi et

al. (2003) reported, that IHT is feasible to use as a quantitative indicator for the interface bonding conditions, ranging between poor bond to a good bond in the asphalt or rigid pavements. However, in thin structures, the variation in the values between the debonded and bonded areas will be small. IHT is an established technique in mechanical, aerospace and naval engineering, which is mainly used for detecting cracks and delaminations accurately in components being used in aforementioned engineering disciplines. However, for civil engineering, the structures are huge, and therefore, this technique has not gained popularity, despite of being accurate and promising, since it is a point testing method, and therefore, time consuming for evaluating large surfaces.

2.6.7 Ground Penetrating Radar (GPR)

The ground penetrating radar (GPR) has been used as an NDT technique in pavement structures evaluation from the past 2-3 decades. The early developments of this technique for pavement structures investigation were observed back in 1970's and 80's (Evans et al. 2008). Since then, it has been a part of NDT industry for pavement structures health monitoring. However, the GPR application in the detection and evaluation of delamination in thin overlays has been found inadequate, and no clear and frequent reports are presently available in this regard (Celaya 2011). The GPR technique is based on the measurement of the travel time of the reflected short impulse electromagnetic wave, along with its amplitude transmitted through the pavements. The reflection of the waves occur based on variations in dielectric properties of materials at the interface (IAEA 2002 and Saarenketo and Scullion 2000). According to Heitzman et al. (2013), delamination can be identified in the GPR profiles by the pulse reflected from the delaminated section. If there are two layers stacked-up in pavements, the reflection of the pulse would be due to the difference in material at their interface, but if they are delaminated, the reflection would be anomalous beyond the ordinary reflections. In reality, the cause of the unusual reflections could be due to any reason, rather than due to a damage or water infiltration etc. only. This will require more sophisticated calibration, especially in multi-layer pavement systems consisting of different materials. In addition, the procedure becomes complex with the inclusion of

rebars, dowels in concrete pavements, etc., and if they are near the delamination, it is hard to associate the reflection to a particular cause. GPR can be used at speeds without interrupting the traffic, and can detect sub-surface anomalies up to depth of 610mm in pavements, while using 1-GHz horn antenna, where with 2-GHz, it can detect down to 380mm (Heitzman et al. 2013). Furthermore, Heitzman et al. (2013) reported that GPR has been used based on individual cases, in identifying the stripping of the asphalt pavements.

A report from Texas A&M Transportation Institute on the use of GPR on stripping detection in an asphalt overlay over concrete has been published (Fujie and Scullion 2007). The results obtained were successful in identifying the stripping in an asphalt overlay but were not sensitive particularly to severity. Similarly, there are several studies on GPR along with infrared thermography technique or FWD, and it was found that GPR is not a stand-alone solution to this problem. However, it is helpful when combined with other NDT techniques in flaws detection.

In another research study by Yehia et al. (2007), it is reported that GPR is a relatively quick and rapid method for the assessment of in-depth sub-surface characteristics, and can be useful in the detection of damage, voids, or delamination in a concrete bridge deck, if these flaws are more than 25mm deep and 25mm diameter. Another review study on the GPR was carried out by Evans et al. (2008), and he concluded that as the dielectric constant of water is approximately around 80, and for the pavement materials, its normally between 2-12, therefore, a large contrast could be observed, and areas with high moisture could be detected. However, the GPR for assessing the bonding material moisture is not well established, and hence, more calibration is required. The sensitivity of GPR to moisture was also questioned by Baright (1999), as it showed false results around steel joints and abutments but on the plus side, it was reported that no surface preparation is required, as GPR is not sensitive to adverse surface conditions. According to IAEA (2002), manufacturing antennas of narrow beams for the radars could be a practical limitation, and therefore, for measuring the accurate distances between surface and subsurface through the antenna would be difficult to achieve, in addition to localize

target in terms of direction. It further reported that GPR has a limitation to the near field closer to the surface, and because of the strong reflections from the rebars in concrete pavements, it tends to mask reflections from the delaminated section. Therefore, it usually fails to locate especially delaminated areas that are only 0.3m wide or less. Moreover, it was reported that one main limitation of the GPR is the inaccuracy due to the fact that the consecutive reflections that are arriving at time intervals with much shorter wavelength than the characteristic pulse width of the antenna in use, and therefore, the reflections due to the small delamination closer to the rebars and relatively closer to the surface, are hard to be distinguished or detected.

In a report published by Rmelie and Scullion (1997) and summarized by Evans et al. (2008), it was concluded that GPR has a good potential in detecting the stripping location and its evaluations. However, it was still recommended that as results have been variable, it should be used in conjunction to some other NDT technique. The size of defects, were not reported in the research studies. Similarly, if the delamination is without air-gap, no information was present, especially in interpreting the results.

2.6.8 Infrared Thermography (IRT)

All objects having temperature greater than the absolute temperature (-273.15ºC) emit infrared radiations (Clark et al. 2003). Thermal imaging or infrared thermography is a technique that converts the invisible thermal radiation pattern, based on its temperature, (as electromagnetic radiation is highly temperature dependent-Stefan Boltzmann law), into a visual image. However, the radiation being captured in the form of a thermogram by the infrared (IR) camera is not based only on surface temperature, but also on its emissivity and ambient conditions, affecting the radiations detected by the IR camera.

Infrared Thermography as an NDT method is based on relating the surface temperature gradient to the internal, or sub-surface flaws. It is mainly used in building surveys for finding moisture ingress, thermal comforts, dampness, thermal bridges etc. and the analysis is mainly qualitative. However, in the last decade, it has gained some

popularity in pavement structures (airfields, bridges, highways). It was reported by Celaya (2011) that IR technology can be used to locate local temperature gradient due to shallow damage under the overlays that is at bond interface. It is believed that air trapped in delamination and cracked zone mostly acts like an insulator, therefore, not allowing the heat to be transferred. This leads to hot and cold zones on the top surface, just over the delaminated or sub-surface damage sections, which is detected by the IR camera in the form of a thermogram. This temperature gradient, is then compared with the sound and defected areas (Moropoulou et al. 2001).

In detecting shallow depth delamination (50-70mm) in the pavements, some promising results were obtained through an IR camera, reported by Tsubokawa et al. (2007). However, Hammons et al. (2005) reported some unfavourable results too, and no information regarding the depth of the defected sub-surface section was obtained with this technique. IRT is a contactless technique that can scan large surface areas in no time, and therefore, saving time and cost. However, since it is very much dependent on environmental conditions, the results are subjective and could give different thermograms for the same defect, but measured at different time of the day. Nevertheless, this technique has been used in conjunction with GPR technique in various studies and has shown promising results.

2.6.9 Combining IRT and IHT techniques

From the literature review studied, it is widely established that in-situ NDT techniques have become an integral part of the road, pavement and bridge management repair process, for selecting proper rehabilitation and reconstruction strategies (Rens et al. 2005, Scott et al. 2003 and Tawfiq et al. 2002).

Table 2-2: summarises number of potential NDT techniques for detecting delaminations.

Table 2-2: Brief review of NDT Techniques capable of detecting delamination.

TECHNIQUE	ADVANTAGES	DISADVANTAGES	CONCRETE	COMMENTS
Visual Inspection	Essential; quick; low cost	Unsuitable to demonstrate internal conditions	Yes	(See 2012)
Sounding	Quick; low cost, accurate and repeatable for concrete overlays	Only initial information affected by subjective factors	Yes	(ASTM D4580-86:2000), IAEA 2002 and Rens et al. 2005)
Impact-Echo and Ultrasonic Test	Detects depth of delamination. Safe	Labour-intensive; Due to non-homogeneous nature of concrete and asphalt the signals need conditioning. Point method. Debonding with no air gap difficult to detect; not sufficiently accurate for asphalt surfacings.	Yes with some reservations	(Abramo 2011, Armitage et al. 2000, Azari et al. 2014, Chaudhary 2013, Garbacz et al. 2017, Hoegh et al. 2011, Mazzeo et al. 2012 and Zhang et al. 2016)
Spectral Analysis of Surface Waves	Relatively fast, efficient, safe	Difficult to interpret; not reliable results for delaminations shallower than 100mm from the surface.	Not consistent data reported	(Armitage et al. 2000 and Nazarian et al. 2010)
Falling Weight Deflectometer	Uses data collected during a routine FWD test	Provides information about possible delaminations over large areas; Not suitable for very	Yes, (heavy version of FWD).	(Al Hakim et al. 1998, Karadelis and Hughes 1998 and Nazarian et al. 2010).

		thin surfacings. Not always successful.		
Impact Hammer Test	Quick, low cost, based on reliable hammer sounding but providing quantitative information	Point test, require calibration	Further research needed	(Cellaya 2011, Ewins 2000, Kruntcheva et al. 2005 and Sangiorgi et al. 2003)
Ground Penetrating Radar	Relatively rapid point test. Comprehensive coverage. Safe. Could determine the depth of delamination	Collection of large amount of data. Does not give size of delamination. Difficult to interpret. Not to be used in wet weather and below freezing. Point/line data	Not consistent results reported	(Fujie and Scullion 2007, IAEA 2002 and Scott et al. 2003)
Infra-Red Thermography	Very rapid, large area scanning. Can determine size of delamination. Operational during day and night-time. More efficient/accurate than other NDT methods. High visibility, fast response rate. Large range of measurement. Portable equipment. Easy data manipulation.	Extreme dependency on environmental conditions. Does not predict depth of delaminations. Debonding with no air gap difficult to detect, hence limited use.	Yes	(ASTM D 4788-03:2013, Celaya 2011, Clark et al. 2003, Hiasa et al. 2017a, Moropoulou et al. 2001, Stimolo et al. 2003 and Weil and Haefner 1989)

Although, many NDT techniques (IE, GPR, IHT, FWD, LWD, USW, and IRT) have been reported for detection and evaluation of sub-surface defect's (delaminations) in pavements, plus they all carry advantages as well as disadvantages, as summarized in

(Table 2-2). However, after an extensive literature survey and to the best of author's knowledge, no established NDT method or programme exists for the reliable detection of delaminations below thin surfacings (40-50mm) and overlays to date.

IRT and IHT are the two initially non-compatible NDT techniques that are carefully chosen for this pilot-study (for detecting and evaluating near sub-surface defects i.e. voids, delaminations) due to their following main advantages over others:

- **IRT** is a Rapid, Cost effective NDT technique.
- It is a contactless technique, which is quite portable and can scan large area in quick time.
- Near surface defects are relatively easy to detect.
- Detection of shape and geometry of defects, are also reported in few studies (Celaya 2011, Hiasa et al. 2017a, 2017b and Stimolo et al. 2003).
- Can detect temperature difference due to a defect up to 0.2-0.3°C (Clark et al. 2003).
- Suitable for high emissivity materials, like concrete, asphalt, water etc.
- Interpretation of thermograms is relatively simple, if used for shallow defects and for qualitative analysis only.
- Along with FEM, better interpretation or evaluation of the void or delamination is possible.
- **IHT**, on the other hand is an established NDT technique that can quantify and evaluate defects, such as cracks, debonding in composite materials, very accurately.

The reason for choosing these two initially non-compatible techniques (IRT is based on electromagnetic energy and IHT is based on stress waves methods) is because, IRT is quite suitable for detecting near sub-surface defects, which in this case is delamination under thin overlay. Though IRT is rapid, and can scan large areas in quick time, however, the reliability of IRT still remains shady (highly dependent on ambient conditions, interpretation is mainly qualitative, not accurate for detecting or assessing

relatively deep defects from the surface) and therefore, it is never used as a stand-alone technique with full confidence, for detecting and evaluating the near sub-surface defects.

On the other hand, IHT is an established NDT technique, especially in automotive or aerospace industry. In Civil engineering, it has been reported in several studies, and has shown promising results for detecting and evaluating defects (Allemang 2003, Curadelli et al. 2008, Foti 2013, Jassim et al. 2013, Karadelis (2012), Ndambi et al. 2002, Razak and Choi 2001 and Salawu and Williams 1995). However, one drawback of IHT is, it is a node based testing technique, therefore, it is relatively slow, and is not feasible for operating on large scale tests.

It is proposed that with the marriage of these two initially non-compatible NDT techniques, both will compensate each other in detecting and evaluating the debonding conditions, beneath thin overlays in concrete pavements. IRT would give a fast or rapid scan of the pavement under test on the first place, while detecting the possible delaminations and making a decision on their classification/severity. However, if the assessment/decision could not be made possible for any particular (uncertain) region during this phase (IRT testing), IHT would be deployed, and evaluate those regions classified 'uncertain' in the first phase (IRT). In other words, IHT would compensate or cover the information missed by IRT in the first phase. In addition, both techniques would be supplemented by Finite Element Analyses (FEA), thus, improving the overall reliability of the method.

Hence, in order to combine both NDT techniques (IRT+IHT), improvements are required, therefore, further literature survey will be focussed on finding the possible room of improvements/research gap in the proposed NDT techniques.

2.7 Infrared Thermography as a Non-Destructive Testing and Evaluation (NDT&E) Technique

Infrared thermography has been in use for the last 3 decades as an NDT method for the civil and building structures, and is still progressing in its applications. Its applications in the pavement structures started in 1980s, but a very limited information on its use was available in those early times. A report published by Bukowski et al. (1983), describes preliminary theoretical and experimental investigations on the voids present beneath concrete pavements. The hypothesis was that the surface temperature above the void will be slightly different from the surface temperature of the sound concrete. Results from this report showed the potential of the IR camera in detecting thin voids, but additional investigation was recommended for further optimisation. Other researchers, Avdelidis et al. (2003), Celaya (2011), Clark et al. (2003), Moropoulou et al. (2001), Poston et al. (1995), Stimolo (2003) and Tsubokawa et al. (2007) have utilized the IRT method for bridge inspection in USA; bridge and road scanning in Switzerland; pavement assessment of the international airport in Athens, Greece, etc. These investigations were carried out through the passive approach, in which no external heating was involved, and it was found that the environmental conditions like solar radiation intensity, relative humidity, wind, and possible shadows from the trees, adjacent buildings and cloud cover have high effect on the results.

Thermographic inspections are divided into two major groups, active thermography (Chatterjee et al. 2011, Maierhofer et al. 2005, Marinetti et al. 1999 and Meola 2013) and passive thermography (Avdelidis et al. 2003, Moropoulou et al. 2001, Poston et al. 1995 and Stimolo 2003). In active thermography, the specimen is thermally excited, using an external stimulus such as lamps, ovens etc., whereas, in passive thermography, the specimen is examined under ambient conditions (Hain et al. 2009 and Kylili et al. 2014). In general, active thermography is a qualitative and quantitative technique, whereas, passive thermography, is used for qualitative analysis only. The passive approach is preferred for large structures like buildings, bridge decks, where active

thermography is recommended for metallic materials or materials having good thermal conductivity (Abdel-Qader et al. 2008).

For civil and pavement structures, infrared thermography was just limited to the passive approach from the past few decades (Chown and Burn 1983 and Petterson and Axen 1980) reported by (Maierhofer et al. 2005). There are not many research studies that have been carried out on the active thermography in the civil structures in practise due to the feasibility issues. Vavilov and Maldague (1994) were pioneers in working on active thermography. Later on others (ARNDT et al. 2006, Chatterjee et al. 2011, Maierhofer et al. 2005, Maierhofer et al. 2006, Meola 2013 and Shepard 1997), performed research on different sub-types of active thermography like impulse, phase and pulse phase thermography. The overall classification is synoptically illustrated in (Figure 2-12).
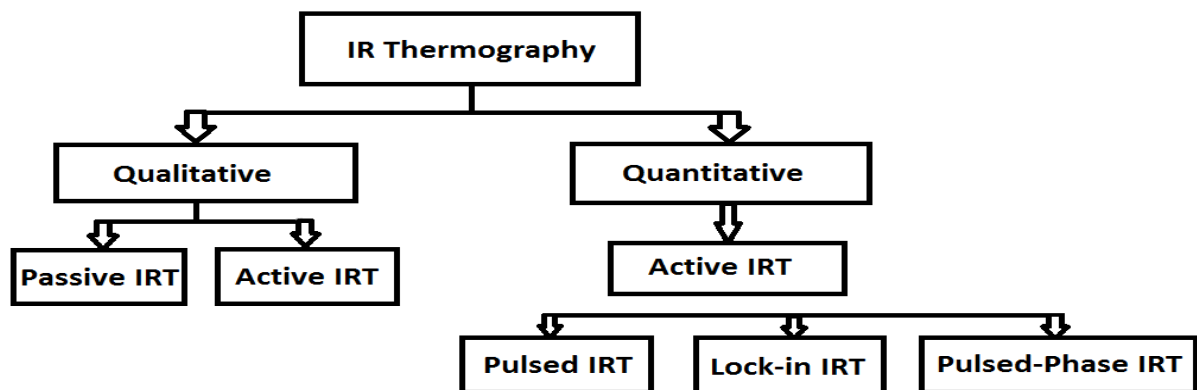
Figure 2-12: Classification of IRT technique.

However, all these experiments were carried out on concrete slabs (simulating concrete walls of the building structures) under controlled laboratory conditions, in order to detect the defects (like voids, delamination etc.). No conclusions have been drawn so far for the use of active thermography in pavement surveys, mainly due to its feasibility issues for heating up the big pavement structures. The further literature review will be

focussed on 'passive thermography', as it is practically implemented for pavements, and is also adopted for this pilot study.

Up to now, a reasonable amount of research has been carried out on the application of passive IRT for bridges, highways or pavements. However, each study was performed under certain conditions, therefore, making it hard to extract generalised conclusions Hiasa et al. (2017a). There are still numerous uncertainties in the assessment methods based on the obtained thermograms from IRT inspection technique. Therefore, according to Hiasa et al. (2016), the reliability of IRT for bridge inspection is still questionable compared to other NDT methods.

Passive thermography as seen earlier is generally used for qualitative analysis. A research study was carried out by Moropoulou et al. (2001), on the detection of delamination at pavements sites in Athens International airport Greece, by Infrared Thermography. A few old and some new sections, also, one with a new 30mm thick asphalt overlay, were brought under scrutiny. The defects were identified based on the ASTM standard D4788-88, according to which there must be a temperature difference of 0.5°C between sound and defected parts. It was found that delaminated sections in the pavements were showing different thermal contrast compared to the sound areas. They were measured in terms of percentage defected area of the whole thermal image, as shown in one of its thermograms (Figure 2-13). But there was no quantitative report generated on the thermograms, based on passive thermography results. The tests were performed in the day time with an IR camera having a scan speed of 15frames/sec and a wavelength region of 8-12 µm. The author found that the IRT method is rapid and cost effective because not much machinery is involved. The main limitation of passive infrared thermography reported was its inability to determine the exact dimensions (size and depth) of the delamination. The severity of debonding was not reported, only detection was observed. It was presumed that the defect observed would be delamination. There was no explanation if the thermogram can give some information regarding the defect type. Moreover, it was not recommended what would be the best time for getting the maximum contrast, although it depends on a case to case study but

comparing the results at different times of heating or cooling should have given some food of thought for the interpretation of thermograms. Thermograms were represented by a black and white palette, where white colour represented delamination and black/grey colour represented sound area. However, the white colour was just used to identify delamination but not to evaluate the degree of delamination.
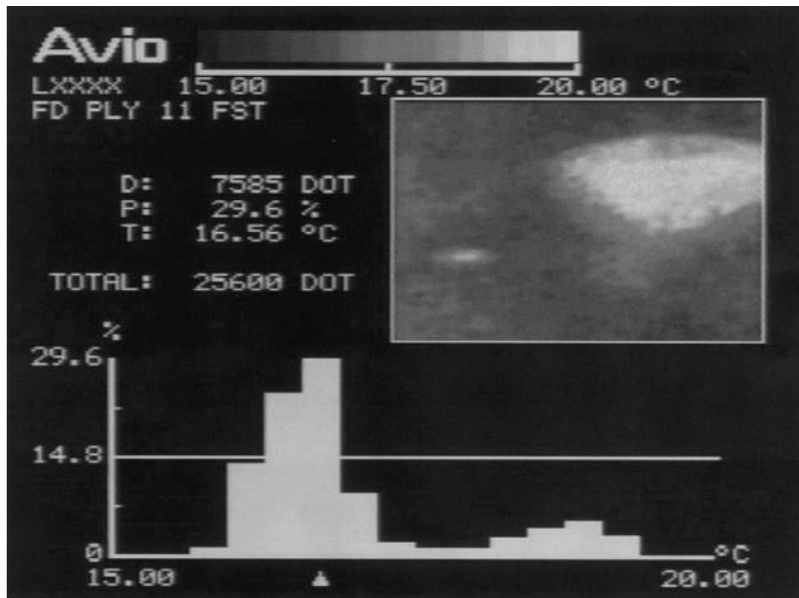
Figure 2-13: Thermogram, showing defected part with temperature contrast (Moropoulou et al. 2001).

It was also proposed probably for the first time and based on the results, to use a supplementary NDT technique to evaluate the flaw. However, the main limitation was stressed in her conclusive remarks, stating the inability of IRT in determining the exact dimensions (depth and thickness) of the delamination. Whereas, no evaluation (quantification) was reported regarding the severity of delamination. This demonstrates that passive-IRT was used only to 'identify' the sub-surface flaw and other NDT techniques were required to do the further assessments.

Similarly, another report published by Stimolo et al. (2003) on the passive infrared thermography as an inspection, and observation tool in bridge and road construction, concluded that to obtain the effective temperature difference related to the sub-surface

fault, optimum timing is required during the 24-hrs day. A graph produced by the above, shows that maximum temperature difference between sound and damaged section in pavements can be obtained during the following observation times in a day: 11:00 - 18:00, 8:00 - 15:00 and from 20:00 - 4:00. These were based on case studies of different environmental conditions like sun position (time, season, solar radiation intensity), geographical position (solar radiation intensity, latitude,), slope and orientation of the pavement, possible shadows (trees, buildings), weather conditions (wind speeds, change from sunshine to cloud coverage, cloud movement, ambient temperature), optical properties of the pavements (emissivity, absorption), and finally the moisture in the ground and in the air that is relative humidity (an excess of moisture changes the thermal conductivity and absorption of the infrared radiations and therefore results too). Moreover, the temperature difference between a 20mm and 320mm deep layer was estimated and plotted, although, no mentioned was made of how they kept monitoring temperatures at these depths. However, one observation is worth mentioning, that in the night the temperature gradient was negative (Figure 2-14), and the direction was from lowest layer towards the surface (blue lines), and for rest of the day, the temperature gradient was positive with its direction, from pavement surface towards the lowest layers (Red lines) as illustrated in graph Figure 2-14.
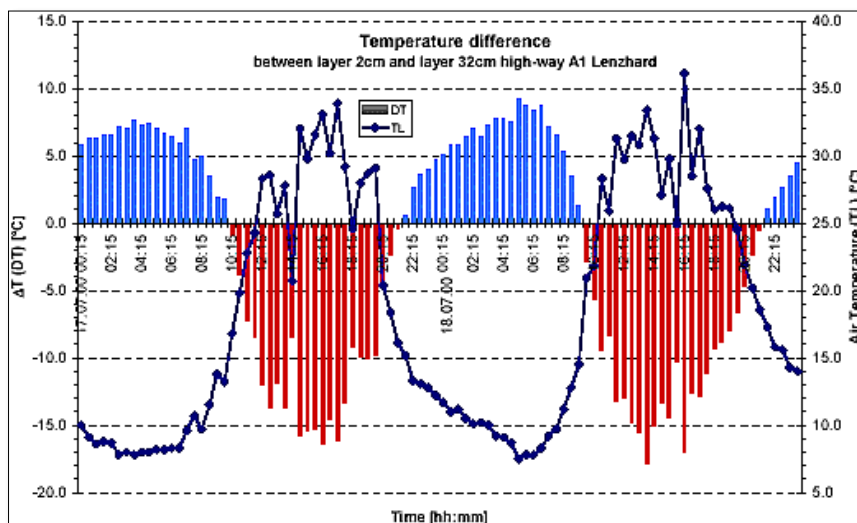
Figure 2-14: Temperature difference (ΔT) between the temperature at depths of 20mm and 320mm along with the temperature of the air (TL), highway A1, Lenzhard CH (Stimolo et al. 2003).

This evidences that the temperature changes following a periodical path throughout the day between positive and negative temperature gradients. This in affect meant that at night, the cooler region in the thermogram will show the defected region, while at day time, the hotter region in the thermogram will represent the defected region. In addition, it was asserted that the low solar intensity would create lower temperature gradient, which might not be sufficient to create the required thermal contrast, therefore, the inspection in an adequate amount of solar energy was suggested to permit a good survey.

The thermograms obtained in this study, showed the defected regions in the pavement structures with high temperature contrast between the defected and sound sections (Figure 2-15). However, no statement was reported on the status of damage.

Secondly, the depths of these damages could not be determined from the thermograms. Indeed, the shapes of the damages could be observed but their sizes were not reported. The times at which maximum thermal contrasts were obtained were reported, but since timings and values of thermal contrasts vary from case to case, no such conclusive timings could be drawn. However, an attempt could be made to find out the optimum time and environmental conditions, for obtaining the best results from the IRT test.
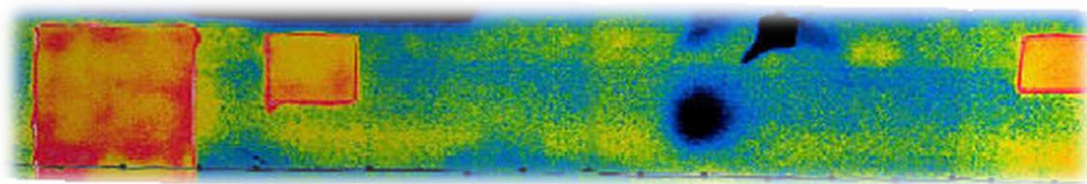
Figure 2-15: Section of a thermogram of selected strip in pavement (Stimolo et al. 2003).

According to Clark et al. (2003), one of the perceived limitations of the IR thermography, is its use in temperate climates, since the low exposure of the sun, and due to low heat intensity, the delamination or debonding defects are not detectable due to small change in temperature.

An investigation was carried out on one span of a bridge on the M1 motorway in Northamptonshire in the UK (Clark et al. 2003). The delamination was detected during the day (Figure 2-16), where the atmospheric temperature was 11°C with relative humidity of 70%.
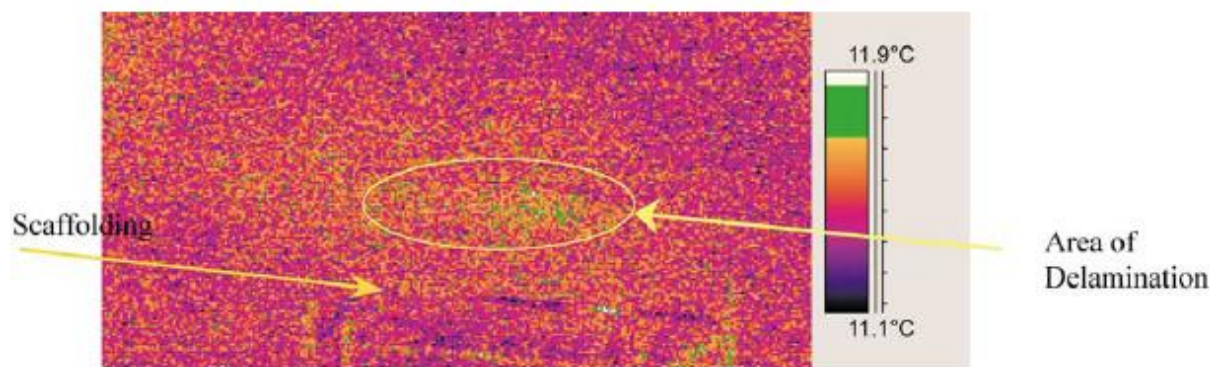
Figure 2-16: Delamination under the bridge deck, detected in thermogram (Clark et al. 2003).

It was observed that the temperature difference of the delaminated area and the sound area was approximately 0.2-0.3^{o}C. This shows that even a small temperature difference could be associated with some sub-surface defect, or material non-homogeneity.

Furthermore, a brief insight of the environmental effects were given. For instance, sunlight will increase the surface temperature, where wind may decrease it. Rain will reduce the temperature of the surface along with variations in the emissivity. This may reduce the chances of identifying delamination, and therefore, make the interpretation of recorded thermograms more difficult. The minimum delaminated area detected was 200mm in diameter, no depth of the delaminations from the surface were reported. In order to quantify and evaluate the defects, more research is required in improving the IRT technique. One serious drawback surfaced during IRT-tests was the false detection of a sound area, classed as a defect, while showing relatively higher temperature than the surroundings. This could be due to non-homogeneity of the material, or a noise recorded by the camera. However, by relating such anomalies to a defect, can lead to wrong interpretation, and consequently, wrong analysis. Therefore, in such cases

49

numerical modelling could be used as an additional tool to supplement the experimental tests. The minimum delamination size (area, thickness and depth) to be identified through IRT, is another challenge that needs further research. No optimum timings for taking thermograms were neither reported nor suggested by the author. Passive thermography is currently more of a qualitative analysis, therefore, further supplementary tools are needed in order for it to gain acceptance as an NDT&E technique.

A slightly different field trial of infrared inspection was carried out by Tsubokawa et al. (2007) at Naha Airport, one of the largest airports in Japan. The runway-taxiway intersection close to the end of the runway, having dimensions 10x10m, was used in this case study. The area under inspection was divided by making grids of 500x500mm. It was first inspected with the Impact Acoustic Method, using a hammer, and the debonded areas were specified and marked with circular chalk lines (Figure 2-17).
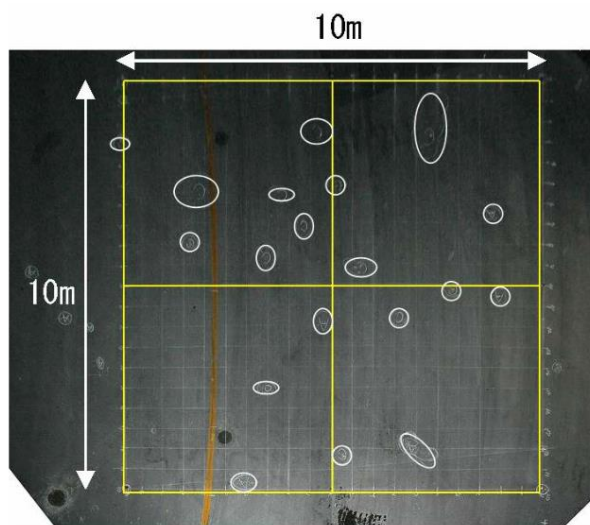
Figure 2-17: Circular chalk lines representing debonding (Tsubokawa et al. 2007).

However, in order to overcome the shortcomings, the role of IRT came into play afterwards, and those marked sections were further analysed through infrared images. Infrared images were taken at a height of 10m, between 00:30am and 5:30am, and were

carried out at intervals of 30 minutes in specified timings. The results from the infrared thermography confirmed the delamination based on the detection of the seven low temperature areas, and were later verified to be at depths of 40-70mm as shown in Figure 2-18.
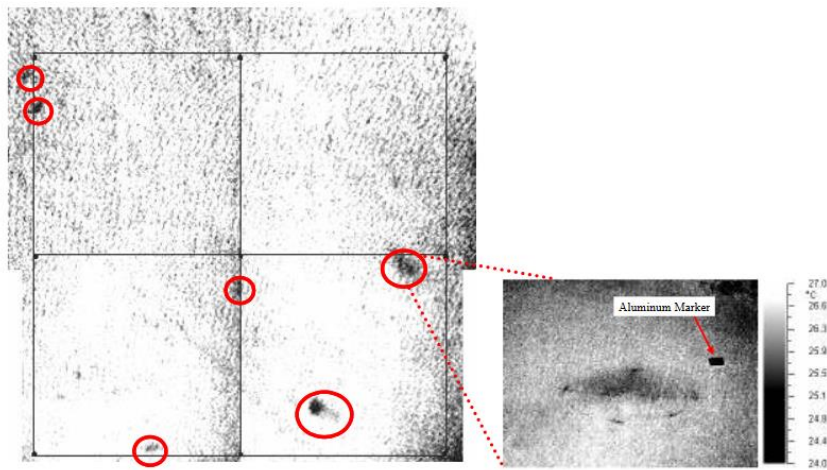
Figure 2-18: De-bonding sections, detected through Infrared Thermography (Tsubokawa et al. 2007).

Grey colour represents low temperatures associated with delamination. Similarly, change of temperature on the surface between delaminated and sound area was plotted (Figure 2-19) using infrared thermography results.
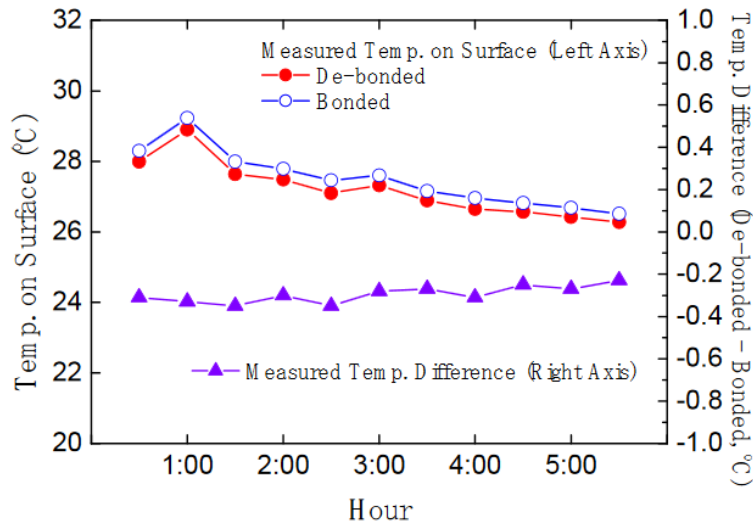
Figure 2-19: Temperature and Temperature difference for the surface above delamination, 50mm deep (Tsubokawa et al. 2007).

These results, showed low temperature at the debonded sections than that of its surroundings recorded during midnight to morning. Further verification was also available by core boring and delamination at the depths of 40-70mm. In this case study, delamination was detected at the depths between 40-70mm, but the severity was not measured on the basis of infrared imaging. The depth was verified through core boring, however, it was not detected and estimated through infrared images or thermograms. Similarly, sizing and shapes were parameters not reported clearly. The analysis was just qualitative.

Another passive approach in infrared thermography was carried out by Celaya (2011) on the asphalt surface with an area of approximately 610x610mm, where the camera was used at the height of 1.2m from the surface (Figure 2-20).

Figure 2-20: Infrared inspection of the HMA pavement (Celaya 2011).

The IR-camera used for this test had a resolution of 240 x 240 pixels, and could be operated in a range of temperature from -10°C to 350°C. Sun was utilised as a source of heat for developing the thermal contrast on the surface, to identify the delamination. Hotspots were observed on the top of delaminated sections and were classed as severe delaminations (Figure 2-21). The same procedure was applied on 10 different sections with prearranged delaminations. It was observed that only the severe delaminations near the top layer were observed in the thermograms, where the depth and size could not be measured. The severity was also verified through core-boring but it was not quantified through the thermograms. The weather and sun orientation are the other crucial factors that can easily manipulate the results. However, did not report the optimum ambient conditions that helped them in detecting the severe delaminations. No information regarding the size or shape of delamination was reported. Hence, the approach was mainly qualitative again.
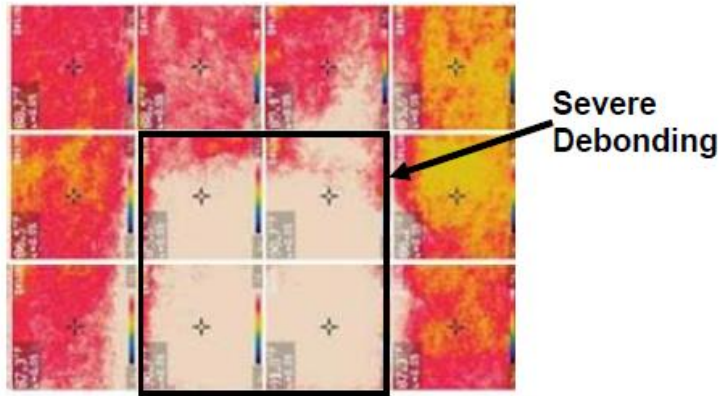
Figure 2-21: Severe debonding detected in the top asphalt layer (Celaya 2011).

It is clear from the above that the Passive-IRT as a stand-alone technique for detection and evaluation of the sub-surface pavement flaws, is still not established, and therefore, various researchers have used IRT in conjunction with other techniques. One popular combination is that with the Ground penetrating radar (GPR). The GPR technique is dependent on the propagation of electromagnetic radiation in very short time. The identification of the targets is based on the contrast between the electromagnetic properties of the object under study and the surrounding medium. This can affect the accuracy and efficiency of the method. Generally, IRT is deployed as the first, indicative tool of identifying the sub-surface flaw, and GPR is then deployed for further assessments of the sub-surface flaw based on the initial IRT detection. However, sometimes the opposite takes place.

A study carried out by Solla et al. (2014), reported that GPR combined with IRT can detect the surface and sub-surface cracks in asphalt-concrete pavements (various densities). These cracks designed for the tests were 3mm wide at depths ranging between 15mm to 550mm. These tests were first carried out on a previously measured cracks with known geometries in a stretch of road in Galicia, Spain, as a requirement for the calibration process. Later, the tests were carried out on the road in use (Ourense-Galicia) for validation purposes. Out of 16 samples, GPR was able to estimate the depths of five, with an average error of 5.5%, where the minimum depth estimated was 40mm. Not all shallow depths less than 40mm were detected. The impacts of depths and

impacts of various fillings in the cracks like bitumen, soil and water were also investigated. It was observed that water filled cracks were more distinguishable than empty cracks, this was due to the high dielectric contrast between the two media. However, an opposite behaviour was observed in the case of cracks filled with natural soil, where the identification of the reflected wave was not as clear as empty cracks. Numerical simulation was also run to assist the interpretation of the obtained results. However, it was not possible to estimate the depth of the cracks. Hence, no direct relation was established between the amplitude of the reflected wave obtained from the crack and the depth of the crack itself. The variations in the amplitudes of various cracks were found to be the indicators of the cracks, though, they did not provide any direct information on their depths. It was presumed that the lack of detection of depths could be because of two different causes: The complex pattern of reflections (signal scattering) observed at the surface due to the larger presence of voids (6%) in the surface, or due to the depth of the crack, since they were less than 40mm deep, from the surface.

The thermographic survey was carried out in the early morning, optimizing the information required. With the infrared thermography, all types of cracks present on the surface were observed, where each crack was characterised based on its temperature difference.

Hence, it was concluded that GPR was used as a first indicator for the flaw detection along the surface and only partial quantification was made possible, whereas IRT was used to complement the first. No tangible solution for detecting and evaluating all the sub-surface flaws were reported.

It was reported by Hiasa et al. (2017a) that under passive thermographic survey, it is not always possible to detect delaminations in overlays. Also between the heating and cooling cycle, there is a transitional state, and therefore, is unavailable for passive IRT-testing (Figure 2-22).
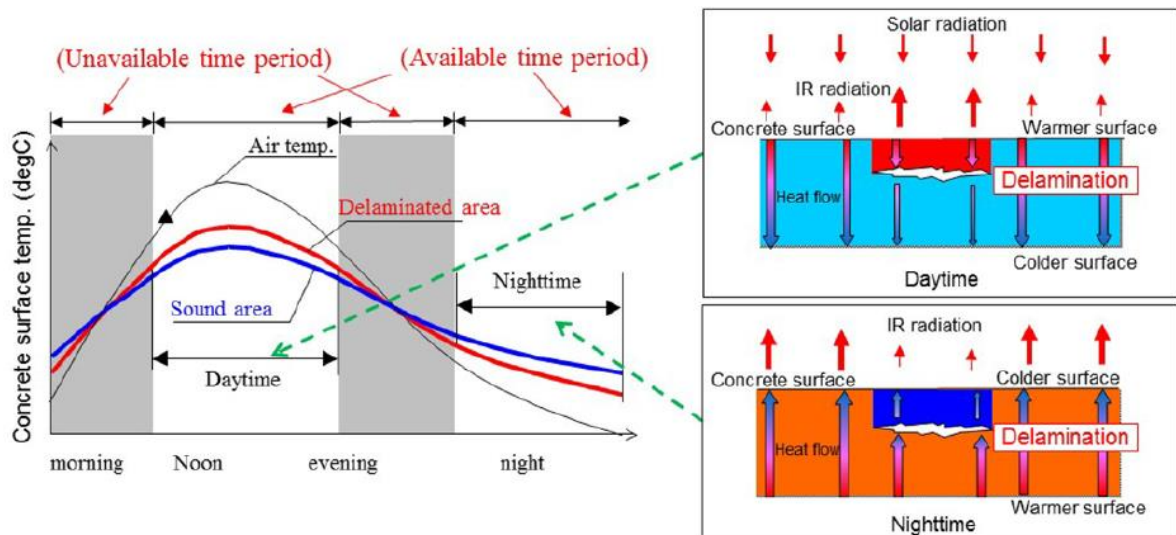
Figure 2-22: Left: Proposed applicable time for IRT. Right: Direction of heat transfer (right) (Hiasa et al. 2017a).

Furthermore, sometimes, the sun orientation, shadows and clouds, cause variations in the colour map of the IRT-thermograms, and therefore, it does not represent the true delamination. Likewise, Washer et al. (2013) argued that if the temperature span for recording the thermograms is set too high or too low, this might result in showing no anomaly in the thermograms, even though there would be some flaws present. It seems that it is important to set the right temperature span for testing, however, this could be adjusted later in post processing of the recorded thermograms too.

Active thermography on the other hand has become popular for evaluating composite materials of high thermal diffusivity with thickness of 10-40mm (Chatterjee et al. 2011 and Marinetti et al. 1999). However, materials like concrete, which have very low thermal diffusivity ($8.75 \times 10^{-7} m^2 s^{-1}$), are less effective under active heating. There are two main limitations with active heating, when applied on concrete surfaces:

1. Requires homogeneous heating, ranging from several minutes to a couple of hours (ARNDT et al. 2006, Chatterjee et al. 2011, Maierhofer et al. 2006 and Marinetti et al. 1999).

2. Requires high power lamps to heat the concrete, which has low thermal conductivity and thermal diffusivity.

Huh et al. (2016) carried out an IRT-experiment on detecting the delamination in concrete, where various size of delaminations were deliberately embedded in concrete specimen at various depths. It was reported that it requires 5 minutes of heating, to detect a delamination (30x30mm, 100x100mm) at the depth of 10-20mm and more than 15 minutes to visualise the delamination (30x30mm) at 30mm depth.

Cotič et al. (2015) reported that though shallow delaminations of 10-45mm deep can be detected in 5-10 minutes, an increase in time of 25-30 minutes will further improve the contrast of the boundaries. He also reported that deeper delaminations, at the depth of around 100mm require a prolong heating of 1-2 hrs.

Maierhofer et al. (2006) reported that voids (polystyrene cubes) embedded in concrete at depth 30-45mm, showed the maximum thermal contrast at 13.3 minutes after switching off the heating source, which was ON for 30 minutes. However, from all these studies, there was not a definite conclusion drawn, on the detectability of defects and their expected behaviour. Therefore, it was hard to quantify the defects as a rule of thumb. All the experiments were performed in different boundaries and environmental conditions, and the results were mainly subjective. Active thermography though showed promising quantification results, since due to controlled setup of heating and recording thermograms, it was relatively easy to evaluate the defects with pre-known properties and their locations. However, for the inspection of heavy structures like bridges or pavements, the active approach of IRT seems impractical. First, due to challenges of providing the uniform heating, and second, due to long time needed to reach the cooling cycle. The latter becomes only possible during night, when there is no solar loading. On the other hand, passive IRT, which is currently more of a qualitative survey technique, and has got some inherent limitations in the evaluation process, still offers advantages over conventional hammer sounding and chain drag inspection techniques, for bridges and pavement structures (Hiasa 2016, Hiasa et al. 2016 and 2017a).

In civil structures, due to large sizes of the concrete bridges or pavements, the test-specimens (containing the delaminations of various sizes and depths) required to simulate them, could be challenging. Also, to subject them to various boundary and environmental conditions, and use this knowledge to assess the real delaminations, becomes time consuming and at times difficult. Therefore, limited test-specimens are prepared for tests under specified boundary conditions. In order to gain confidence in these conditions, Finite Element (FE) modelling for IRT has started gaining acceptance in simulating the thermal contrasts of the specimen under tests (Cannas et al. 2012, Khan et al. 2015, Krishnapillai et al. 2006, Restrepo and Loaiza 2013, Rumbayan and Washer 2014, Vavilov 2007 and Vavilov et al. 2002). Various parametric studies considering the factors of delaminations, detectability, size, depth etc. are being explored by means of FE-modelling. However, the 'evolution' of delamination or its classification based on its severity, still needs further research and verifications.

It has been reported by Hiasa et al. (2017a) that during FE-simulations, the area of delaminations was the most crucial factor, thickness also effects the thermal contrasts between the sound and delaminated regions. Similarly, in the past few parametric studies carried out by Hiasa et al. (2017b), various sizes of delaminations were investigated. Few of them were experimentally validated. To simulate the inspection of real concrete bridge deck by IRT, a lab-scaled test was conducted by Hiasa et al. (2016) on two specimens with embedded foamed sheet and cardboard delaminations at depth, 13mm and 25mm respectively. However, for simplicity, an assumption was made that both artificial delaminations had similar thermal conductivities and specific heat capacities. The test was carried out in a sunny day and the recordings were carried out for 24 hours. The modelling of the specimen was carried out in the Heat transfer module of the 'COMSOL Multiphysics' software. The temperature distribution of the delaminated and sound areas were validated via the experimental results with an accuracy of 87-90% correlation. However, the effects of depths or thicknesses were not clearly reported, and therefore, no evaluation was carried out, or discussed regarding the deliberately created delaminations.

Estimation of the depth is a serious drawback of passive IRT. However, by combining FE-simulation with experimentations can help with this issue. Hiasa et al. (2017a) modelled various delaminations with a constant area of 400x400 mm but with thicknesses of 1mm and 10mm and at various depths of 30mm, 40mm, 50mm and 60mm from the top-surface. The aim was to compare the real delaminations, which were already assumed to be at 60mm depth with FE-models. It is important to mention that the thickness of the delamination was another unknown parameter in addition to the depths. Therefore, in comparison, more than one combination (thickness and depth) in the FE-simulation showed similar results to the experimental readings, which was at constant depth of 60mm. Hence, all those similar FE-results to the experimental readings were taken, and an estimation for the range of depths was made. The estimation was made to be between 50-70mm, which was close to 60mm, confirmed by the already drilled core sample. However, the impact of two unknown parameters, i.e. thickness and depth were not investigated independently.

Rocha et al. (2019) conducted a study on the evaluation of passive infrared thermography method for detecting delamination in two concrete specimens, simulated by polystyrene plates of number of thicknesses (3, 6 and 12mm) and depths (25, 50 and 75mm). The results showed that the detection of delaminations were possible, however, nearer the delamination to the surface and larger the size, it was easy to detect, while, the depth was increased, it became difficult to identify. Again, the study was primarily qualitative, and no details regarding the quantification of defects were reported.

An investigation carried out by Raja et al. (2020), showed the influence of environmental conditions (wind velocity and solar radiations) in detecting delamination in concrete bridge deck. It was reported that the heat flux (solar loading) plays a major role in the development of thermal contrast (ΔT), whereas, its effect was reduced gradually with the increase in depth of delamination. However, no clear conclusion was drawn on the optimal time of the tests, the wind speed and the heat flux.

The principal findings from the IRT literature survey are as follow:

- Passive thermography is mainly employed as a qualitative analysis technique, which is carried out under the ambient conditions.
- IRT is an established technique for building surveys, however, for pavement surveys, there is still room for improvements.
- One of the limitations associated with IRT reported, is its inability to detect the exact dimensions (size and depth) of delaminations.
- No evaluation or quantification of the detected delaminations through its thermograms was clearly stated.
- There were evidences that the temperature gradient followed a periodic path in a day, the hot spots in the thermogram representing a defect when captured in a day time, were replaced by a cold spot, when recorded at night time. However, no clear statement on the optimum time and ambient conditions for the best results from IRT were reported
- The minimum temperature difference observed between the delaminated area and the sound area was approximately 0.2-0.3ºC.
- One serious drawback was the false detection of a sound area, classed as a defect, merely judged on the their local temperature differences. By relating such anomalies to a defect, can lead to wrong interpretation, and consequently, wrong analysis. Therefore, in such cases numerical modelling could be useful as an additional tool to supplement the experimental tests.
- The near surface and large sized delaminations were easy to detect, however, complications were encountered with the detection, as the depth was increased.
- The weather conditions (shadow, clouds, wind speed, solar loading) and sun orientation are the other crucial factors that can easily manipulate the results and can make the interpretations of the thermograms more difficult. However, no clear conclusion was drawn on the optimal sun orientation, the wind speed and the heat flux.
- One of the report suggested that it takes 5-10 minutes to detect shallow delaminations of 10-45mm deep, while an increase in time of 25-30 minutes

heating will further improve the contrast of the boundaries. However, from all these studies, no final verdict is possible, on the detectability of defects and their expected behaviour. As all the experiments were performed in different boundaries and environmental conditions, and the results were mainly subjective.

- Active thermography in the lab scaled tests, showed promising quantification results, due to controlled setup of heating and recording thermograms, moreover, it was relatively easy to evaluate the defects with pre-known properties and their locations. However, for the inspection of heavy structures like bridges or pavements, there are two main limitations with an active approach of IRT. First, due to challenges of providing the uniform heating, and second, due to long time needed to reach the cooling cycle. The latter becomes only possible during night, when there is no solar loading. On the other hand, passive IRT is currently more of a qualitative survey technique, and has got some inherent limitations in the evaluation process.

- Few parametric studies considering the factors of delaminations, detectability, size, depth etc. were explored by means of FE-modelling. However, the 'evolution' of delamination and its classification based on the thermograms/thermal images interpretations, still needs a thorough research and verification.

2.8 Vibration based NDT damage detection techniques

According to Rytter (1993), the damage assessment scale in any inspection process is classified into four levels:

1. Level I: Detection of damage in the structure.
2. Level II: Level I plus localisation of the damage in the structure.
3. Level III: Level II plus evaluation of the damage in the structure.
4. Level IV: Level III plus prognosis of remaining service life of the structure.

By employing experimental modal analysis (EMA) via 'Impact Hammer Testing' or similar other NDT technique, one can scrutinise the dynamic characteristics of a structure leading to determining the first three levels of inspection process. Most methods provide structural models along with experimental data in order to trace the damage location (Level II). On evaluating the damage (Level III), the model needs to be updated, and should be robust enough to describe the effect of the damage (cracks, delaminations, voids etc.) on the dynamic characteristics of the structure. However, if there is no such model available then the damage metrics have to be determined by our experimental calibration processes. It is also worth mentioning that the classification of the type of damage, is generally considered as an extra step between the Level II and Level III (Fritzen 2005). The highest and also the most sophisticated level in the inspection process is the prediction of the remaining service life of the structure (Level IV). A fatigue analysis along with a fracture mechanics model or a structural design assessment is essential to predict the development or evolution of the damage. Hence, the measurements taken from the accurate sensors system along with robust mathematical models could lead to estimate the life of the structure.

According to Doebling et al. (1996), non-destructive damage detection techniques are classified as local or global damage identification methods. X-rays and ultrasonic methods are examples of local damage detection techniques, whereas, vibration based NDT techniques are classified as global damage identification methods. The difference between the two is that in local damage detection techniques, the location of the damage should be known, and accessible prior to the inspection, which in most cases (civil and aerospace engineering) is not guaranteed. However, in global damage detection techniques, this information is not always required. Therefore, this advantage of global damage detection techniques over its counterpart has made it popular, and is being exploited in various inspection processes to detect the uncertain and inaccessible damages, also involving complex analysis of the damage in complicated structures.

During the last three decades, extensive research has been carried out in vibration based detection techniques. Owing to the advantages of analysing defects in complex

structures without pre-knowing the defect's location. As a result, significant progress has been made in this area (Carden and Fanning 2004, Doebling et al. 1996, Fan and Qiao 2011 and Sohn et al. 2003).

A broad range of algorithms and methods have been developed so far in vibration based NDT techniques, to solve various defect related problems, encountered in structures, ranging from elementary structural components (plates and beams) to complicated structural systems, buildings and bridges, sports stadia (Karadelis 2009 and Fan and Qiao 2011).

According to Ručevskis et al. (2009), vibrations based damage detection NDT techniques are generally based on the dynamic characteristics of the structure, in which modal parameters (modal frequencies, mode shapes and damping ratios) are directly related to the stiffness of the structure. Therefore, change occurring in the dynamic features implies a loss of stiffness. However, this can be misleading, if only one parameter, stiffness, is being considered while evaluating the modal parameters. Hence, it is equally important to analyse the structures dynamic behaviour, and the mass in conjunction with the calibrated experimental and FE-model, especially while analysing the voids in the structures.

Vibration based damage detection NDT techniques can be broadly classified as either 'model based' or 'response based' also known as 'non-model based method' (Farrar and Doebling 1997, Fan and Qiao 2011 and Huang et al. 2012). 'Model based methods' include detailed numerical models of the structures under inspection along with experimental data. Whereas, 'non-model based methods' rely only on experimental data.

Lee et al. (2004), on the other hand, classified the vibrations based NDT techniques into four main categories based on the different features being analysed in the damage detection method. These methods are tabulated and presented in (Table 2-3).

Another broad classification is shown by Bakhary (2008), in which the damage detection methods are categorised into three: 'direct methods', 'model updating methods' and 'Artificial Neural Network (ANN) methods'. In this case, direct methods are based on variations in dynamic behaviour, that is change in natural frequencies, mode shapes, or change in frequency response functions. In model updating methods, the model calibration is carried out by a set of reference parameters. These parameters are then updated by using initial suitable values. Sometimes, an algorithm is applied to find the optimum values for the updated parameters that could range from stiffness of the springs of the boundary conditions, to the Young's Modulus of the material. All the updating parameters are physically meaningful, since, the model can be made useful in predicting the variations in dynamic behaviour of the structure with time (Fritzen 2005). This also helps in reducing the number of tests, hence, save time and cost. Neural Networks (NNs) or Artificial Neural Networks (ANN) based damage assessment methods are in use for the last three decades (Pandey and Barai 1994), however, they have recently achieved significant success. These methods involve cause-effect relation of defects and the change in dynamic behaviour (features) that are mapped by specific algorithms, trained to given inputs and outputs data. This mapping is done under the artificial neural network (ANN), and the approach is called supervised learning (Fritzen 2005).

The other approach in ANN is known as unsupervised learning, in which, the algorithm does not make use of the targeted trained data, and instead, it uses a collection of un-labelled samples, that are classified based on the features in the data. Hence, no such target outputs are defined, and it's hard to determine how the output result of the learning process will look like. The former model is more challenging to apply in case there is no extensive data set available to train the model. Hence, unsupervised learning will be more accurate when using smaller data sets. On the flipside, when an extensive dataset is available, this method should be applied in order to predict outcomes. For more information please refer (Adeli 2001).

In one study, Wang (2010) classifies such damage detection methods into three extensive categories: 'methods based on vibrations', 'methods governed by artificial intelligence' and 'methods relying on wavelet analyses'. The first two methods were briefly discussed above and are more popular compared to the latter. In 'wavelet analyses', the data is analysed in the time series unlike common vibrations methods, where the data is analysed in frequency domain (modal analysis). Wavelet analysis tool is used to decompose the time series into time-frequency space (Wang 2010). In frequency spectrum, each frequency component in the signal is derived from the collective contribution, recorded from all sections during the analysis. Therefore, it does not pass any information regarding the occurrence time of the frequency component and its variations with time (Wang et al. 1997). Instead, with the decomposition of the time signal into time-frequency domain or time-scale domain, it is possible to track the development of the frequency components along the duration. This particular property of time-frequency localization is generally exploited in rotating machineries, where, various mechanical faults (cracks propagation etc.) are detected by observing the abnormal transients in the associated vibration signal. This observation of abnormalities in the vibration signals are caused by the shock or impact due to the engagement of the defected section in the mechanical components in the machine (Wang et al. 1997). These wavelet analysis-based methods are generally useful, if, tracking of the flaw development is the objective. On the other hand, with stacks of data-files recorded in time-series, it makes it hard and complex to analyse the data. In addition, a lot more memory is required to store the recorded data in time-domain.

Table 2-3: Damage detection methods categorised by (Lee et al. 2004).

Category		Methodology
Modal Parameters	Natural Frequencies	Frequency variation
		Residual force optimisation
	Mode shapes	Mode shape variations
		Modal Strain energy
		Mode shape derivatives
Matrix Methods	Stiffness-based	Optimisation technique
		Model updating
	Flexibility-based	Dynamically measured flexibility
Machine Learning	Genetic Algorithm	Stiffness parameter optimisation
		Minimisation of the objective function
	Artificial Neural Network	Back propagation network training
		Time delay neural network
		Neural network system identification with neural damage detection
Other techniques		Time history analysis (wavelet Transform)
		Evaluation of FRFs

This research focuses on the method based on modal parameters (modal analysis), as it is relevant to IHT-technique, proposed for this work.

2.8.1 Modal Parameters based methods

Impact hammer testing is a modal parameter based method. In essence, this discusses and compares the modal properties, usually classified as natural frequencies and corresponding mode shapes. Moreover, in complex modes of vibrations, the damping ratios and complex mode shapes can be added. These parameters are the essence of identifying the defects in global assessment methods. The variations in these parameters play a key role in determining the structural health, since, they are associated with the physical properties (mass, stiffness and damping). Any change in the physical properties of a structure or in its boundary conditions, signifies a change in dynamic behaviour, characterized by modal parameters (Dackermann 2010, Farrar, et al. 2001 and Owen and Pearson 2004). According to Hearn and Testa (1991), the most widespread modal parameters in vibrations based damage detection methods are natural frequencies and mode shapes.

Natural frequency based analysis utilises change in natural frequencies as a tool for damage detection. The choice of using natural frequency variations is widely accepted because, first, the natural frequencies are conveniently computed from just few accessible nodes on the structure, hence, resulting in lower cost and easy implementation; second, the natural frequencies are generally less contaminated by test noise (Fan and Qiao 2011).

The majority of early researches was based on natural frequencies shifts, and was related to very simple structures and structural elements (Adams et al. 1978). One of the pioneered and commonly cited papers, based on natural frequencies shift in the damage structure was published by Cawley and Adams (1979). According to them, a single point in a damaged structure is enough to detect, locate and roughly quantify damage by using natural frequencies shift. However, the scheme they presented, also included the use of finite element analysis along with experimental tests, and therefore, this technique was applicable to all structures that were amendable to finite element analysis. They based their scheme on the frequency shift for two different modes in a

damaged composite material. A grid of possible damaged points were considered, and an error term was introduced that compared the measured frequency shifts to those predicted by a FE-model, based on a local stiffness reduction. The number of mode pairs were considered for all potential damage locations, and the mode pair that showed the lowest error between the measured and predicted FE natural frequencies, was used as an indicator of the damage location.

The amount of literature present on the damage detection using shifts in natural frequencies is extensive. Doebling et al. (1996, 1997) and Salawu (1997) have presented an excellent and thorough reviews on the use of natural frequencies variations for detecting damage in a structure. Gudmundson (1982) derived an explicit expression of natural frequencies relating to a wide range of damage. This method also had the ability to account for loss in mass (voids etc.) in addition to loss in stiffness, while estimating the natural frequencies. Stubbs and Osegueda (1990a, 1990b) developed a method, based on the Cawley and Adams (1979) work by using the sensitivity of modal frequency shifts. In their method, they introduced an error function for each mode and each structural member, assuming that only one structural member is damaged. The member that showed the least error or best correlation between the predicted and measured modal frequency, was determined to be the damaged one among the others. Furthermore, the authors pointed out that the frequency shift method relies on the accuracy of the sensitivity matrices, which were computed using FEM. This increased the dependence of the method on an accurate prior numerical model.

Liang et al. (1992) addressed the issues of estimating frequency sensitivity, measured for a simply supported beam having a single crack. A characteristic equation was derived based on the development of an analytical relationship between first order changes in Eigen-frequencies and the damage location along with severity. Morassi (1993) showed that the frequency sensitivity for any beam like structure can be overtly estimated, based on a reference undamaged system, and is proportional to the potential energy stored for the relevant mode shape at the cross-sectional area where the crack exists. Moreover, it was reported that the ratio of frequency shifts of two different

modes, tends to be the function of crack location only. Salawu (1997) noticed that the presence of damage in a structure possesses reasonable alteration in its natural frequencies. It was further reported that for damaged and undamaged structure of known dimensions, the natural frequencies were chiefly related to the stiffness of the system. Moreover, Doebling et al. (1997) and Farrar and Doebling (1997) noticed that the resonant frequencies have considerably low statistical variations from random errors when compared to the other modal parameters. Further research studies, investigating shifts in modal frequencies as indications of damage, were performed by (Adams et al. 1978, Al-Qaisia and Meneghetti 1997, Balis et al. 1995, Hearn and Testa 1991, Narkis 1994, Richardson and Mannan 1992, Sanders et al. 1992, Skjaerbaek et al. 1996, Stubbs and Osegueda 1990a, Villemure et al. 1996 and Wang and Zhang 1987).

Ndambi et al. (2002), carried out a number of experiments on reinforced concrete (RC) beams, in order to monitor the changes in their dynamic behaviour. Two RC beams of 6m length each, were designed for this purpose. A set/combination of two different tests were performed on each designed RC beam. The first test, comprised static loading carried out on each simply supported RC beam (Figure 2-23). The loading configuration was different, resulting in a symmetrical and an asymmetrical test. Step loading was applied in order to introduce cracks gradually in each beam. The static loading and the supports were then removed, and each beam was suspended by four springs, simulating the free-free boundary conditions. The latter set-up was modified for the dynamic testing. It was observed and concluded that Eigen frequencies were influenced by the progressive cracks accumulation in each RC beam. However, the damage location in each beam didn't show any effect on the Eigen frequencies evolution. Moreover, it was observed that Eigen frequencies were reduced monotonically for all modes due to the progressive cracking process. However, the first mode shape in the symmetrical case and second mode shape in the asymmetrical loading showed the highest drop in their natural frequencies (6% and 3% respectively).
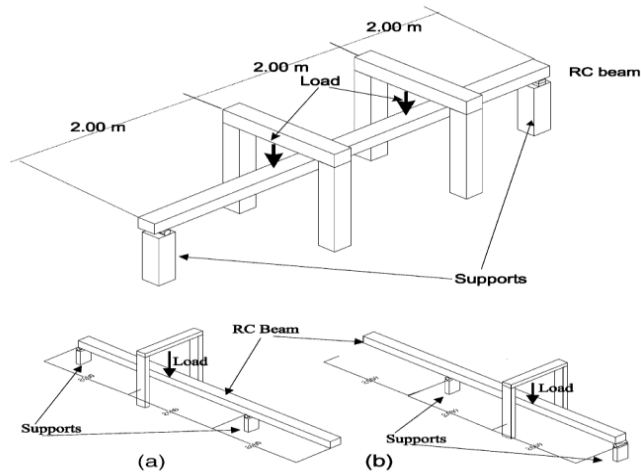
Figure 2-23: Static load: (a) Symmetrical. (b) Asymmetrical loading configurations (Ndambi et al. 2002).

Shi et al. (2000) highlighted that natural frequency is practically more feasible and accurate to be determined than the incomplete mode shapes that depend on the number of nodes being excited. In addition to using natural frequency results to detect damages like cracks only, it was reported in several research studies (Gadelrab 1996, Kim and Hwang 2002, Paolozzi and Peroni 1990 and Sultan et al. 2012) that natural frequencies variations could be used to detect delamination. However, it was also reported that sometimes, damage detection by the natural frequencies based method becomes limited, because of the requirement of very precise measurements. This generally happens for the under-developed damages and is associated with the lower natural frequencies (Doebling et al. 1998).

In order to be certain of damage presence in the structure, recent developments have shown that coupling the measured natural frequencies with other modal parameters, results in better assessment of the damage. Garesci et al. (2006) presented a method for the damage identification and its localisation in the damaged mechanical components. Numerical model updating was employed based on the experimental modal analysis (EMA) data, to localise the damage in the component. The FE-computed natural frequencies and Mode-shapes were compared with the experimentally acquired modal parameters. The developed method was initially applied on a regular rectangular shaped

steel plates that had small milled slots at various locations on the surfaces and were subjected to free-free boundary conditions. Afterwards, the method was extended to a more complex shaped component, a flawed piston rod, subjected to a free-free boundary condition. The outcome of both tests was positive, as the method was able to detect the defects accurately in both the damaged components.

However, the method becomes complex, and the results more difficult to interpret, if the specimen is subjected to various types of constraints unlike simple free-free boundary conditions. The modification in the constraints can introduce uncertainties in the modal parameters, and therefore, the variations in the modal parameters due to the presence of sheer damage, could be polluted by the in appropriate constraints modification. Hence, the effective constraint condition has to be analysed, and simulated precisely in the FE-model in order to interpret the data accurately.

Mohan et al. (2014) carried out a numerical study on damage detection in a cantilever steel beam by using the frequency change correlation approach. They adopted Damage Location Assurance Criteria (DLAC), which is a correlation based approach between the experimental and the numerical frequency change ratios. The focus was on the identification of a single damage per beam and its position, based on DLAC correlation approach that was limited to detect single damage occurrences. For this particular study, three 2D FE-models of cantilever beams were developed, each incorporating damage but at different locations (Figure 2-24)
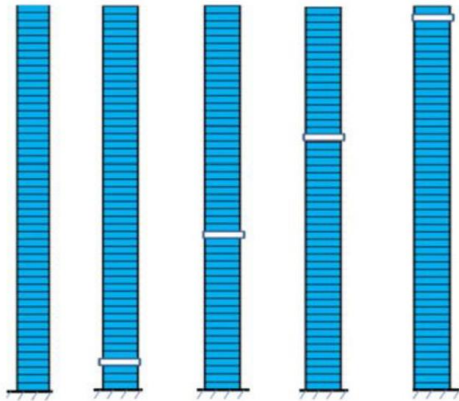
Figure 2-24: Undamaged and damaged 2D FE-models of Cantilever beam (Mohan et al. 2014).

The decreased mass concept was considered in the numerical model to represent damage. The natural frequencies shift for the first four modes for undamaged and damaged beams was compared, and by applying the DLAC correlation analysis, the locations of the damages, were matched with the actual. This method proved to be robust when applied to continuous systems only. Secondly, DLAC value for the damages showed inaccuracy, near the support, hence, resulting in uncertainty in interpretation. Moreover, it is a trial and error approach for calculating the DLAC value for all the supposedly damaged elements one by one, and therefore, it is very tedious and not feasible for complex or large structures.

Bangade and Kulkarni (2017) studied the composites with delaminations, by performing experimental and numerical modal analyses. He reported, that natural frequencies of the E-glass epoxy composite beam, fixed at one end (cantilever position), showed variations, when the delaminations were introduced. Further, it was found that with the increase in delamination area, natural frequencies were reduced. The first three mode shapes for both cases (sound and delaminated) were also reported, however, no clear visual signs of delaminations were observed in the latter case.

Similarly, a steel cantilever beam with multiple cracks was examined by Altunışık et al. (2019). Natural frequencies and corresponding mode shapes of circular hollow section and box section, were estimated by experimental and analytical models. Ambient

vibrations were performed on the laboratory models of cantilever beams. A 17 channel data acquisition system accompanied by 6 uniaxial accelerometers were deployed for the data collection, by exciting a 1000mm long beam (Figure 2-25).

Figure 2-25: Lab scaled model of steel cantilever beams, mounted with accelerometers (Altunışık et al. 2019).

The measurements were taken and compared for the undamaged and damaged beams within the selected bandwidth of 0-1500Hz. A successful indication of the damages was illustrated by the computed mode-shapes, and by the variations in natural frequencies. It was observed that with the increase in the number and severity of cracks, there was a decrease in the natural frequencies, for both beams. An error of 10% for the lower modes and more than 10% for higher modes was observed between the experimental and analytical readings. This showed that for the higher modes, the discrepancies were more. However, model updating was required here, but it was not in the scope of this study.

Although the methods based on natural frequency shifts have been used successfully from the past three decades, there are still several common limitations associated with it.

Modal frequencies are considered to be a global property of the structure, and therefore, the shifts in this parameter cannot be used solely to identify more than level-1 damage (Doebling et al. 1997). In other words, the frequencies cannot give the spatial information about structural changes. An exception to this drawback occurs at higher natural frequencies, where the modes are linked to local responses. Multiple frequency

shifts can be used to extract spatial information about structural damage, because variations in the structure would cause different combinations of changes in the modal frequencies. However, several researchers have pointed out that generally, there are insufficient number of frequencies that show enough significant changes to determine the damage location uniquely (Doebling et al. 1998).

One fundamental limitation with the natural frequencies shifts methods, is the numerical modelling of the complex structures and damages. This is due to the fact that cracks and delaminations are not easy to model. Various elements are used to model such defects. For instance, modelling of crack as a rotational spring, based on fracture mechanics, loses its credibility in higher frequency modes and in deep crack cases Fan and Qiao (2011). Hence, this approach is only suitable for the slender beams incorporating small cracks, and the range of vibrations modes are also then limited to fewer modes (1-4), that are used for the damage detection. Another limitation is the non-uniqueness of the solution of damage severity and location. First, it is obvious that the damage with the same severity and at symmetric locations in a symmetrical specimen, will result in similar natural frequencies shifts. Second, damage with different degree of severity at different locations can also cause a similar natural frequencies shift in few frequency modes. This problem is more prominent for multiple defects in a structure. Therefore, it is very important to consider other modal parameters as well (mode shapes particularly) in conjunction with natural frequencies.

Compared to natural frequencies, the advantage of considering mode shapes and their derivatives as a base for detecting the damage is quite evident. First, mode shapes enclose local information, hence, makes them suitable to identify local damages. Second, they can be used directly for multiple damage case scenarios (Fan and Qiao 2011).

According to Farrar and Doebling (1997), employing mode shapes, which are also known as the local property of the structure, are more powerful than natural frequencies for detecting damages. However, according to Fan and Qiao (2011), the disadvantages

of mode shapes are also obvious. First, acquisition of complete mode shapes, require a number of sensors (depending upon the structure size and modes of vibrations). Second, the acquired mode shapes are more susceptible to noise contamination than the associated natural frequencies.

In order to compare two set of mode shapes, the most common and oldest method available for direct comparison is known as Modal Assurance Criteria (MAC) (Allemang and Brown 1983). The MAC number can be measured as the similarity between two mode shapes, and is ranged between 0 and 1. The MAC number, 0, represents dissimilar match, and 1, represents perfect match. The MAC number is nothing but a statistical indicator that shows the degree of correlation between mode shapes (Pastor et al. 2012). Another similar statistical indicator is the Coordinate Modal Assurance Criterion (COMAC). This compares two mode shapes at each degree of freedom, and hence, shows the contribution of each degree of freedom to the MAC for a given mode pair. West (1984) presented it, which is possibly the first systematic use of mode shape information for the damage localisation without the aid from FEM. He used the Modal Assurance Criteria (MAC), for determining the degree of consistency for the mode shapes set for the space orbiter body flap, before and after, exposing it to environmental acoustic tests. The change in MAC number across the different mode shapes was used for damage identification and localisation.

Fox (1992) showed that the MAC number is relatively insensitive to the damage in a beam with a small saw cut. However, it was found that a MAC value based on measurement points that are in the close vicinity of the nodal points for a certain mode, was a sensitive indicator of damage, causing change in mode shapes. Further, it was shown that the graphical comparisons of relative changes in mode-shapes were evident to be the best way to locate damage visually in conjunction with the resonant frequencies.

Full scale forced vibrations tests before and after repairing, were conducted on two lane reinforced-concrete Highway Bridge with 104m span, (Salawu and Williams 1995). The

aim of the tests were to investigate any correlation, existed between the repair works and the change in dynamic behaviour of the bridge. A purpose built hydraulic vibrator was employed to artificially excite the bridge, and several accelerometers were used to record the dynamic behaviour of its deck. Moreover, a single degree of freedom model was used for measuring natural frequencies, mode-shapes and damping ratios. It was found that the modal frequencies were altered slightly due to repair work, however, no particular trend was observed in damping ratios, whereas, comparison of mode-shapes before and after repair work gave an indication of the damage location.

The applications of mode-shapes based damage detection methods, have been investigated by many authors (Allemang 2003, Foti 2013, Jassim et al. 2013, Kam and Lee 1992, Kim et al. 1992, Osegueda et al. 1992, Rizos et al. 1990, Saitoh and Takei 1996, Salawu and Williams 1995, Srinivasan and Kot 1992 and Yuen 1985). The prime focus was to find the change in mode-shapes along with the MAC values measured for pairs of mode-shapes. The results were promising and were encouraged to be used in conjunction with the natural frequencies for damage identification and localisation.

An experimental and numerical study was carried out by Karadelis (2012) on the modal parameters identification of the 'Grandstand Terraces'. The RC terrace units were placed and tested on a specially built steel frame, resting on the floor in the Civil Engineering laboratory, Coventry University (Figure 2-26).
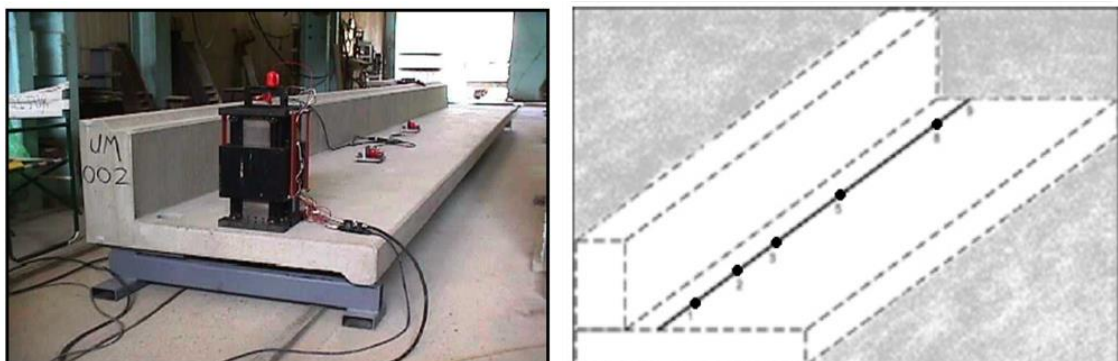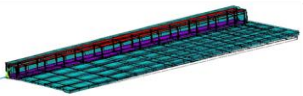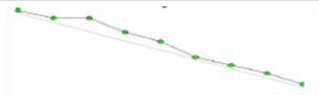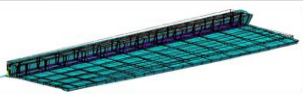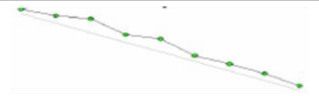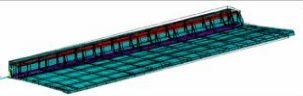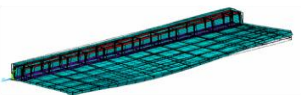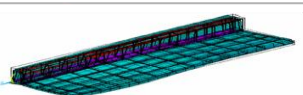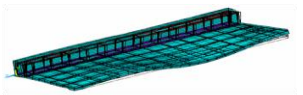
Figure 2-26: A terrace unit resting on the steel frame and its corresponding modal test grid (Karadelis 2012).

The shaker was used for providing the excitation, where the accelerometers measured the response. The Spectrum Analyser (FFT), performed the time and frequency domain analyses, estimated the frequency response functions (FRFs), and the modal parameters were extracted. In parallel, the FE-model updating and fine tuning were carried out until the results matched with the experimental ones. The final updated FE-model showed an accuracy of approximately 96%. The computed mode shapes were also in good agreement (Table 2-4). The conclusions were drawn that the experimental procedures might not be adequate to depict certain complex mode shapes accurately, at higher modes of vibration, and therefore, must be assisted by the FEA, in order to capture those complex mode shapes with certainty and accuracy. Moreover, it was found that the dynamic properties of the terrace units were highly sensitive to two parameters, the physical properties of the concrete and the support conditions.

Table 2-4: Experimentally and Numerically computed modal parameters (Karadelis 2012).

Mode No.	Experimental Modal Analysis Mode Shape	FE Modal Analysis Mode Shape	f (Hz) Exp. Theo. ζ_{exp} (%)	Comments
1			12. 1 0 12. 24 — 1.4	The fundamental bending mode of vibration.
2			14.7 0 1 4.55 — 2.0	Predominantly torsional. May also be showing small amount of bending.
3			30.0 6 30 .7 0 — 1.2	Similar to Mode 2.
4			40. 0 1 4 4 .56 — 1.0	The second (flexural) mode of vibration.
5			67.3 7 1 .4 — 1.6	Near perfect flexural mode with a small amount of torsion.
6	?		103.00	Bending Mode

Iliopoulos et al. (2016), predicted the dynamic behaviour of a monopole Offshore Wind Turbine (OWT), located in the Belgian North Sea. The dynamic response (natural frequencies, mode-shapes) were recorded by the limited number of vibrations sensors

(accelerometers) for a duration of 2 weeks, when the wind turbines were in parked conditions. This experimental data was further utilised for FE-model updating, whereas, three mode shapes, obtained from experiment were compared with three corresponding mode shapes, from the FE-model (Figure 2-27).
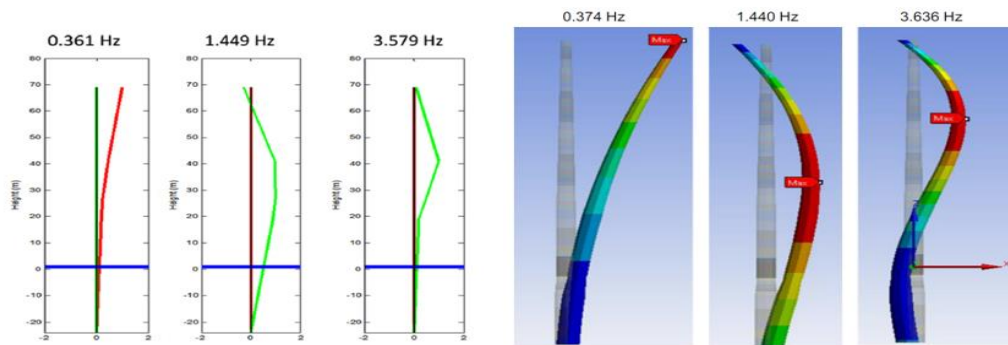
Figure 2-27: Experimental (Left) and Numerical (Right), first three mode shapes of foundation tower (Iliopoulos et al 2016).

In addition, the MAC number was also utilised to compare the mode shape pairs. Good agreement was shown between the two pairs of mode shapes. Hence, credibility of the modal parameters (natural frequencies and mode-shapes) was achieved, and the latter were confidently utilised for monitoring the structure's dynamic behaviour.

Altunışık et al. (2017), reported another successful application of modal parameters, natural frequencies and mode shapes, for the detection of a multiple cracked cantilever beam, having hollow circular section. The study comprised of experimental and numerical modal analyses. It was found that the cracks strongly affected the natural frequencies of the beam, which were decreased, compared to that of undamaged one. The numerically computed mode shapes for the severe damaged condition were more profound in identifying cracks, compared to the experimentally obtained ones (Figure 2-28). This shows the usefulness of updated numerical models, that can compensate the experimental tests shortcomings.
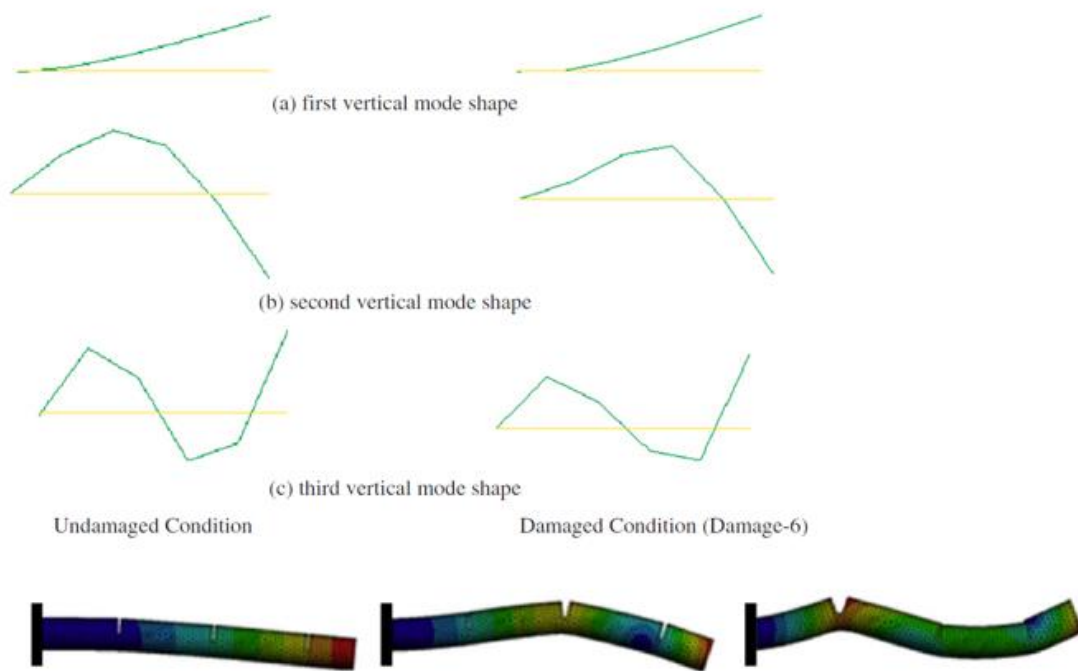
Figure 2-28: Experimentally (above), and Numerically (below) computed first three mode shapes for severely damaged cantilever beam (Altunışık et al. 2017).

Another modal parameter, that is not as widely utilized as other modal parameters, for indicating the damage in structures is 'damping'. This is due to the inconsistencies and complexities generally associated with this parameter. Slastan and Pietrzko (1993) reported that modal damping values were insensitive to provide sufficient information about a damage in concrete beams. Whereas, Pandey and Biswas (1994) found that damping in the wide-flange steel beam was increased due to cracks. Similarly, Saravanos and Hopkins (1995) reported that the delaminated composite beam had lower flexural damping than the laminated configuration, however, in small sized delaminations (less than 10% of beam span), the damping parameter could not give any significant information. According to Modena et al. (1999), the cracks in reinforced concrete (RC) beams caused considerable variations in the damping ratios, compared to the sound RC beams.

Razak and Choi (2001) investigated the effect of corrosion on the modal parameters of RC beams. Modal tests were carried out on three RC beams, two of them were induced

with the damage (corrosion), where the third one was undamaged, and used as a 'control beam'. The modal parameters were extracted and compared against the ones obtained from a control beam. It was observed that natural frequencies and damping ratios showed variations. Natural frequencies showed a consistent drop for all modes in both damaged beams, compared to the control beam. However, the damping ratios showed an inconsistent trend when compared for the first three modes. The second and the third modes for both damaged beams were slightly higher than the corresponding ones from the 'control beam', while for the first mode, the behaviour observed for both damaged beams was opposite. This suggested that the trend for damping ratios for the damaged beams is mode dependent.

A pilot study on the timber floor systems was carried out by Soltis et al. (2002). Vibration testing techniques were employed on the three floors system, where two of them were built with new joists and one with salvaged. Natural frequencies and damping ratios were estimated for each floor, and it was found that the former parameter was more precise than the latter, in indicating the decay of the timber. The deterioration in the salvaged floor was detected by a decrease in natural frequency (9% approx.), while an increase in damping ratio (11% approx.) was observed, compared to that of new floors.

Curadelli et al. (2008), reported the damage detection by means of structural damping of RC beam. Experimental tests followed by numerical simulations were conducted in this study. The authors concluded damping as a promising damage indicator, when the cracks were introduced in the RC beam. Furthermore, the natural frequencies also showed decent variations in the damaged structure. Similarly, Gomaa et al. (2014) highlighted the sensitivity of modal parameters by conducting theoretical and experimental modal analyses on the steel beam. Artificial cracks were introduced in the lower beam flange at mid-span. It was reported that all the modal parameters were observed as promising indicators of crack identifications, however, damping ratio, seemed to be a more sensitive indicator.

In general, 'damping' is not an established modal parameter, for the damage detection, and therefore, it is not as frequently reported to be a reliable damage indicator as other modal parameters (natural frequencies and mode shapes). Although, there are number of its successful applications, as reported by some of the researchers. However, further investigation is still required in order to use it as a credible indicator for damage detection in vibration based techniques.

The main highlights from the IHT survey are stated below:

- Any change in the physical properties of a structure or in its boundary conditions, signifies a change in its dynamic behaviour, characterized by modal parameters. The most widespread modal parameters in vibrations based damage detection methods are natural frequencies and mode shapes.
- It was observed that natural frequencies were influenced by the cracks accumulation in the concrete structures. However, the damage location didn't have any significant effect on the natural frequencies evolution.
- Some researchers highlighted that natural frequency is practically more feasible and accurate to be determined than the incomplete mode shapes that depend on the number of nodes being excited. In addition to using natural frequency results to detect damages like cracks only, it was reported in several research studies that natural frequencies variations could be used to detect delamination. However, it was also reported that sometimes, damage detection by the natural frequencies based method becomes limited, because of the requirement of very precise measurements. This generally happens for the under-developed damages and is associated with the lower natural frequencies.
- In order to be certain of damage presence in the structure, recent developments have shown that coupling the measured natural frequencies with other modal parameters, results in better assessment of the damage.
- Numerical model updating is commonly employed in parallel to the experimental modal analysis (EMA), to localise the damage in the component.

The FE-computed natural frequencies and mode-shapes are then compared with the experimentally acquired modal parameters.

- The variations in the modal parameters due to the presence of sheer damage, could be polluted by the in appropriate constraints modification. Hence, the effective constraint condition has to be employed, and simulated precisely in the FE-model in order to interpret the data accurately.

- It was observed that in most of the cases, the error computed between the experimental and theoretical readings was less than 10%, for the lower modes, however, for the higher modes, the discrepancies were more, and therefore, necessitating the FE-model updating.

- One fundamental limitation with the natural frequencies shifts methods reported, is the numerical modelling of the complex structures and damages. This is due to the fact that cracks and delaminations are not easy to model.

- Another drawback associated with natural frequencies shifts method is the non-uniqueness of the solution of damage severity and location. First, it is obvious that the damage with the same severity and at symmetric locations in a symmetrical specimen will result in similar natural frequencies shifts. Second, damage with different degree of severity at different locations can also cause a similar natural frequencies shift in few frequency modes. This problem is more prominent for multiple defects in a structure. Therefore, it is very important to consider other modal parameters as well (mode shapes particularly) in conjunction with natural frequencies.

- The two main advantages reported for mode shapes in detecting the damage are: First, mode shapes enclose local information, hence, makes them suitable to identify local damages. That means the graphical comparisons of relative changes in mode-shapes were evident to be the best way to locate damage visually in conjunction with the resonant frequencies. Second, they can be used directly for multiple damage case scenarios.

- In contrast, the two main drawbacks associated with mode shapes, and discussed in the literature are: First, acquisition of complete mode shapes, require a number of sensors (depending upon the structure size and modes of vibrations).

Second, the acquired mode shapes are more susceptible to noise contamination than the associated natural frequencies.

- One remark on the experimental modal analysis was that the experimental procedures might not be adequate to depict certain complex mode shapes accurately, at higher modes of vibration. Therefore, in such cases, it must be assisted by the FEA, in order to capture those complex mode shapes with certainty and accuracy.

- Damping ratio, was not as frequently reported to be a reliable damage indicator as other modal parameters (natural frequencies and mode shapes). However, there were number of its successful applications, reported by some of the researchers. Further research is still required in order to consider, if it can be utilized as a credible indicator for damage detection in vibration based techniques.

2.9   Research Gaps in the Literature Review

After carrying out, a critical literature survey on Infrared thermography (IRT) and Impact hammer Test (IHT), several drawbacks, and the areas for improvements were identified for each technique.

It is important to mention that the reliability of IRT is not as established as IHT technique, because of the vast number of research literature available for the latter, spanning several different disciplines of engineering (automotive, aerospace, mechanical, civil, structural etc.). Therefore, the weight will be thrown in improving the IRT's reliability. Table 2-5 summarises the research gaps for each NDT technique (IRT and IHT) that will be considered while carrying out the laboratory tests.

Table 2-5: Limitations, and Improvement areas of the NDT methods (IRT and IHT).

NDT Technique	Room for Improvement/Research Gap	Limitations/Comments
Infrared Thermography (IRT)	• Comprehensive Quantitative and Qualitative analysis of delamination has never been reported. • Effects of Depth and thicknesses (delamination) on the thermograms have not been investigated with rigour. • The 'evolution' of delamination or their classification (degree of debonding) not reported. • The use of FEM for passive IRT is still new and needs further work along with experimental testing in ambient conditions. • Optimum ambient conditions for the best IRT performance is yet to be explored.	Camera resolution plays key role in detecting small temperature contrast due to defects. IRT not possible in windy weather condition (more than 25km/hr). IRT not possible at very low temperatures (snow etc.). Shadows, local sunshine, Cloudy weather affects the results. Interpretation of defects due to low thermal contrast is difficult. Deep defects are undetectable. Contaminants on the roads, affect the results interpretation too. ASTM D 4788-03:2013 , Avdelidis et al. (2003), Celaya (2011), Clark et al. (2003), Moropoulou et al. (2001), Stimolo (2003) and Tsubokawa and Yukitomo et al. (2007).
Impact Hammer Test (IHT)	• Delamination detection beneath thin concrete overlays (highways) and its dynamic behaviour (modal analysis), while supported on subgrade is never reported. • The 'evolution' of delamination (voids) in concrete pavements is never reported. • The use of FEM in parallel to experimental modal analysis of the above, and replicating real support conditions require further probe. • Damping ratio is a controversial damage indicator, and needs further investigation.	Mainly used in testing steel beams and reinforced concrete beams for detecting cracks. IHT is suitable in detecting delamination in epoxy graphite composites. Generally free-fee boundary conditions are considered during modal analysis of a beam in the laboratory. The literature is available mainly on evaluation of bridges, therefore, only the bridge support conditions have been simulated in the lab-based testing. Curadelli et al. (2008), Garesci et al. (2006) and Ndambi et al. (2002).

2.10 Summary

The literature review was intended to be critical for the existing NDT techniques, which are used for the delamination detection in concrete pavements. However, the focus of the literature review was, Infrared Thermography (IRT) and Impact hammer Test (IHT), the two NDT techniques, selected for this research study. The justification of the techniques was made, and the room for improvement for both techniques was discussed. Moreover, the research gap was highlighted, and the main points to be investigated during the course of this pilot study were clearly stated (Table 2-5).

Chapter 3 - Research Methodology

3.1 Introduction

The aim of this Chapter is to propose a correct and logical pathway to reach the objectives promised earlier, in Chapter one.

On top, Methodology should have a more generalised, more global purpose. One should be able to replicate the methods adopted in one investigation and create similar methods in another, comparable type of research.

There are two broad ways of approaching research. Primary research deals with information collected through original, or personal research, whereas, secondary is information that has been collected in the past, mainly by others. Both have advantages and disadvantages.

Research (data), and research analyses, such as quantitative is a systematic, largely empirical-experimental investigation that may be assisted by statistical, mathematical or computational (approximation) techniques. On the other hand qualitative, although a widely accepted scientific method, it is nevertheless based largely on observation, rather, than gathering and crunching numerical data. The schematic in Figure 3-1 provides an overview of the research methods in general. Mishra and Alok 2017 provides a more integrated account and elaborates on the above.

This thesis will be based on a strong methodological basis, traces of which were reported in Chapter 1, Introduction. It endeavours to explain and justify the types of research adopted in assembling and analysing a relatively diverse and "dissimilar" number of data. Any scientific and theoretical (not necessarily mathematical) concepts used/developed during experimentation, or during processing of data, will be highlighted, or given special attention and then blended with the research.

The selection of methods presented will be the result of a conscious and reflective research process. Advantages, disadvantages, limitations, weaknesses, etc of the former will be discussed and explained, and a clear link between the choice of methods implemented and the analytical tools used will be established.
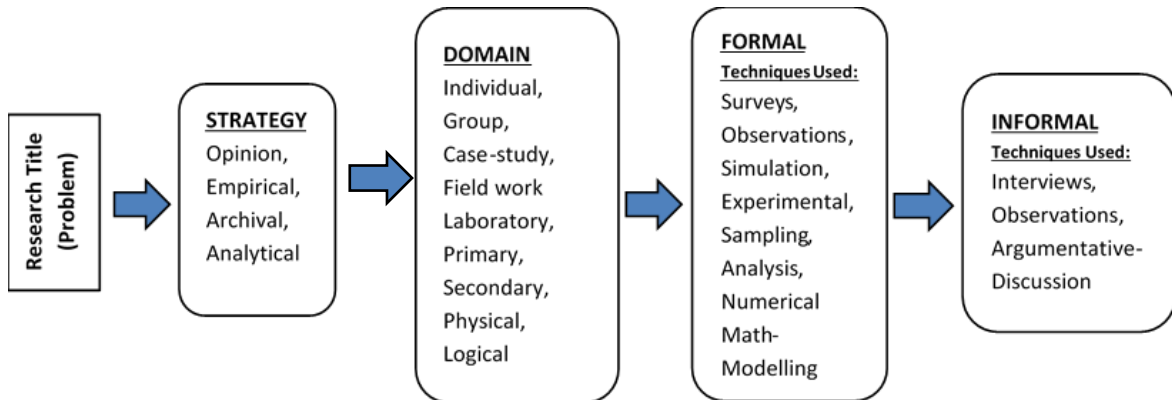
Figure 3-1: Summary of the Research Methodology Framework.

3.2 Research Methodology

The aim of the methodology is to transform the research into a number of concepts and by using valid arguments provide an informative and sound account of the project itself.

3.2.1 *Hypothesis*

The scope of the project is to improve the reliability of the two well-known non-destructive methods, Infrared Thermography and Impact Hammer Testing, and use them together to develop a new method to assess the quality of bond between the top (thin) layer and the one beneath in concrete pavements.

IRT and IHT are two unrelated NDT techniques, which have not been used together in any of their applications. However, there is evidence to suggest that by improving and perfecting these two initially incompatible techniques, and by integrating them and

taking additional support from number of Finite Element Models, one should be able to detect-assess and evaluate the delamination in thin overlays (rigid pavements).

3.2.2 Research Questions

In getting deeper and deeper the subject mainly via the Literature Review the following main research questions were generated:

1. How can these two NDT techniques, IRT and IHT be perfected to provide a more rigorous and reliable account of the fault?
2. Is it possible to obtain an accurate quantitative and qualitative account of the bond beneath the top thin layer through the combination of IRT & IHT and the finite element analysis?
3. More specifically could thermograms, natural frequencies, mode shapes, damping, as well as a number of other parameters related to the pavement under test, be the key indices for evaluating the delamination severity (between the top, thin overlay and the main layer beneath it)?
4. Can a new advanced Finite Element Model or number of FE-models (coupled: thermal-structural) be developed, incorporating the above two (initially) incompatible methods together in a reliable way, and replace the time consuming and costly experimental work and provide an accurate account of the pavement condition?

3.3 Custom-made Methodology

In a nutshell, the aim of this research is to yield a generalised framework in developing a method capable of detecting the condition of the bond of a rigid pavement, between the top (thin) concrete overlay and the thick concrete layer below, by joining two popular but apparently incompatible non-destructive testing (NDT) techniques, infrared thermography (IRT) and impact hammer testing (IHT).

To achieve this, a primary type of research is to be adopted, combined with a largely quantitative analysis approach, as defined earlier. In this case, quantitative analysis is closely allied with investigating the performance of IRT and IHT as two distinct NDT techniques, and then join them together via the finite element method.

Infrared Thermography (IRT) Technique

All objects emit electromagnetic radiation uniquely related to the object's temperature. Infrared thermography (IRT), provides images (*thermograms)* representing surface temperatures by measuring the magnitude of infrared radiation emitting from the surface of an object. This is attained by means of high resolution infrared cameras, and although, the latter have been used fairly productively to '*locate'* delaminations occurring in pavement layers (flaw bond), or similar conditions in the past, their use and contribution is primarily restricted to measuring heat losses from cavity walls. As it has been demonstrated in the Literature Review, IRT has certain limitations because the observed (radiometric) temperature can be affected by a large number of factors such as the object's absolute temperature and emissivity, the emissivity of nearby objects, the ambient temperature, the atmospheric filtering of energy, the distance from the object to the scanner, to mention but a few (Weil and Haefner 1998).

All the aforementioned will be examined and certain parameters/factors will be scrutinised experimentally and numerically in an effort to improve proficiency, accuracy, and confidence of the method. Most importantly, and it is understood that the following constitutes a first, efforts will be directed in developing a relatively informal and simplified way/procedure not only to detect the flaw bond but also to make a first assessment of its structural condition. The finite element method assisted by carefully conducted laboratory tests, will play a crucial role in the above, by developing successful FE-models, and by using the latter to partially replace the time consuming and sometimes limited capacity lab-tests. In other words, if required for future, these FE-models would be utilized to carry out pre-planned parametric and sensitivity studies,

to reveal the most common parameters affecting the performance of the IRT method, when used for bond evaluation, and how they are affected.

Impact Hammer Test (IHT) Technique

When a structure is excited by means of a pulse, it responds with its eigenvalues (natural frequencies) eigenvectors (mode-shapes) and enclosed damping. The purpose of Impact Hammer Test (IHT) is to compliment the evaluation procedure started by the IRT, by providing the detailed information '*missed'* by the latter, and by delivering the *assurance* that is usually short in most NDT-techniques.

The method was initiated and developed in the aerospace industry, and it was soon adopted by all motor vehicle manufacturers who wanted to perfect their products by eliminating any unwanted vibrations, hence, improve safety and comfort. The same method is also used in the electrical and electronics industries, and even in domestic appliances manufacturing today.

Only relatively recently, due to the drift towards long spans and slender, "*tuneful"* structures, and with the advent of suitable vibration equipment, the IHT-method has become popular with civil engineering projects. It has therefore been used to estimate the dynamic properties of large structures like bridges and stadia. It is obvious from this introduction that the method is well established, relatively accurate, and postulated. However, it has a couple of serious drawbacks that it is very slow to produce reliable results and it necessitates skilled operators. Hence, it has been decided to use it as a last resort and essentially, when the information obtained by the IRT is inconclusive.

Development of a New-NDT&E Method (IRT+IHT)

The adaptation of the method to suit the relatively "*fast*" and reliable requirements sought by testing long stretches of roads and airfields is an important issue. It is anticipated that for this, the combination of a tailored made/modified version of the

LWD (light weight deflectometer) combined with impact hammer procedures and mounted on a specially adapted vehicle, can improve the speed of flaw bond evaluation without compromising in accuracy. However, this is outside the scope of this research.

The finite element method (FEM) is employed once again to help with experimental investigations in a similar manner as highlighted earlier, and replace the copious laboratory based parametric and sensitivity studies.

The incompatibility of the two NDT techniques, Infrared Thermography and Impact Hammer Testing, was mentioned at the beginning. It was also mentioned that aside of that setback, the two have to be joint into one and work as an integrated method. In broad terms this can be achieved with the aid of the FEM. Hence, "*coupled*" finite element analysis is proposed. In brief, the method should start by scanning the road using IRT techniques. Calibration of the latter should be suitable for a "*three way system*" in place.

A first assessment and estimation of the fault should provide some information of the quality of the bond beneath the surface of the pavement. This should be classified as sound, partially damaged and critically damaged, and therefore, requiring the corresponding attention. It is understood from the state-of-the-art literature review carried out earlier, that this has never been attempted before. It would be allied with efforts to improve accuracy and extend the use of IRT, and therefore, make a contribution to the method.

If, after the above, the information provided by the IRT is inconclusive, then the IHT-method should be called. In this case the test vehicle should turn back to the suspected stretch of road/airfield to perform a *quick* IH-Test.

The latter can be done using a virtual grid of the portion of the road under modal analysis. The LWD could be released from the test vehicle, and any accelerations at the nodes can be measured by using a bar with a number of accelerometers attached,

lowered to the road surface. The weight should be dropped on the road surface using an on-board computer. The data collected should be passed to a remote, central computer using *blue-tooth* technology. Processing should be carried out with the aid of FE-models, now used as prediction tools. Assessment and decision making should be done automatically, and a technical report will be generated.

The Schematic in Figure 3-2, outlines the research methodology, where Figure 3-3 and Figure 3-4 shows the summarised procedures for performing IRT and IHT respectively (Details are available in respective Chapter 04 and 05).
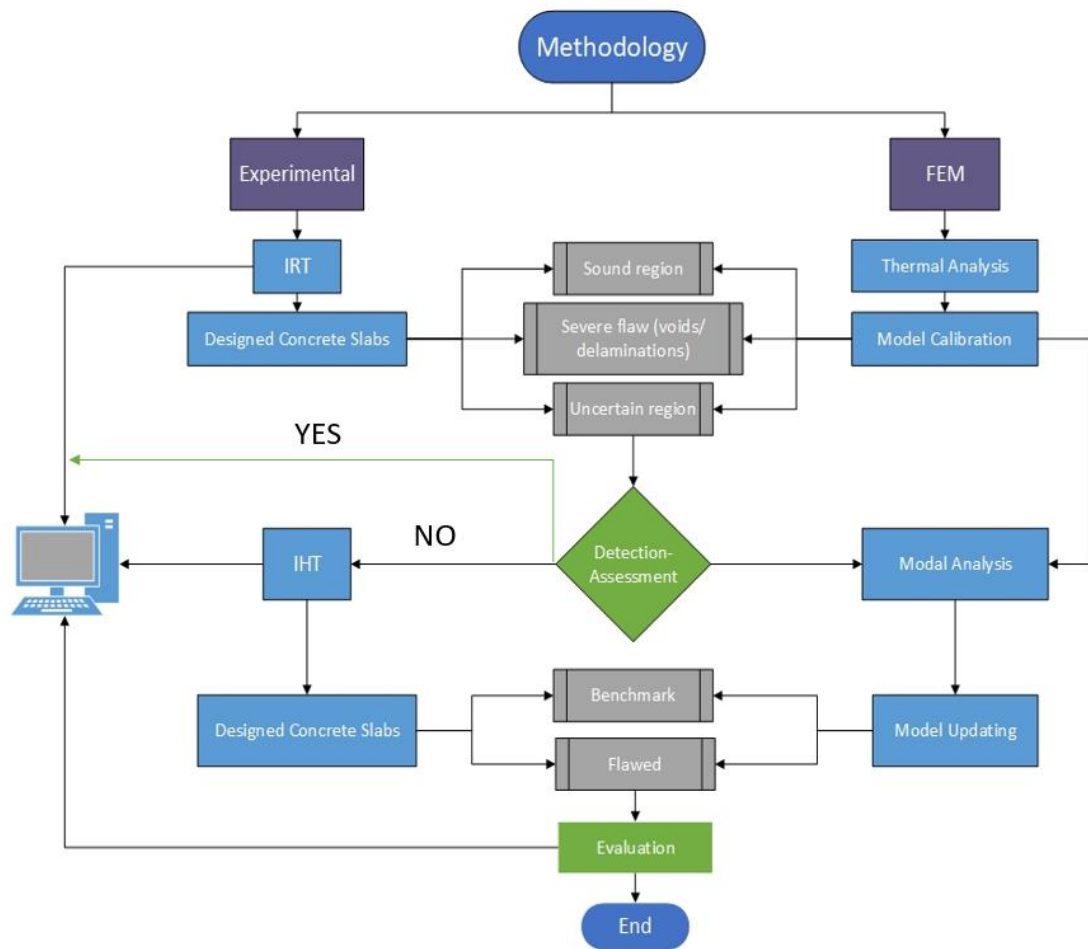

Figure 3-2: Research Methodology Flowchart.
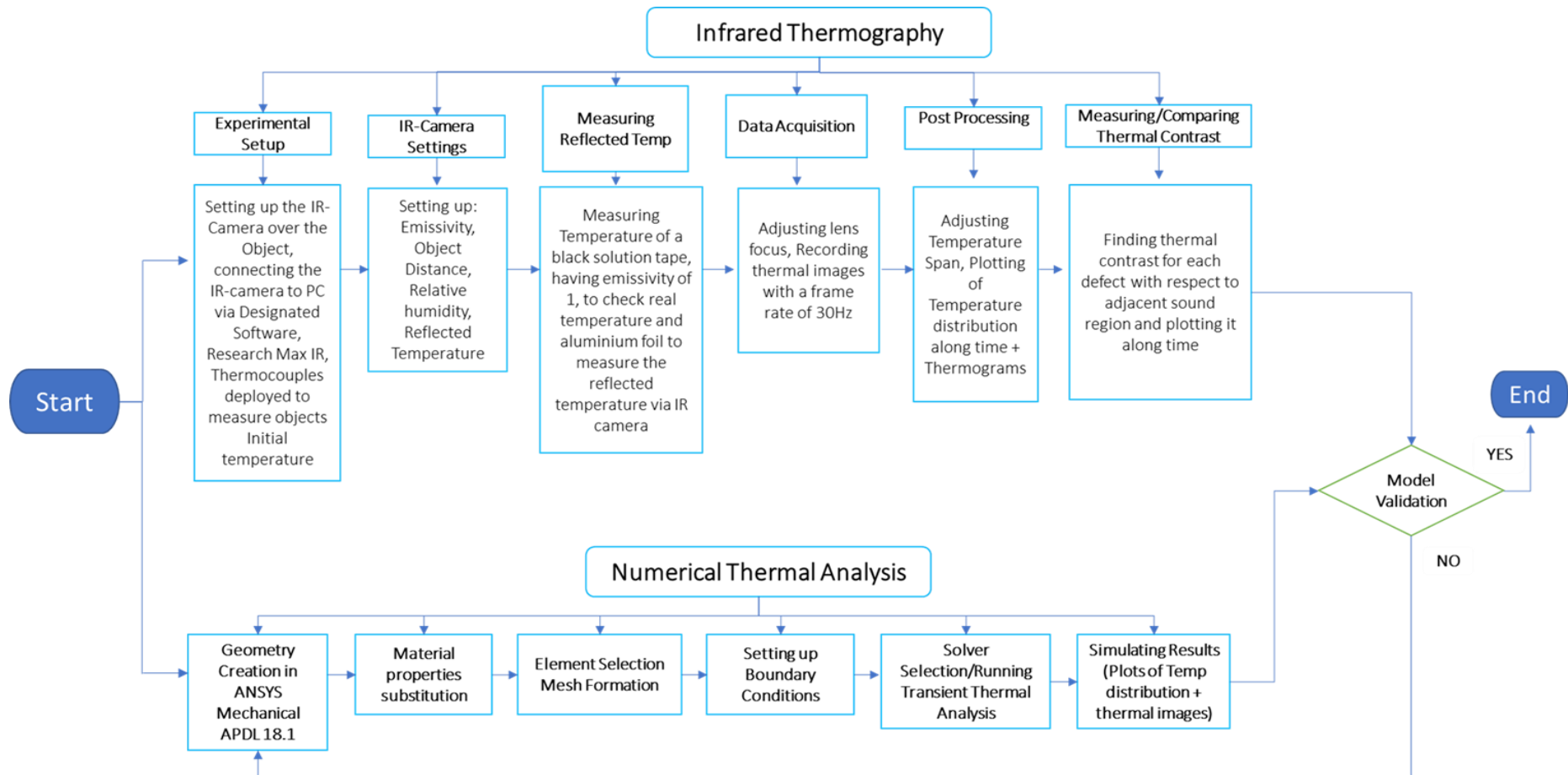
Figure 3-3: Synoptic procedure for Infrared Thermography Test.
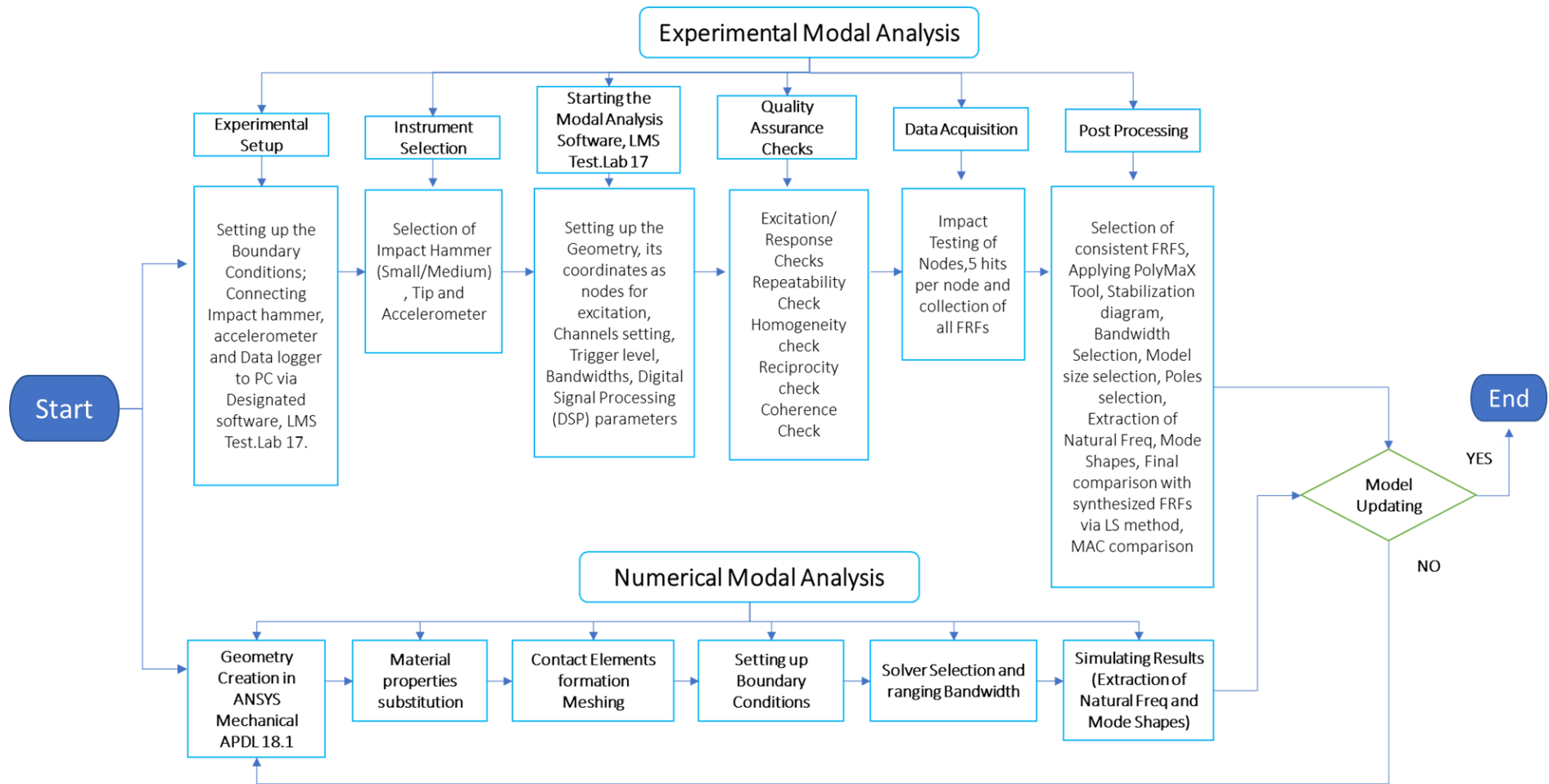
Figure 3-4: Synoptic procedure for Impact Hammer Test.

3.4 Summary

This chapter discussed the research methodology, and briefly the overall ideas to base the next chapters (4, 5 and 6). Moreover, it included the research hypothesis and the relevant research questions, followed by a full comprehensive programme of three phase-methodology and finally, the summarised procedures of both NDT techniques, IRT and IHT in a form of synoptic chart. The first phase included IRT as the first NDT technique to be employed experimentally, aided with FEA, on the special cast concrete slabs (*sound/flawed*), where the first assessment would be made on the defects characterisation. The second phase comprised of IH-Testing of the similar and additional cast slabs system on various support conditions (*purposely built soffit* and *designed subgrade*) along with FEA, and further evaluation would be made. The focus of both NDT techniques would be based on the 'research gaps' highlighted earlier in Chapter 2, Literature Review. Finally, in the third and last phase, the two aforementioned NDT techniques would be integrated (IRT+IHT), with the help of tuned/calibrated FE-models and guidelines for the ''new''NDT&E method would be developed, for the detection and assessment of the void/delamination below thin overlays with reliability and accuracy.

Chapter 4 - Experimental and Numerical Study of Infrared Thermography Method

4.1 Introduction

This chapter consists of two important sections as demonstrated in Figure 4-1.
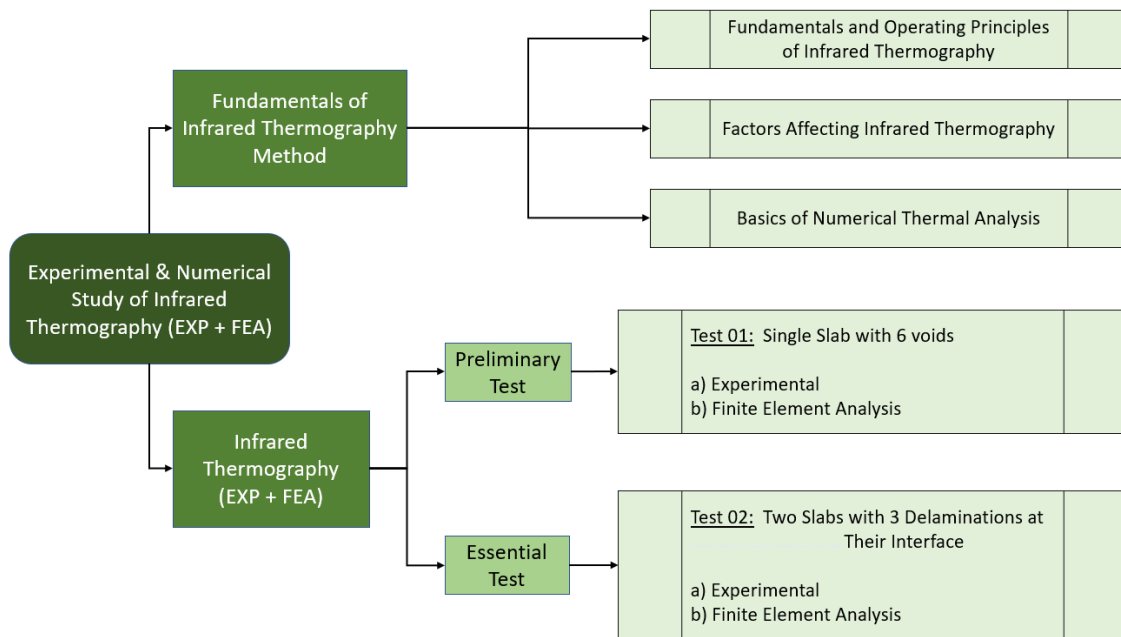
Figure 4-1: Synoptic Plan of Chapter 4.

4.2 Fundamentals of Infrared Thermography Method

Infrared thermography is based on the natural physical phenomenon that all objects above absolute zero (-273.15°C), emit electromagnetic radiation (IAEA 2002). These radiation does not need medium to travel.

Infrared thermography is based on three well known laws of electromagnetic radiation: 'Plank's law of radiation', 'Kirchhoff's law' and 'Stefan Boltzmann law' (Gaussorgues

1994). The details are available in Gaussorgues (1994). However, from these laws of radiation, it is concluded that temperature has a significant impact on energy and emissivity of an object, which in turn is an important parameter in the working of infrared thermography. Emissivity is a surface property, and is the ratio for emission of a real body to that of the black-body under the same temperature, direction and spectral band of interest. It is a dimensionless quantity that spans between 0 to 1 (FLIR Systems 2013, Maldague 2000 and Wild 2007). It is also sometimes mentioned as emission coefficient and is denoted by ε.

$$\varepsilon = \frac{E}{E_s} \qquad (4.1)$$

where,

  E = Thermal emission of a real body (Wm^{-2})
  E$_s$ = Thermal emission of a *black body* (Wm^{-2})

The ideal amount of radiation that can be emitted by a body is that of a 'black-body'. In reality, the amount of radiation emitted is much less than that of the black-body, especially at certain wavelengths. Thermography is based on emission by objects.

According to Wild (2007), emissivity is dependent on wavelength, temperature, surface texture of the body, geometry and size of the body, and it is generally not constant. Therefore, several types of emissivity are introduced, such as: *spectral-directional emissivity*, the emissivity of a surface at a certain wavelength and temperature in a specific direction. Similarly, *spectral-hemispheric emissivity* is defined as the average emissivity over all possible directions and wavelengths. Normally, the emissivity values tabulated for measurement purposes are the average values provided for the normal incidence angle over the whole spectral range and for the specified temperature (Gaussorgues 1994 and Maldague 2000).

Electromagnetic radiation (infrared) can be reflected, absorbed or transmitted through a surface. This can be quantified through Kirchhoff's law, which states that the sum of reflected, absorbed and transmitted radiation through a surface is equal to 1, i.e. R+A+T =1 (FLIR Systems 2013, Galbraith 2013 and Lowe 2008). Since, Absorptivity = emissivity, A could be denoted by ε. The final form of Kirchhoff's law can be stated as:

$$\varepsilon + r + \tau = 1 \qquad\qquad (4.2)$$

where,

ε = Emissivity, r = Reflectivity and τ = Transmissivity of the material.

If the object is opaque, $\tau = 0$, and therefore, the equation reduces to:

$$\varepsilon + r = 1 \qquad\qquad (4.3)$$

Equation 4.3 is very important in thermography, because high emissivity means the object has low reflectivity and vice versa. In IRT, it is required to have a high emissivity in order to get the accurate readings (FLIR Systems 2013 and Lowe 2008). As in this case, most of the radiosity (total radiations emitted plus reflected) would be mainly due to emitted infrared radiations by the object, and therefore, providing the accurate surface conditions of the object.

4.2.1 Infrared Thermography operating principles and Equipment

Infrared thermography is defined as the process of acquisition and analysis of thermal information obtained from non-contact thermal imaging devices. Based on the electromagnetic radiation laws, the infrared thermography operating principles can be defined. Infrared thermographic systems utilize the phenomenon that every object having temperature above absolute zero radiates infrared radiation. These radiation are detected by the IR cameras or IR thermometers. These radiation correspond to various wavelengths that are associated with surface temperature. Therefore, the final thermal image which is obtained from the IR camera is presented in the form of thermal contrast (FLIR Systems 2013, IAEA 2002 and Lowe 2008).

IR-camera operates based on the incident infrared radiation (collected from surrounding and specimen under investigation) that are focussed by the lens before reaching the detector. The detectors are used to detect the temperature of the surface. Each pixel represents the temperature at a point on the surface. The detector is composed of IR sensitive elements, which are arranged in a form of array called Focal Plane Array (FPA). These miniature elements and their number determines the pixels or resolution of the IR camera. A *micro-bolometer* is a type of detector that is generally used in the IR camera. When the radiant energy strikes the detector, it rises its temperature and changes its electrical resistance. The change in resistance is measured and processed into the temperature gradient, which is presented in the form of thermal image and analysed in a thermal imaging software. The block diagram of IRT functioning is shown in (Figure 4-2).
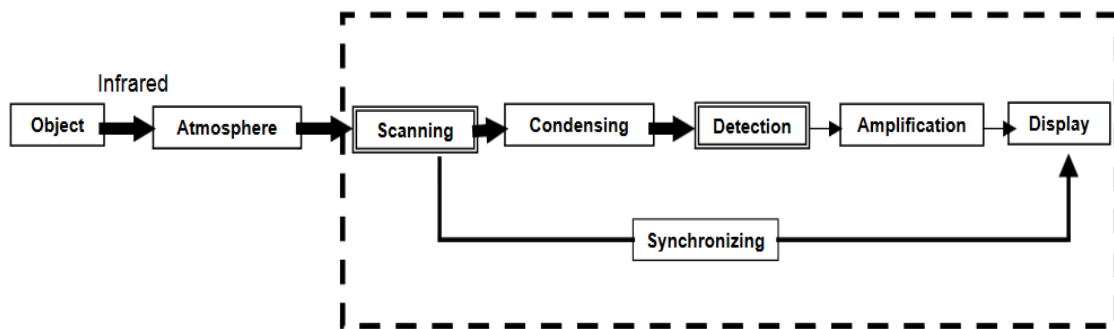
Figure 4-2: Block Diagram of IRT functioning (Nippon Avionics CO LTD 2017).

It is very important to mention here that humidity can have a major interference with infrared systems. Water vapours present in the air, absorbs the infrared radiation, if they are in the mid-infrared range. These vapours appear gas to the infrared camera detectors and gives false readings. In addition, these vapours can also condense on the optics or metal detectors and cause the infrared beam to be diffracted, hence, giving erroneous readings. Therefore, relative humidity is an important parameter to consider while taking thermograms especially in very humid conditions.

Broadly an IRT system consists of Infrared camera and thermal imaging software. Furthermore, the complete IRT system can be divided into four main sub-systems.

First is the IR camera, which apparently looks like a portable video camera (Figure 4-3), used with interchangeable lenses.

Figure 4-3: Infrared Camera (FLIR Systems 2013).

In IR camera, detectors define the traceable range of wavelengths in infrared band. The detectable range lies between 2 and 14 microns. The range 2-5.6 microns is generally used for visualising the object's temperature, if it is in the range between 40°C to 2000°C. However, for ambient and low temperatures 8-14 microns range is generally used. It is also quite important to consider the atmospheric windows to get the maximum transmissivity for infrared radiations. Therefore, many cameras are operated in the range of 3 to 5 or 8 to 12 microns, as atmospheric window complements this range. The other window exists is between .78 and 3microns, depending upon the weather and cloud cover etc.

The second major component in a IR camera is the microprocessor coupled to the camera display monitor. It's a real time component that records and converts the electrical signal into thermal image. The thermal image could be presented further in a different colour palettes, but grey and white is one of the common type of representation. Warmer areas are represented by the lighter grey tones or white, whereas dark grey tones represent the colder regions. Different colours (8, 16 or 256) in a palette are assigned to different temperature range displayed in the thermal image. It is important to note that these colour assignments to temperature ranges do not have any physical meaning, hence, they are also known as fake colour maps (Gaussorgues 1994 and Vavilov and Maldague 1994).

The third component in the camera is the user interface. It is used to control the camera parameters like emissivity, relative humidity, distance from the object, video recording, and so on.

Fourth sub-system in the IR equipment is the computer and thermal imaging software. Computer and software in the infrared scanning system are used for the data acquisition and analysis of the thermograms. The computer allows for the transfer of live images of the infrared scenes and instrumentation videotapes, from infrared camera to storage. In fact, the IR-camera can be controlled live through thermal imaging software. Thermograms recorded can be analysed at the same time. These images can be stored

and retrieved later for further enhancements or interpreting purposes. In new cameras, both, visual and thermal image can be taken at the same time and therefore, making comparisons easier.

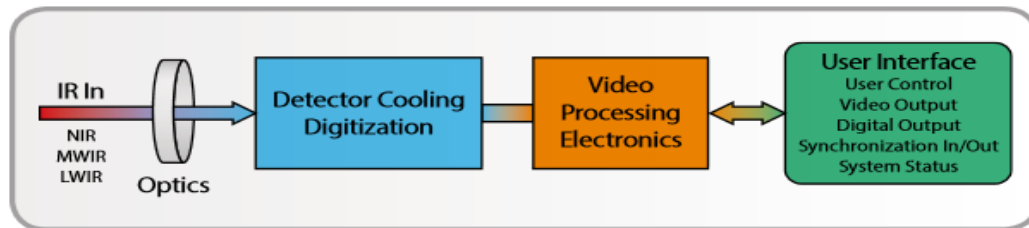A simplified block Diagram of the IR equipment is shown in (Figure 4-4).

Figure 4-4: Simplified Infrared Camera block diagram (West 2012).

4.2.2 Factors Affecting Infrared Thermography

Thermal images obtained from infrared camera, measure the temperature distribution over the surface. This temperature gradient is caused as a result of a dynamic process. This temperature distribution doesn't remain constant and varies with time. Since, the temperature distribution varies from time to time over the same surface during the heating or cooling phases (as discussed in Ch 2, Literature Review), therefore, the results interpretation should take account of these conditions, where one particular surface can produce different thermograms due to different surroundings and surface temperature.

To detect the internal structure anomalies like delamination, voids etc. other physical properties should be taken into consideration (heat capacity, thermal conductivity, thermal diffusivity, density) in addition to the spectral properties (emissivity, reflectivity, transmissivity) of the specimen (Gaussorgues 1994). Among the spectral properties, emissivity is the most important parameter or object characteristic that should be selected correctly for the surface under consideration. Naturally, any interior surface defect has an impact on the temperature distribution over the surface, as the heat propagating through the object is affected by the defects, and therefore, a time delay before the temperature changes is observed. Hot spots and cold spots are observed due to the temperature variations at the defected regions, and are picked by the IR camera in the form of thermograms or thermographs. For instance, a sub-surface void can act as an insulator and accumulate the heat, and therefore, a hot spot will be observed during the day time, and a cold spot at night when the heat transfer reverses its direction.

In infrared thermography, temperature distribution of the surface is only measured and is represented by thermograms. This temperature distribution is influenced by three factors: subsurface configuration, surface condition, and environmental conditions (Gaussorgues 1994). In inspecting the object, the subsurface configuration is the key, or usually the most important factor in infrared thermography as it results in affecting the heat flow through the object.

The three possible ways of transferring thermal energy from warmer to cooler regions are conduction, convection and radiation. In sound concrete, there is least resistance in conduction of heat, whereas, in defected concrete the heat flow is interrupted, therefore, decreasing the thermal conduction and giving the signs of anomalies in the concrete.

A heat source is required in order to cause a heat flow. Since pavements testing involves large areas, sun is the ultimate source (heat), which does not incur any costs and gives an even distribution of heat, if the surface is fully exposed. Both times (day and night) can be utilized for infrared thermography, although, the process would be reversed in the night time with the warm regions acting as heat source. This approach of testing is known as **'Passive Thermography'**. In lab testing, artificial heating may be used too, in order to examine the specimen under heating. This is called **'Active thermography'**, but is only suitable for lab work or on small full-scale tests depending upon the cost and time feasibility.

Surface condition is another important factor that has a profound effect on the accuracy of the thermal images. The material's ability to radiate infrared is measured by its emissivity. The emissivity is high for rough surfaces and low for smooth surfaces, and is also affected by the geometry, shape, impurities on the surface, etc. Two surfaces with same temperature but different emissivity values will give different temperature distribution profiles in the thermal images. Surfaces with low emissivity will give more uncertainty in the results, therefore infrared thermography is suitable for highly emissive surfaces (Gaussorgues 1994).

The final main factor affecting the temperature distribution of the surface in the thermogram is the environmental conditions surrounding the surface (IAEA 2002). The latter is however a very broad term, and it should be looked at some more detail, as follows (IAEA 2002):

- **Ambient Temperature:** The effect of ambient temperature on the testing is negligible when heating or cooling process is taking place by some external source. However, it can have an effect on the time span during which high temperature contrast is achieved. It is important to avoid testing if ice or water is present on the surface and also if the temperature is below 0°C, since water freezes filling the sub-surface voids.

- **Solar Radiation:** It is preferable to do testing 3hrs after sunrise or after sunset, as this is the time of rapid heating or cooling, or, late night, when temperature is low and heat transfer takes place from warmer regions to cooler regions. It is also important to note that shades and shadows can affect the results, so it is better to do 3hrs after sunsets in such cases.

- **Cloud Cover:** Cloudless weather is more suitable for testing. Clouds reflect the infrared radiation, and thereby, slow down the process of infrared radiation detection by the IR camera. In such situations night or little cloud is recommended for testing.

- **Wind Speed:** Measurements should be taken if the wind speed is less than 15mph (25km/hr). High gusts of wind cool the surface rapidly, and do not allow the heat to transfer deep into the concrete, therefore, sub-surface anomalies may not be highlighted in the thermal images.

- **Surface Moisture:** Moisture has a negative impact on the test results, since, it disperses the surface heat, masks the temperature gradient and finally the sub-surface anomalies. Therefore, it is not recommended to do testing in the presence of the standing water or snow on the surface.

Once appropriate conditions are established, IRT can be performed on the relatively large area. The thermograms taken, and their interpretation can be carried out by using IRT or other relevant software, and sub-surface anomalies can be detected.

4.2.3 Basics of Numerical Thermal Analysis

The basics of thermal analysis are based on the three modes of heat transfer: 'Conduction', 'Convection' and 'Radiation'. The first two modes are going to be discussed in this section, since, both modes will be employed in the numerical modelling for IRT, whereas, the third mode is more relevant to the experimental IRT, and therefore, has been discussed in the previous section.

4.2.3.1 Heat transfer-Conduction

When a temperature gradient exists in a body, energy transfer takes place, the flow of energy in the body is from high temperature zone to lower temperature zone. This mode of heat transfer is called conduction, and this heat transfer rate per unit area is directly proportional to the normal temperature gradient, given by (Holman 2010):

$$\frac{q_x}{A} \sim \frac{\partial T}{\partial x}$$

With the inclusion of proportionality constant,

$$q_x = -kA \frac{\partial T}{\partial x} \tag{4.4}$$

Where q_x (W) is the heat transfer rate and $\frac{\partial T}{\partial x}$ is the temperature gradient in the direction of heat flow. k (Wm^{-1}C^{-1}) is the positive thermal conductivity constant of the material, A (m^2) is the area normal to the heat flow, and the negative sign is used in order to satisfy the second law of thermodynamics, which states that heat must flow from high temperature region to low temperature region i.e. downhill on the temperature scale, as indicated in Figure 4-5.
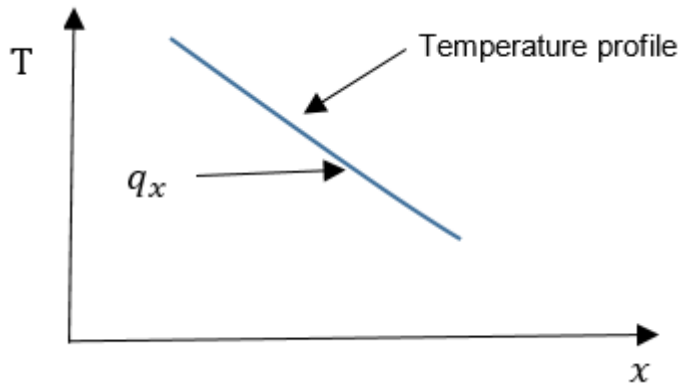
Figure 4-5: Direction of heat flow (Holman 2010).

Equation (4.4) is known as Fourier's law of heat conduction, named after the French mathematical physicist Joseph Fourier, who had a substantial contribution in the analytical treatment of the heat transfer in solids. This equation (4.4) also sets the bases of the governing equation in heat transfer in solids.

A system in heat transfer can be in steady state i.e. the temperature doesn't vary with time, this makes the problem simple and just by the integration of the equation (4.4), and substituting the right values, the problem can be solved for the desired quantity. In contrary to the steady state, a system can go through transient state, in which the temperature is time dependent, and there could also be heat sources or sinks in the solids. The solution for this type of system is complex, and the governing equations for complex situations are modified accordingly.

For a general case, where the temperature in the body is changing with time and the heat sources may also be present in the body, the governing equation for a unit volume with heat conducting in all the three coordinates' directions can be derived based on the following energy balance (Figure 4-6):
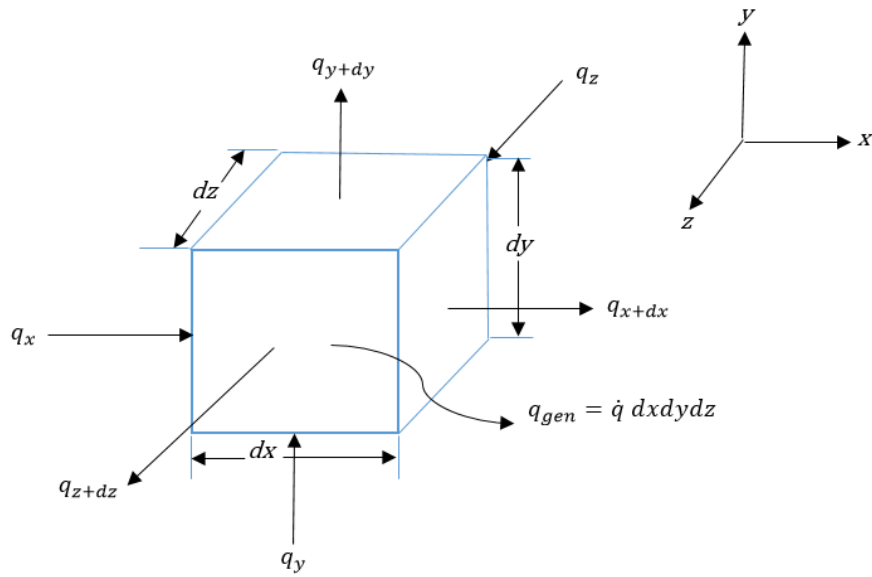
Figure 4-6: Elemental volume for 3-D heat flow by conduction (Holman 2010).

Energy conducted in the left face + heat generated within the element = change in the internal energy + energy conducted out through right face

$$q_x + q_y + q_z + q_{gen} = q_{x+dx} + q_{y+dy} + q_{z+dz} + \frac{dE}{d\tau} \qquad (4.5)$$

Where the energy quantities are represented by

$$q_x = -k\,dydz\,\frac{\partial T}{\partial x} \qquad (4.6)$$

$$q_{x+dx} = -\left[k\frac{\partial T}{\partial x} + \frac{\partial}{\partial x}\left(k\frac{\partial T}{\partial x}\right)dx\right]dydz \qquad (4.7)$$

$$q_y = -k\,dxdz\frac{\partial T}{\partial y} \qquad (4.8)$$

$$q_{y+dy} = -\left[k\frac{\partial T}{\partial y} + \frac{\partial}{\partial y}\left(k\frac{\partial T}{\partial y}\right)dy\right]dxdz \qquad (4.9)$$

$$q_z = -k \, dxdy \, \frac{\partial T}{\partial z} \tag{4.10}$$

$$q_{z+dz} = -\left[k\frac{\partial T}{\partial z} + \frac{\partial}{\partial z}\left(k\frac{\partial T}{\partial z}\right) dz \right] dxdy \tag{4.11}$$

Energy generated within the element $q_{gen} = \dot{q} \, dxdydz$ (4.12)

Change in internal energy per unit time $\frac{dE}{d\tau} = \rho c \, dxdydz \, \frac{\partial T}{\partial \tau}$ (4.13)

Combining the above relations gives the general three dimensional conduction equation:

$$\frac{\partial}{\partial x}\left(k\frac{\partial T}{\partial x}\right) + \frac{\partial}{\partial y}\left(k\frac{\partial T}{\partial y}\right) + \frac{\partial}{\partial z}\left(k\frac{\partial T}{\partial z}\right) + \dot{q} = \rho c \frac{\partial T}{\partial \tau} \tag{4.14}$$

If thermal conductivity is constant, the equation (4.14) can be written

$$\frac{d^2 T}{dx} + \frac{d^2 T}{dy} + \frac{d^2 T}{dz} + \frac{\dot{q}}{k} = \frac{1}{\alpha}\frac{\partial T}{\partial \tau} \tag{4.14a}$$

Equation (4.14a) is called the three dimensional heat flow equation. Where, $\dot{q}$ is heat generated per unit volume (Wm^{-3}), $\alpha = \frac{k}{\rho c}$ is an important term known as thermal diffusivity of the material. The greater the value of α (m^{2}s^{-1}), the faster the heat will diffuse through the material. The high value of thermal diffusivity, α, could either be due to high value of thermal conductivity, k, which will cause the rapid energy transfer rate or from a low value of volumetric heat capacity, ρc. Which means less energy would be absorbed and required to raise the temperature of the body while passing through it, and therefore, more energy would be available for further transfer.

4.2.3.2 Heat Transfer-Convection

Convection is the mode of heat transfer, which involves the motion of fluid particles to carry the energy from one place to another by the movement of fluids. It is the dominant form of heat transfer mode in liquids and gases (Holman 2010). However, in many conduction heat transfer problems, convection is related to the boundary conditions imposed on the conduction problem.

A heated wall with temperature ,T_w, when come in contact with the fluid with temperature, $T\infty$, the velocity of the fluid at the boundary of the wall will appear as shown in Figure 4-7. The velocity at the boundary would be reduced to zero as a result of viscous effect. Since, due to zero velocity of the fluid layer at the boundary, the heat must travel via conduction mode of heat transfer at the interface. Therefore, the heat transfer must be computed by using equation (4.4) by incorporating fluid thermal conductivity property and the fluid temperature gradient at the wall. However, the temperature gradient is dependent on the velocity at which the fluid carries away the heat i.e. a high velocity fluid will create a high temperature gradient and so on. Therefore, the temperature gradient created at the wall is determined by the flow field. Nevertheless, it is understood that the physical mechanism of heat transfer at the wall is a conduction process (Holman 2010).
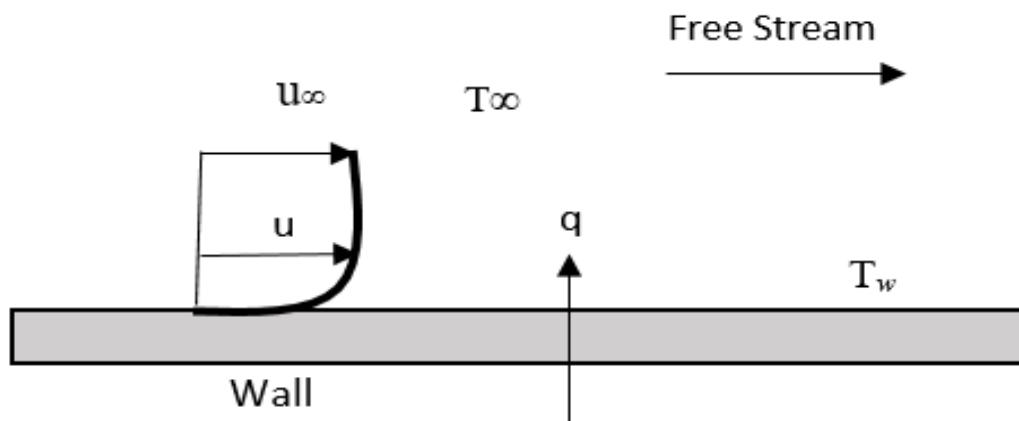
Figure 4-7: Heat transfer of a plate by convection (Holman 2010).

This overall effect of convection can be expressed by using Newton's law of cooling:

$$q = hA(T_w - T_\infty) \qquad (4.15)$$

Equation (4.15) is the defining equation of heat transfer convection, and it shows the relationship between the heat transfer rate to the overall temperature difference between the wall and the fluid and the surface area A. The quantity h, is called the *convection heat-transfer coefficient*. An analytical calculation could be done for determining h-value, however, in complex systems it is recommended to determine the h-value experimentally. The convection heat-transfer coefficient is sometimes cited as *film conductance* because of the conduction mechanism being involved in the thin stationary fluid layer at the wall surface. The heat transfer coefficient has the units of watts per square meter per Celsius degree, when the heat flow is in watts.

In addition to the thermal properties (thermal conductivity, specific heat) of the fluid, the convection heat transfer also depends on the viscosity of the fluid. This is expected, since, the viscosity influences the velocity profile, and ultimately the heat transfer rate at the interface between the wall and fluid.

A convection can be classified as free or forced. If a heated wall is exposed to the ambient air, the motion of the air particles would be due to the density gradients formed near the wall. This is called free or natural convection. However, if the wall is exposed to the fan blowing air, this is called forced convection.

4.3   Selection of Passive Infrared Thermography (IRT)

Passive infrared thermography is a term that is used when an object is subjected to thermography tests under ambient conditions (as discussed earlier). Solar energy is generally the main source of heating to produce the temperature gradient in the body under test. In this chapter, a designed concrete slab with six purposely made voids and Two-slabs stacked system with three delaminations at their interface, is subjected to passive thermography test. Active thermography was the other possible approach, proposed initially to be adopted for this test due to its evaluating nature and feasibility to operate under laboratory conditions. However, the idea was abandoned based on trial tests of the specimen-slab under halogen heat lamps and by using heating chamber in the laboratory conditions, it was decided to adopt passive thermography for these particular testing (Please see APPENDIX C, trial test setup). Some of the issues faced during the trial tests under heating lamps or the heating chamber were as follows:

1. Non-uniform heating of the specimen-slab's surface, caused by the heat-lamps resulted in higher temperature of the regions and edges (closer to the lamps) than the defected regions.
2. Heating the whole-slab by setting a fixed temperature in the heating chamber, resulted in no temperature gradient between the top and bottom surface. Therefore, first not all the defects were detected in the thermal images recorded and second, the detected ones (shallow voids) didn't show clear boundaries definition in the thermograms, when recorded during the cooling phase.

Moreover, the inability of producing the real ambient conditions (like convection due to the wind etc.) in the laboratory was one extra reason to adopt a more practical way of testing that of 'Passive IRT'.

The aim of this 'Passive IRT-test' was to detect the sub-surface defects efficiently by utilising the solar energy (passive approach). Furthermore, to evaluate these detected defects (voids/delaminations) based on their thicknesses and depths from the surface.

4.4 Test 01 (Experimental). Single slab with 6 flaws (Voids)

In order to replicate a real life scenario in the laboratory that is, simulate delaminations, a rectangular shaped concrete specimen, slab, with six predefined voids was constructed by inserting corrugated cardboard cuts just before casting (Figure 4-8). Corrugated cardboards are light in weight and have good insulation properties (thermal conductivity is close to the value of air), hence, suitable to simulate voids. To avoid soaking problems they were wrapped with cling film. All voids were taken to be of the same square dimensions (Figure 4-9), whereas, their thicknesses and positions from the surface (depth) were varied to simulate void sizes at various depths (Table 4-1).

The aim of this preliminary investigation was to examine if these voids could be detected and evaluated, and then predicted via reverse engineering approach by using passive infrared thermography. This should test the limitations of the method, paving the way for the next stage, where the delamination (initial, intermediate and severe) at a known depth of 40mm, could be detected via infrared thermography.
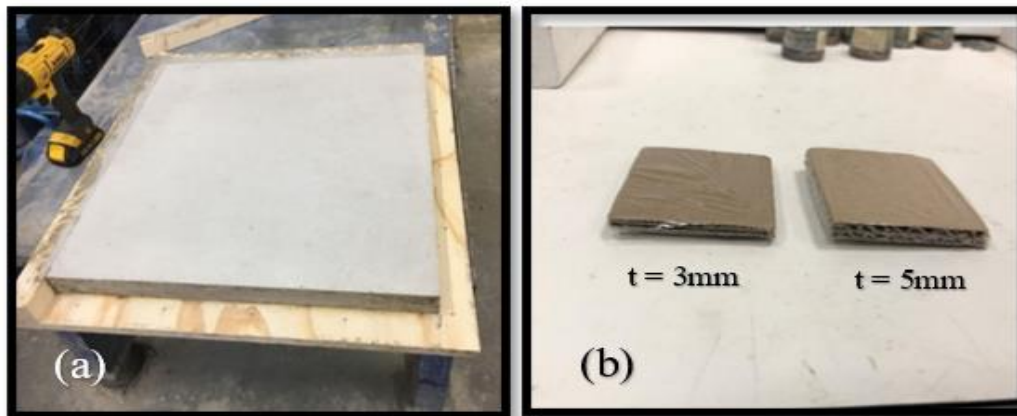

Figure 4-8: (a) Concrete slab (specimen) containing 6-pre-cast voids, (b) Corrugated-cardboards with thickness 3mm and 5mm.
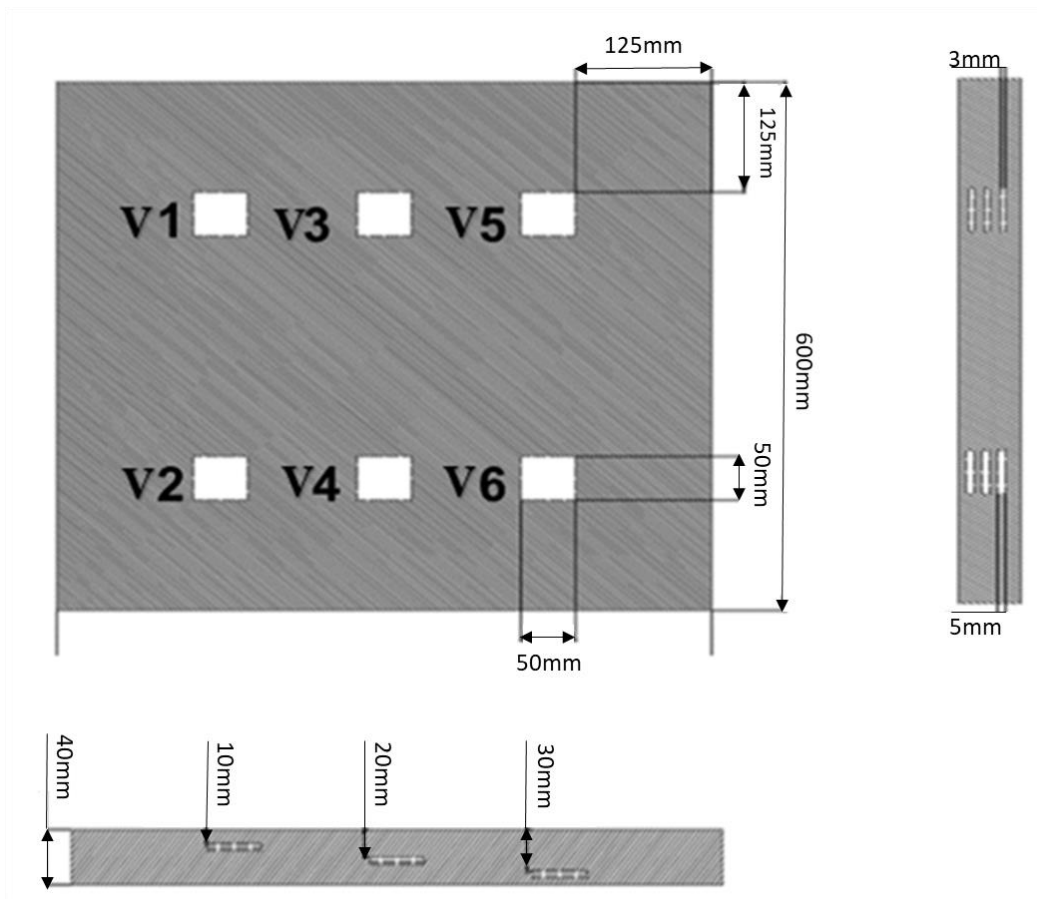
Figure 4-9: Details of concrete slab (specimen) and all six-voids.

Table 4-1: Essentials of the concrete slab with six-precast voids.

Essential Descriptions:	Dimensions (mm)	Voids Depths from top (mm)
Concrete Slab	600x600x40	
Void-V1 (Shallow-Thick)	50x50x5	10
Void-V2 (Shallow-Thin)	50x50x3	
Void-V3 (Mid-depth-Thick)	50x50x5	20
Void-V4 (Mid-depth-Thin)	50x50x3	

114

Void-V5 (Deep-Thick)	50x50x5	
		30
Void-V6 (Deep-Thin)	50x50x3	

4.4.1 Test Setup and Procedure

The experimental setup (Figure 4-10) for the recording of thermograms comprised a commercial IR camera (FLIR T620), controlled by '*Research Max IR'*, a specialist thermal imaging software developed by the FLIR Systems Inc. 2016, kindly provided by our industrial collaborators, Thermal Vision Research Ltd. A laptop was used to operate the camera via the *Research Max IR* software (FLIR Systems Inc. 2016), a tripod stand to hold the camera, and two thermocouples were utilized to measure the initial and final temperature readings of the designed concrete slab specimen. Details are available in Table 4-2.

Table 4-2: Specifications of specimen, thermocouple and IR-camera.

Essentials	Specifications
Concrete slab	600x600x40mm
FLIR T620bx IR camera	680x480 pixels; temp range: -40°C to 650°C; FOV: 25° x 19° / 0.25m; spectral range: 7.5 to 14μm; frame rate: 30Hz
Thermocouple	K series (-270-1260°C)

The test setup was arranged outside the Civ Eng labs of the University in a sunny day with a surrounding ambient temperature of 29°C and maximum wind speed of 9.7kph (6mph). Solar radiations were the main source of heating the slab with the maximum *irradiance* of 280Wm^{-2} (NASA LaRC 2018). Solar irradiance is defined as the power

received from the sun per unit area (watt per square metre, Wm^{-2}). It can be measured in the space or at surface of the earth, after atmospheric absorption and scattering. The slab was placed outside the lab and exposed fully to the solar radiations. The IR camera was held by the tripod stand (vertically), 2m away from the slab, focussing at 90° (Figure 4-10).

The initial settings of the camera were adjusted by setting the emissivity to 0.95 (the default value for concrete), measured reflected temperature of 26°C, object distance of 2m, and atmospheric temperature of 29°C with a relative humidity to be 54%.
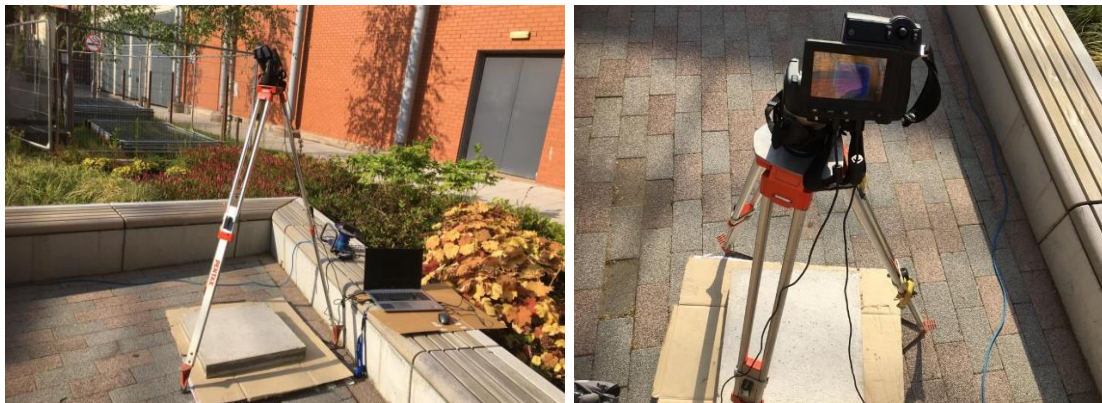
Figure 4-10: Setup of Test 01-IRT. Thermograms recording during the heating phase.

The initial temperature of the slab measured just before the test starts was 28°C ±1 and the time at the start of the test was 13:20 BST. The test lasted 1200s (20 min), until there was no significant change in thermal contrast of the thermograms. The recorded frames were then imported for thermal image tuning, using the *Research Max IR* software (FLIR Systems Inc. 2016).

4.4.2 Results and Discussion

4.4.2.1 Analysis of Thermograms and Temperature distribution profile

It was noticed with satisfaction that all six voids despite of their different depths and thicknesses were detected in the thermograms. The first indication of the voids were observed (in the thermograms) just after 300s (5mins) of exposure to the sun. By adjusting the temperature ''span'', the boundaries of the voids were *sharpened* and the *thermal colours* were exaggerated. Shallow voids showed higher thermal contrast compared to mid-depth and deep voids (Figure 4-11).
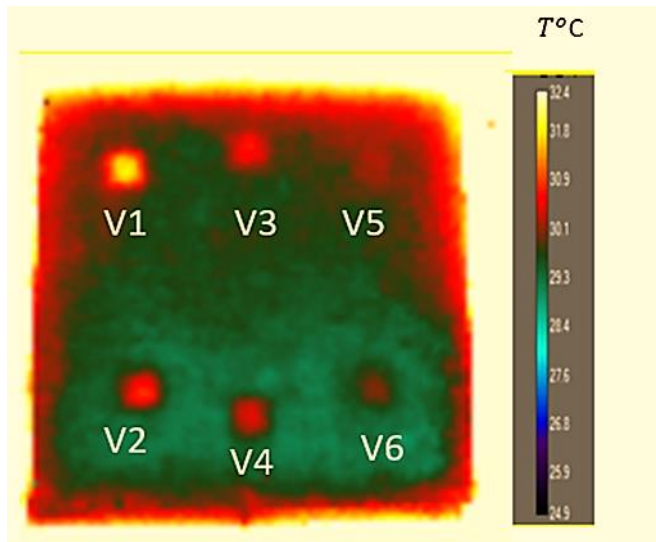
Figure 4-11: Tuned thermogram, frame recorded at 1200s.

The recorded frames were then analysed by creating regions of interest (RoIs) over all voids and sound regions (where no voids existed) on the surface. The average temperature of the number of pixels forming RoIs was taken for each void region as well as the sound region. The temperature profile for each void and sound region against time is plotted in Figure 4-12, where key for Figure is tabulated below (Table 4-3).
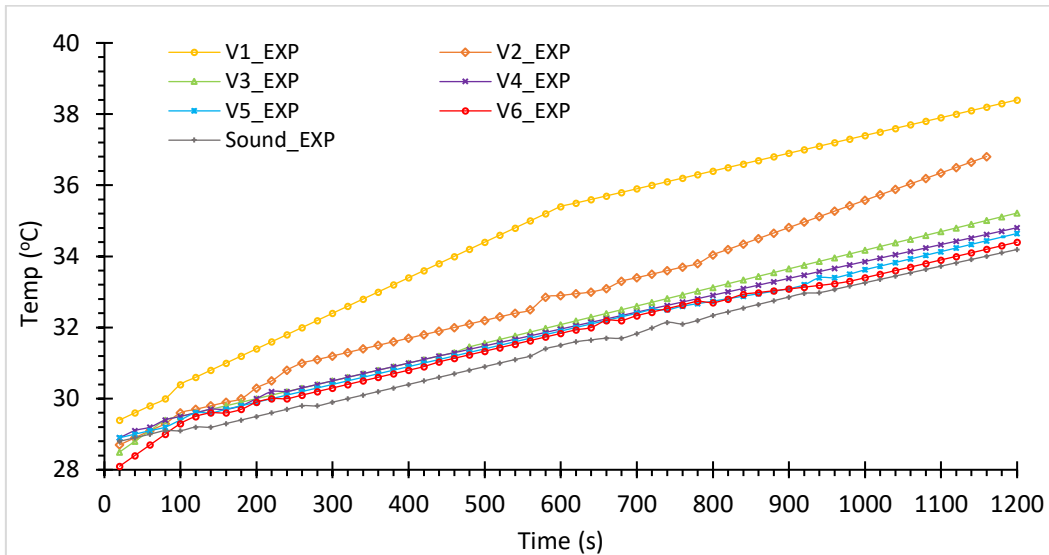
Figure 4-12: Temperature profile for all voids (V1-V6) and sound region-Experimental IRT-Test 01.

Table 4-3: Key for Figure 4-12. A display of Void Depths, Void Types and Temperature at 1200s.

V (voids)	VOID Depth (mm)	VOID Type (mm)	Temp (ºC) @ 1200s	Comments
V1		Thick (5)	39	Shallow-thick
	Shallow (10)			
V2		Thin (3)	37	Shallow-thin
V3		Thick (5)	35.2	Mid-depth-thick
	Mid.D (20)			
V4		Thin (3)	34.8	Mid-depth-thin
V5		Thick (5)	34.6	Deep-thick
	Deep (30)			
V6		Thin (3)	34.4	Deep-thin
Reference	NA	NA	34.2	Reference area (no-defects)

From Figure 4-12, it was observed that the shallow thick void (V1) showed the highest rise in temperature compared to its corresponding shallow thin (V2), mid-depth voids (V3, V4) and the deep voids (V5, V6). Whereas, mid-depth voids (V3, V4) showed slightly higher temperatures compared to the deep voids (V5, V6). The sound region temperature showed the least rise in temperature compared to the voids. Initially, both the voids and the sound region had similar temperatures, one overlapping the other and hard to distinguish. However, after 80s, a clear distinction between the voids and the sound region temperatures was spotted, which remained there until stead-state conditions were reached. The rise in temperature is approximately linear, hence, easy to predict against time for all voids and sound region.

4.4.2.2 Thermal Contrast Estimation

In order to evaluate defect visibility, enhance image quality, and ultimately quantify the condition of these voids, a common practise in NDT, to estimate/scrutinize the optimal time for observation is recommended. In that regard, a thermal contrast is defined in infrared thermography (NDT). Thermal contrast requires the use of temperature in both, sound and flaw areas, however, its definition is a critical issue. Thermal contrast is generally categorized into four main types: Absolute, Standard, Normalized and Running (Venter 2016). Standard contrast is adopted for this analysis. It is by far the most advantageous, since, it supresses the impact of infrared reflections Venter (2016). Standard thermal contrast is defined as follows:

$$\Delta T_{(t)} = \frac{T_d(t) - T_d(t_0)}{T_s(t) - T_s(t_0)} \qquad (4.16)$$

where,

$T_d(t)$ = Surface temperature of the defected area at any measured time, t.

$T_d(t_0)$ = Initial Surface temperature of the defected area.

$T_s(t)$ = Surface temperature of sound or reference area at time t.

$T_s(t_0)$ = Initial surface temperature of the sound or reference area.

To use equation 4.16, the following cases should be considered:

$$\text{When } t \geq t_o \quad \begin{cases} T_s(t) - T_s(t_0) > 0 \\ \\ \Delta T_{(t)} \neq 0 \end{cases}$$

It is apparent that equation 4.16 is not valid at time, t = 0. Similarly, if $\Delta T_{(t)} = 0$, the body is, or has reached, its thermal equilibrium. $\Delta T_{(t)}$ has no unit as it is a ratio of temperatures.

4.4.2.3 Experimental Thermal Contrast (ΔT). An initial comparison of all Voids (V1-V6)

Thermal contrasts (ΔT) were calculated for all voids (V1-V6) and plotted against time as shown in Figure 4-13, aided by its key in Table 4-4.
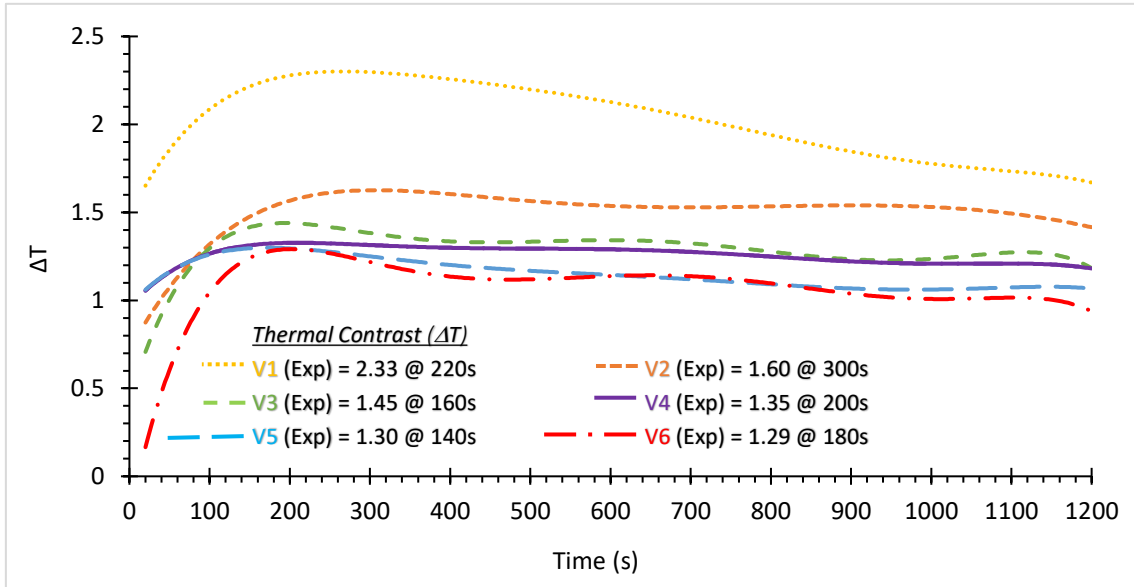

Figure 4-13: Experimental thermal contrast (ΔT). Preliminary comparison between all voids (V1-V6).

Table 4-4: Key for Figure 4-13. A display of Void Depths, Void Types and Thermal Contrasts ΔT, together with their time taken to reach peak ΔT.

V (voids)	VOID Depth (mm)	VOID Type (mm)	ΔT	T@ Peak (s)	Comments
V1		Thick (5)	2.33	220	Shallow-thick
	Shallow (10)				
V2		Thin (3)	1.60	300	Shallow-thin
V3	Mid.D (20)	Thick (5)	1.45	160	Mid-depth-thick

V4	Thin (3)	1.35	200	Mid-depth-thin
V5	Thick (5)	1.30	140	Deep-thick
Deep (30)				
V6	Thin (3)	1.29	180	Deep-thin

By comparing the thermal contrasts (ΔT) calculated for all voids (V1-V6), it can be seen that shallow voids (V1, V2), showed high thermal contrast (ΔT) values compared to mid-depth voids (V3, V4) and deep voids (V5, V6) showed the lowest ΔT values.

It was observed that initially the thermal contrast (ΔT) values were overlapping, and a distinction between the shallow thin (V2), mid-depth (V3, V4) and deep thick (V5) voids was not possible. However, after reaching a certain time, 80s in this case, the required temperature gradient and a pattern started developing, providing more certainty/confidence in results. Voids were now distinguishable based on their thermal contrast (ΔT) values, and a preliminary assessment could be made based on their peak values and the time taken to reach them.

By looking at the patterns developed (thermal contrasts) for all voids (V1-V6), a similar trend could be observed among them, irrespective of their depths and thicknesses. All thermal contrast histories show a sudden rise, reaching a peak value and then dropping gradually, becoming steady floating around time. It is noted that the values of these peaks and the timings reaching peaks are not the same. This could be sufficient to make preliminary assessments on the void's location or condition.

Each void group is discussed separately, in more detail, below:

4.4.2.4 Experimental Thermal Contrast (ΔT). Comparison between Thick and Thin Voids at same Depths

An experimental thermal contrast (ΔT) comparison was made (Figure 4-14) between shallow-thick void (V1) and shallow-thin void (V2), in order to study the effect of thicknesses of voids on their thermal contrast values, when compared at the similar shallow depths (10mm).
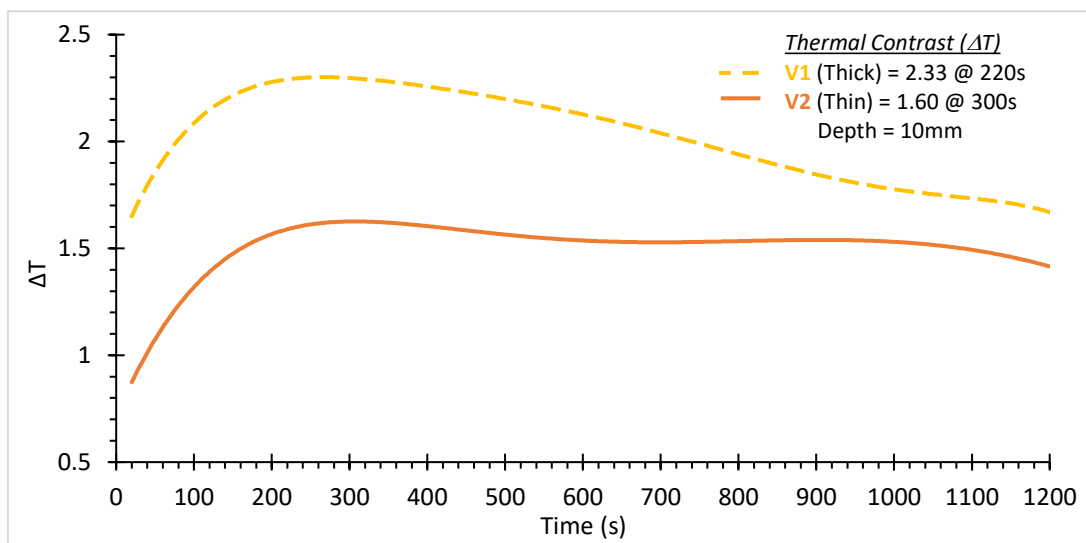

Figure 4-14: Experimental thermal contrast (ΔT) comparison between shallow thick (V1) and shallow thin (V2) voids.

Shallow-thick void (V1) showed the highest thermal contrast (ΔT: 2.33 @ 220s) compared to shallow-thin void ,V2 (ΔT: 1.60 @ 300s). This was due to the effect of thickness of the void, since the heat flow according to Fourier's law of heat-transfer in conduction, is inversely proportional to the thickness of the medium (Equation 4.4).

Hence, the heat transfer rate of the thick void V1 was reduced compared to the thin void (V2), causing a rise in temperature at a higher rate, at a similar shallow depth (10mm).

It was observed for both voids that after reaching their respective peak values (ΔT), there was a gradual drop in their thermal contrasts (ΔT), and were further reduced until they began to approach steady-state. This indicates that the starting time period, i.e. from the development of the trend until it reaches its peak value, can be crucial while evaluating the void, compared to later time periods.

One observation showed that thick void, V1 took less time (220s) to reach its peak value (ΔT), compared to its corresponding thin void (V2), that took more time (300s) to reach its peak value (ΔT). This was also due to the higher heat accumulation rate above the thick void compared to the thin.

A comparison was made between the experimentally obtained thermal contrasts (ΔT) of mid-depth thick (V3) and mid-depth thin (V4) voids, in order to distinguish their differences at the similar mid-depths i.e. 20mm (Figure 4-15).
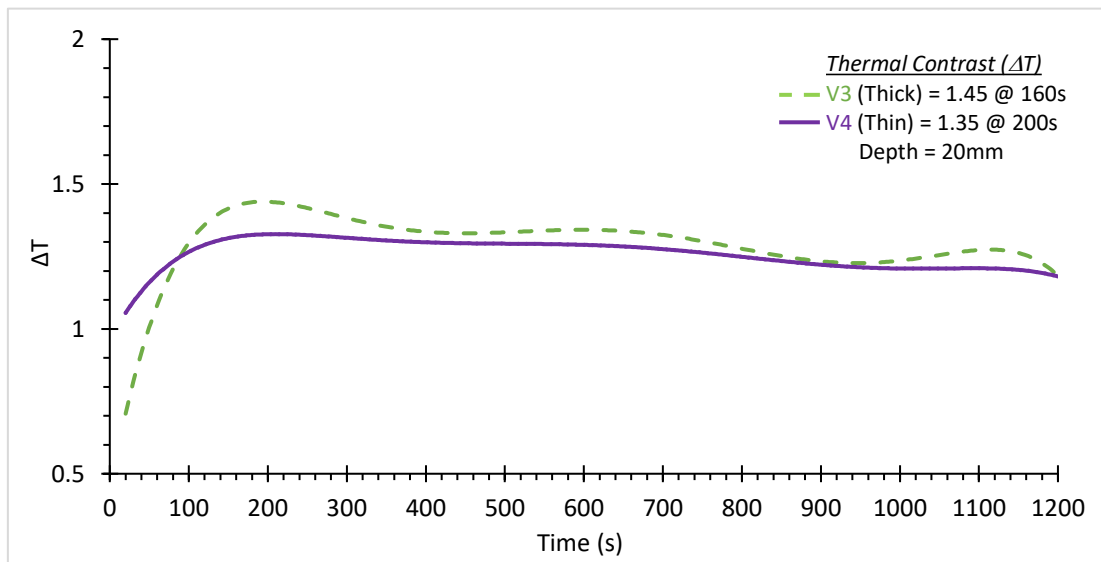
Figure 4-15: Experimental thermal contrast (ΔT) comparison between mid-depth thick (V3) and mid-depth thin (V4) voids.

Mid-depth thick void (V3) showed higher thermal contrast (ΔT: 1.45 @ 160s) compared to mid-depth thin void, V4 (ΔT: 1.35 @ 200s). The difference between their peak values was not significant. It was observed that the deeper the voids, the lesser the difference between their thermal contrasts (ΔT) and the more difficult to detect.

However, noticing their thermal contrast (ΔT) profile, the thick void (V3) was showing slightly higher values compared to the corresponding thin void (V4). This is promising because it can become the platform to support a void (flaw-bond) recognition and evaluation method (procedure) later on.

Similar to shallow voids, the mid-depth thick void (V3) also took less time (160s) to reach its peak value (ΔT), compared to its corresponding thin void (V4) that took more time (200s) to reach its peak value (ΔT). This was again due to similar reasons as discussed above.
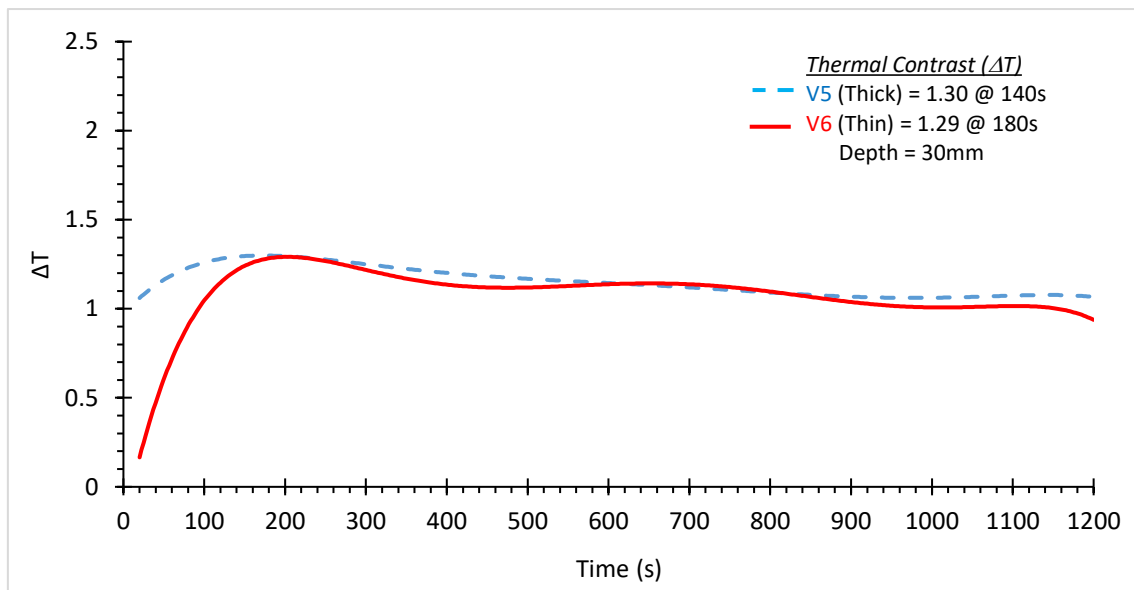
Figure 4-16: Experimental thermal contrast (ΔT) comparison between deep thick (V5) and deep thin (V6) voids.

By comparing the thermal contrast (ΔT) of deep thick (V5) and deep thin (V6) voids, it was observed that the difference between their values was very small and hard to distinguish, and at some regions, there was also some overlapping involved (Figure 4-16). However, by looking at their thermal contrast (ΔT) values, deep thick void (V5) showed its peak value of 1.30 at 140s, where deep thin void (V6) showed its peak value of 1.29 at 180s.

By scrutinizing the timings of each void reaching their peak values and the overall trend, it was observed that the deep thick void (V5) on an average showed higher values of thermal contrasts (ΔT) compared to deep thin void (V6).

Secondly, the time taken by deep thick void (V5) to reach its peak value was 140s, considerably less compared to deep thin void (V6) that showed its peak value at 180s. This again endorsed the phenomenon observed in the previous two-cases.

A summary of the above comparisons is tabulated below (Table 4-5).

Table 4-5: Summary of ΔT Comparison between 'Thick and Thin' Voids at similar Depths.
Note: (ΔT) = Thermal Contrast

V (voids)	ΔT	T@ Peak (s)	ΔT Comparisons
V1 (Shallow-thick)	2.33	220	Shallow-Thick void (V1) showed higher peak value (ΔT), compared to its corresponding Shallow-Thin void (V2).
V2 (Shallow-thin)	1.60	300	Time taken by Shallow-Thick void (V1) to reach its peak value (ΔT) was less compared to the time taken by Shallow-Thin void (V2).
V3 (Mid.D-thick)	1.45	160	Similar to Shallow-Thick void, Mid-depth thick void (V3) also showed higher peak value (ΔT), compared to its corresponding Mid.Depth-Thin void (V4).
V4 (Mid.D-thin)	1.35	200	Similarly, the time taken by Mid.Depth-Thick void (V3) to reach its peak value (ΔT) was less compared to the time taken by Mid.Depth-Thin void (V4).
V5 (Deep-thick)	1.30	140	Despite of the small differences between their peak values (ΔT), Deep-Thick void (V5) still showed high value (ΔT) compared to its corresponding Deep-Thin void (V6).
V6 (Deep-thin)	1.29	180	Similar to the above (ΔT) trends, the time taken by Deep-Thick void (V5) to reach its peak value (ΔT) was less compared to the time taken by Deep-Thin void (V6).

4.4.2.5 Experimental Thermal Contrast (ΔT). Comparison between Thick Shallow (V1), Mid-depth (V3) and Deep (V5) Voids

The plots discussed before, were the comparison of thermal contrasts (ΔT) between thick and thin voids at similar depths. Now, a comparison is made between thick voids (V1, V3, V5) only at various depths (Shallow, Mid-depth, and Deep), in order to study the effect of depths on thick voids (Figure 4-17).
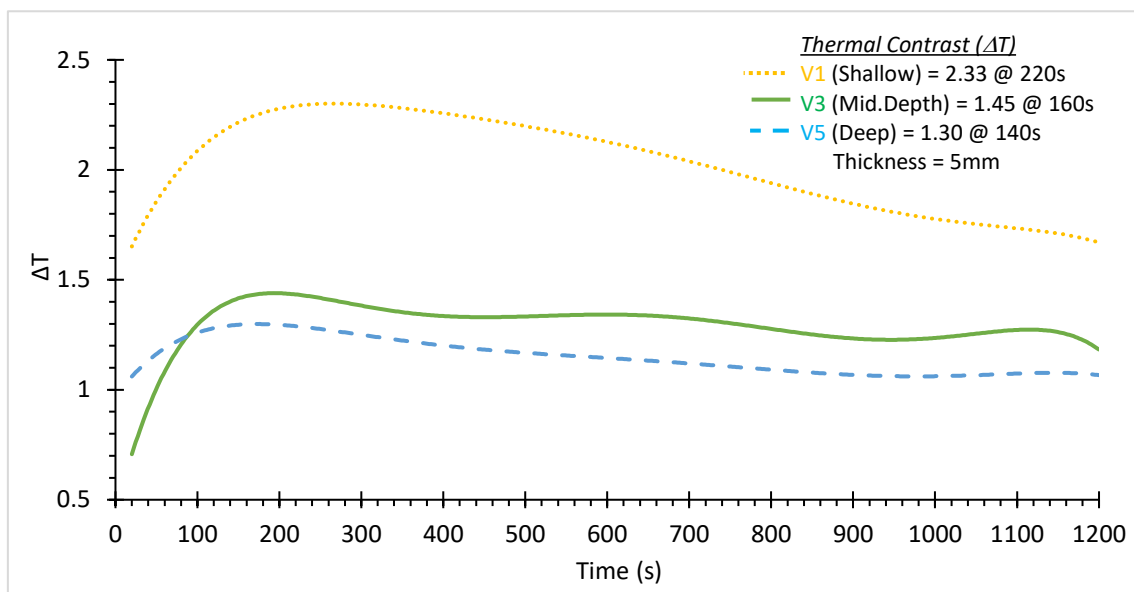
Figure 4-17: Experimental thermal contrast (ΔT) between shallow (V1), mid-depth (V3) and deep (V5) thick voids.

From Figure 4-17, it was observed that shallow-thick void (V1) showed the highest value of thermal contrast (ΔT), 2.33 taking place at 220s, followed by mid-depth thick void (V3) with peak value (ΔT) of 1.45 at 160s, and deep-thick void (V5), with peak value (ΔT) of 1.30 at 140s.

The shallow thick void (V1) showed significant difference in its thermal contrast (ΔT) values compared to the mid-depth (V3) and deep-thick (V5) voids. Although, mid-depth

(V3) and deep (V5) voids showed close values of ΔT, however, they were distinguishable indicating that they can be used to predict the void's type.

By looking at the peak values of ΔT for each thick void (V1, V3, V5), it can be seen that the closer to the surface the void exists, the higher the peak value of a thermal contrast (ΔT), and the longest the time taken to reach that peak value (Figure 4-17).

In contrast, the deeper the void is, the lower would be the peak value, and the shorter would be the time taken to reach that peak value.

4.4.2.6 Experimental Thermal Contrast (ΔT). Comparison between Thin Shallow (V2), Mid-depth (V4) and Deep (V6) Voids

This was aiming to look at the effect of depth only for similar, thin voids (Figure 4-18).
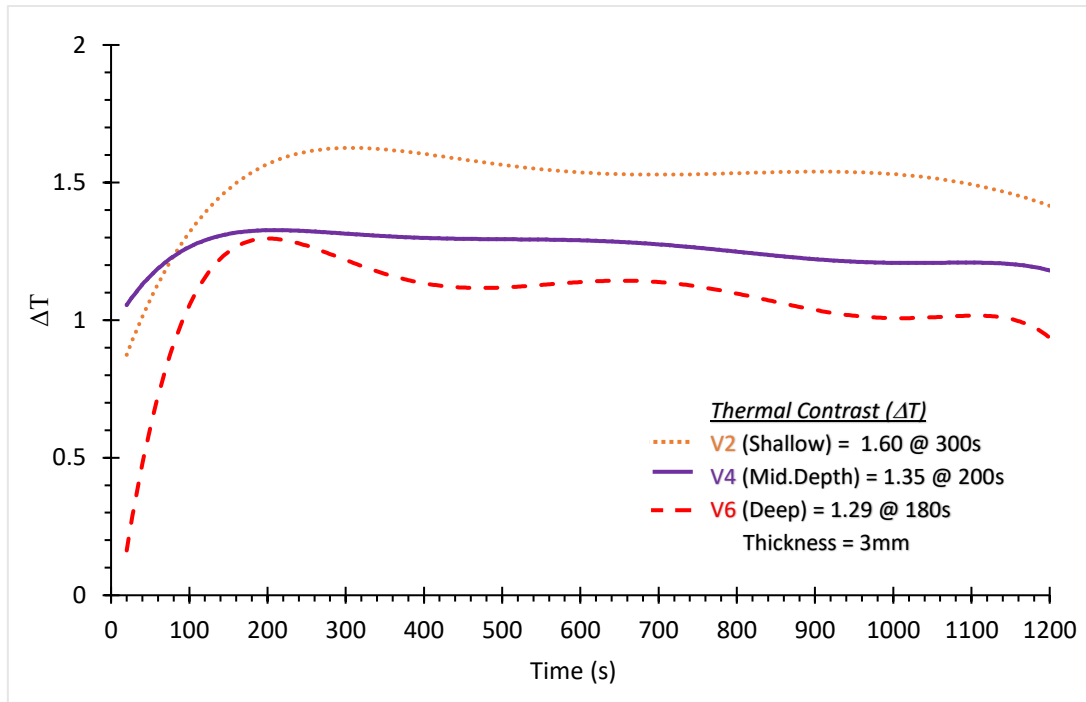
Figure 4-18: Experimental thermal contrast (ΔT) between shallow (V2), mid-depth (V4) and deep (V6) thin voids.

A comparison of thermal contrasts (ΔT) between thin voids (V2, V4, V6), revealed a similar pattern shown by thick voids (V1, V3, V5). Shallow thin void (V2) showed the highest thermal contrast (ΔT) value of 1.60 observed at 300s, followed by mid-depth thin void (V4) with a peak value (ΔT) of 1.35 at 200s and deep thin void (V6) with peak value (ΔT) of 1.29 at 180s.

Again, the shallow void (V2) took longer time, to reach its peak value (ΔT), followed by the mid-depth (V4) and the deep thin (V6) voids respectively (Figure 4-18).

130

The repeated pattern of thermal contrasts (ΔT) in thin voids as observed earlier in thick voids, endorses the phenomenon that as the depth of the voids from the surface is increased, the peak value (ΔT) decreases and becomes significantly low, when it is in the mid-depth region (20mm), and even lower with deep region (30mm).

A summary of the comparison of all thick and thin voids is shown below (Table 4-6).

Table 4-6: Summary of ΔT Comparison between Shallow, Mid.Depth and Deep voids (Thick and Thin). Note: (ΔT) = Thermal Contrast

V (voids)	ΔT	T@ Peak (s)	ΔT Comparisons
V1 (Shallow -Thick)	2.33	220	Shallow-Thick void (V1) showed the highest peak value (ΔT), compared to Mid.Depth-Thick (V3) and Deep-Thick (V5) voids respectively .
V3 (Mid.D-Thick)	1.45	160	Time taken by Shallow-Thick void (V1) to reach its peak value (ΔT) was more compared to the time taken by Mid.Depth-Thick (V3) and Deep-Thick (V5) voids respectively.
V5 (Deep-Thick)	1.30	140	
V2 (Shallow-Thin)	1.60	300	Similarly, Shallow-Thin void (V2) showed high peak value (ΔT), compared to Mid.Depth-Thin (V4) and Deep-thin (V6) voids respectively.
V4 (Mid.D-Thin)	1.35	200	Alike thick-void's (ΔT) trend, the time taken by Shallow-Thin void (V2) to reach its peak value (ΔT) was more compared to the time taken by Mid.Depth-Thin void (V4) and Deep-Thin (V6) voids respectively.
V6 (Deep-Thin)	1.29	180	

4.4.3 Inferences from the Experimental IRT-Test 01

1. All the six voids were first detected in about 300s (5mins) in the recorded thermograms, however, with time, the visual appearance of deeper voids got much sharper. Also, it was noticed that shallow voids (V1, V2) were sharp and clear, compared to mid-depth voids (V3, V4), where deep voids (V5, V6) showed the least contrast, and were blurrier compared to the shallower voids.

2. In general, thick voids (V1$_{(\Delta T)}$: 2.33, V3$_{(\Delta T)}$: 1.45 and V5$_{(\Delta T)}$: 1.30) showed higher thermal contrasts (ΔT) compared to their corresponding thin voids (V2$_{(\Delta T)}$: 1.60, V4$_{(\Delta T)}$: 1.35 and V6$_{(\Delta T)}$: 1.29).

3. Shallow voids (V1$_{(\Delta T)}$: 2.33, V2$_{(\Delta T)}$: 1.60) showed higher thermal contrast (ΔT) values compared to mid-depth (V3$_{(\Delta T)}$: 1.45, V4$_{(\Delta T)}$: 1.35) and deep voids (V5$_{(\Delta T)}$: 1.30, V6$_{(\Delta T)}$: 1.29) showed the least thermal contrast (ΔT) values.

4. Thin voids (V2 @ 300s, V4 @ 200s and V6 @ 180s) took longer to reach their peak values of ΔT compared to corresponding thick voids (V1 @ 220s , V3 @ 160s and V5 @ 140s).

5. Deep voids (V5, V6) always took less time to reach their peak values ΔT compared to the mid-depth (V3, V4), and shallow voids (V1, V2) took the longer to reach peak. This phenomenon was observed in both cases for thick and thin voids cases.

The above two concepts (4,5) may also be seen in a reversible methodological approach:

Given: two voids, V1, V2 with formation times t_1, t_2 respectively.
such as: $\Delta T_{V1} > \Delta T_{V2}$

Then:
$\begin{cases} if: t_1 > t_2, \Rightarrow V1 \text{ is nearer to surface (shallower) than V2} \\ if: t_1 < t_2, \Rightarrow V1, V2 \text{ are at the same depth and V1 is thicker (more damaged) than V2} \end{cases}$

6. It was noticed that depth and thicknesses were compensating each other in using timings of the peak ΔT values. This may add complication in the detection and evaluation procedures in-terms of accuracy and confidence.

7. The difference of thermal contrast (ΔT) values between thick and thin voids when compared via their depths, reduced significantly as the depth was increased, and it became difficult to differentiate between thick and thin voids. This was noticed in thick mid-depth (V3) and thin mid-depth voids (V4) and was more profound between thick-deep (V5) and thin-deep (V6) voids.

8. Similar patterns of thermal contrasts (ΔT) were observed in all voids (V1-V6): a sudden rise, a peak, a gradual drop and a steady-state. However, the values of peaks and the time taken to reach these peaks were different from void to void. This is promising, and can be used as the basis for a detection and evaluation procedure.

9. It is important to mention that sometimes the specimen doesn't have a uniform temperature. After exposing it to heat source, this non-uniformity delays the pattern (thermal contrasts) to be developed. Therefore, sometimes it takes longer to observe an established pattern, as initially there could be a random thermal contrasts profile.

10. The best time recommended to carry out test is noon-time, since, the solar intensity is also high and possibility of detecting sub-surface defects (voids/delaminations) is maximum. In addition, due to the position of the sun (zenith) at this time of the day, the casting of shadows from the surrounding objects (buildings trees et.) on the specimen are minimised. Which further, reduces the possibility of non-uniform heating.

11. It was also observed during the same tests that optimum results were achieved, if the wind speed was less than 10kph (6mph approx.). It was found that wind speeds above 16kph (10mph) affected the surface temperature (increasing the rate of heat convection and creating an unstable thermal gradient) of the target specimen, and therefore, reduced the ability of the infrared camera to detect the fault.

12. The best time to assess the void's condition/evaluation was the time taken by ΔT to reach peak.

13. As the depths were increased, the differences between the peak values, ΔT, for mid-depths (V3, V4) and deep voids (V5, V6) became smaller. In real case scenario, where the depths and thicknesses of the voids are not known prior to test, it will become difficult to classify such voids with confidence. This is probably a limitation of the IRT technique and further evidence is necessary. In such circumstances, it is proposed that IRT test will stop and IHT will take over to do the further assessments/evaluations.

14. A very promising, way of detecting and evaluating voids hidden under a concrete surface, using an IR-camera was observed, where the whole decision from the void detection until its evaluation could be made in 300 seconds, starting from the heating of the specimen under test. This investigation showed that the best time to detect and evaluate the voids/defects is the time, when the temperature gradient is maximum, and in this case it was observed at the beginning of the heating process.

4.5   Finite Element Analysis (FEA)

This section describes the development of a finite element model, based on the corresponding experimental ones.

The finite element method (FEM) was introduced in the late 1950s and early 1960s by the engineers for solving numerically the partial differential equations in structural engineering (Diaz et al. 2006). Finite element method brings numerous advantages to the economical and practical side of the experiment. On one hand, it avoids the possibility of carrying out time consuming complex projects, and therefore, saving time and money. On the other hand, it solves the problems, which are technically difficult to solve manually. Besides that, it also helps in predicting the behaviour of the specimen under various loading conditions, hence is equally important in analysing the risk and safety factors as well. In addition, it can also be deployed for parametric studies or what-if-studies, where, each parameter can be studied at a time and its effect on the solution can be analysed carefully (sensitivity-analysis). Today there are many FE-codes (ANSYS, ABAQUS etc.) developed that can solve complex mathematic models for many engineering problems that are difficult to deal manually. Mathematical models can be defined as the set of differential equations dictated by a corresponding set of initial and boundary conditions. FEM is a numerical procedure employed to solve large class of engineering related problems involving complex stress and dynamic analyses, electromagnetism, fluid dynamics, and many more. In this section, transient thermal analysis is adopted to reproduce the results obtained during IRT tests.

Hence, Finite element analyses (FEA) were carried out in parallel to experimental IRT tests, and ANSYS Mechanical APDL 18.1 (ANSYS 2018) was employed for modelling and analyses purposes. The aim was to develop a global FE-model that can aid the experimental tests and be used as a predictive tool, without compromising in accuracy and rigour. In addition, it can also replace the experimental tests and this way, repetition of the experimental tests could be avoided, hence, making substantial savings in time

and effort. The model was developed, calibrated and updated using experimental input and realistic boundary conditions.

4.5.1 Test 01 (Numerical modelling). Single slab with 6 flaws (Voids)

A 3-D model of a concrete slab was developed. Six "*Volumes*" (representing voids) were created and *glued* (not *added*) to retain their own properties in the concrete slab model at positions they represented the six corrugated cardboards embedded in the in-situ concrete slab (Figure 4-19). The dimensions are listed in Table 4-7.
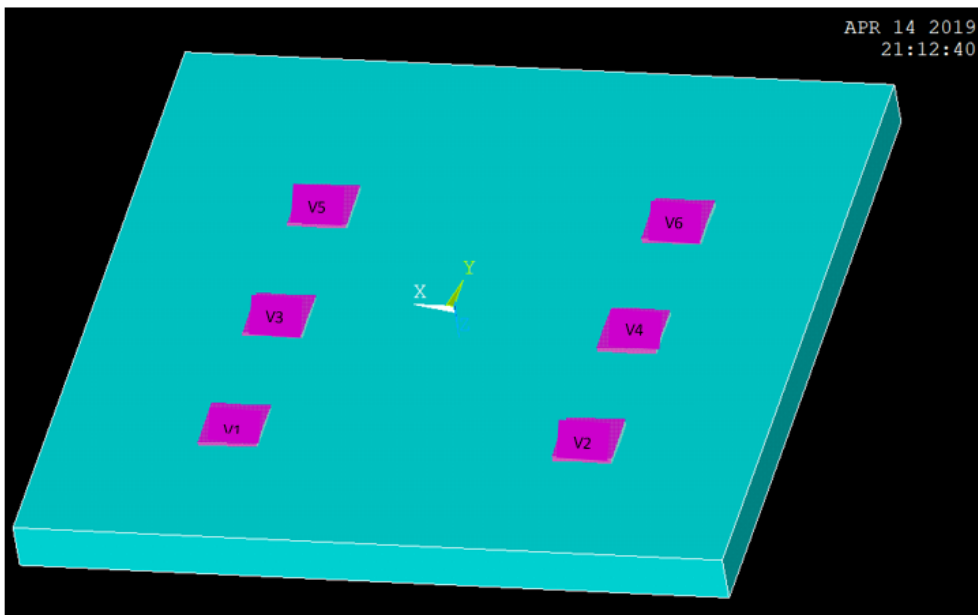
Figure 4-19: FEA model of the concrete specimen containing voids (ANSYS 2018).

The same definitions and nomenclature with the real tests were used for clarity.

Table 4-7: Details of the specimen under test.

Essentials	Dimensions (mm)	Voids Depths from top (mm)
Concrete Slab	600x600x40	
Void-V1 (Shallow-Thick)	50x50x5	10
Void-V2 (Shallow-Thin)	50x50x3	10
Void-V3 (Mid-Depth-Thick)	50x50x5	20
Void-V4 (Mid-Depth-Thin)	50x50x3	20
Void-V5 (Deep-Thick)	50x50x5	30
Void-V6 (Deep-Thin)	50x50x3	30

After developing the CAD model, appropriate material properties, element types, and mesh sizes for the voids and slab were selected, to be inserted in the model. These are reported in Table 4-8.

Table 4-8: Details of parameters, used in developing the FE-model.

Input parameters	Concrete	Corrugated cardboard
Element type	SOLID278	SHELL132
Mesh size (mm)	10	1
Mesh shape	Tetra	Tetra
Density (Kgm^{-3})	2222.1	45
Thermal conductivity (Wm^{-1}K^{-1})	1.75	.047
Specific heat capacity (JKg^{-1}K^{-1})	880	1700

The homogeneous thermal solid element, SOLID278, was adopted for modelling the concrete slab (Figure 4-20-a). This element geometry showed compatibility with the structure of the concrete slab.
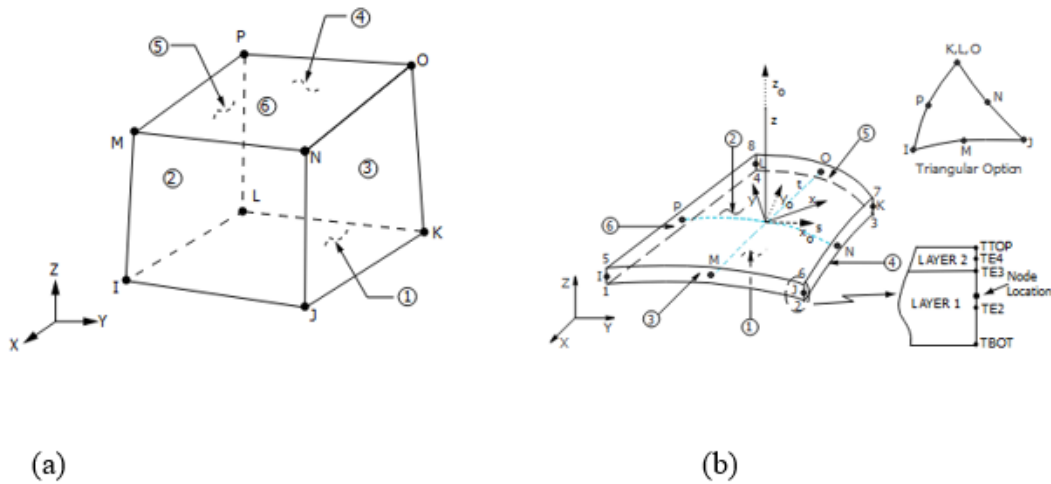
Figure 4-20: (a) SOLID278 element, featuring 8 nodes. (b) Shell 132 element, featuring 8 nodes and two layers (ANSYS 2018).

Moreover, SOLID278 is an 8-node cubic element with a single degree of freedom, temperature, at each node and isotropic material properties (Figure 4-20-a). It is applicable to a 3-D, steady state, or transient thermal analysis. It is suitable for modelling a general 3-D solid heat conduction. In addition, it supports convection, or heat flux, as an input for surface loads at the element faces. The element is available in two forms, *homogenous thermal solid* and *layered thermal solid*. The former supports isotropic material properties, whereas the latter, supports anisotropic properties (ANSYS 2018). Isotropic thermal properties (thermal conductivity, specific heat) were taken for the concrete slab, as the heat transfer in concrete depends on density of the mix and is independent of the direction of strength, unlike its mechanical properties, like Modulus of Elasticity, Poison's ratio.

SHELL132 was another element adopted to represent six voids in the concrete slab (Figure 4-20-b). The corrugated cardboard was regarded as a thin-wall, light, layered honey-combed structure, mainly used as a packaging material. The three-layer version of the element chosen, showed good compatibility with the thin walled, corrugated card board structure. Assumptions of linear temperature variation in the layers were considered, and isotropic thermal properties were taken as an initial assumption.

SHELL132 is a 3-D layered shell element possessing in-plane and out-of-plane (though thickness) thermal insulation capabilities (Figure 4-20-b). The element has 8 nodes allowing up to 32 temperature degrees of freedom per each node. This element is applicable to a 3-D steady-state or transient thermal analysis (ANSYS 2018).

Material properties were estimated indirectly (based on the volume and mass) in the laboratory. Densities for concrete and corrugated cardboard were estimated to be 2222.1kgm^{-3} and 45kgm^{-3} respectively, whereas specific heat values and isotropic thermal conductivities were reproduced from similar research. Essentially, specific heat capacity of 880 Jkg^{-1}k^{-1} was chosen for concrete (Hiasa et al. 2017a) and 1700 JKg^{-1}K^{-1} for the corrugated cardboard (Engineering ToolBox 2001). Finally, thermal conductivity of 1.75Wm^{-1}k^{-1} for concrete (Lafarge Tarmac Limited 2015) and 0.047Wm^{-1}K^{-1} for corrugated cardboard (Gibbs 2013), were adopted in developing the model (Table 4-8).
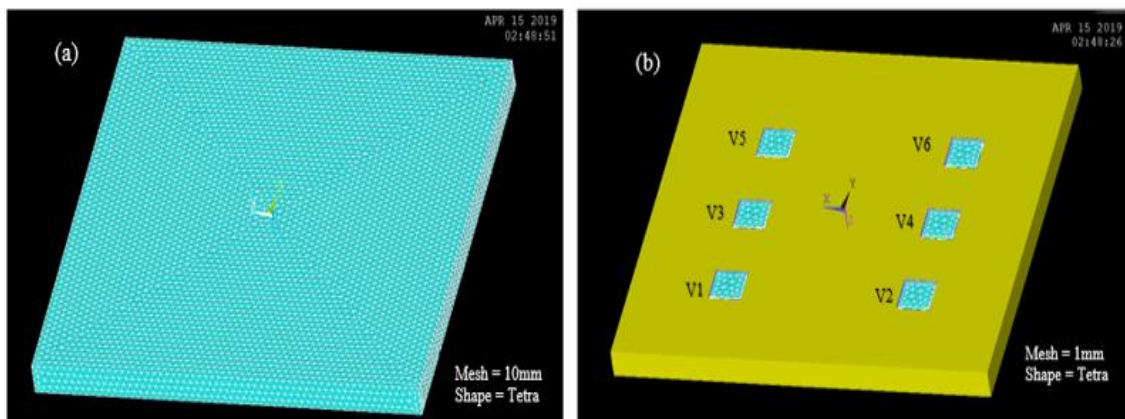
Figure 4-21: (a) Tetra mesh (10mm) for concrete slab, (b) Tetra mesh (1mm) for volumes representing voids (ANSYS 2018).

Once the element types and material properties were inserted, the mesh type and size were selected for each element type. The mesh shape tetra was adopted, as it showed compatibility with the designed models with voids. An element size of 10mm was selected for regions of the slab away from the voids as illustrated in Figure 4-21-(a). It was observed that by reducing the mesh size resulted in more computational time with insignificant variations. However, to get better accuracy at the regions representing voids, a finer mesh size of 1mm was adopted via mesh management tool.

Transient Thermal Analysis

Transient thermal analysis was carried out contrary to steady-state thermal analysis. If a solid object is suddenly subjected to a change in environmental conditions, sometime elapses before reaching a thermal equilibrium state. The latter is referred as the steady state condition, and the thermal analysis carried out at steady state is called steady-state thermal analysis (Holman 2010). The interim period, before the equilibrium is established, is known as transient time, and this unsteady state is called transient state, where, the thermal analysis referred to this case is called '*transient thermal analysis*'. In transient thermal analysis, the change in internal energy with time and the variations in boundary conditions with time are taken into an account.

The boundary conditions (Figure 4-22) were applied in the form of thermal loads. The initial conditions (temperature) of the slab was taken to be 28°C. This was checked initially, before the start of experiment, by using k-type thermocouples (Section 4.4.1). The top surface, was subjected to a normal heat flux of 280Wm^{-2}, since the maximum *solar irradiance* at the time when experiment was performed was around 280Wm^{-2} (NASA LaRC 2018).
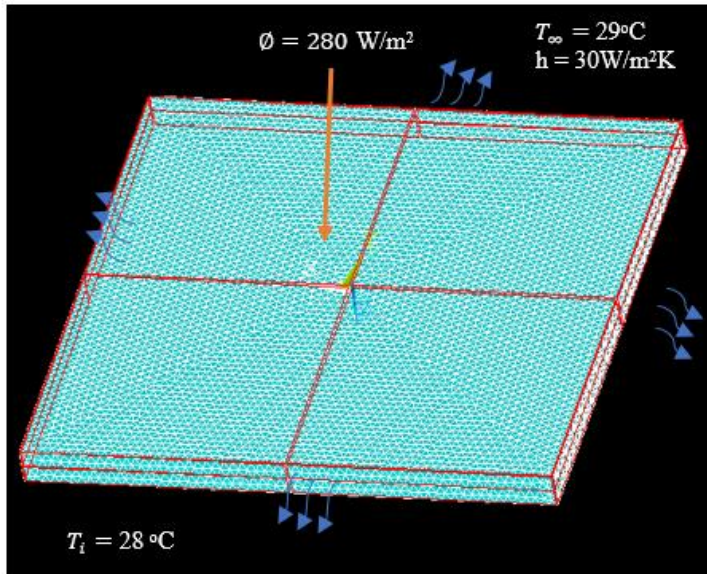
Figure 4-22: Boundary conditions applied to the FE-model, ANSYS Mechanical APDL 18.1 (ANSYS 2018).

The sides of the slab were subjected to convection with bulk temperature of 29°C, the ambient temperature. A convective heat transfer coefficient of $30 Wm^{-2}K^{-1}$ was estimated, where the maximum wind speed taken to be 9.7kph (6mph) (NASA LaRC 2018).

The bottom surface of the slab was given an initial temperature of 29°C based on the thermocouple readings.

ANSYS Mechanical APDL 18.1 (ANSYS 2018) provides the option of two types of transient loading. Stepped loading and ramped loading.
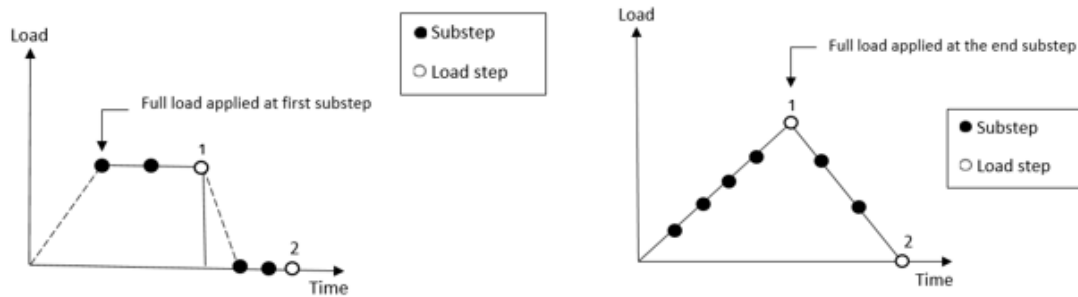
Figure 4-23: Representation of a stepped loading and ramped loading approach, (ANSYS 2018).

In stepped loading, the full value of load is applied at the first sub-step and remains constant for the rest of the load sub-step (Figure 4-23). Whereas, in ramped loading the load value increases gradually through each sub-step, until it reaches the maximum /full value that occurs at the end of the load step (Figure 4-23).

Stepped loading was selected on the basis that when the specimen (concrete slab) was subjected to the heat source, sun, the thermal load or heat flux, was already at its peak from the beginning of the test. That means, full intensity of thermal load was applied on the specimen from the very beginning.

The option, 'small displacement (thermal) transient analysis' was chosen, since, not very high displacement was expected during the thermal loading. The time at the end of the load step was taken to be 1200s, similar to the time recorded during the experiment. The time step size was chosen to be 1s, where the minimum time step was 0.5s. This was chosen to compare each frame captured per second with that of the IR-camera.

The default Newmark time integration algorithm was implemented as it is recommended for implicit transient analysis (ANSYS 2018). A major advantage is that it is unconditionally stable and computationally efficient with an input amplitude decay factor of 0.005. This parameter controls the numerical *dissipation* by minimising the error at each step (Moorthy et al. 1993), and therefore, the numerical noise (noise is usually shown as numerical dissipation).

The default, sparse direct solver was adopted based on the software recommendation ANSYS Mechanical APDL 18, (ANSYS 2018). This selection was made after some custom trials and a subsequent comparison between with the sparse solver and preconditioned conjugate gradient (PCG) solver (recommended for large size models and bulky structures, ANSYS 2018). It was observed that the program chosen solver produced optimum results, nearer to experimental results.

In the Sparse Direct Solver, the finite element matrices are sparsely populated, that allows the simultaneous equations system to be solved efficiently by minimising the operation counts.

The linear matrix equation (4.17) can be written as:

$$[K]\{u\}=\{F\} \tag{4.17}$$

Where,

[K]= Global Stiffness Matrix,

{u}= Global Vector of Nodal Displacement

{F}= Global Applied Load Vector

In direct sparse solver, the linear matrix equation (4.17) is solved by triangular decomposition of Matrix [K] into following equation:

$$[L][U]\{u\}=\{F\} \tag{4.18}$$

Where:

[L]= Lower Triangular Matrix

[U]= Upper Triangular Matrix

By substituting {w}=[U]{u} in the above equation (4.18) and by solving the triangular matrix system for {w} by using forward pass operation, we can obtain {u}, given by:

$$[L]\{w\}=\{F\} \qquad (4.19)$$

Now, by the back substitution operation on a triangular matrix, we can compute {u}, given by:

$$[U]\{u\}=\{w\} \qquad (4.20)$$

When [K] is a symmetric matrix, the above procedure could be substituted as:

$$[K]=[L][L]^{T} \qquad (4.21)$$

Similarly, [K] can also be written as:

$$[K]=[L][D][L']^{T} \qquad (4.22)$$

Where,

[D]= Diagonal Matrix

[L']= Inverse of Lower Triangular Matrix

The diagonal terms of matrix [D] could be negative in some cases of non-linear finite element analysis. This allows the generation of [L'] without the consideration of a square root of a negative number. Therefore, equations (4.18) through (4.20) can be written as:

144

$$[L'][D][L']^T\{u\}=\{F\} \tag{4.23}$$

$$\{w\}=[D][L']T\{u\} \tag{4.24}$$

$$[L']\{w\}=\{F\} \tag{4.25}$$

and

$$[D][L']T\{u\}=\{F\} \tag{4.26}$$

The sparse direct solver is designed to solve the non-zero entries in stiffness matrix [K], as the [K] is generally sparsely populated with coefficients around the main diagonal. In general, non-zero coefficients appear in [L] or [L'] at the corresponding coefficient locations, where matrix [K] had zero entries.

The sparse direct solver minimizes this fill-in by reordering the equation numbers in the matrix [K]. The performance of a direct solver is optimised by equations reordering procedure.

This involves relabelling the variables in the vector {u}. Further, it permutes the rows and columns of [K] and also the corresponding rows of [F], hence minimising the fill-in. Thus, when the decomposition steps are performed on the reordered [K] matrix via equation (4.18) or equation (4.23), the fill-in occurring in [L] or [L'] matrix are minimised. In other words, the matrix is compressed to a sparse matrix by dropping all the zeros present, far from the diagonal matrix (Figure 4-24).

$$\begin{bmatrix} B_{11} & B_{12} & 0 & \cdots & \cdots & 0 \\ B_{21} & B_{22} & B_{23} & \ddots & \ddots & \vdots \\ 0 & B_{32} & B_{33} & B_{34} & \ddots & \vdots \\ \vdots & \ddots & B_{43} & B_{44} & B_{45} & 0 \\ \vdots & \ddots & \ddots & B_{54} & B_{55} & B_{56} \\ 0 & \cdots & \cdots & 0 & B_{65} & B_{66} \end{bmatrix} \Rightarrow \begin{bmatrix} 0 & B_{11} & B_{12} \\ B_{21} & B_{22} & B_{23} \\ B_{32} & B_{33} & B_{34} \\ B_{43} & B_{44} & B_{45} \\ B_{54} & B_{55} & B_{56} \\ B_{65} & B_{66} & 0 \end{bmatrix}$$

Figure 4-24 Conversion of a (square-diagonal) matrix to a sparse matrix (ANSYS 2018).

In addition, if the matrix is symmetric, it takes advantage of symmetry, and further reduces the storage, as only one half around the diagonal elements in the matrix would be used. This significantly reduces the time and storage space on one hand, but on the other hand results in a slight reduction in accuracy.

4.5.1.1 Test 01 (IRT). Thermogram and Temperature distribution profile. Comparison between FEA and EXP

The final frame, captured from the FE-transient thermal analysis, is compared with the corresponding experimental one, as illustrated in Figure 4-25. Please see APPENDIX A for more frames comparison.
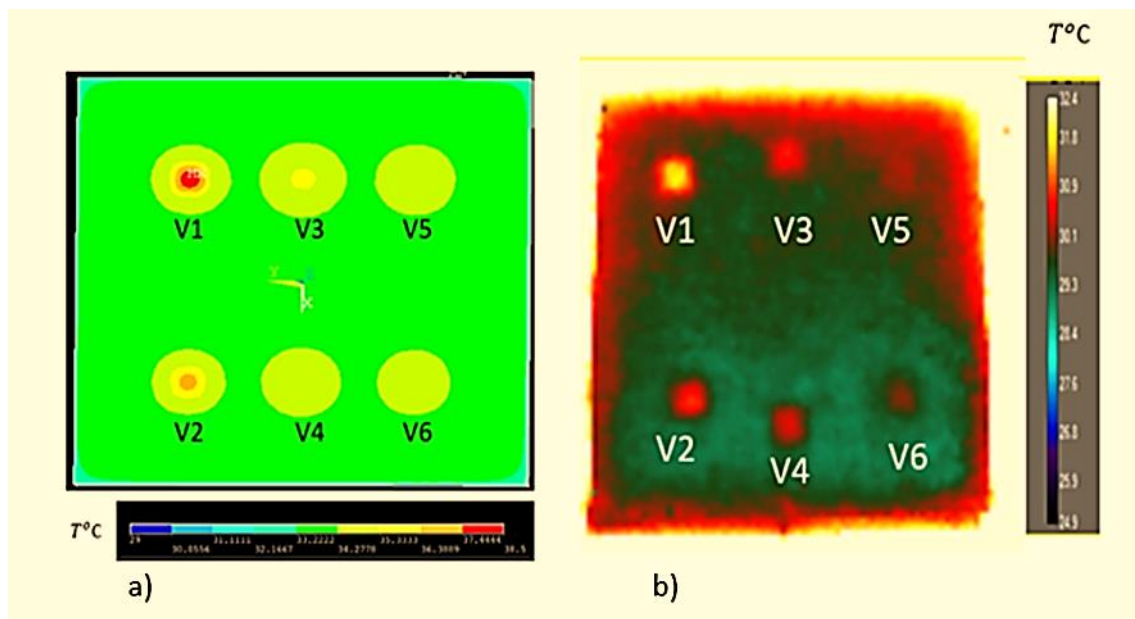
Figure 4-25: Contour plots of nodal temperatures for voids. (a) FE-Thermal image, frame captured at 1200s (b) EXP-Thermogram recorded at 1200s.

All the six voids were depicted in the simulated FE-thermal image, as shown in (Figure 4-25). Shallow voids (V1, V2), showed clear boundaries compared to the mid-depth voids (V3, V4), whereas, deep voids (V5, V6) showed no defined boundaries exactly as they were observed in the experimental testing. In the simulated FE-thermal image, the shallow (V1, V2) and mid-depths (V3, V4) voids, were first detected at approx. 300s, this was similar to experimental testing, where all voids were first detected at 300s. However, the deep voids (V5, V6) appeared later, at approx. 600s. Indications are that this discrepancy is attributed due to the increased depth. The resolution of the FE-

thermal image, was unable to represent the relatively minute differences in the temperatures, compared to the experimentally obtained thermograms.
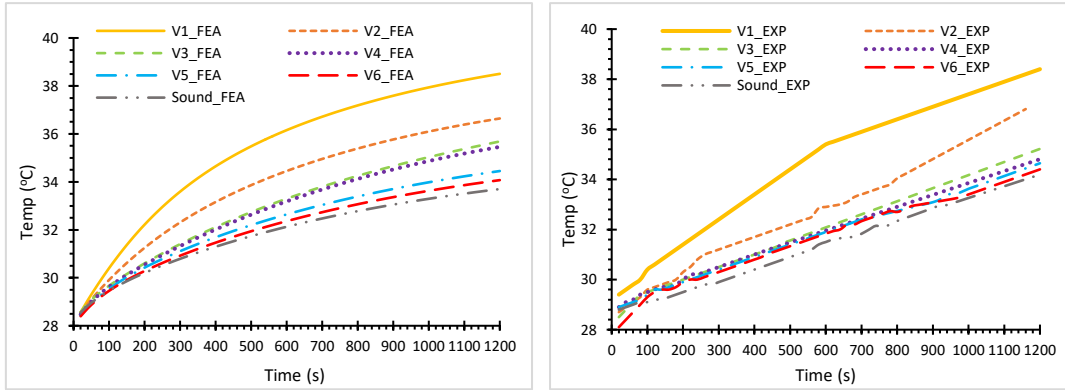
Figure 4-26: Temperature distribution against time, for all voids and reference area. Left: FEA and Right: EXP.

Table 4-9: Key for Figure 4-26. A display of Void Depths, Void Types and Temperature at 1200s.

V (voids)	VOID Depth (mm)	VOID Type (mm)	Temp (°C) @ 1200s		Error (%)
			EXP	FEA	
V1		Thick (5)	39	38.5	1.2
	Shallow (10)				
V2		Thin (3)	37	36.6	1.1
V3		Thick (5)	35.2	35.7	-1.4
	Mid.D (20)				
V4		Thin (3)	34.8	35.5	-2.0
V5		Thick (5)	34.6	34.5	0.3
	Deep (30)				
V6		Thin (3)	34.4	34.1	0.9
Reference	NA	NA	34.2	33.7	1.5

By plotting their temperature distribution profiles (Figure 4-26), it was observed that shallow thick void (V1) showed the highest rise in temperature, compared to its corresponding shallow thin (V2), mid-depth (V3, V4) and the deep (V5, V6) voids. Whereas, mid-depth voids (V3, V4) showed slightly higher temperatures compared to the deep voids (V5, V6). The sound region temperature showed the least rise in temperature compared to the voids. It is reasonable to state so far, that the deeper the void the less the temperature rise, and therefore, the harder to detect and predict. This trend was similar to the one obtained during experimental test (Figure 4-26).

By comparing, the numerically simulated temperatures of each void to the corresponding experimentally ones obtained at 1200s, a good correlation on an average of 98.8% (approx.) was achieved (Table 4-9).

In order to evaluate the voids, thermal contrasts as explained earlier (Section 4.4.2.2), were calculated for each void, and compared with the corresponding experimental ones.

4.5.1.2 Shallow Voids (Thick,Thin). Thermal Contrast (ΔT) Comparison between FEA and EXP

A thermal contrast (ΔT) comparison was made for the shallow voids (V1,V2) obtained from the FE-simulation and experimental testing (Figure 4-27).
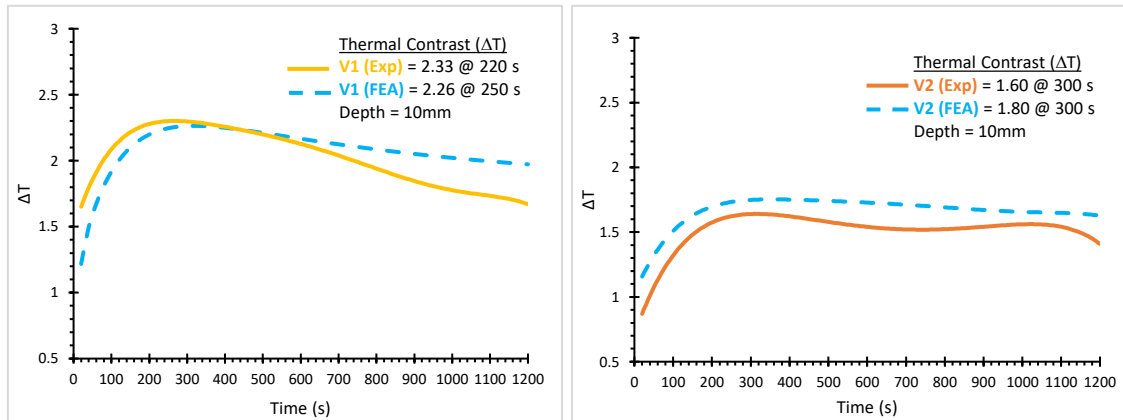
Figure 4-27: Thermal contrast (ΔT) comparison FEA vs EXP. Left: Shallow thick void (V1). Right: Shallow thin void (V2).

The maximum value of thermal contrast (ΔT) obtained from FEA (Figure 4-27), for the shallow thick void (V1) was as follows:

(ΔT)
$V1_{FEA}$ = 2.26 @ 250s
$V1_{EXP}$ = 2.33 @ 220s

The trend of both (FEA+EXP) graphs are quite similar and a close correlation was observed, however, there is a small discrepancy between the two of less than 7% approx. on an average, which was mainly observed at the cooling-down period.

The maximum value of thermal contrast (ΔT) obtained for the shallow thin void (V2) from FEA (Figure 4-27) was as follows:

<u>(ΔT)</u>

$V2_{FEA} = 1.80$ @ 300s

$V2_{EXP} = 1.60$ @ 300s

Both showed peak values exactly at the same time, which is very encouraging, however, a slight discrepancy in the overall trend was observed and on an average, disagreement was about 10%.

4.5.1.3 Mid-depth Voids (Thick,Thin). Thermal Contrast (ΔT) Comparison between FEA and EXP

A thermal contrast comparison (ΔT) between the FE-simulation and experimental testing for the mid-depth thick (V3) and mid-depth thin (V4) voids was made as illustrated in Figure 4-28.
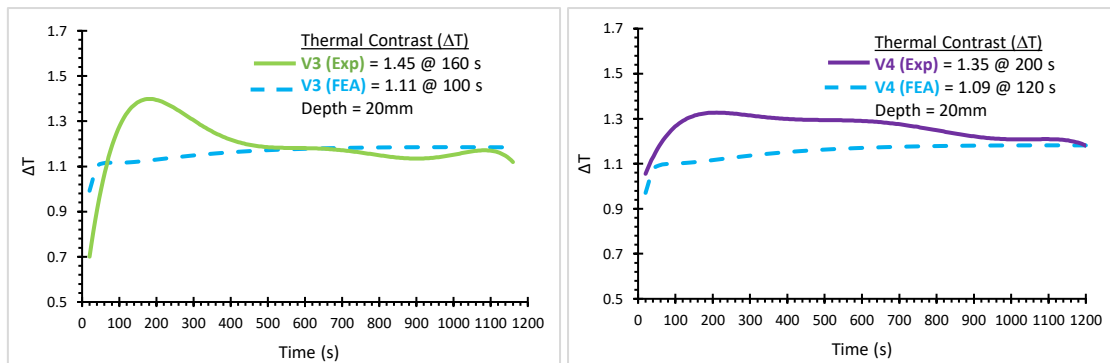
Figure 4-28: Thermal contrast (ΔT) comparison FEA vs EXP. Left: Mid-depth thick void (V3). Right: Mid-depth thin void (V4).

FEA results (Figure 4-28) for mid-depth thick void (V3) showed the first peak of thermal contrast (ΔT), as follows:

(ΔT)

$V3_{FEA} = 1.11$ @ 100s

$V3_{EXP} = 1.45$ @ 160s

The trend in the FE-analysis was similar to experimental testing. After reaching the first peak value, there was a small drop. The graph continued to rise marginally to approximately 600s, where it levelled and held horizontal at a steady-state of ΔT= 1.12.

Any differences between voids V3 and V4 at mid-depth should be very important since these values can be used to distinguish between thick and thin voids (early and later

stage defects, or initial stage and full debonding) at similar depths. This phenomenon of rise and fall after reaching peak values was more apparent in experimental testing but in the latter case, it can be attributed to *noise* rather than some other, significant and related phenomenon. The overall percentage error between the two was estimated to be 8%.

The thermal contrast (ΔT) of Mid-depth thin void, V4, obtained from the FE-analysis (Figure 4-28) showed its first peak value as follows:

(ΔT)

$V4_{FEA} = 1.09$ @ 120s

$V4_{EXP} = 1.35$ @ 200s

Once again the overall trends were similar. However, there was a slight discrepancy in their peak values, ΔT, along with their occurrence timings. The average inconsistency between FEA and experimental results was approximately 9%.

4.5.1.4 Deep Voids (Thick, Thin). Thermal Contrast (ΔT) Comparison between FEA and EXP

A comparison between numerical and experimental time histories of thermal contrast (ΔT), for the deep thick (V5) and deep thin (V6) voids is shown below (Figure 4-29).
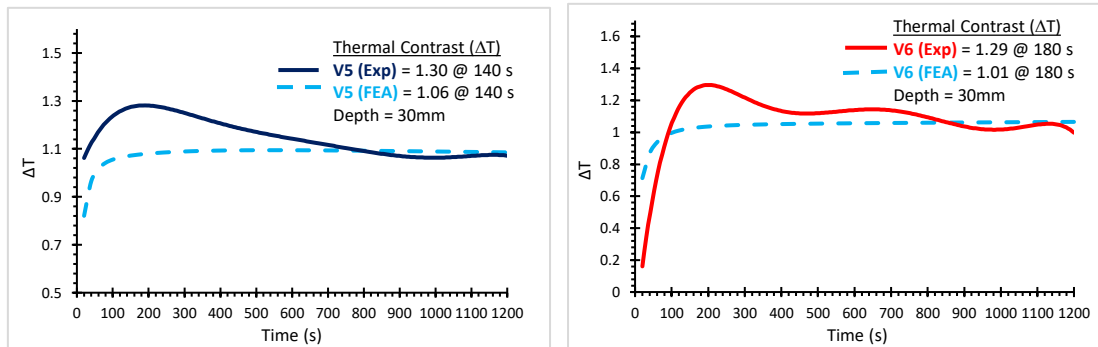
Figure 4-29: Thermal contrast (ΔT) comparison FEA vs EXP. Left: Deep thick void (V5). Right: Deep thin void (V6).

The first peak value of thermal contrast (ΔT) obtained from the FE-simulation (Figure 4-29) for the deep thick void (V5) was as follows:

(ΔT)

$V5_{FEA} = 1.06$ @ 140s
$V5_{EXP} = 1.30$ @ 140s

The trends of FEA and experimental graphs, were similar, and both peaks, ΔT, were observed at the same time, but with slight variations in their values. However, it was observed that the deeper the void the lesser the variations become in the FE results. Since, the initial peak at a particular time period is important for recognition, and distinguishing thick and thin voids at the same depth, any small variations in the trend

after that is insignificant. The average percentage error betweent the FEA and experimental values of thermal contrasts was calculated to be approx. 9%.

The first peak value of thermal contrast (ΔT) of deep thin void (V6), obtained from the FE-simulation (Figure 4-29) was as follows:

(ΔT)

$V6_{FEA} = 1.01$ @ 180s

$V6_{EXP} = 1.29$ @ 180s

Similar trends were observed between the two, and again both peaks, ΔT, occurred at the same time, but showing slight discrepancy in their peak values. The overall average error calculated for the FE-simulation and experimental thermal contrasts (ΔT), was about 5%.

4.5.1.5 Inferences from FEA and Exp IRT Results Comparison (Test 01)

1. Acceptable correlation was achieved between numerical and experimental results, with an accuracy of 98.8% for all voids. However, for the estimated ΔT values, the average error was slightly high but below 10% for all voids.

2. All the six voids were detected in the thermal images, and it was observed that as the voids got deeper and thinner, their visualisation got blurrier, similar to the experimentally obtained thermograms. In addition, in the FE-thermal image, the shallow (V1, V2) and mid-depth (V3, V4) voids appeared at approx.300s, similar to the experimental tests, where the deep voids (V5, V6) appeared later at 600s. This discrepancy could be attributed to the increased depth, as the resolution of the FE-thermal image, was unable to represent the relatively minute differences in the temperatures, compared to the experimentally obtained thermograms.

3. The trend of thermal contrasts obtained from the FE-simulation, followed quite closely that of experimental testing.

4. Shallow voids (V1$_{FEA}$: 2.26, V2$_{FEA}$: 1.80) always showed higher thermal contrasts (ΔT) compared to the mid-depth (V3$_{FEA}$: 1.11, V4$_{FEA}$: 1.09) and deep voids (V5$_{FEA}$: 1.06, V6$_{FEA}$: 1.01), similar to experimentally obtained trend.

5. Thick voids (V1, V3, V5) always showed higher thermal contrast (ΔT) values, than their counterparts, thin voids (V2, V4, V6) at various depths (shallow, mid-depth, deep). This was also endorsed by experimental results.

6. Thick (V1, V3, V5) and thin (V2, V4, V6) voids when compared at their respective depths (10mm, 20mm, 30mm) also showed the similar trend in FE-simulation as observed in experimental results. The thick voids (V1, V3, V5) always showed high peak value, and also observed at an earliest time compared to their respective thin voids (V2, V4, V6). This was observed both in experiment and FE-simulation. However, in mid-depth (V3, V4) and deep voids (V5, V6) comparison, the difference between their thermal contrast (ΔT) values at their corresponding depths was small.

7. Shallow voids (V1$_{FEA}$ @ 250s, V2$_{FEA}$ @ 300s) always took more time to reach their peak values ΔT compared to the mid-depth (V3$_{FEA}$ @ 100s, V4$_{FEA}$ @ 120s), and deep voids (V5$_{FEA}$ @ 140s, V6$_{FEA}$ @ 180s). This phenomenon was observed in both cases for thick and thin voids cases. However, when compared mid-depth (V3, V4) voids, there were slight discrepancies observed in the timings of their occurrences (peaks) in FE-simulations. This also indicates that as the voids get deeper and thinner, the analyses gets complicated.

8. In short, two are the main factors affecting (influencing), the detection and evaluation of the voids: The position of the void relative to the surface of the slab; The size (thickness) of the void itself. There are of course a number of other factors, such as density of the material, distance of the camera from the object under test (optimum can be found relatively easily) etc. that then can be 'arranged'.

4.6 Test 02 (Experimental). Two-Slabs stacked system with 3-flaws (Delaminations) at the Interface

After drawing preliminary conclusions from testing on the single cast concrete slab (with designed voids at various thicknesses and depths), it was decided to apply the gained knowledge to a more realistic scenario. Therefore, in this test, an effort was made to replicate the real life delamination flaw, which is largely present at a constant depth i.e at the interface between the top overlay (40-50mm) and base. In order, to reproduce this, two concrete slabs of the same sizes were casted, one on top of another, with three deliberate delaminations (introducing similar patterns of corrugated cardboards as per Test 01), at their interface and at known depth of 40mm (Figure 4-30). However, this time, delaminations of very small thicknesses (1mm, 2.5mm and 5mm) were introduced, to represent the 'evolution' of delamination from *'Initial'* to *'Intermediate level'* and finally to *'Severe-delamination'*. The details of delaminations are shown in Figure 4-31.

Figure 4-30: Casting of Two-slabs stacked system with three delaminations at the interface.
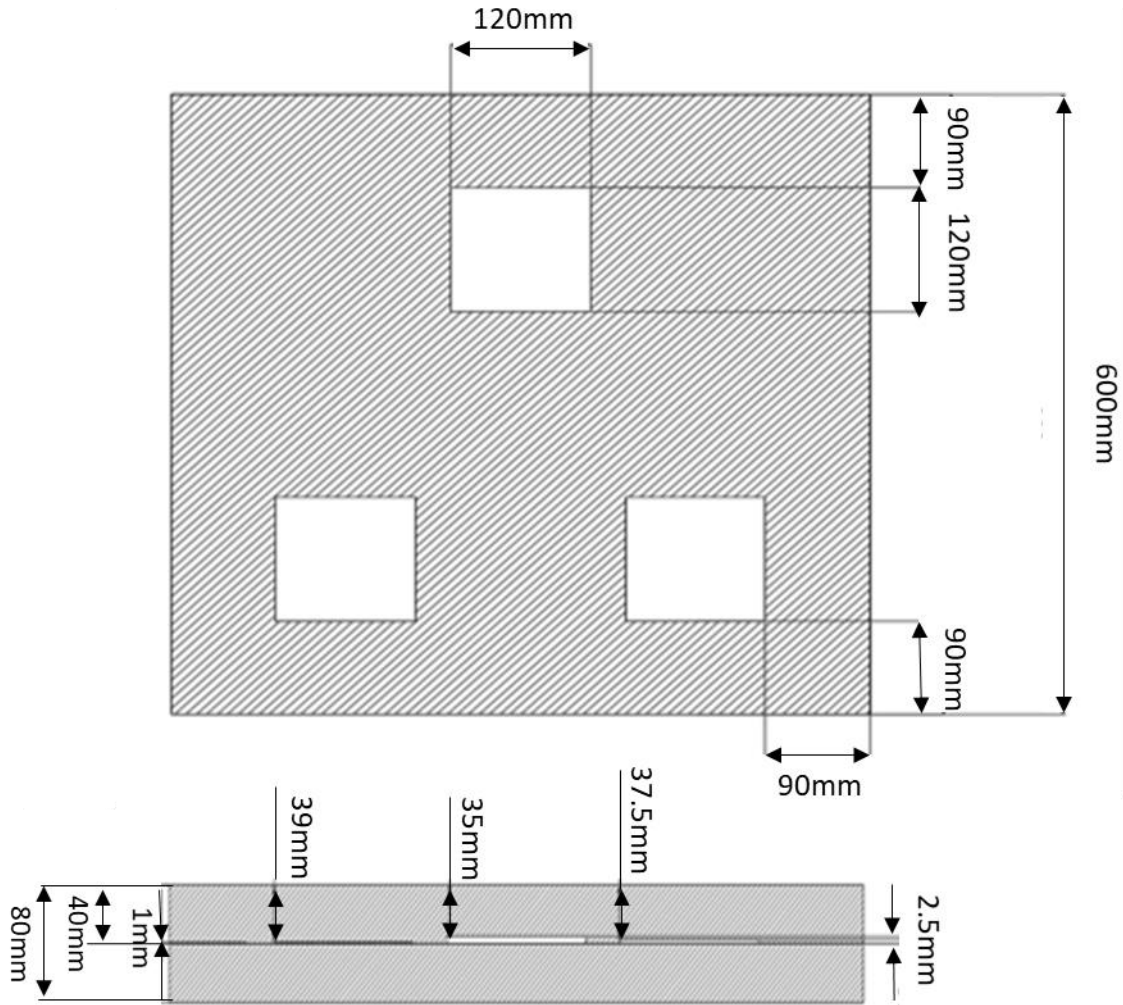
Figure 4-31: Details of Two-cast concrete slabs system with three delaminations at the interface.

The aim of this test was to examine, if the 'evolution' of delamination could be detected and evaluated via the IRT technique.

4.6.1 Test Setup and Procedure

Similar to Test 01, the test setup was arranged outside the Civ Eng labs of the University in a hazy sunshine day, and passive thermography was adopted. In order to avoid the non-uniform heating of the slab from its edges, insulating material was placed around the sides, exposed directly to the sun, as shown in Figure 4-32. The surrounding

ambient temperature was 31°C with the maximum wind speed of 8kph (5mph). Solar radiations with an average irradiance of 290Wm^{-2} (NASA LaRC 2018) were recorded for that particular time of testing. The IR camera was held by the tripod focussing at 90° (vertically) and at a distance of 2m from the slab (Figure 4-32). The initial settings of the camera were adjusted as follows: Emissivity = 0.95 (the default value for concrete), Measured reflected temperature = 33°C, Object distance = 2m, Atmospheric temperature = 31°C and Relative humidity = 42%.
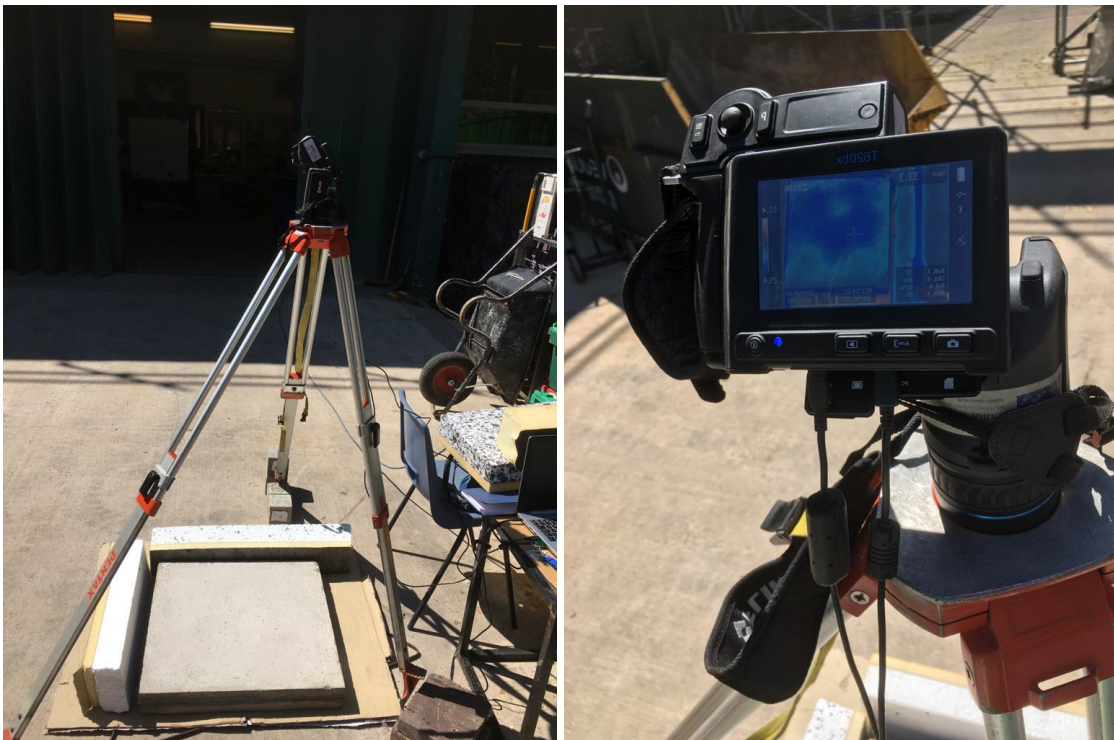
Figure 4-32: Setup of Test 02-IRT. Thermograms recording during the heating phase.

The initial average temperature of the slab measured just before the test starts, was 29.6°C ±1, and the time at the start of the test was 13:00 BST. The test lasted 1390s (23 min approx.), until there was no significant change in thermal contrast of the thermograms. The recorded frames were then imported for thermogram tuning, in the *Research Max IR* software (FLIR Systems Inc. 2016).

4.6.2 Results and Discussion

4.6.2.1 Analysis of Thermograms and Temperature distribution profile

It was observed with contentment that the acquired thermograms revealed all three delaminations, despite of their 40mm depths and very small thicknesses (Figure 4-33). Even, a 1mm thick, delamination (D3) was visible. However, the first impression of all the three delaminations was observed (in the thermograms) after 710s (12mins approx.) of exposure to the hazy sunshine conditions. By adjusting the 'temperature-span', the boundaries of the delaminations were *sharpened* and the *thermal colours* were exaggerated. The 5mm thick delamination (D1) showed higher thermal contrast compared to 2.5mm (D2) and 1mm thick (D3) delaminations. It was observed that the shapes of delaminations detected were not as clear as they was noticed for the voids in previous test. This was due to the increase in their depths and decrease in their thicknesses. The 1mm, thick delamination (D3), had the most vague appearance among other delaminations (Figure 4-33). This also highlights the limitations of IRT, for detecting and evaluating deep and thin defects (early stage of delamination).
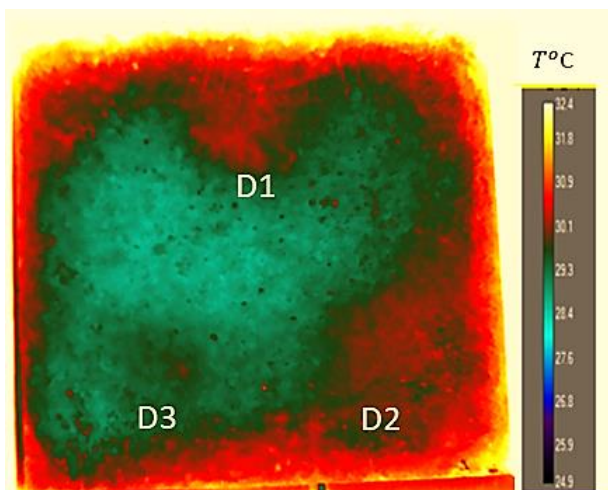
Figure 4-33: Thermogram showing all three delaminations in IRT Test 02.

Regions of interest (RoIs) were created and analysed for all the delaminations and sound region. The temperature profile for each delamination and sound (robust) region against time were normalised and is plotted in (Figure 4-34).
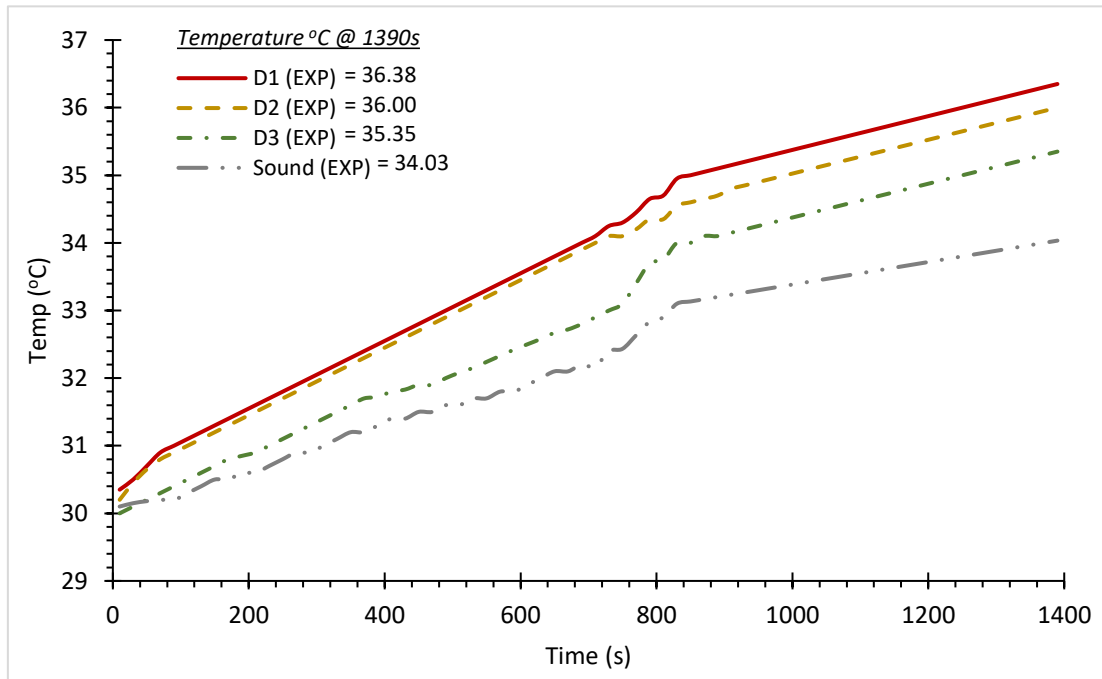
Figure 4-34: Temperature profile for all three delaminations in Test 02.

From Figure 4-34, it was observed that D1,the 5mm-thick delamination (severe) showed the highest rise in temperature compared to D2, the 2.5mm thick delamination (intermediate) and D3, the 1mm thick delamination (initial). The difference between 5mm and 2.5mm at the depth 40mm was insignificant for the first 750 secs but after that it became prominent. The 1mm thick delamination was clear from the start, though, showing significantly less temperature difference compared to the two. The sound region, showed the least rise in temperature compared to all delaminations. It is also important to note that, the day was hazy, and therefore, the rise in temperature was not uniform and the sun rays were blocked several times by clouds hindering the rise in temperature. It was also observed that at 750s, there was a steep rise in temperature till 830s. This was due to the short time window when the sun rays were not interrupted by

any cloud. After that, it became hazy again and remained till the end of experiment. The rise in temperature was approximately linear for all delaminations and sound region.

4.6.2.2 Experimental Thermal contrasts for all Delaminations (D1-D3). Two-slabs stacked system

Thermal contrasts (ΔT) were calculated for all voids (D1-D3) and plotted against time as shown in Figure 4-35.
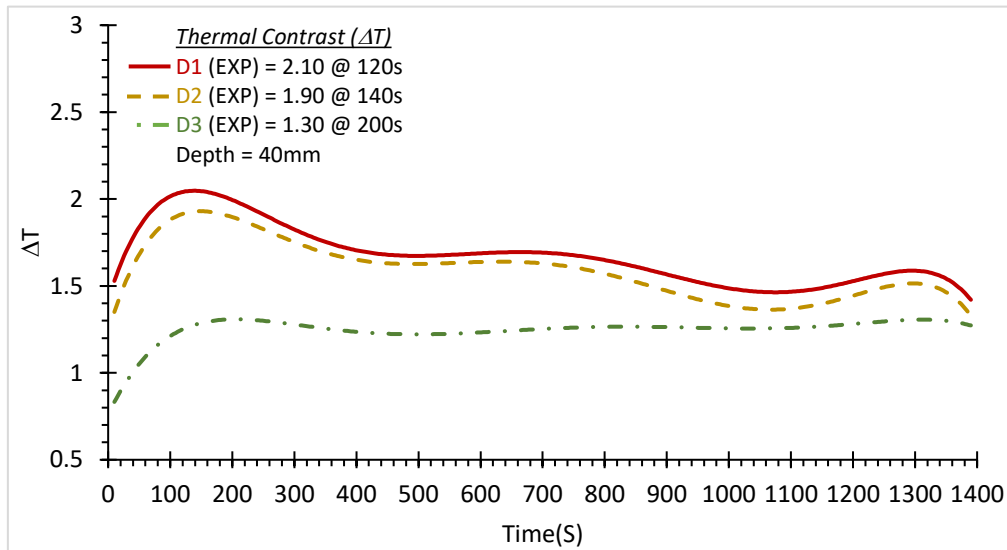
Figure 4-35: Thermal contrast (ΔT) for all three delaminations in Test 02.

By comparing the thermal contrasts (ΔT) for all three delaminations (D1, D2, D3), it was noted that D1, 5mm thick delamination (severe) showed the highest thermal contrast (ΔT: 2.10 @ 120s), compared to D2, 2.5mm thick delamination, 'intermediate', (ΔT: 1.90 @ 140s). Whereas, D3, 1mm thick delamination (initial) showed the least value of thermal contrast (ΔT: 1.30 @ 200s).

The patterns developed (thermal contrasts) were similar for all delaminations (D1, D2, D3). The thermal contrast histories provided a sudden rise, reaching the peak values and then dropping gradually, and becoming steady floating around time. The rise and falls of ΔT for D1, D2 are probably attributed to the clouds interrupting the sun rays.

It was noticed that the that 5mm thick delamination (D1) took less time (120s) to reach its peak value (ΔT), compared to 2.5mm thick delamination (D2), that took more time (140s) to reach its peak value (ΔT). Whereas, 1mm thick delamination (D3), took the longest (200s) to reach its peak value (ΔT). This pattern was similar to the one observed earlier in Test 01, where all thick voids took lesser time when compared to thin voids at similar depths, to reach their peak values (ΔT).

4.6.2.3 Inferences from the Experimental IRT-Test 02

1. It was observed with satisfaction that all the three delaminations (D1, D2, D3) were detected in the recorded thermograms, despite of their small thicknesses and increased depth of 40mm.

2. All delaminations (D1, D2, D3) were first revealed by 710s (12mins approx.), from the start of the recording. However, the' *initial*' delamination (D3), was not as revealing as the '*intermediate*' (D2) and '*severe*' (D1) delaminations in the captured thermograms. This shows that IRT faces difficulties, when dealing with very thin or early stage detection of delamination. This limitation was also noticed earlier in Test 01, while detecting and evaluating the deep-thin void (V6).

3. The 5mm thick delamination (D1), showed the highest thermal contrast value (ΔT: 2.10 @ 120s), followed by 2.5mm thick delamination, D2 (ΔT: 1.90 @ 140s), and the 1mm thick delamination (D3), showed the least (ΔT: 1.30 @ 200s) thermal contrast value.

4. It was also noticed from the ΔT histories developed, that D3, '*initial*' delamination (1mm thick) took the longest time (200s) to reach its peak value compared to D2 '*intermediate*' (2.5mm thick) and D3, '*severe*' (5mm thick) delaminations. This trend endorsed the one obtained earlier in Test 01, where thin voids (V2, V4, V6) were taking longer to reach their peaks (ΔT) compared to thick voids (V1, V3, V5) at similar depths.

5. Almost similar trend of ΔT was observed for each delamination, 'a sudden rise', 'a gradual drop' and then 'steady-state' till the end. This was again quite similar to the ones observed for the voids in Test 01. However, as the voids get deeper and thinner, the detection, evaluation and interpretation becomes more complicated compared with their counterparts shallow voids. This is also a limitaion observed to the IRT, and which could pave way for the IHT to take over and do the further evaluation of the bond quality (delaminations).

166

4.7 Test 02 (Numerical modelling). Two-Slabs stacked system with 3-flaws (Delaminations) at the Interface

The corresponding FE-models were developed in a similar way to Test 01, therefore, no details of the full-procedure will be reported here as the procedure has been deemed similar to Test 01. However, this time, a 3D numerical model, consisting of two concrete slabs bonded together and sandwiching three delaminations (*severe, intermediate* and *initial*) was developed in the ANSYS Mechanical APDL 18.1 software (ANSYS 2018). Boolean operation, 'overlap' was applied between delaminations and the top concrete slab (Figure 4-36). This ensured the continuity between concrete and delaminations. Relevant dimensions are listed in Table 4-10 and Table 4-11.
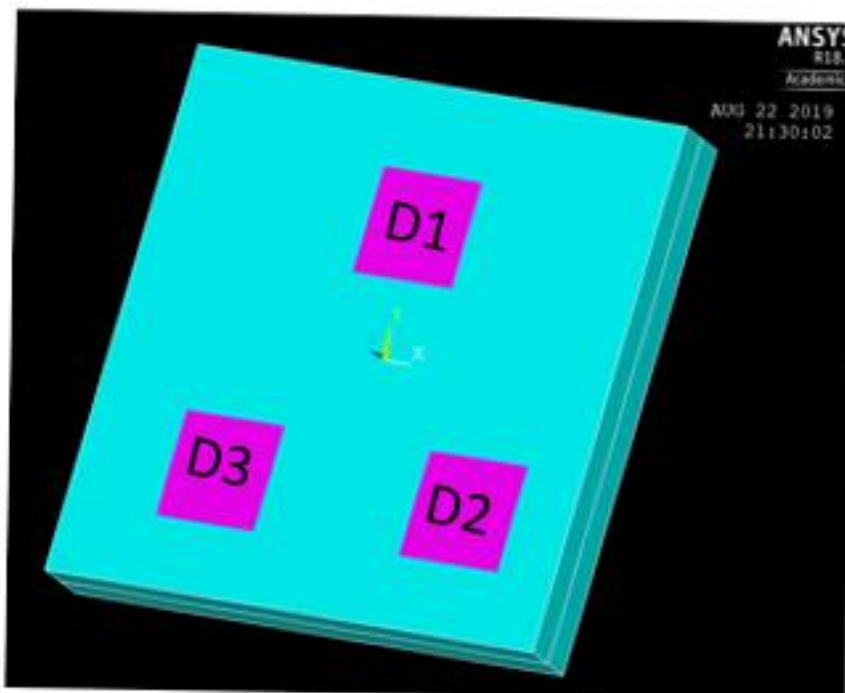
Figure 4-36: FE-model of the two bonded concrete slabs containing three delaminations. ANSYS Mechanical APDL 18.1 (ANSYS 2018).

Table 4-10: Test 02 (IRT). Details of the two concrete slabs & embedded delaminations.

Essentials	Dimensions (mm)	Depths from top (mm)
Concrete Slabs	600x600x40	
Delamiantion-D1 (Severe)	120x120x5	40
Delamiantion-D2 (Intermediate)	120x120x2.5	40
Delamiantion-D3 (Initial)	120x120x1	40

Table 4-11: Test 02 (IRT). Details of input parameters to develop FE-model.

Input parameters	Concrete	Corrugated cardboard
Element type	SOLID278	SHELL 132
Mesh size (mm)	10	.5
Mesh shape	Tetra	Tetra
Density (Kgm^{-3})	2301	45
Thermal conductivity (Wm^{-1}K^{-1})	1.75	.047
Specific heat capacity (JKg^{-1}K^{-1})	880	1700

The interface conditions are of some interest. The contact (CONTA 174) and target (TARGE 170) elements were first defined. The underlying slab was intact compared to the top, (presence of delaminations), therefore, it was taken as the target surface and the top slab as the contact surface. The contact behaviour, '*always-bonded*' was chosen as both slabs were fully-intact elsewhere.

The ambient boundary conditions at the time of test were depicted in FE-analysis. Table 4-12 offers all the necessary information in a synoptic form.

Table 4-12: Test 02 (IRT). Ambient conditions recorded at the time of experiment.

Ambient conditions	
Heat flux (Wm^{-2})	270
Initial Temperature (^{o}C)	30
Ambient temperature (^{o}C)	31
Convective coefficient (Wm^{-2}K^{-1})	26
Time step (s)	1
Total time (s)	1390s

The analysis was executed, and the contour plots + temperature distribution profiles of all voids were recorded for comparisons.

4.7.1 Test 02 IRT. Thermogram and Temperature distribution profile. Comparison between FEA and EXP
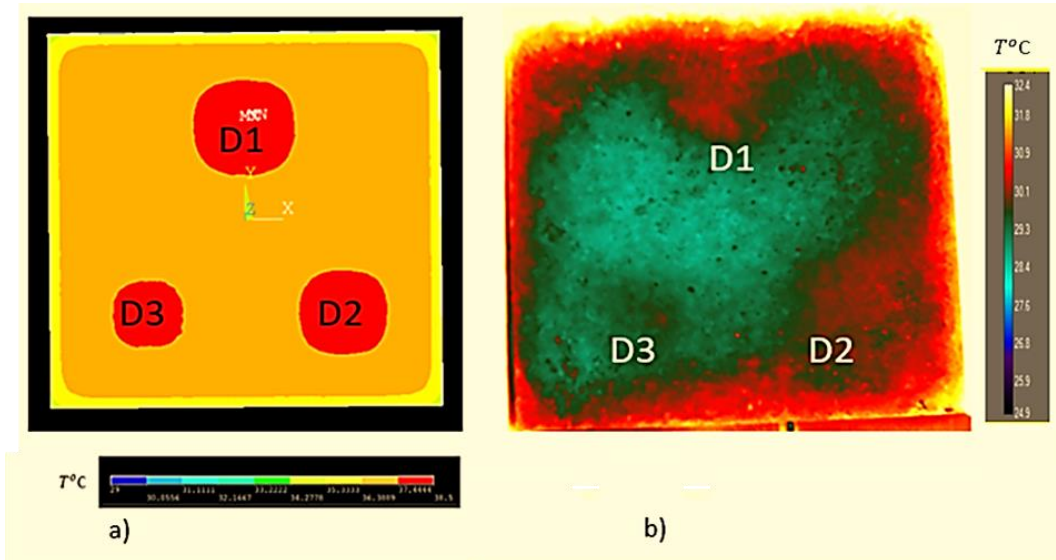
Figure 4-37: (a) Thermal image, captured at 1390s (b) Thermogram recorded at 1390s.
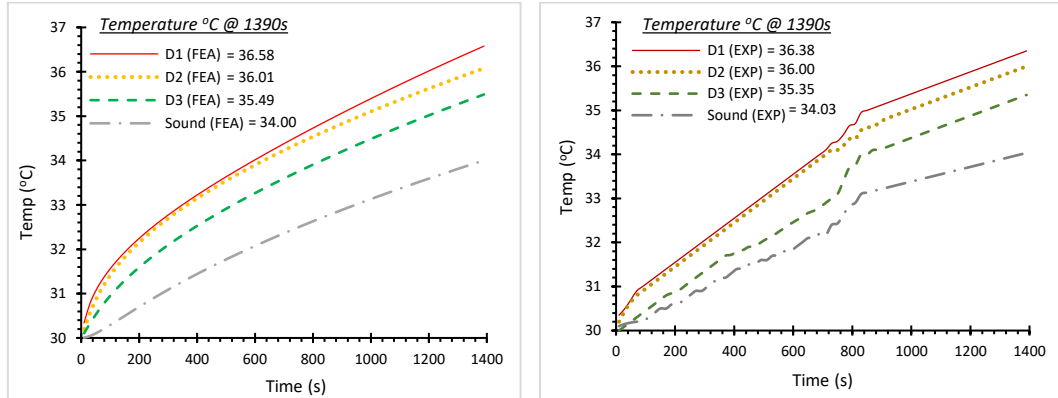
Figure 4-38: Temperature distribution against time, for all delaminations and reference area. Left: FEA. Right: EXP.

All the three delaminations were revealed in the FE-simulated thermal image and were much sharper than the corresponding thermogram (Figure 4-37). However, the 5mm thick delamination, D1 (*Severe*) was relatively more exaggerated in size, and was revealed slightly earlier at 710s than the other two delaminations, which surfaced at

750s. Whereas, in experimental thermogram, all the delaminations appeared at 710s. This slight discrepancy can be due to relatively small thicknesses of the delaminations (D2, D3), resulting in minute thermal contrast that was not displayed initially by the FE-thermal image, however, with time, the defects got sharper. Moreover, 3mm thick delamination, D2 (*Intermediate*), and the 1mm thick delamination, D3 (*Initial*), apparently appeared small in size, also indicating the difficulties of detecting accurately, the thin defects with the increased depth. Please see APPENDIX B for more frames and comparisons.

A comparison of average nodal temperatures (EXP+FEA) were plotted in Figure 4-38, from the thermal image and thermogram, both captured at 1390s (Figure 4-37). It was observed from the FE-temperature profiles, that the D1 (*Severe*), showed the highest temperature rise followed by D2 (*Intermediate*), whose temperature profile was similar and close to D1, for the first 700s and then a clear difference between the temperatures could be observed. The D3 (*Initial*), showed the lower temperature rise among the other delaminations and was evident from the beginning, whereas, the sound region showed the least temperature rise. This was also validated by the corresponding experimentally obtained temperature profiles, to a good accuracy of approx. 99%.

4.7.2 Severe delamination (D1). Thermal Contrast (ΔT) Comparison FEA and EXP
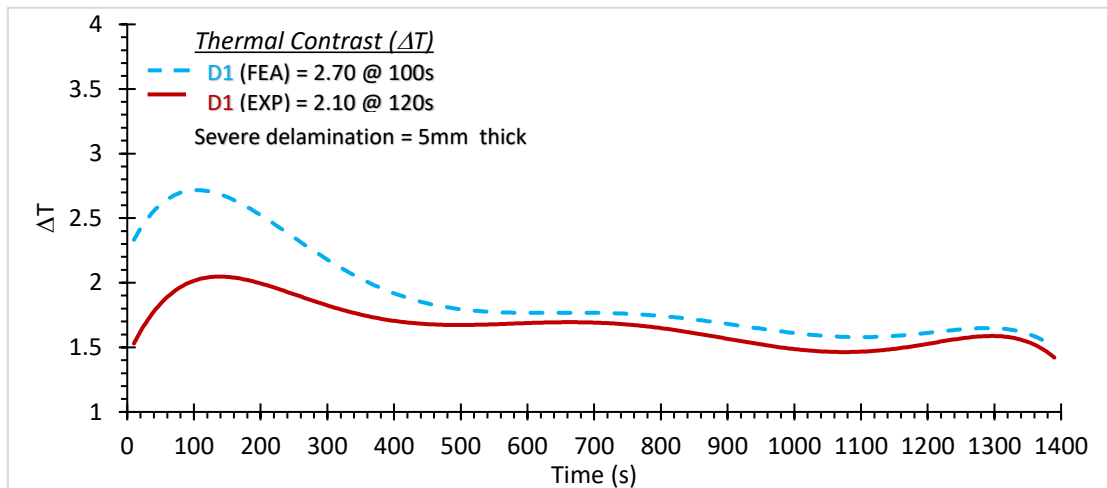
Figure 4-39: Thermal contrast (ΔT) comparison between FEA Vs EXP results for Severe delamination, D1 at 40mm depth.

By plotting the thermal contrasts (ΔT) profile of severe delamination (D1) from the FE-simulation and the experimental testing, a similar pattern (ΔT) was obtained (Figure 4-39). The peak value (ΔT) obtained for severe delamination, D1, in FE-simulation is as follows:

(ΔT)

$D1_{FEA} = 2.70$ @ 100s

$D1_{EXP} = 2.10$ @ 120s

The overall %error came out to be 12 approx. However, initially the error was relatively high. This could be most probably due to the small cloud patches continuously interrupting the sun rays at the beginning of the test. This endorses the findings by Raja et al. (2020) that the weather conditions (shadow, clouds, wind velocity, solar loading) affects the thermal contrast and thermogram display significantly.

4.7.3 Intermediate delamination (D2). Thermal Contrast (ΔT) Comparison FEA and EXP
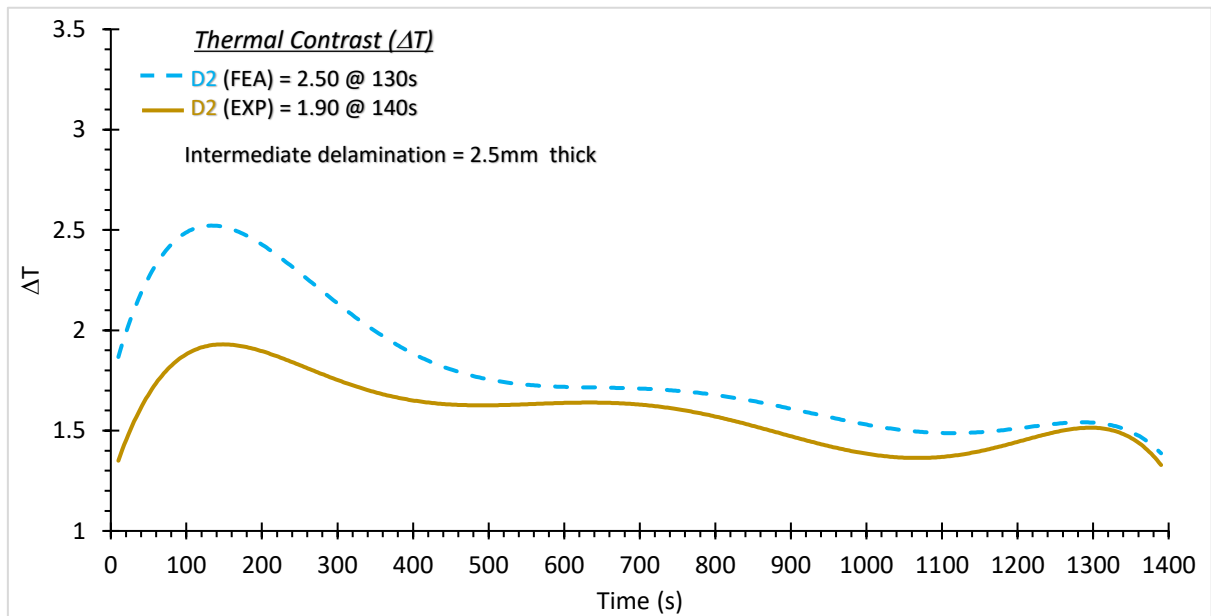
Figure 4-40: Thermal contrast (ΔT) comparison between FEA Vs EXP results for Intermediate delamination, D2 at 40mm depth.

By comparing the FE-simulation and experimentally obtained thermal contrasts (ΔT) plots, it was observed that similar pattern (ΔT) was obtained from both (Figure 4-40). However, the peak value (ΔT) obtained for intermediate delamination, D2, from the FE-simulation is as follows:

(ΔT)

$D2_{FEA}$ = 2.50 @ 130s

$D2_{EXP}$ = 1.90 @ 140s

Again a very close correlation between the two was observed , where the average error% came out to be 12 approx.

4.7.4 *Initial delamination (D3). Thermal Contrast (ΔT) Comparison FEA and EXP*
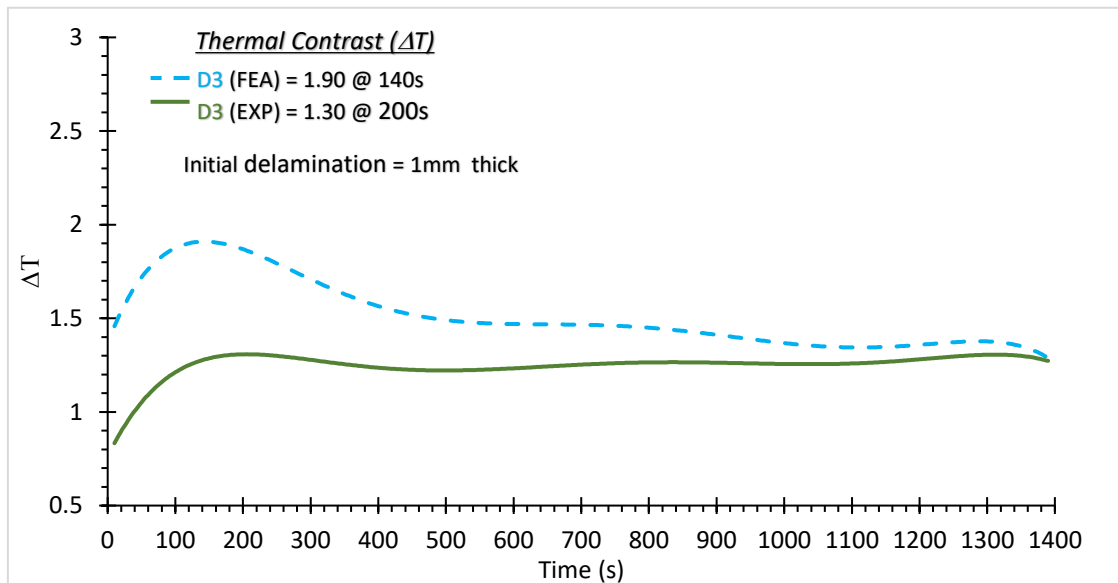
Figure 4-41: Thermal contrast (ΔT) comparison between FEA Vs EXP results for Initial delamination, D3 at 40mm depth.

By comparing the thermal contrasts (ΔT) values obtained from the FE-simulation and experimentally recorded values for initial delamination, D3 (1mm thick), it was observed that similar trends (ΔT) were achieved from the both (Figure 4-41).

The peak value (ΔT) obtained for initial delamination, D3, in FE-simulation is as follows:

(ΔT)

$D3_{FEA} = 1.90$ @ 140s

$D3_{EXP} = 1.30$ @ 200s

An error% of 20 approx. was observed on an average, which was relatively high but overall a good correlation was observed in the trend.

4.7.5 Inferences from FEA and EXP IRT Results Comparison (Test-02)

1. A good correlation was obtained between the two, FEA and EXP results, with a decent accuracy of 99% for all delaminations. However, the estimated ΔT values showed relatively higher %error and on an average it was just below 15%, which is still an acceptable range in transient analysis. The developed FE-model could be used further for parametric and what-if studies.

2. All the three delaminations (D1, D2, D3) were detected in the thermal images and their visibility were much profound than the corresponding thermogram. However, the severe delamination, D1 (5mm thick) was more exaggereated in its appearance, followed by intermediate delamination, D2 (2.5mm thick) and finally the initial delamination, D3 (1mm thick) that showed the downsized appearance. In addition, the severe delamination, D1 appeared at 710s in FEA, similar to the experimental themrogram, whereas, the intermediate (D2) and initial (D3) delaminations, were revealed slightly late at 750s. This slight discrepancy can be due to relatively small thicknesses of the delaminations (D2, D3), resulting in minute thermal contrast that was not tracked initially by the FE-thermal image, however, with time, the defects got sharper.

3. The trend of thermal contrasts obtained from the FE-simulation was similar to the ones obtained in experimental testing: 'a sudden rise, a peak, a gradual drop and a steady-state'.

4. A severe delamination, D1 showed the highest ΔT (2.70) value followed by intermediate delamination, D2 (2.50) and the initial delamination, D3 (1.90) showed the least ΔT values. These trends were also validated by the experimental tests.

5. A severe delamination, D1 took the least time (100s) to reach its peak ΔT value followed by intermediate delamination, D2 (130s) and the initial delamination, D3 took the longest (140s) to reach its peak ΔT. Similar trend was observed in experimental results, and was also endorsed by the Test 01, where thick voids took less time to reach their peaks (ΔT) compared to the corresponding thin voids.

6. It can be concluded that the 1mm thick delamination are hard to detect visually and based on their very small thermal contrast values, when compared to the 2.5mm thick or 5mm thick delaminations. Hence, there are more uncertainties associated with such defects and therefore, IRT alone might not be sufficient to examine them accurately. In such cases, IHT will be required to do the further evaluations and complement the former technique.

4.8   Summary

This chapter discussed the experimental and theoretical routes of 'Infrared thermography method', and its use as a NDT&E technique for '*exposing*' and '*quantifying*' the flaws in specially designed concrete slabs.

After underlining the basics of IRT (EXP+FEA) and the factors affecting the IRT method, the laboratory scaled tests were outlined. A preliminary test (a single cast concrete slab with 6-voids) followed by its numerical model, and the key findings from both (EXP+FEA) were highlighted. It was found that 'thickness and depth' of the voids have significant effect on the obtained thermograms and thermal contrast values. The shallow-thick void (10mm, 5mm), showed the highest thermal contrast value and thermogram display, however, as the depth was increased and thickness was reduced, the detection as well as the assessment became difficult. This uncertainty for deeper and thinner voids (30mm, 3mm) was also obvious in the corresponding FE-model.

After detecting and quantifying the defects (voids) in the preliminary tests, the essential test was carried out. This time, a Two-slabs stacked system including 3-delaminations (voids), was brought under scrutiny. The '*evolution*' of delamination (initial, intermediate and severe) at a constant depth of 40mm was analysed and assessed by the IRT method, also aided by its corresponding FE-model. However, again it was observed that as the thickness was reduced, in the case of initial delamination (1mm), the uncertainty was increased, and it was recommended to carry out IH-Tests for such 'uncertain' defects.

Chapter 5 - Experimental and Numerical Study of Modal Analysis

5.1 Introduction

This chapter is divided into two main sections and their sub-sections as demonstrated in Synoptic Form (Figure 5-1)
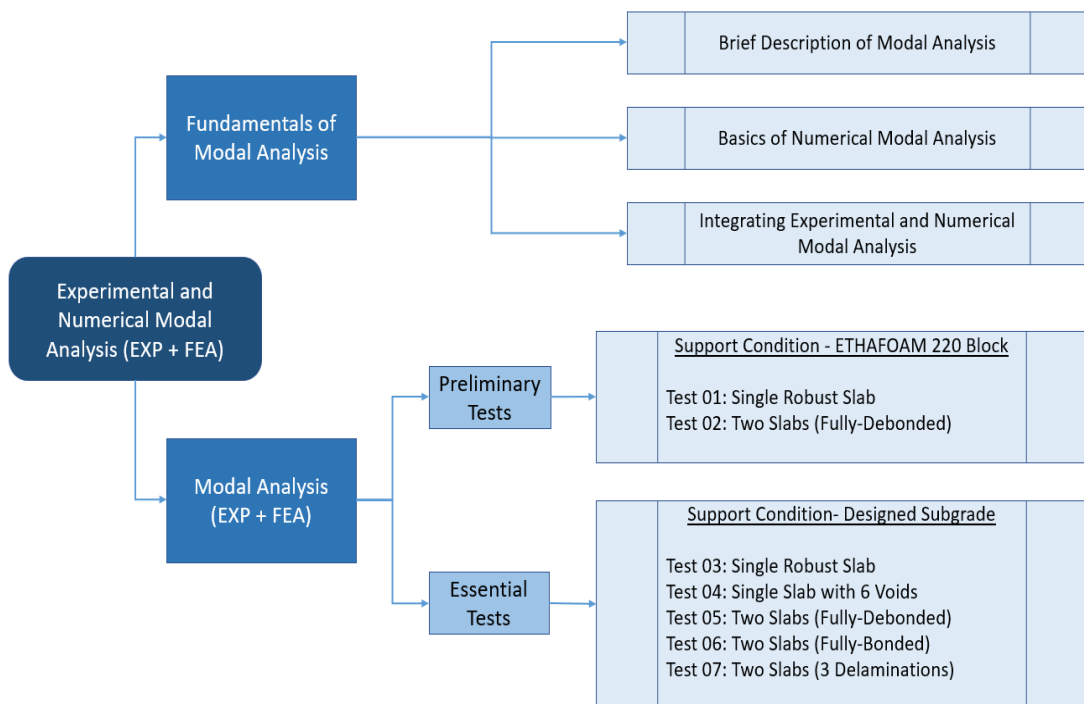
Figure 5-1: Synoptic Plan for Chapter 5.

5.2 Fundamentals of Modal Analysis

Modal analysis (MA) is a process, whereby the inherent dynamic characteristics of a structure are described, while estimating its dynamic properties such as Natural frequency, Mode-shape and Damping ratio, and using them to formulate the mathematical model for its dynamic behaviour (Avitabile 2001, Ewins 2000 and He and

Fu 2001). This mathematical model is referred to as the modal model of the system, whereas, the information provided regarding the dynamic characteristics of the system is known as its modal data (He and Fu 2001: 02).

Ewins (2000: 20), has classified the structure's dynamic characteristics into three related stages. These stages, when put into context, pave the way for what will be called the 'theoretical route' for vibration analysis. The three stages through which a typical vibration analysis progresses are illustrated in Figure 5-2.
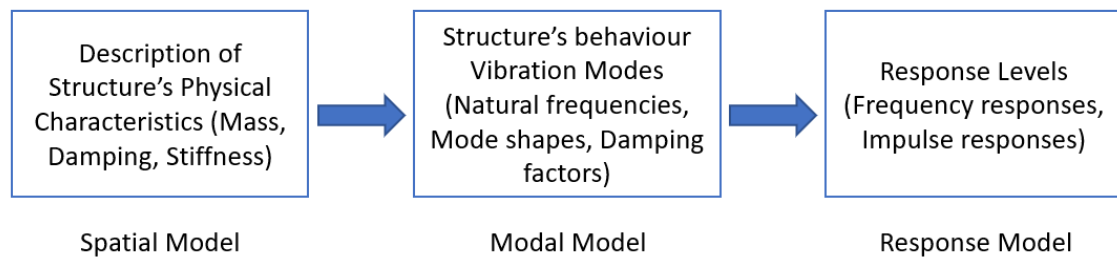
Figure 5-2: Theoretical route for vibration analysis (Ewins 2000).
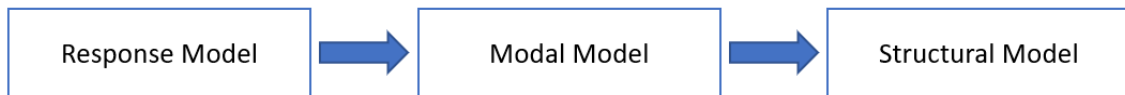
Figure 5-3: Experimental route of Modal Analysis (Ewins 2000).

The experimental route for modal analysis is in the reverse direction (Figure 5-3), where on the input excitation force (via impact hammer, or shaker), the response is recorded (usually by accelerometers). The latter will be converted into FRF's (via data acquisition software), and the estimation of natural frequencies, mode shapes and damping ratios will be carried out, which could be useful in predicting the structural properties.

5.2.1 Experimental Modal Analysis (EMA) and Basic Equipment

Modal testing is an experimental technique, applied to estimate the modal model of a linear time-invariant vibratory system. The theoretical basis of this technique is centred upon establishing a very useful relationship between the vibrational response at some location on the structure under test, and excitation at the same or different location, as a function of excitation frequency. This useful relationship is often a complex mathematical transfer function and is known as frequency response function or FRF in short. Combinations of excitation and responses at various locations result in a complete set of frequency response functions (FRFs). This set is collectively represented by FRF matrix of the system, which is usually symmetric, hence, reflecting the structural reciprocity of the system.

In experimental modal testing, there are three main components as the basic requirements for each test setup. These are excitation source, response source and data acquisition system.

The Excitation Source

It is known that to estimate the dynamic characteristics of structures, they have to be excited and the response signal is measured. For excitation, there are two non-destructive instruments, namely instrumented impact hammer and electromagnetic vibration shaker (Figure 5-4). Due to its availability, relatively low cost and its accessibility to the various points of measurements, impact hammer is more popular and is also adopted for this study. Moreover, it can be operated by one person only, by easily roving hammer to the various points on the structure under test. In addition to these merits, impact hammer is also fast to use as compared to its counterpart and has got various tips, ranging from softer rubber tip to the stiffest steel tip. These tips basically control the frequency content under study. It is understood that the harder the tip, the shorter the pulse duration and higher the frequency content. However for massive structures, more energy is required to excite the structure in addition to the

dictation of varying input force, which cannot be consistently provided by the hammer, so the shaker is preferable in such circumstances.

Figure 5-4: Impact Hammer, Piezoelectric triaxle accelerometer and Data logger. A Shaker, as an excitation source (PCB 2011).

The Response Source

For response measurement, any of the motion transducers for measuring displacement, velocity and acceleration can be used. However, accelerometer is a generally used transducer for measuring the vibrational response signal of the structure under test in the form of acceleration response time histories. In this study also, a uniaxial piezoelectric accelerometer is adopted to acquire the response data (Figure 5-4).

The Data Acquisition System

The data acquisition system is the most important part of modal testing, since all measurements as a result of the structure's excitation, are recorded in the data acquisition system as time histories. This is further converted into frequency domain by

the Fast Fourier Transform (FFT) and is displayed in the form of frequency response functions (FRFs).

Conventionally, the data acquisition system has three main units, namely, signal amplification unit, data acquisition unit (Figure 5-4) and personal computer. These units can come separately and are operated via a software interface. The data loggers are connected to the PC via cables and are operated by their software. Excitation source (impact hammer/ shaker) is connected to one of the input channels, whereas, the response source (accelerometer) is connected to one of the output channels of the data logger. For instance in this study, the 4 channel data logger used, had one channel dedicated to the hammer (also known as the *reference channel*) and the second channel was connected to the uniaxial accelerometer. This data logger also had the capacity to connect to a Shaker.

Data Processing

After acquiring the data in time histories, signal processing is carried out on the acquired data. Briefly, the first step in data processing for the transient signal is to employ the autocorrelation function, based on averaging the time signal, to convert the transient random signal into a new function of time, which is then ready for the '*Fourier Transformation*'. Power spectral densities (PSD), (normalising the amplitudes of the signals) is applied. Finally, the coherence functions and the frequency response functions (FRFs) along with their components (magnitude, phase, real and imaginary parts) are calculated and plotted.

Modal parameters estimation is the next step after calculating the FRFs, which is the final stage of Experimental Modal Analysis (EMA).

i.   Fourier Transform (FT)

The application of Fourier Transform is very established in signal processing, and it is a powerful technique to represent complex time signals in frequency domain, which is relatively easier to interpret (Maia and Silva 1997: 13). The time data is recorded, and it provides very useful information but since the data is too much, and therefore, complicated to interpret in the time domain, a frequency domain is conveniently used for interpreting the same data (Figure 5-5). These days either Discrete Fourier Transform or Fast Fourier Transform (FFT) is being deployed, the latter is a much quicker transform technique, and is derived from Discrete Fourier Transform (DFT). However, in this study DFT was deployed as it was inbuilt in the adopted 'modal-testing software', LMS Test.Lab 17 (LMS 2017).
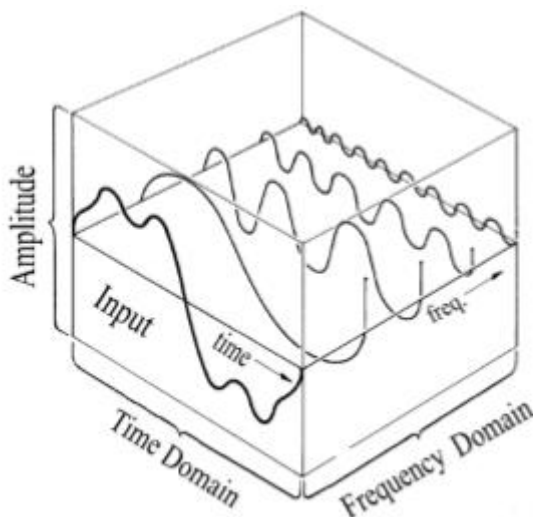
Figure 5-5: Discrete Fourier Transform (Maia and Silva 1997).

Briefly in DFT, the analogue (continuous) time signal is first converted into the digital (discrete) time signal via A/D converter and by deploying DFT, it is further converted into discrete frequency signals as illustrated in Figure 5-5 (Maia and Silva 1997).

ii.   Frequency Response Function (FRF) and its Components

The exercise of modal testing involves the measurement of frequency response functions (FRFs) or impulse responses of the structure under test. For a linear system, the excitation and response signals obtained initially in time domain are fed into a spectrum analyser that after transforming them into frequency domain via FFT eventually computes and displays the measured input-output signals in the form of FRFs (Figure 5-6). The measured FRFs contain all the essential information of the inherent dynamic properties of the structure under test, which is extracted in the form of modal parameters such as natural frequencies, their associated mode shapes and damping ratios to characterise the system. Therefore, the accuracy of the measurement of FRFs is quite substantial to the success of modal test, though theoretically, it is only dictated by the system (He and Fu 2001: 80).
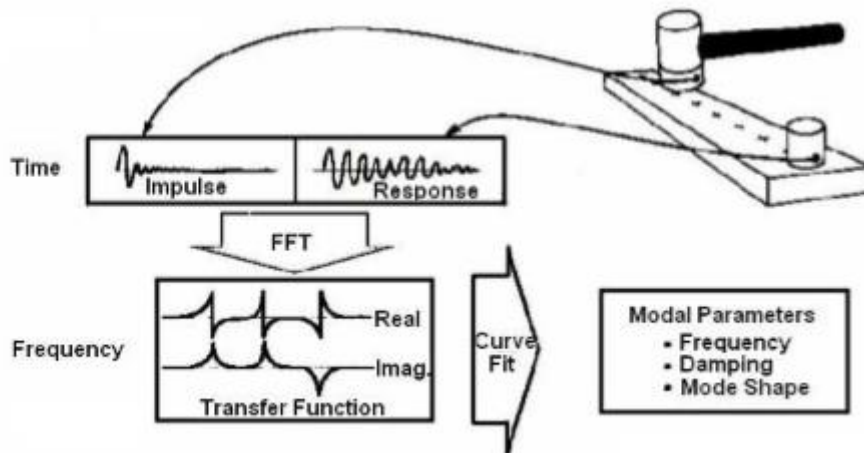
Figure 5-6: Transfer function (Schwarz and Richardson 1999).

For a linear system, the input-output and FRF relationship, can be expressed mathematically by (Ewins 2000, Fe and He 2001 and Maia and Silva 1997).

$$H(\omega) = \frac{X(\omega)}{F(\omega)}$$
(5.1)

Where,

$X(\omega)$ = Output response signal in frequency domain

$F(\omega)$ = Input excitation signal in frequency domain

$H(\omega)$ = Frequency Response Function (FRF)

In real life modal testing, the excitation and response signals can be made of random signals (white noise etc.), or can be corrupted by the random interference, which in turn cannot be treated as periodic, or non-periodic signals, and therefore, Fourier Transform cannot be applied at the first place. To treat such noisy signals, an 'auto-correlation' function is applied in order to identify the periodicity in the observed physical signal. In other words, it normalizes the signals and converts them into a new time domain function, which is a real and even value function (only magnitude and no phase) and can now be Fourier Transformed.

After the Fourier Transformation, an important function called 'Auto-Spectral Density' or 'Power Spectral Density' (PSD) is applied on the signal. A Power Spectral Density (PSD) is the measure of the signal's strength across frequency spectrum, and it is used to normalise the amplitude by the frequency resolution. PSD has the amplitude units of g^2/Hz.

The representation of the FRF can be done in two common coordinate systems (Figure 5-7), rectangular coordinates (real part vs frequency and imaginary part vs frequency) and polar coordinate system (amplitude vs frequency, and phase vs frequency). In the rectangular coordinate representation, the imaginary part shows maximum at resonance, whereas the real part is zero. In the polar coordinate system, at resonance, the magnitude reaches the maximum, while the phase lag approaches 90°. These characteristics of the FRFs enables the modal parameter identification of the system.
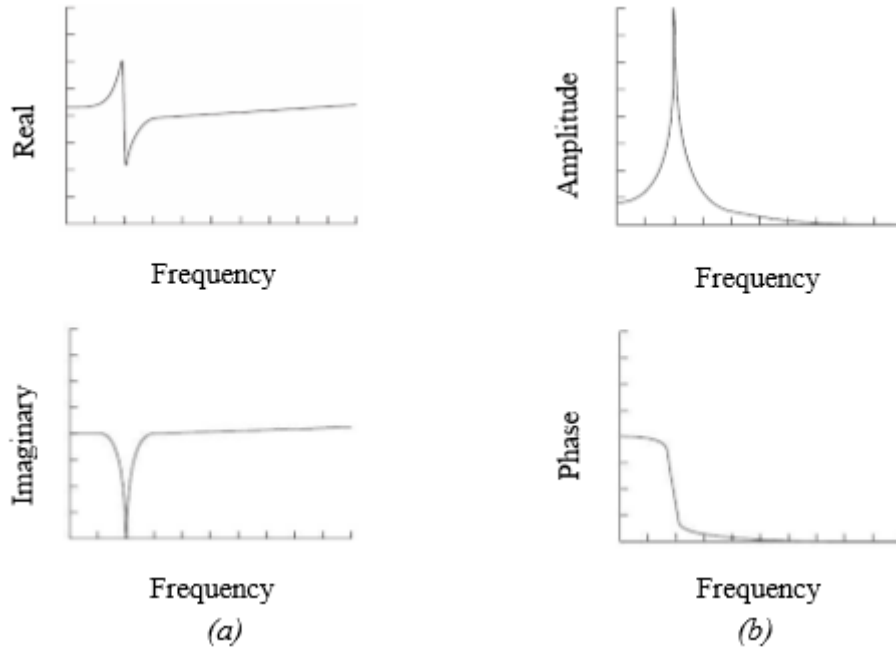
Figure 5-7: FRF representation in (a) rectangular and (b) polar coordinates for a single degree of freedom system (Dackermann 2010).

For a single degree of freedom system (SDOF), the resulting transfer function in its simplest form, can be expressed in Polar coordinates as per Equation (5.2) & (5.3) and in rectangular coordinates as depicted in Figure 5-8.

$$\frac{X(\omega)}{F(\omega)} = \left[\frac{1}{m}\right]\left[\frac{1}{\sqrt{(\omega_n{}^2-\omega^2)^2+(2\xi\omega\omega_n)^2}}\right] \tag{5.2}$$

$$\emptyset = arctan\left[\frac{2\xi\omega\omega_n}{\omega_n{}^2-\omega^2}\right] \tag{5.3}$$

Where: ω_n = undamped angular natural frequency of the system (rad/s), ω = excitation (input) frequency and ξ = damping ratio
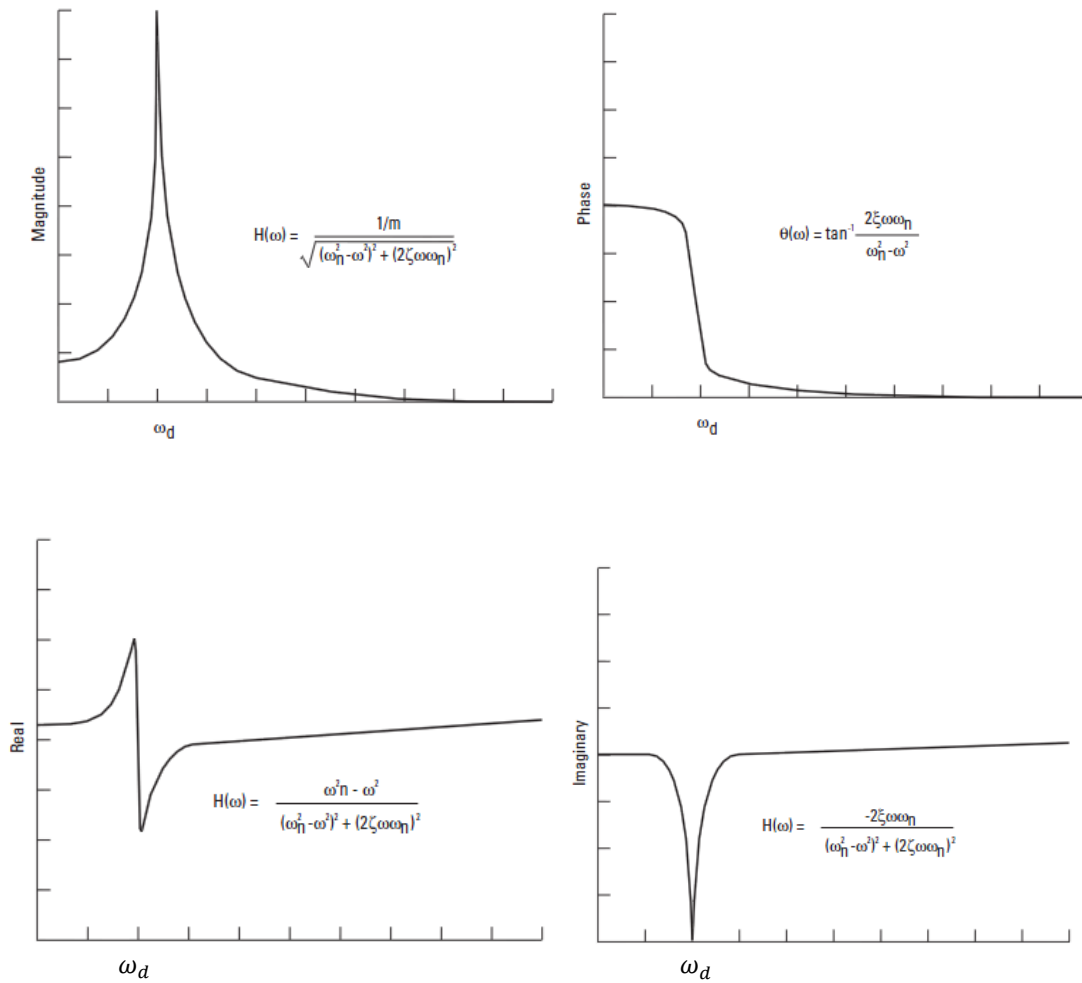
Figure 5-8: FRF response of SDOF by Polar coordinates (top row) and Rectangular coordinates (bottom row) (Agilent Technologies 2000).

$$H(\omega) = \frac{1/m}{\sqrt{(\omega_n^2 - \omega^2)^2 + (2\zeta\omega\omega_n)^2}}$$

$$\theta(\omega) = \tan^{-1}\frac{2\xi\omega\omega_n}{\omega_n^2 - \omega^2}$$

$$H(\omega) = \frac{\omega_n^2 - \omega^2}{(\omega_n^2 - \omega^2)^2 + (2\zeta\omega\omega_n)^2}$$

$$H(\omega) = \frac{-2\xi\omega\omega_n}{(\omega_n^2 - \omega^2)^2 + (2\zeta\omega\omega_n)^2}$$

Modal Parameters Estimation

Theoretical modal analysis deals with the eigenvalue problem, whereas the experimental modal analysis is based on curve-fitting theoretical expressions to the actual measured data as illustrated in Figure 5-9.
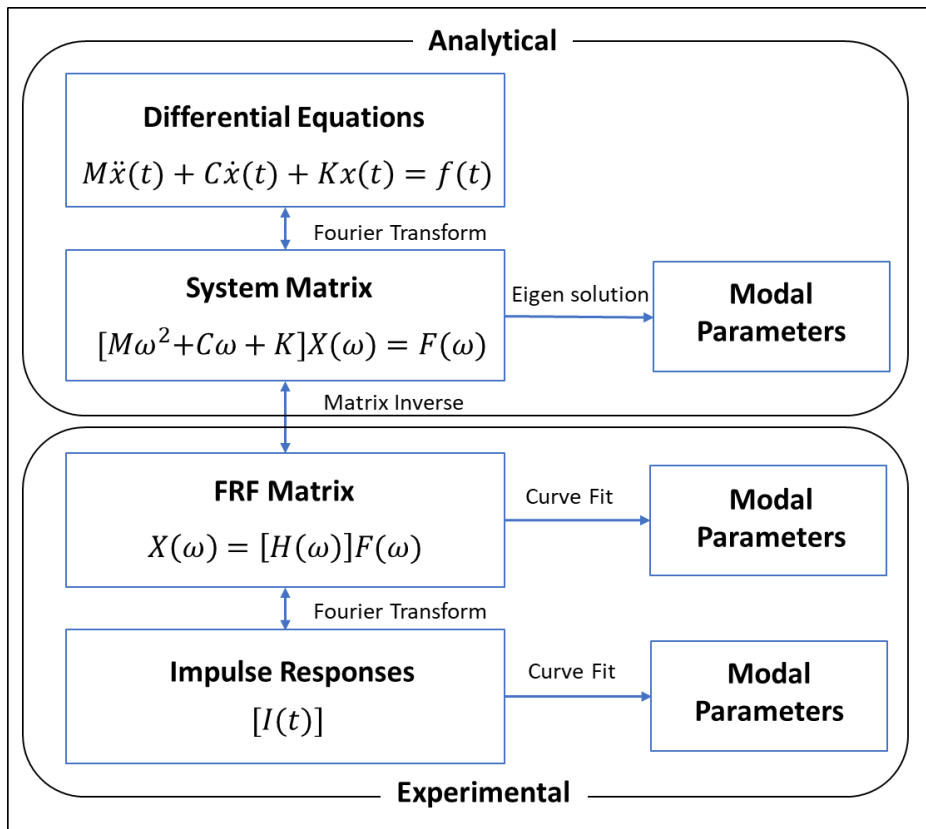
Figure 5-9: Modal parameters estimation techniques (Schwarz and Richardson 1999).

In experimental modal analysis (EMA), the modal parameters are mainly extracted by means of FRFs and curve fitting techniques, which is matching of mathematical model to the set of acquired data points.

Natural frequencies are estimated by picking the highest amplitude or peaks in the FRF set, whereas, the width of the resonance frequencies are used for estimating damping ratios for each mode. They are identified by a very simple and quick method known as 'half-power bandwidth' (He and Fu 2001).

Mode shapes of a structural system can be extracted from the obtained FRF by means of a simplistic approach, commonly referred as *Peak Picking* or *Quadrature Picking*, based on the assumption that all the response is dominated by the single mode (Agilent Technologies 2000).

Two Possible Approaches of Impact Hammer Testing

It is possible to get the complete mode shapes by completing just one row or column in the FRF matrix (reciprocity). In practice, there are two possible approaches of getting the complete mode shapes, when modal test is carried out via Impact hammer.

One is by moving the accelerometer to record readings at all the nodes, while exciting a structure at the fixed node (via Impact hammer), called *roving accelerometer test*.

The second approach, also adopted in this study, is by keeping the accelerometer fixed, therefore, measuring the response in one direction at one fixed node and exciting the structure at all the nodes separately in all directions as (via Impact hammer), called *roving hammer test*. Incomplete information can yield incomplete mode shapes, therefore, it is important to make sure there is a complete minimum set of FRFs measurements in order to get the complete mode shapes (Agilent Technologies 2000).

The table below shows some drawbacks and benefits of each approach (Table 5-1).

Table 5-1: Benefits and Drawbacks of roving hammer test and roving accelerometer test.

Two roving Approaches	Benefits	Drawbacks
Roving Hammer Test	• More convenient in most of the cases. • Faster • Accurate when proper protocols followed.	• All of the points in most structures cannot be excited in all the three directions.
Roving Tri-axial Accelerometer Test	• 3D motion at all test points can be measured easily.	• Time consuming due to removing and mounting accelerometer at all points. • Can cause inaccuracy in measurements due to their effective weight, especially when roving over light specimens.

5.2.2 Finite Element (FE) Modal Analysis

The basic governing equation of theoretical modal analysis, is based on the general equation of motion for a 'Multi-Degree-of-Freedom' (MDOF) systems.

The objective of modal analysis is to determine the natural frequency, damping ratios and each geometrical mode shape of several vibration modes until, the system behaviour is adequately characterised over some frequency band of interests. Modal analysis is the linear analysis. Even if the system is somewhat non-linear, the best linear approximation to the actual system is estimated. Each mode of vibration can be modelled at each node in the structure as a single degree of freedom resonator, possessing a certain natural frequency and some damping ratio, which are common to all nodes on the structure.

The basic governing equation of motion for the MDOF system (undamped) with N degrees of freedom, can be expressed in matrix form as follows (Ewins 2000):

$$[M]\{\ddot{x}(t)\} + [K]\{x(t)\} = \{f(t)\} \tag{5.4}$$

Where,

    M = Mass Matrix (N x N)
    K = Stiffness Matrix (N x N)
    $x(t)$ = Displacement vector (N x 1)
    $\ddot{x}$(t) = Acceleration vector (N x 1)
    $f(t)$ = Force vector (N x 1)

Since in theoretical modal analysis, the free vibration response of the system, with the initial excitation is considered. Hence, no external force is considered to determine the natural modes of the system.

$$\{f(t)\} = \{0\} \tag{5.5}$$

By assuming the solution of the form exists:

$$\{x(t)\} = \{X\}e^{i\omega_n t} \tag{5.6}$$

Where, $\{X\}$ is an Nx1 vector of time independent amplitudes.

The trial solution (5.6) leads to the condition, which must be satisfied for the solution to exist i.e.:

$$([K] - \omega_n^2[M])\{X\}e^{i\omega_n t} = \{0\} \tag{5.7}$$

For which, only the non-trivial solutions satisfies the equation:

$$det\left|[K] - \omega_n^2[M]\right| = 0 \tag{5.8}$$

The solution of the equation (5.8) consists of an Eigen problem with N values of ω_n^2, also known as the undamped system's natural frequencies. Substituting the values of ω_n^2 back into equation (5.6) will yield a set of relative values for $\{X\}$, i.e. $\{\psi\}$, also known as mode shapes, for their corresponding natural frequencies.

Hence, the complete solution of the Eigen problem can be expressed in two N x N matrices, so called the Eigen-matrices:

$$[\ddots \bar{\omega}_r^2 \ddots] = \begin{bmatrix} \omega_1^2 & \cdots & 0 \\ \vdots & \ddots & \vdots \\ 0 & \cdots & \omega_N^2 \end{bmatrix} ; \quad [\psi] = [\{\psi_1\}\{\psi_2\} \dots \{\psi_N\}]$$

Where, $\bar{\omega}_r^2$ is the rth eigenvalue or *squared undamped natural frequency*, and $\{\psi\}_r$ is the corresponding Eigen vector, also known as *mode shape.*

Generally, in many engineering applications, the damping effects are ignored, and the system matrices are also symmetric i.e. the transpose of the matrix is equal to itself. Since the damping is a complex parameter, which is complicated to characterise, due to its very indeterministic nature. Therefore, it is generally ignored in modal analysis of static systems in particular. However, in the systems where the damping effects are unneglectable (especially in non-linear analysis, rotating systems and damped systems with symmetric or unsymmetrical matrices) the damping effects are considered to their approximation (Ewins 2000).

5.2.3 Integrating Experimental & Numerical Modal Analyses

In modal analysis, FE-model updating is an established procedure, following the experimental one. That is, numerical modelling is carried out in conjunction with the experimental tests, where the FE-model is undergoing continuous updating, until acceptable correlation between the two is achieved. This is also sometimes known as 'FE-model calibration' although the updating procedure goes significantly beyond calibration.

The purpose of calibration (and in part, that of updating) is to provide essential information to the numerical models (similar material properties, boundary conditions, etc.) and use them for analyses along with the experimental results and therefore, eventually, can replace the repetitive and complex experimental tests, and save time and cost. The results of the modal analysis should be used as input to more detailed and demanding (complex) type of dynamics analyses such as Transient Dynamic analysis, Harmonic Analysis, Random Vibration analysis in an effort to use the FEM as an accurate predicting tool.

The updating procedure is based primarily on the sensitivity of the selected physical parameters, so that the correlation between the target values and the corresponding simulated results improve. The procedure is gradual, and the correlation between the experimental results and predicted results (FE-results) improve, as the model becomes "tuned".

Figure 5-10 summarizes the updating method in the form of symbolic-flowchart.
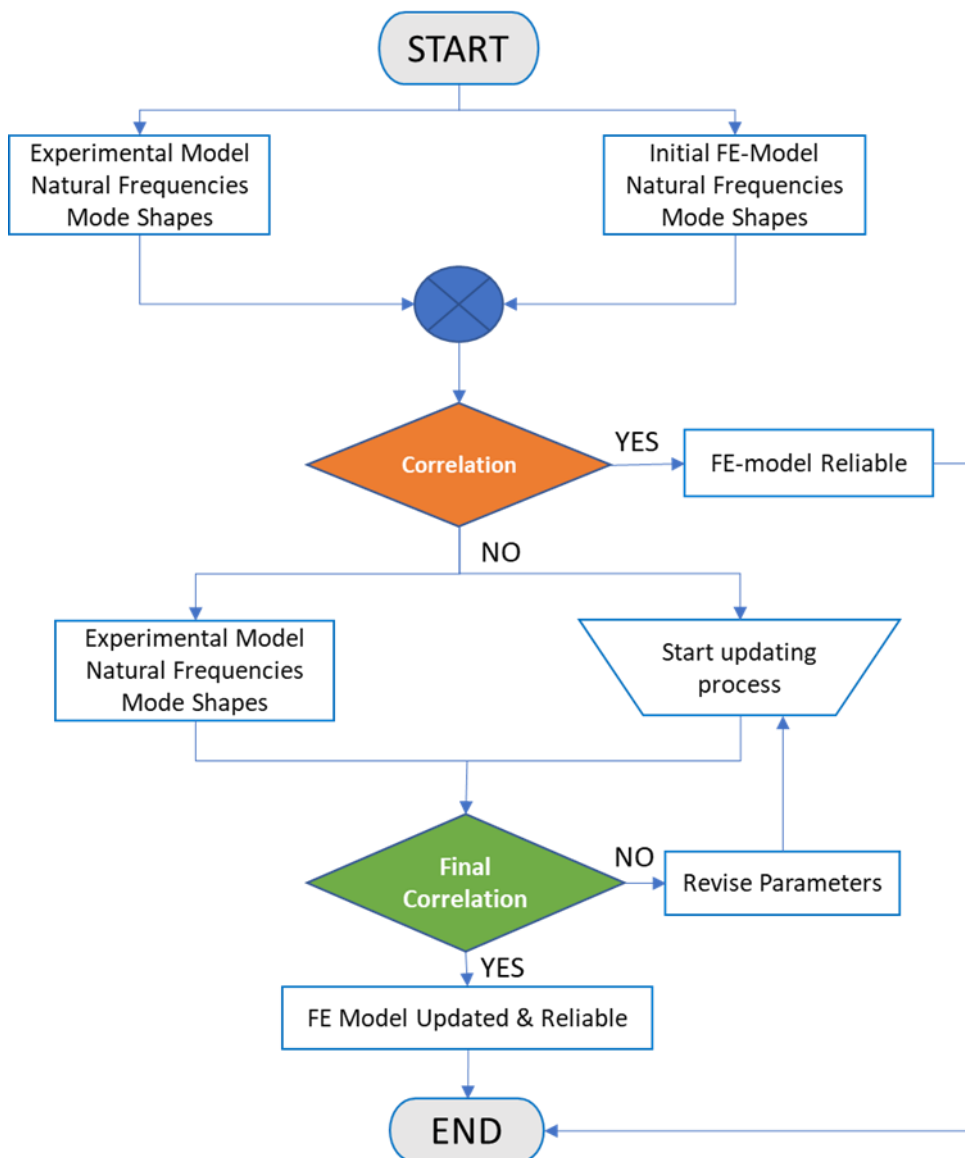
Figure 5-10: Synoptic procedure for FE-model updating.

The sequence of steps followed and the selection of physical parameters in FE-model updating could be tailored based on the mode of application and analyst decision. However, the basic procedure, also adopted in this study is as follow:

1-Initial FE-model: First, an unrefined model, or an initial FE-model is created. This model is typically used to capture the elementary dynamic response of the system, and as the basis for similar tests to compare. This is achieved by simply accurately modelling the stiffness and mass components of the structure as accurately as possible (Sanayei and Sipple 2014). For lumped mass modelling, generally considered in impact hammer testing, a model refinement is carried out by subdividing the mesh size until there is no longer variation in the model response over the frequency bandwidth. This model refinement suggests the adequacy of the mesh and mass distribution.

According to Karadelis (2012), it is also possible that the change in final parameters do not allow for a physical interpretation. That means, these could be just simple numerical substitution, for reducing the deviations between the experimental and numerical results. Whether the latter are physically accepted or rejected, highly depends on the mode of application of the model. For instance, a disproportionate increase in the thickness of the shell elements, might influence the static analyses results, however, has no effect on the modal analysis (Karadelis 2012). Therefore, it is left onto the analyst to decide and justify during the manual updating process, whether the resulting FE-model is realistic and acceptable, or not.

2- Material Properties (First update): According to Kwak and Filippou (1990) and Sherif and Dilger (2006), FEA overestimates stiffness. Karadelis (2012), has attributed it to the material properties, the stiffness variation in different directions and the interaction compatibility issues between two or more materials. Since stiffness is directly related to the square of natural frequencies, an over-estimation of the natural frequencies is expected. Therefore, the first update is based on the variation of the material parameters. The starting point for these variations are based on the specifications available for the given specimen. For instance, if it is made in the

laboratory as per certain standards (BS/ISO), the density and Young's modulus can be estimated. On the contrary, if the specimen is taken from the manufacturer, these physical and mechanical properties can be found on the catalogue provided. This makes the first update easier, and by slightly changing (increasing/decreasing) the estimated/provided values of Young's Modulus and the density in the FE-model (materials), the results can approach the measured experimental response. However, deviations and errors are still expected (and are present) at this stage but noticeable improvement can be observed if the right values are taken.

3-Inclusion of defects/ voids (Second update): This step is only taken if the test specimen has a defect/void. If the specimen is built with "*deliberate*" defects/voids, it is easier to model them, since, their positions and size is known. This is the case for this study as well, where, for FE-model development purposes, the voids/delaminations are deliberately created in the real specimens and therefore, their positioning and sizes are known.

Once the defects are modelled geometrically, the right element type, mesh shape and size are selected, based on mesh compatibility for the present voids and the specimen. It is expected that with the right design of the defects/voids, the overall matching between experimental and numerical results will improve.

3-Support Stiffness (Third update): Accurate simulation of boundary conditions or support conditions, play a vital role in the accuracy of the FE-model. As the FE-model is modified, the support conditions also need reviewing. This would include the selection of the correct contact (stiffness) elements used at interface between the specimen and its support, as well as restraining certain degrees of freedom.

The latter is directly influenced by the experimental setup and the type of support condition considered. However, sometimes the whole support conditions are not modelled, based on the required analysis. As they could complicate the procedure and would necessitate more information for modelling the complex support structure, which

194

might not be available easily. Therefore, in such cases, their effect or their influence on the overall analysis can be taken into an account, by carefully incorporating the stiffness elements and degrees of freedom. However, the accurate selection and justification of these parameters depend on the analyst's level of understanding of the problem, and also on the requirement of the analysis (This tactic is also applied in this study, while taking into an account the effect of Subgrade on the specimen, rather modelling the whole subgrade as a support condition, which was not only complex but also not a necessity of the analysis. Details on Pg: 224-225). Once, this is done, it is very much expected to observe close results with the corresponding measured ones.

4-Solver (Fourth update): Solver selection could be revised in the updating procedure, as the overall system (FE-model) is getting into final shape. The final tuning and the accuracy of the FE-model is influenced by the selection of solver type. Its selection depends on the complexity of problem dealing with, and also on the required output. In ANSYS, variety of solution techniques are available for the user. For small-large, symmetrical problem, ANSYS recommends the Block Lanczos eigenvalue extraction method (ANSYS 2018). This is also adopted in this study, (Details available on Pg: 209-210). Briefly, it uses the sparse matrix solver, and is especially powerful method, to extract the eigenvalues (natural frequencies) for the desired part in the eigenvalue spectrum of the system. In addition, it also reduces significantly the computational time of the simulation and adds accuracy to the solution. Another solver that ANSYS recommends for modal analysis is the PCG Lanczos solver but it is recommended for large systems only (ANSYS 2018). However, the selection of the solver depends on the type of system under consideration, its size, complexity and the bandwidth of natural frequencies, the analyst interested in. This in essence, further improves the accuracy of the final results in comparison to the measure ones, and overall it helps in fine-tuning the FE-model.

It is important to mention that these are the basic guidelines/procedure, which are also adopted in this study. The overall FE-modelling and updating has been carried out throughout the chapter, as the experiments were progressed.

5.3 Processing & Analysis of Experimental & Numerical Modal Tests & Results

The central aim of these tests was to replicate, by scaling down in the laboratory, a number of different types of delaminations (flaw bonds) otherwise met in actual road and airport pavement sites. The plan for the series of Preliminary and Essential IHT tests is illustrated in Figure 5-11.
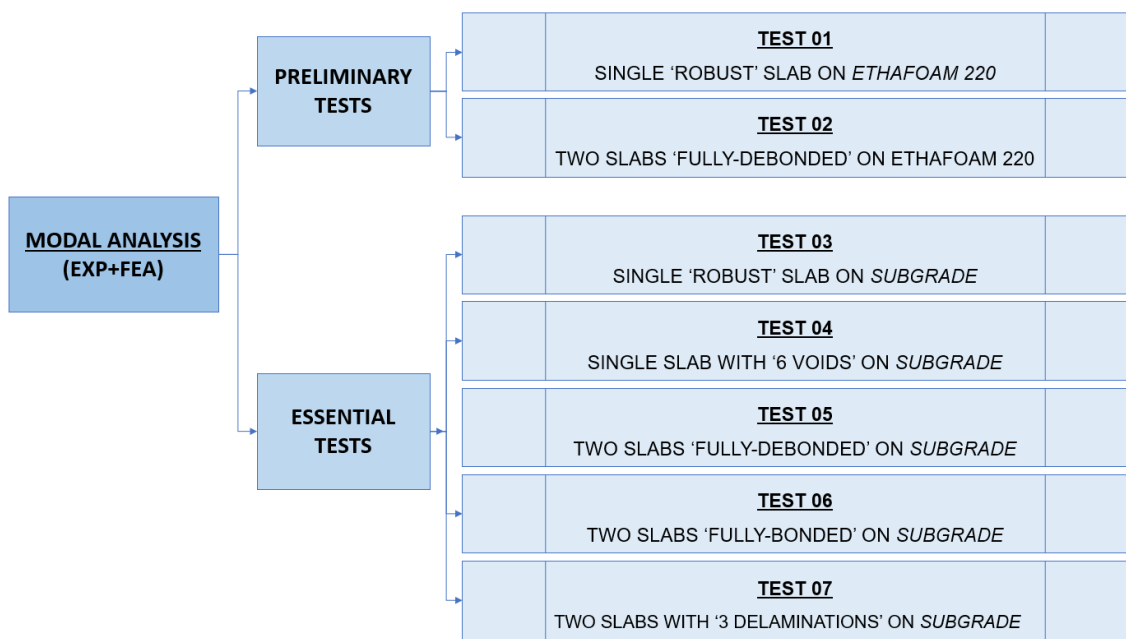
Figure 5-11: Schematic plan of IH-Tests.

5.3.1 *Preliminary Tests (Dynamic Properties of control specimens)*

Two Preliminary Tests were planned and carried out prior to the Essential (main) tests. The reason was twofold: First, to develop a hands-on experience with IHT technique. Second, to start with the simplest possible arrangements (as close as possible to "all-free" support conditions), determine the dynamic behaviour and properties of each slab system (Test 01), and relate the latter to the condition of the bond between them (Test 02).

Concrete slabs with dimensions 600x600x40mm were cast for the IH-tests, keeping in mind that the top concrete overlay is 40 to 50mm thick in real rigid pavements. Their physical properties were estimated via other non-destructive testing methods like the Rebound Hammer and Ultra-sonic Pulse Velocity. In addition concrete cubes were prepared as samples of same mix and by crushing them, their compressive strengths were recorded and their Young's Modulus were estimated. The averaged estimated properties of 5-samples are shown in Table 5-2.

Table 5-2: Physical and mechanical properties of concrete slabs.

Slab size (mm)	Mass (kg)	Estimated Density (kgm^{-3})	Young's Modulus (E) GPa
600x600x40	30	2300	38

5.3.1.1 Test 01 (Experimental). Single concrete slab supported on 'ETHAFOAM 220'

The dynamic properties of the simplest possible concrete slab system were investigated. The system was later used as a *control specimen*, or "*benchmark*". That is, the results obtained were compared with similar, or slightly more complex systems and differences were noted. The later were useful in helping to develop the flaw-bond detection and assessment procedures.

It is well known that the best way to obtain an accurate account of the dynamic properties of a structure is to avoid any other means that they influence these properties. It is also known that boundary (support) conditions do have a major effect on natural frequencies, mode shapes and damping of any structure (Karadelis 2012).

Suspending these slabs with thin, flexible, steel wire and carrying out modal analysis, as it is normal in the automotive industry, should be the way forward. However, this turned out to be impractical when combined with modal analysis based on the roving hammer method. First, because it restricted the free movement of the hammer, and second, because readings taken near the suspending wires were influenced by the former.

An alternative solution was to provide support from the soffit of the slab. This should be such as not to interfere with the hammer and of course, the results. It was found that the use of ETHAFOAM 220, a lightweight, low mass – low stiffness – high damping foam-generated material, otherwise used for packaging, was the best choice (Dow 2001). Table 5-3 demonstrates the basic properties of the material.

Table 5-3: Physical and mechanical properties of ETHAFOAM 220.

ETHAFOAM 220 (mm)	Compressive Strength (GPa)	Elastic Modulus (GPa)	Density (kgm^{-3})
300x300x50	65e^{-6}	24e^{-6}	20

Modal analysis was carried out with the concrete slab supported on a block of ETHAFOAM 220. Conventional setup for the excitation of slab was employed (Figure 5-12). A small impact hammer (D86C03) with the sensitivity of 2.25mV/N was connected to the force channel (reference) of the 4channel data logger. The blue tip was selected due to its high stiffness properties. For the response measurement a triaxle piezoelectric accelerometer with a sensitivity of 101.4907mV/N was connected to the output channel. The data logger was connected to a PC and operation took place via the dedicated software, LMS Test.Lab 17 (LMS 2017).

Figure 5-12: Test 01. Single 'robust' concrete slab, supported on ETHAFOAM 220.

Briefly, the slabs were gridded, and nodes were numbered from 1 to 25.

The roving hammer method combined with the lumped mass approximation method were used to perform the analysis. Hence, the accelerometer was placed on a node (14), dictated by a preliminary FEA, and the hammer was moved around in a predefined way, exciting the structure. It is very important to position and number the nodes in the

virtual (digitised) system exactly as they are in the real grid. LMS Test.Lab 17, software provides a choice of coordinate systems, however, the rectangular coordinate system was used to define the nodes (Figure 5-13). Input Channel 1 was allocated to the hammer and output Channel 2 to the accelerometer.
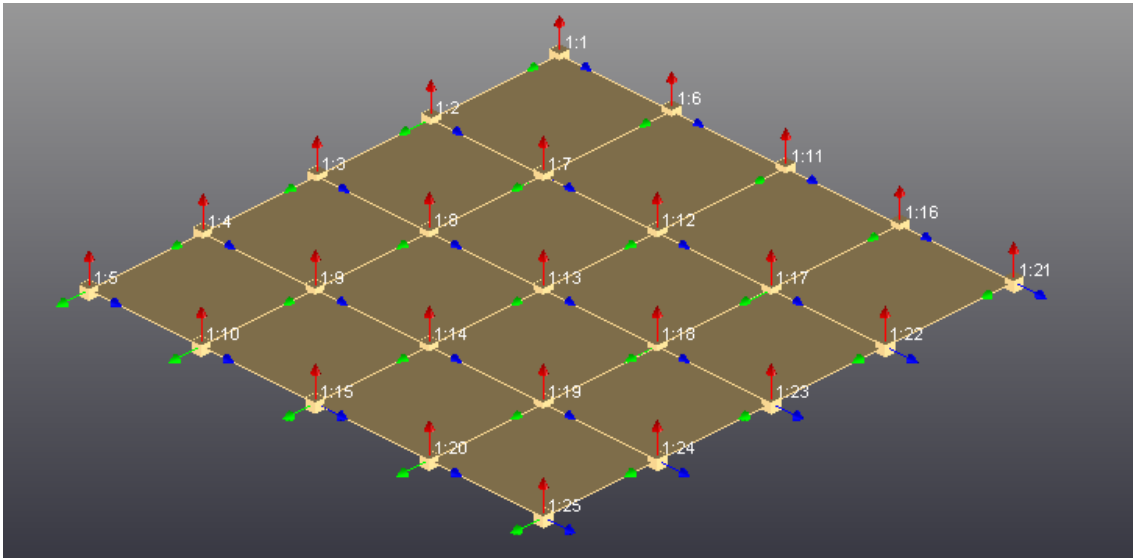
Figure 5-13: Nodes (1-25) defined for excitation in Test 01, LMS Test.Lab 17 (LMS 2017).

The *trigger level*, the minimum threshold in voltage that the sensor can detect and record the signal, was set by the software via the '*auto ranging function*', for both, hammer and accelerometer after several strikes on the structure. The Bandwidth (1250 Hz) that shows the frequency range in which the structure is going to be excited with the number of modes, was then defined along with the interrelated other Digital Signal Processing (DSP) parameters such as spectral lines (1024), resolution, and acquisition time (1 sec), that were selected based on the recommendations of the software (LMS 2017).

After setting up all pre-requisite conditions, modal testing of the slab was performed. To comply with the repeatability of the FRFs, 5 knocks at each node were carried out and their average was taken. The a*ccept* and *reject* capability also helped in keeping the record of rightly measured FRFs. This is important, since few bad hits can bring

inaccuracy to the average. The data acquisition was stopped after measuring all the FRFs from the defined nodes on the slab. Finally, during the last phase, the acquired FRFs were processed to obtain natural frequencies, damping ratios and mode shapes.

Modal Analysis software (LMS Test.Lab 17) was then used to process the acquired data. A selection of modal data was initially carried out. "*Noisy*" FRFs were separated and excluded. To extract the modal parameters, time and frequency domain can be used. Time MDOF is an algorithm, which extracts the modal data based on the impulse response function. Generally, this method is not recommended, since, it creates *mathematical poles* rather than *structural poles*, therefore, resulting in more solutions than the real ones in the stabilisation diagram. Hence, to avoid confusion only the structural poles were considered and by using '*PolyMAX'*, an algorithm developed by Siemens, the mathematical poles were removed, and only structural poles with a cleaner and accurate stabilisation diagram were displayed (Figure 5-14).
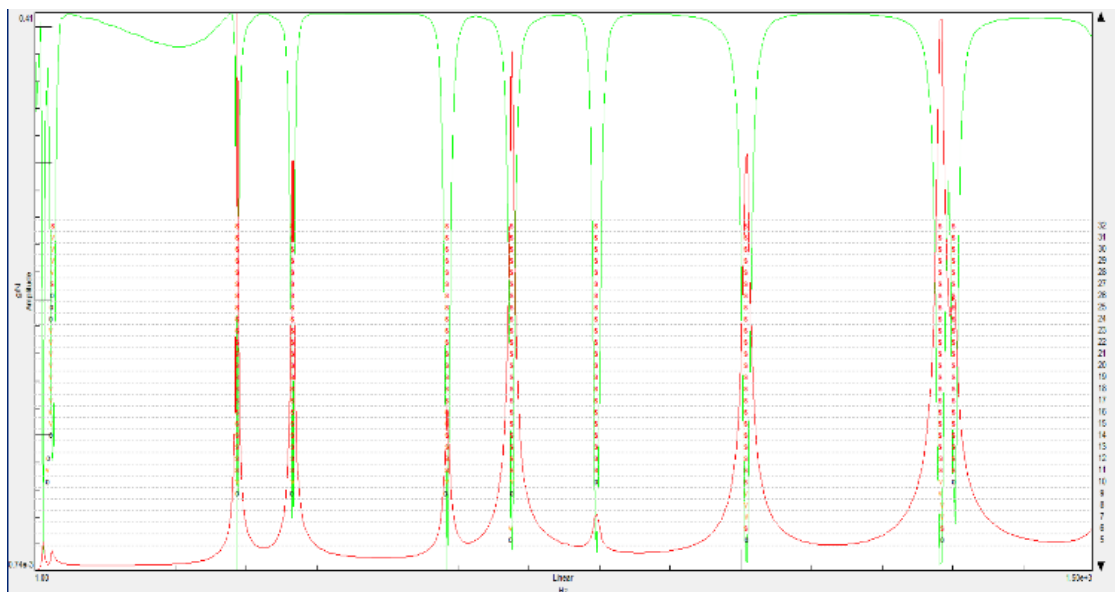
Figure 5-14: Stabilization Diagram (Polymax), LMS Test.Lab 17 (LMS 2017).

The Stabilisation diagram is a synthesized FRF (which has unknown parameters like natural frequencies, mode shapes, damping ratios, participation factor) that is, a theoretical fitting on the measured FRFs.
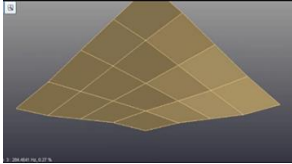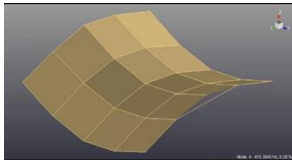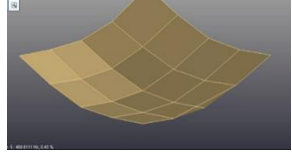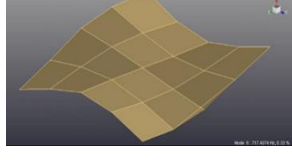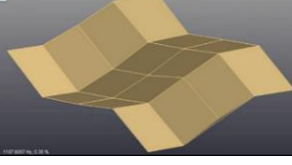
The bandwidth selection is always made between two *saddles* (anti-resonances), otherwise the partial information of one mode shape can enter into the other, and therefore, affecting the original mode shapes.

The first stage where modal parameters can be extracted from the acquired FRFs is the '*Stabilization chart*'. A model size was set in order to fit all the peaks. This is the degree of polynomial the selection of which is dependent on the acquired FRFs (not a fixed rule). However, the smaller the model size the faster will be the computation.

The coefficients of the polynomials called *Poles* were then selected. These eventually create a matrix whose number of columns depend on the degree of polynomial and the number of rows on the number of selected peaks.

Mode-shapes along with natural frequencies and damping ratios were then extracted based on selected poles and bandwidth. The degree of correlation and the degree of error determines the accuracy of the FRFs measured, by comparing it with synthesized FRFs. The results are tabulated below in Table 5-4.

Table 5-4: Test 01. Single 'robust' Slab on ETHAFOAM 220**.** Experimentally acquired Modal parameters.

Mode Nos	Mode Shapes	Natural Frequency (Hz)	Damping ratio (%)
1	 Diagonal bending mode	284.48	0.27
2	 1st Bending mode *(saddle)*	415.41	0.28
3	 Buckling mode *(trough)*	468.63	0.45
4	 1st Torsional mode	717.41	0.33
5	 2nd Bending mode	1204.89	0.35

The corresponding to mode shapes, natural frequencies are displayed along with corresponding damping ratios obtained from the Test. The first two mode shapes were displaying rigid body motion and ignored. Hence, the first acceptable mode shape showed diagonal bending followed by a saddle, etc, as shown in Table 5-4.

The modal assurance criterion (MAC) is a statistical indicator, that is used quite often in modal analysis in order to rate the degree of consistency between mode-shapes. It can be used as an orthogonality check for the mode-shapes. It is important to note that the MAC number indicates consistency but not validity, and it is not capable of distinguishing between local discrepancies and systematic errors. (Fotsch and Ewins 2000 and Pastor et al. 2012). The MAC number ranges between 0 – 1, with 1 representing fully consistent and orthogonal mode-shapes.

The MAC number was estimated during the post processing in LMS Test Lab17.1 software and a matrix representation was generated as illustrated in Figure 5-15.
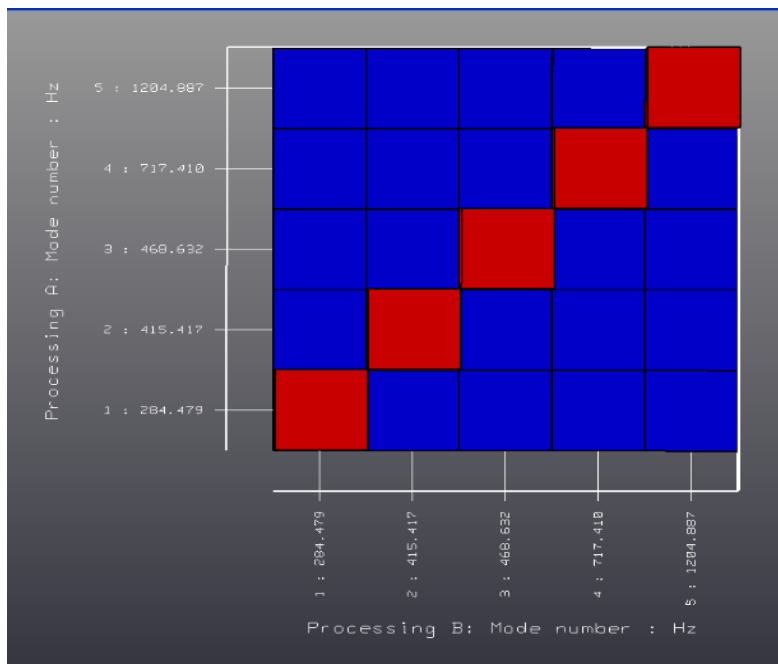
Figure 5-15: Test 01. MAC number representation for each mode-shape. The diagonal red blocks representing consistency (100%) for each mode-shape.

A good consistency was observed, when each mode-shape was compared with itself and the rest. The diagonal red blocks represent 100% consistency of mode-shapes that means a MAC number of 1. The diagonal matrix can also be interpreted that the mode-shapes showed orthogonality between themselves. Hence, all the mode-shapes extracted, were fully consistent.

204

5.3.1.2 Test 01 (Numerical Modelling). Single concrete slab supported on 'ETHAFOAM 220'

Owing to the complex nature of the experimental modal testing and analysis, it is highly recommended to supplement the experimental testing with the finite element modelling. The purpose of the finite element (FE) modelling is twofold: First, to predict the dynamic behaviour of the structure, subjected to complex loadings and/or displacements that otherwise would be hard to determine. Second, to calibrate the numerical model with the real-time boundary conditions, and use it along with experimental results to enhance confidence of testing, analysis and interpretation.

The dynamic characteristics of the FE model are determined by solving an Eigenvalue problem of the system. This involves the estimation of the natural frequencies (eigenvalues) and mode shapes (eigenvectors) based on solving the mass and stiffness matrices. The material properties such as density, elastic modulus and Poisson's ratio were estimated, while carrying out compressive strength-tests on a number of samples of the same mix, of which the original specimen (concrete slab) was made.

ANSYS Mechanical APDL 18.1 (ANSYS 2018) was considered to be the suitable code for modelling the concrete slab and estimating its dynamic behaviour. A linear modal analysis was run after applying appropriate boundary conditions, and the obtained modal parameters were compared with those from the experimental modal analysis. For this purpose, a 3D FE-model of the concrete slab with dimensions, 600x600x40mm, was developed in ANSYS workspace. In laboratory conditions the slab was rested on the special ETHAFOAM 220. In order to provide similar support conditions, the ETHAFOAM 220 was modelled with similar dimensions, 300x300x50mm, (Figure 5-16).
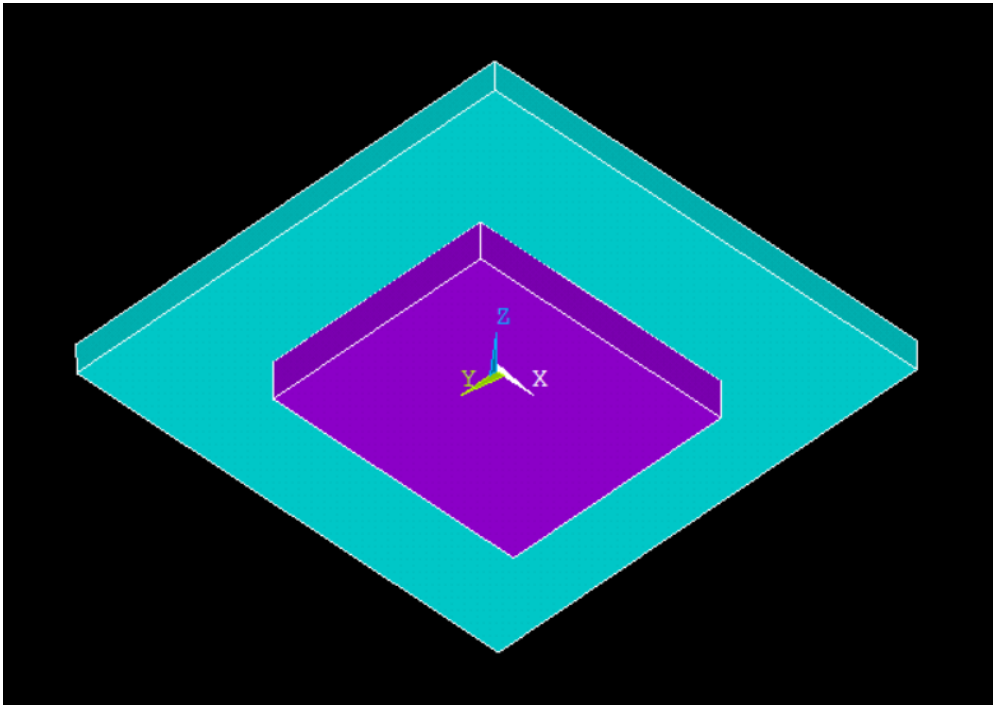
Figure 5-16: Test 01. FE-model of a concrete slab and ETHAFOAM 220, ANSYS Mechanical APDL 18.1 (ANSYS 2018).

Materials properties were then defined for the concrete slab and ETHAFOAM 220 as per Table 5-5. All properties were estimated in the laboratory. Density was calculated based on the measured mass and volume of both, concrete slab and ETHAFOAM 220 support. Typical values of Poisson's ratio were inserted in the model. A catalogue provided by the manufacturer of ETHAFOAM 220 was used for E-value and Poisson's ratio of the latter (Dow 2001).

The selection of elements was then carried out for both the slab and ETHAFOAM 220 (Table 5-5).

Table 5-5: Test 01. Elements, material properties and mesh types for the slab and ETHAFOAM 220.

Input parameters	Concrete Slab	ETHAFOAM 220
Element type	SOLID65	SOLID185
Density (kgm^{-3})	2300	20
Elastic Modulus (GPa)	38	24e^{-6}
Poisson's ratio	0.2	0.3
Mesh size (mm)	5	5
Mesh shape	Hexagonal	Hexagonal
Interface Contact pairs	TARG170	CONT174
Initial allowable penetration max (mm)		1
Initial allowable penetration min (mm)		0.5

Element SOLID65 was selected for the concrete specimen. This element is conventionally used for modelling concrete structures. This is mainly because it is capable of simulating cracking in tension and crushing in compression. Although, in modal analysis neither of the latter is used, other properties like the modulus of elasticity and uniform density were utilised. SOLID65 is defined by 8 nodes and possesses isotropic material properties. It also has the capability to model the reinforcement behaviour by incorporating rebars in concrete material with different orientation angles. The loads can be applied on the nodes and pressures could be the input as surface loads on the element faces, as shown by the circled numbers (Figure 5-17). It also possesses the prism and tetrahedral options, which can be adjusted based on the type of model and analysis. In modal analysis, the mesh shape was taken as hexagonal to give the better representation of the rectangular concrete model.
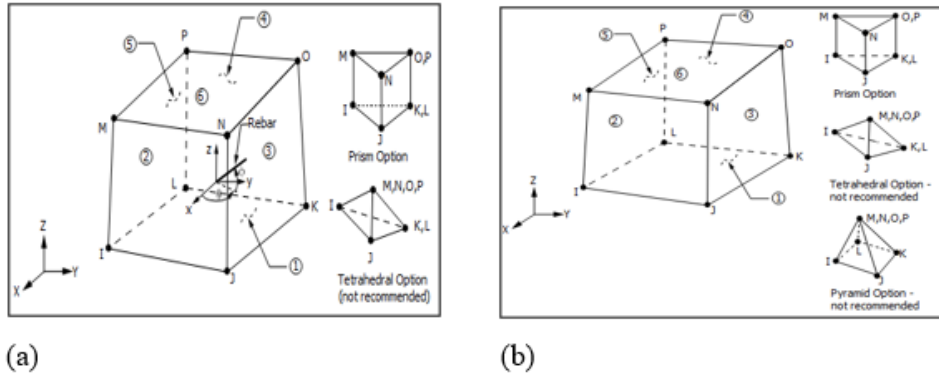
Figure 5-17: Test 01. (a) Geometry of SOLID65 element. (b) SOLID185, homogeneous structural solid element (ANSYS 2018).

Element SOLID185 was chosen for modelling ETHAFOAM 220 behaviour. It has a mixed formulation capability for simulating the little deformation of nearly incompressible elastoplastic materials, and ETHAFOAM 220 does possess the elastoplastic behaviour. Moreover, it is a homogeneous structural solid element, and is defined by 8 nodes, with 3DOFs per node, : translations in x,y,z nodal directions. It allows for tetrahedral and pyramid degeneration options, although, a hexahedral mesh shape was chosen. Pressures can be inputted as surface loads on the element faces represented by circled numbers (Figure 5-17). Isotropic material properties (Table 5-5) were fed for the ETHAFOAM 220, as the only deformation, expected was in z-direction. A reasonable size of 5mm, fine mesh was chosen for both materials allowing for stability of the results and reasonable computational time.

In ANSYS Mechanical APDL 18.1 (ANSYS 2018), surface to surface interface models are appended with contact elements in pairs, i.e. CONTAC171, 172, 173 or 174, and TARGE169 or 170. The target elements are considered to be *master* elements (generally used for rigid surface) that dictate the contact elements, represented as *slave* elements, a set of discrete contact points associated to certain constraint equations. Contact stiffness is generally required to ensure compatibility condition at the interface. Ideally, no penetration was anticipated at the concrete- ETHAFOAM 220 interface; only a slight deformation.

Therefore, it is recommended to prescribe a very small value of initial penetration which in this case was of the order of 1mm (max) and 0.5mm (min). This is because by providing a zero penetration, it is automatically assumed that the normal contact stiffness, k_N, becomes infinity (Equation 5.9). which is not structurally correct, and would result in ill-conditioning computations. Hence, in order to impede this possibility and to ensure mathematical equilibrium, an arbitrary infinitesimal, U_N value is generally introduced in the equation, ANSYS Mechanical APDL 18.1 (ANSYS 2018). Finally, a rough contact surface was selected with an assumed friction coefficient of 0.5 between specimen and support condition (Engineering Toolbox 2004). Linear Modal Analysis was carried out.

$$\sigma_N = k_N \cdot \mu_N \tag{5.9}$$

σ_N = Normal contact pressure (Nmm^{-2})

k_N = Normal contact stiffness (Force.length^{-3})

μ_N = Normal penetration (mm)
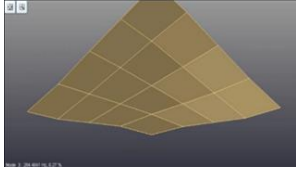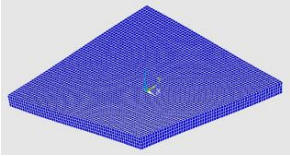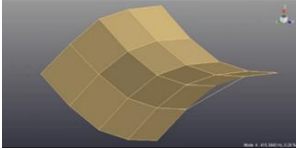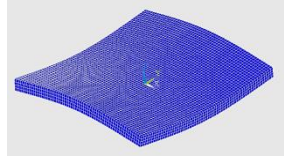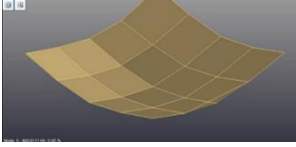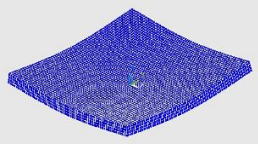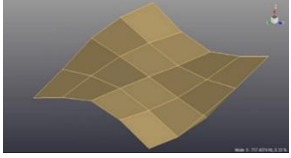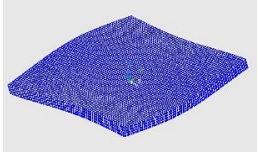
Boundary conditions were defined based on the laboratory work. It was observed during the experimental modal testing that the concrete specimen was firmly supported/rested on the ETHAFOAM 220. Therefore, full constraints to all degrees of freedom were given to the foam but with .01 displacement allowance, because of its flexible nature. This was in compliance with real foam behaviour.
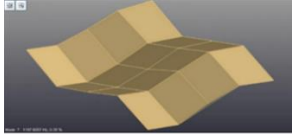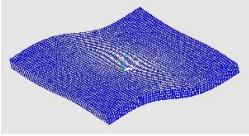
ANSYS 2018, provides special equation solvers to perform the modal analysis, these equation solvers are known as Eigen-solvers which are used to solve for natural frequencies (Hz) and mode shapes. In executing the modal analysis for undamped systems, ANSYS offers three Eigen-solvers: The sparse solver based Block Lanczos solver, the PCG Lanczos solver and the supernode solver. The Block Lanczos, sparse solver was selected as the mode extraction Eigen-solver. It is a is very robust and efficient algorithm typically recommended for the models within the range of small to large sizes in contrast to PCG Lanczos solver that is recommended for large models and

high degree of freedom(more than 100,000) systems. Block Lanczos employs the sparse matrix solver (Details on Pg 143-146). The bandwidth was set to 1250Hz similar to the one selected in experimental modal analysis and the simulation was run.

The natural frequencies and mode shapes obtained from the analysis are compared with experimentally computed modal parameters, (Table 5-6).

Table 5-6: Test 01. Single 'robust' slab on ETHAFOAM 220. Experimentally and Numerically obtained Modal parameters. A comparison.

Mode Nos	EXP Mode-Shapes	FEA Mode-Shapes	EXP Nat Freq (Hz)	FEA Nat Freq (Hz)	Error (%)
1	Diagonal bending mode	Diagonal bending mode	284.47	281.62	1.0
2	1st Bending mode *(saddle)*	1st Bending mode *(saddle)*	415.41	410.65	1.1
3	Buckling mode *(trough)*	Buckling mode *(trough)*	468.63	474.51	-1.2
4	1st Torsional mode	1st Torsional mode	717.41	712.13	0.7

| 5 | | | 1204.89 | 1224.4 | -1.6 |
| | 2nd Bending mode | 2nd Bending mode | | | |

A good correlation was achieved between the experimental and FE-obtained modal parameters. On an average, an error of less than 2% with respect to experimental results, was observed between natural frequencies of corresponding mode-shapes. Hence, the developed FE- model was verified and deemed to be suitable to (partly) replace time consuming laboratory testing.

5.3.1.3 Test 02 (Experimental + Numerical). Two-slabs stacked system, fully-debonded, supported on 'ETHAFOAM 220'

It was essential to carry out several tests on single slabs in order to achieve consistency and conformity with the modal analysis method. Next, it was decided to examine a system of two fully-debonded slabs, one resting on top of the other and supported on ETHAFOAM 220, to investigate their dynamic performance, and note and comment on possible variations with Test 01 (Figure 5-18). These (expected) differences should be enormously important in providing the foundation for the development of the detection and classification of the damage (flaw-bond) at the interface of the slabs.

Figure 5-18: Test 02. Two slabs 'fully-debonded', supported on ETHAFOAM 220.

Similar data acquisition procedures were followed except that a few additional nodes were defined at the soffit of the lower slab, in order to make sure that both the slabs are excited, and the obtained results are in conformity with the corresponding finite element model.

The DSP parameters selected for Test 02 are reported as: Bandwidth: 1280 Hz, Spectral Lines: 1024, Acquisition Time: 1 sec.

The Modal Assurance Criterion (MAC) was estimated for the obtained mode-shapes and is represented in a matrix form (Figure 5-19). It was noticed that all mode-shapes showed a MAC number of 1, except of the third mode-shape that showed a MAC number of 0.9. it can be said that a reasonable consistency was achieved overall.
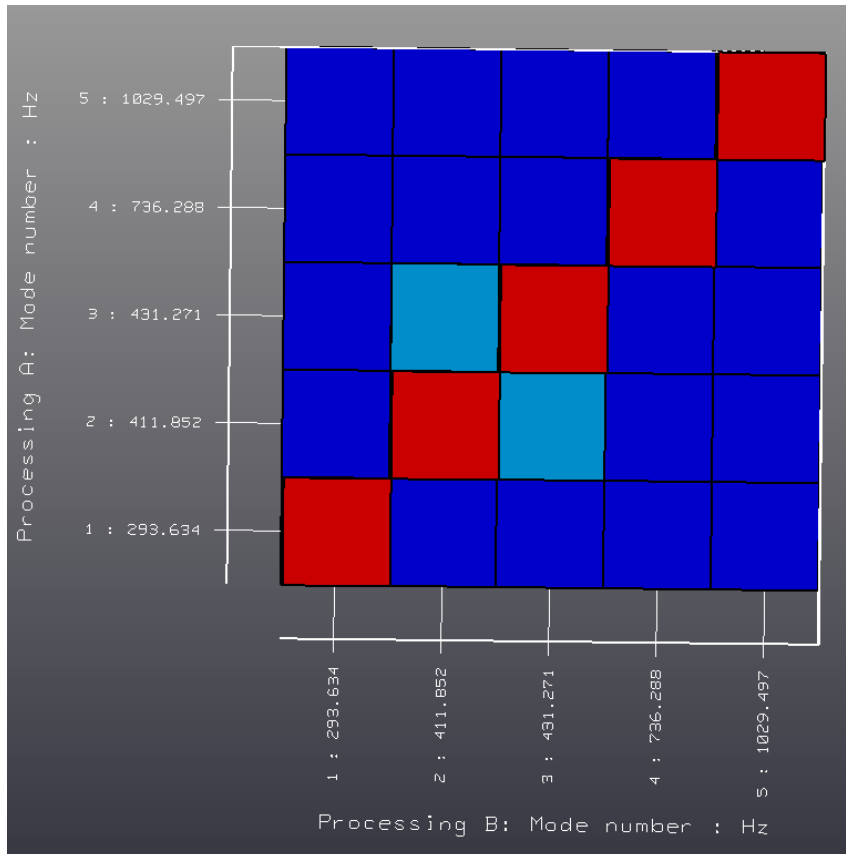
Figure 5-19: Test 02. MAC number for every mode-shape. Diagonal red blocks represent consistency (100%) for each mode-shape. Light blue blocks show 90% consistency of the 3rd mode-shape.

The corresponding FE models were developed in a similar manner to Test 01 (Section 5.3.1.2). This time, two similar concrete slabs (600x600x40mm), one on top of the other, fully-debonded were developed, while resting on the same, ETHAFOAM 220 (300x300x50mm), support (Figure 5-20). No details for the development of the FE-model will be reported here, as the procedure has been deemed to be similar to Test 01. Figure 5-20 gives a general view of the model and Table 5-7 offers all the information in a synoptic form.

213
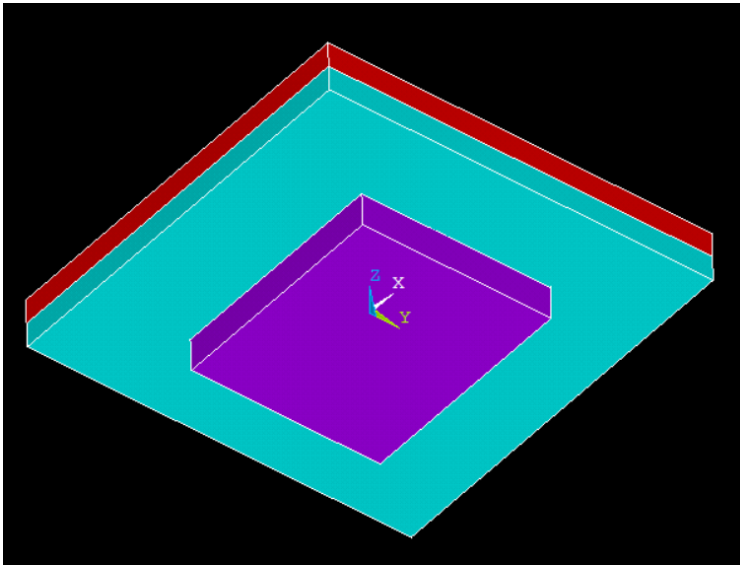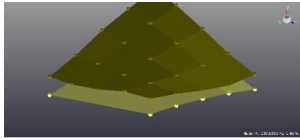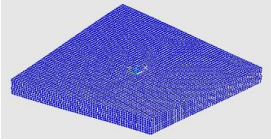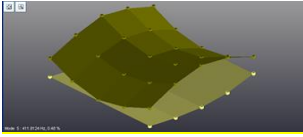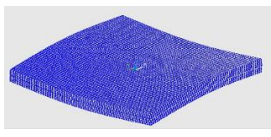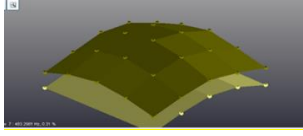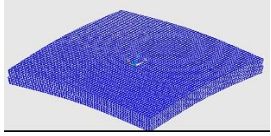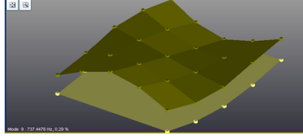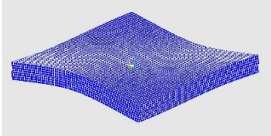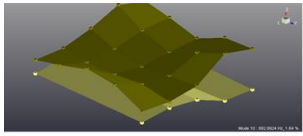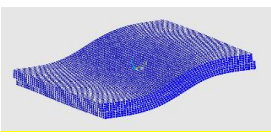
Figure 5-20: Test 02. FE-model of two-slabs, fully-debonded stacked system, resting on ETHAFOAM 220. ANSYS Mechanical APDL 18 (ANSYS 2018).

Table 5-7: Test 01. Elements, material properties and mesh types for the concrete slabs and ETHAFOAM 220.

Input parameters	Slab @ Top	Slab @ Bottom	ETHAFOAM 220
Element type	SOLID65	SOLID65	SOLID185
Density (kgm^{-3})	2300	2300	20
Elastic Modulus (GPa)	38	38	24e^{-6}
Poisson's ratio	0.2	0.2	0.3
Mesh size (mm)	5	5	5
Mesh shape	Hexagonal	Hexagonal	Hexagonal
Interface Contact pairs (1)	TARG170	CONT174	
Initial allowable penetration max (mm)		0.001	
Initial allowable penetration min (mm)		0.0001	
Interface Contact pairs (2)		TARG170	CONT174
Initial allowable penetration max (mm)			2
Initial allowable penetration min (mm)			0.5

The results are shown in Table 5-8, for comparison.

Table 5-8: Test 02. Two slab system, 'fully-debonded', on ETHAFOAM 220. Experimentally and Numerically obtained Modal parameters. A comparison.

Mode Nos	EXP Mode-Shapes	FEA Mode-Shapes	EXP Nat Freq (Hz)	FEA Nat Freq (Hz)	Error (%)
1	Diagonal bending mode	Diagonal bending mode	293.63	288.40	1.8
2	1st Bending mode *(saddle)*	1st Bending mode *(saddle)*	411.85	420.54	-2.1
3	Buckling mode *(trough)*	Buckling mode *(trough)*	431.27	425.60	-1.2
4	1st Torsional mode	1st Torsional mode	736.29	729.26	0.7
5	2nd Bending mode	2nd Bending mode	1029.50	1030.36	-0.1

A good correlation was reached between modal parameters obtained from FE-analysis and the corresponding experimental analysis, with an average percentage error of 1.2%

approx. Note that the mode-shapes obtained from experimental tests showed augmented delamination compared to the ones obtained from the FE-analysis.

5.3.1.4 Results Discussion- Preliminary Tests (01-02)

The results obtained from Test 01 (Single 'robust' slab on ETHAFOAM 220) and Test 02 (Two 'fully-debonded' slabs on ETHAFOAM 220) are going to be compared. At this stage, a preliminary comparison between their modal parameters was done, in order to make an initial observation regarding their dynamic behaviour and the differences between a single 'robust' slab and two 'fully-debonded' slabs, supported on ETHA-block. This will make bases for latter experiments, where various types of bonding would be present, and a common ground or bench mark would help in analysing and interpreting the results. In addition, some tentative decisions were made. This should help developing the detection and classification procedures for the condition of the bond between "layers" at a later stage.
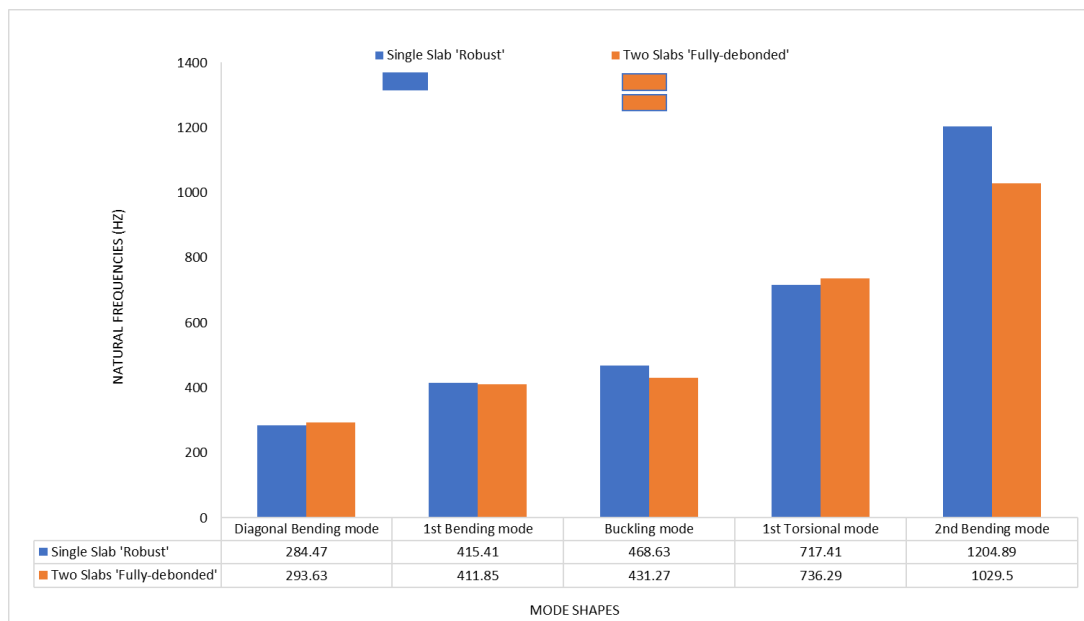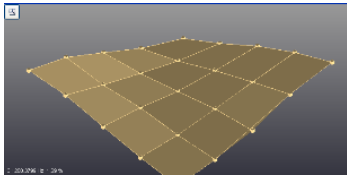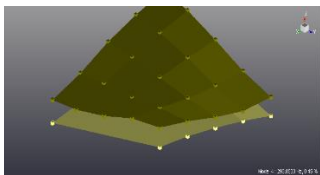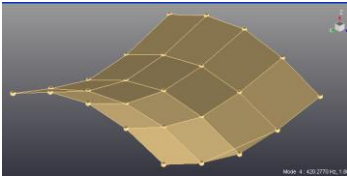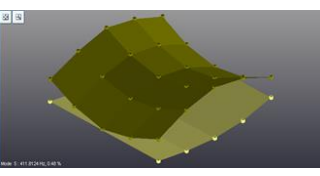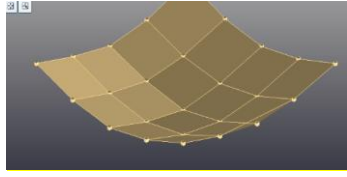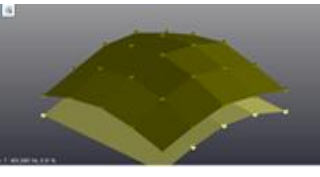
Figure 5-21: Tests 01+02. Experimental Natural frequencies (and corresponding mode-shapes). Comparison between Single 'robust' slab and Two slabs, 'fully-debonded,' on ETHAFOAM 220.

At this stage there is not obvious or reasonable trend that can be extracted from Figure 5-21. The natural frequencies of the singe slab are shown lower at the 1st and 4th modes of vibration and higher at the 2nd, 3rd and 5th modes compared with the corresponding

double slab system. Hence, an explanation/justification will be attempted at a later stage when, it is hoped that the presence of more tests should reveal drifts and tendencies.

Preliminary observations from Table 5-9 showed that the mode-shapes of one-slab system were similar to those of the two-slabs system. However, after a more careful study some differences were emerged. The two-slabs system was showing signs of separation. It was deducted that the dynamic behaviour of a single slab system (Test 01) can be considerably different than that of a double slabs system (Test 02), and this can be depicted in a modal analysis. This also demonstrates that the method of experimental (and arguably numerical) modal analysis is efficient, and can be used to distinguish between fully bonded and debonded pavement layers.

Table 5-9: Tests 01+02. Experimental Mode shapes. Comparison between 'One-Slab' system and 'Two-Slabs' system.

Mode Nos	One-Slab system	Two-Slabs system
1	Diagonal bending mode	Diagonal bending mode
2	1st Bending mode *(saddle)*	1st Bending mode *(saddle)*
3	Buckling mode *(trough)*	Buckling mode *(trough)*

4	 1st Torsional mode	 1st Torsional mode
5	 2nd bending mode	 2nd bending mode

A first comparison between damping ratios from Test 01 (single slab system) and Test 02 (double slabs system) is given in Figure 5-22. Single slab produce a significantly lower damping ratio for modes 1, 2, 4, 5 compared to double slabs system. This should be expected as, in general, the higher the mass non-participating in the motion, the higher the damping present (double slab system acts as a damper compared to the single slab system when the two slabs do not vibrate in unison). However, mode 3 produces an approximately equal damping between single and double slabs. This indicates that mode 3, a purely buckling mode, is very tuneful, and that the two-slab system does vibrate in unison.
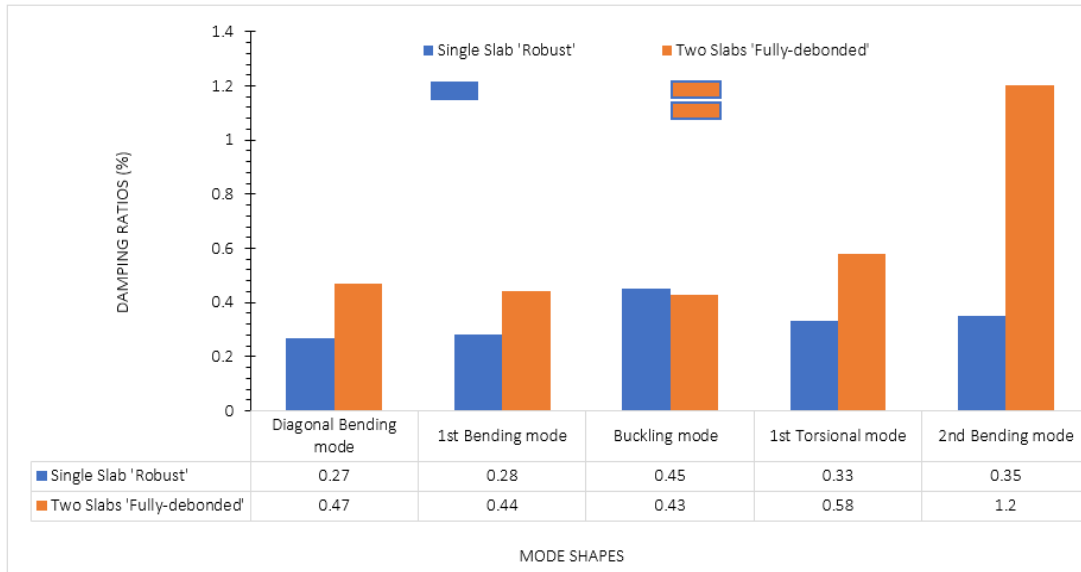
Figure 5-22: Tests 01+02. Experimental Damping ratios. Comparison between Single 'robust' slab and Two slabs, 'fully-debonded' on ETHAFOAM 220.

The following can be summarised:

1. Two slabs, 'fully-debonded' showed an average 3% higher natural frequencies for *diagonal* bending and 1st *torsional* mode, compared to single 'robust' slab for similar mode shapes. However, single slab showed about 1% higher value (natural frequency) in *1st bending* mode, 8% in *buckling* mode and about 15% higher value in *2nd bending* mode.

2. Mode Shapes of two slabs, 'fully-debonded' showed separation, as illustrated by the (exaggerated) mode-shapes animations, in the experimental modal analysis and were endorsed by preliminary FEA.

3. Damping ratios of two slabs, 'fully-debonded' showed 29% (approx.) higher values compared to single 'robust' slab for all the similar mode shapes except, *buckling* mode, which was approximately equal to the single slab.

5.3.2 Essential Tests

After carrying out 'preliminary tests', it was decided to carry out 'essential tests'. The latter were planned to be conducted on number of concrete slabs (robust/flawed), while replacing the simplest support conditions (*ETHAFOAM 220*) with a designated subgrade. A sandpit was designed that could be representative of a real subgrade (See APPENDIX D for more details). However, some size restrictions were applied due to lack of space. The synoptic plan for all the 'essential tests' is illustrated in Figure 5-23.
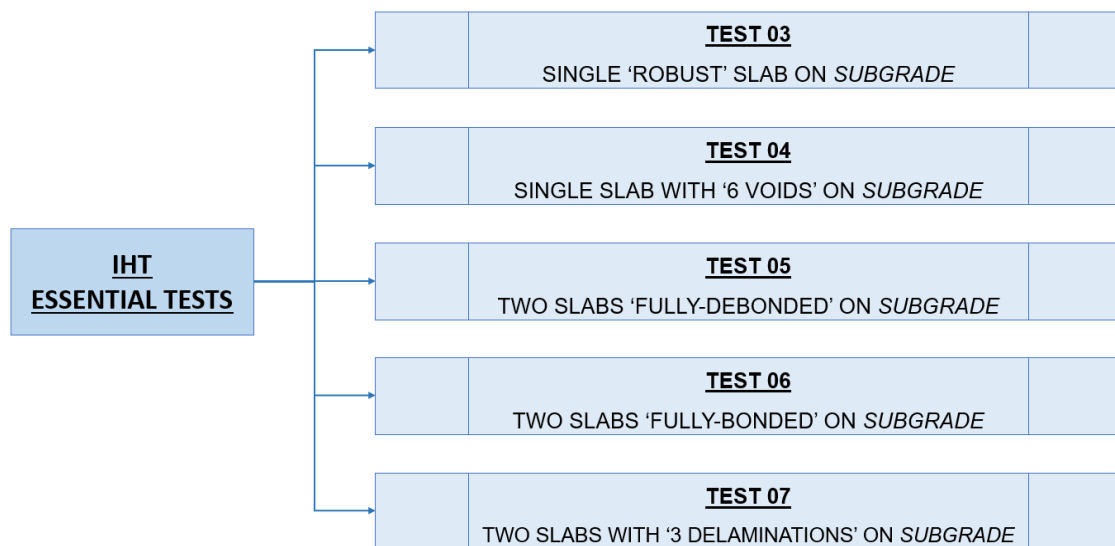
Figure 5-23: Synoptic Plan of IHT-Essential Tests.

Selection of Impact Hammer for Essential Tests

By introducing the subgrade support, it was anticipated that the high damping behaviour of the soil, will make it difficult for the slab to vibrate. Therefore, it was proposed initially, to carryout tests by using a medium sized impact hammer-86D20, in contrast with small hammer-86C03 that was already in use during ETHAFOAM 220 support conditions. However, after carrying out number of trial tests with both hammers (small sized and medium sized), it was decided to proceed with the small hammer for the following reasons:

- Exciting the slabs with the medium sized hammer resulted in poor correlation between the synthesized and measured FRFs in the post processing.

- It was observed that by exciting the slab with the medium sized hammer resulted in the un-necessary excitation of the whole setup including the lab floor. As a consequence, non-linearities influenced the results significantly, and resulted in poor and overdamped FRFs, hence, inaccurate modal parameters were obtained, when cross-checked with corresponding FE-model.

- On the other hand, the small sized hammer showed much clear FRFs, and reasonable correlation with the FE-model was also noticed.

5.3.2.1 Test 03 (Experimental + Numerical). Single slab, flawless (robust), supported on subgrade

The aim of this test was to obtain a first impression of the dynamic behaviour of a single concrete slab (robust), while supported on the subgrade (Figure 5-24), and use it as a control slab , '*controlled specimen-I'* for the similar tests to follow.

Similar data acquisition procedures to Test 01, were followed. However, the tip of the impact hammer was changed, as more input energy was required to excite the resting slab due to damped support condition. Hence, after carrying out some trial hits with various tips, '*steel tip'* was selected as optimum with the chosen DSP parameters i.e. Bandwidth: 2000Hz, Spectral Lines: 1024, Acquisition Time: 0.25s.

Figure 5-24: Test 03. Single 'robust' concrete slab, supported on subgrade.

A MAC number of 1 was achieved for all the mode-shapes, showing 100% consistency for all the acquired mode-shapes (Figure 5-25).
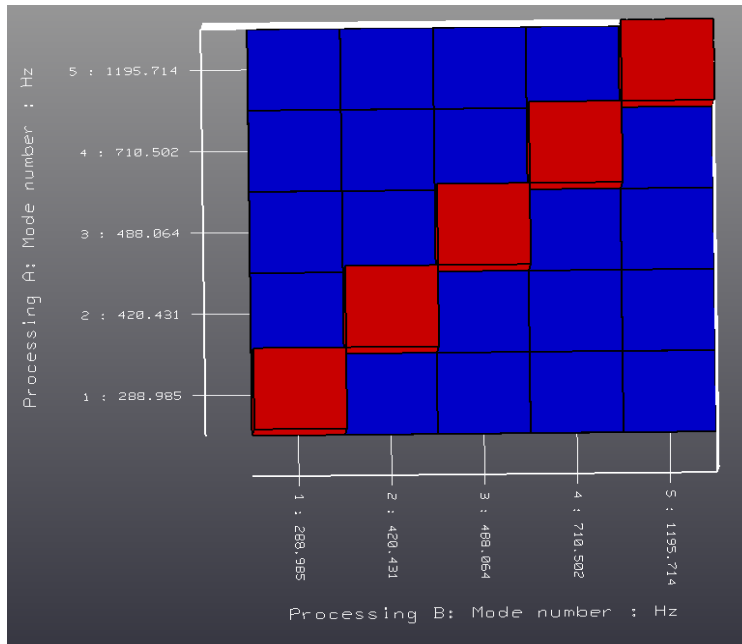
Figure 5-25: Test 03. MAC number representation for each mode-shape. The diagonal red blocks representing the consistency (100%) for each mode-shape.

The corresponding FE model was developed in a similar fashion to Test 01 (Section 5.3.1.2), therefore, no details will be reported here. However, to model the support condition (subgrade), there were two possible approaches. First, to model the subgrade with all its due dimensions and inherent properties (damping, stiffness, cohesive value, frictional angle, dilatancy angle etc.). This was complex and only suitable, if an analysis of the soil behaviour was the objective. Second, to model only the '*surface effect*' of the subgrade on the supported slab. Here, only the surface effect of the subgrade on the slab was accounted for the modal analysis. This means, the elastic support of the subgrade on the slab was considered while computing the modal parameters (natural frequencies, mode shapes) for the slab, but the behaviour of the soil was not computed. This was also in agreement with the aim of real testing, where the objective of the test was to excite the slab only and to extract its modal parameters, while the subgrade represented support conditions. The second approach was adopted, as it will suffice the requirement for this particular FE-analysis. To simulate the subgrade reaction, SURF154 elements were selected and attached to the soffit of the slab.
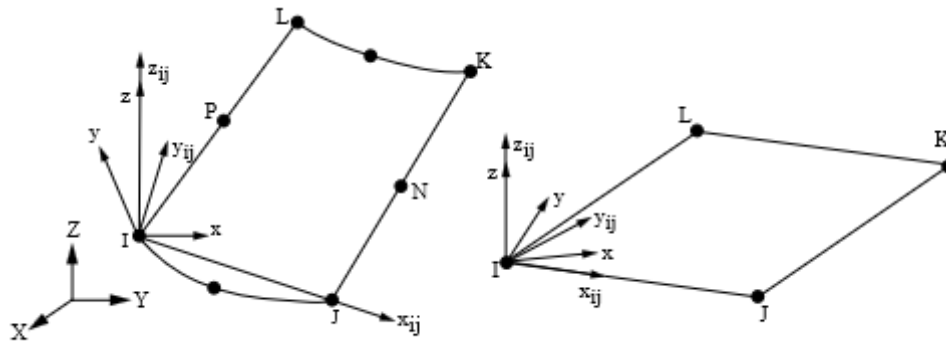
Figure 5-26: Geometry of SURF154. ANSYS Mechanical APDL 18.1 (ANSYS 2018).
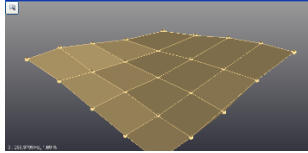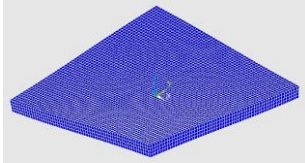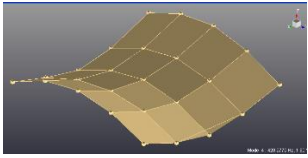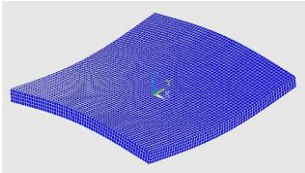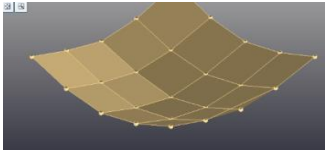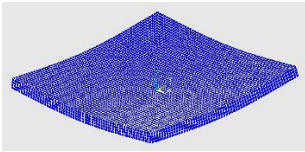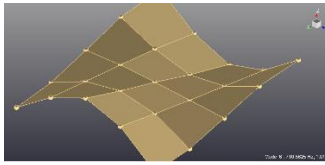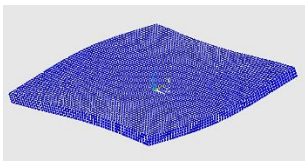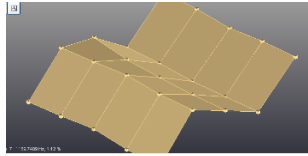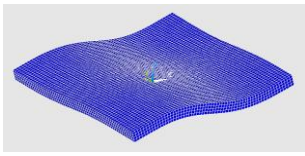
SURF154 is defined by four or eight nodes and the material properties (Figure 5-26). It can be overlaid over the face (area) of any 3-D element, and can be used for various loads and surface effect applications, simultaneously in 3-D structural analyses. '*Elastic Foundation Stiffness*' (EFS) is generally defined for these surface elements, this represent the underneath foundation stiffness, which in this case was subgrade. The foundation stiffness of the subgrade was estimated to be 16.5MPa, by carrying out California bearing ratio (CBR) tests in the lab, on the soil sample taken from the subgrade.

Element SOLID185 was chosen for concrete specimen in contrary to SOLID65, which was used earlier in Test 01. This selection was made based on the elements compatibility of the concrete specimen to the surface element of the subgrade.

The natural frequencies and mode shapes obtained from the FE-simulation are compared with experimentally computed modal parameters, (Table 5-10).

Table 5-10: Test 03. Single 'robust' slab on subgrade. Experimentally and Numerically obtained Modal parameters. A comparison.

Mode Nos	EXP Mode Shapes	FEA Mode Shapes	EXP Nat Freq (Hz)	FEA Nat Freq (Hz)	Error (%)
1	Diagonal Bending mode	Diagonal Bending mode	288.99	289.67	-0.4
2	1st Bending mode (saddle)	1st Bending mode (saddle)	420.43	422.35	-0.5
3	Buckling mode (trough)	Buckling mode (trough)	488.06	474.27	3
4	1st Torsional mode	1st Torsional mode	710.50	708.59	0.3
5	2nd Bending mode	2nd Bending mode	1195.71	1194.50	-0.4

A very reasonable correlation was achieved between the experimentally acquired modal parameters (Natural frequencies + Mode shapes) and numerically based results, with an average error of about 1% with respect to experimental results. Hence, adding

226

confidence to the acquired modal parameters that could be used later for evaluation purposes.

5.3.2.2 Test 04 (Experimental + Numerical). Single slab with 6 flaws (voids) supported on subgrade

The same single slab embedded with 6-voids, and tailored to fit IRT (Ch 05-Test 01), was also tested with IHT by resting the slab on the subgrade (support condition) as per Figure 5-27.

The aim of the test was to note any possible differences between the modal parameters of the 'Robust' slab with those of the 'Flawed'. This would be used later on to develop the flaw-bond detection method.
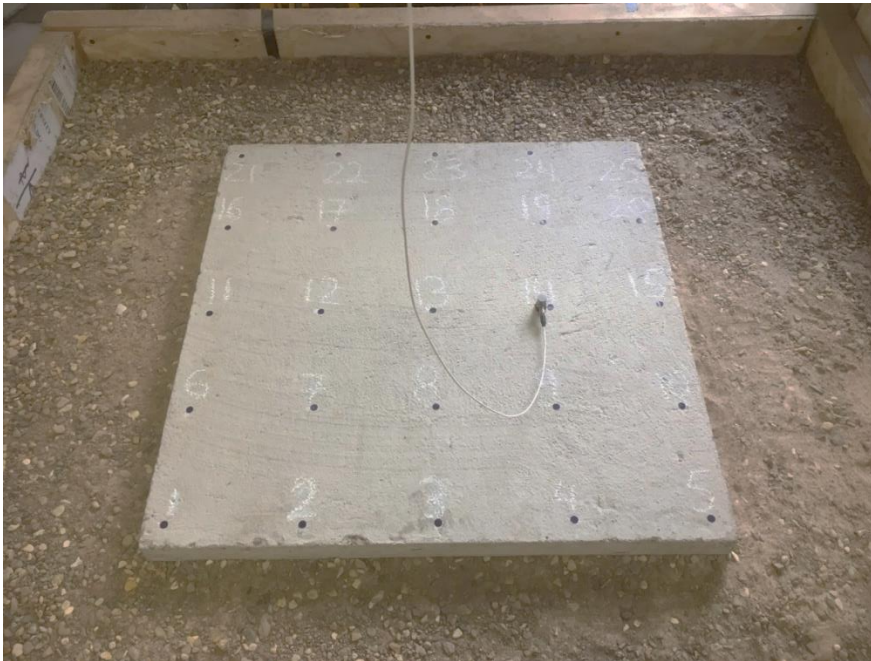
Figure 5-27: Test 04. Single slab with '6 Voids', supported on subgrade.

The test was carried out after numbering the nodes on the surface and allocating one node to the accelerometer based on trial hits and comparing the best response (Figure 5-27).

The DSP parameters selected for this test are represented as: Bandwidth: 2048Hz, Spectral Lines: 1024, Acquisition Time: 0.5s.

The MAC number was estimated for all the mode-shapes, and it was observed that the buckling mode showed 85% consistency, hence, 0.85 MAC number, where the rest of the mode-shapes showed 100% consistency with MAC number, 1 (Figure 5-28).
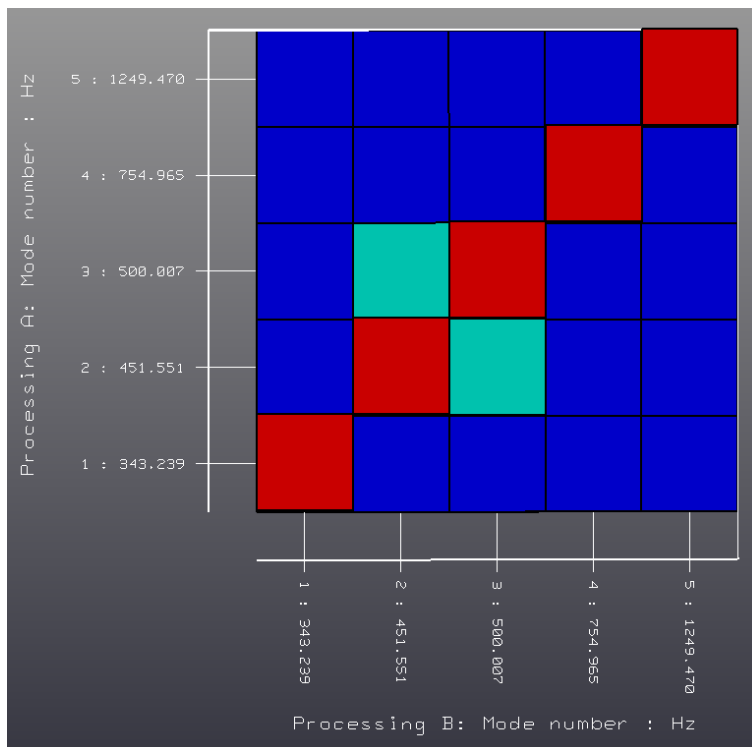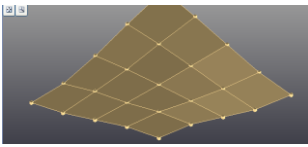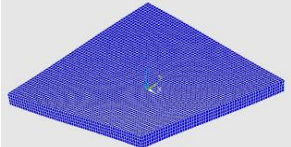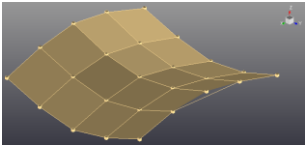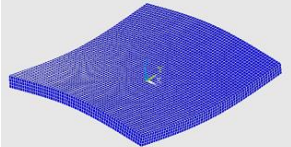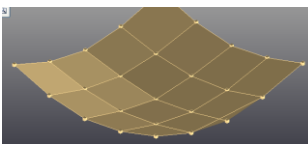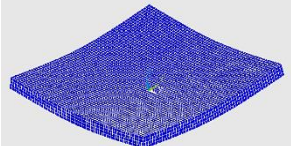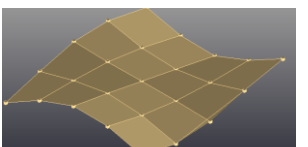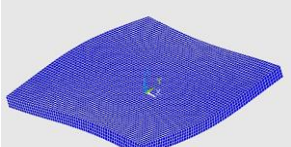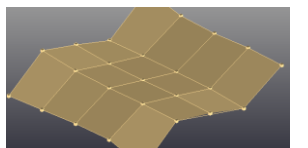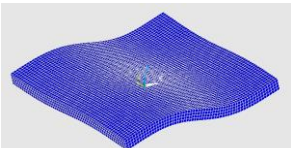
Figure 5-28: Test 04. MAC number representation for each mode-shape. The diagonal red blocks represent consistency (100%) for each mode-shape. The light green blocks show 85% consistency of the third mode-shape.

The FE-model developed earlier for 'thermal analysis' (Section 4.5.1), was modified to suit the 'FE-modal analysis'. The modification was done by employing the 'support conditions' and the 'elements' suited for 'FE-modal analysis'. The rest of the procedure and the details were similar to the Test 03, therefore, no details will be reported here.

229

The natural frequencies and mode shapes obtained from the FE-simulation are compared with experimentally computed modal parameters (Table 5-11).

Table 5-11: Test 04. Single slab with '6 Voids' on subgrade. Experimentally and Numerically obtained Modal parameters. A comparison.

Mode Nos	EXP Mode Shapes	FEA Mode Shapes	EXP Nat Freq (Hz)	FEA Nat Freq (Hz)	Error (%)
1	Diagonal Bending mode	Diagonal Bending mode	343.24	313.08	8.7
2	1st Bending mode (saddle)	1st Bending mode (saddle)	451.55	451.05	0.11
3	Buckling mode (trough)	Buckling mode (trough)	500.01	509.93	-1.98
4	1st Torsional mode	1st Torsional mode	754.97	765.40	-1.38
5	2nd Bending mode	2nd Bending mode	1249.47	1282.80	-2.66

A good correlation was observed between the experimentally and numerically acquired modal parameters (Natural frequencies + Mode-shapes), with an average error of approx. 3% with respect to experimental results (Table 5-11). A pattern of mode-shapes similar to the one obtained from the single '*robust*' slab (Test 03), was observed (Table 5-10). However, the natural frequencies were increased compared to the former, hence, showing a clear difference between single '*robust*' and single '*flawed*' slab.

5.3.2.3 Test 05 (Experimental + Numerical). Two-slabs stacked system, fully debonded, supported on subgrade

After carrying out a number of tests on a single concrete slab (robust/flawed), it was decided to continue with two similar slabs, one on top of another, simulating a fully delaminated system supported on the subgrade (Figure 5-29).

Figure 5-29: Test 05. Two slabs, 'full-debonded' supported on subgrade.

The aim of this experiment was to investigate, any patterns of modal parameters developing, as observed in the previous series of tests, where the slabs-system were supported on the *'ETHAFOAM 220'*. This should also act as a 'benchmark', '*controlled specimen-II'* for similar tests (two-slabs system) to follow.

Briefly the slab was gridded, nodes were numbered (1-25) and the initial DSP parameters were adjusted: Bandwidth: 1280Hz, Spectral Lines: 2048, Acquisition Time: 0.64s.

The MAC number, estimated for the obtained mode-shapes is represented in a matrix form (Figure 5-30). It was observed that the second mode-shape, in-plane bending, showed a MAC number of 0.9. However, all the other mode-shapes showed a good MAC number of 1, hence, a reasonable consistency was observed overall, between all mode-shapes.
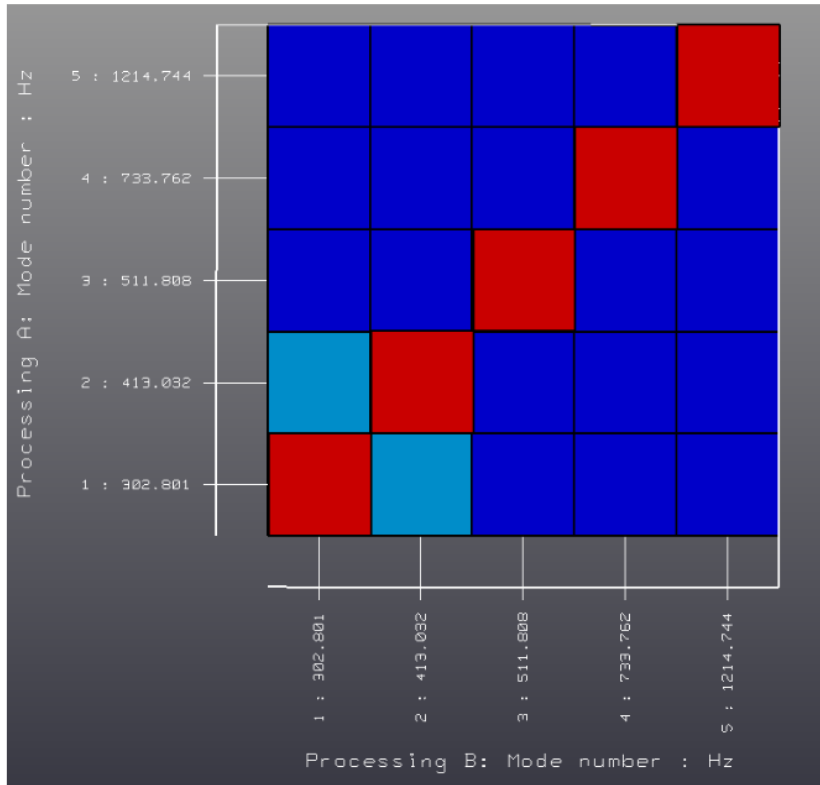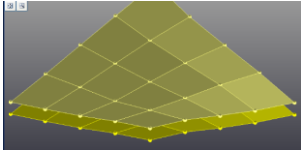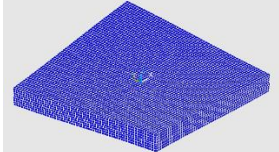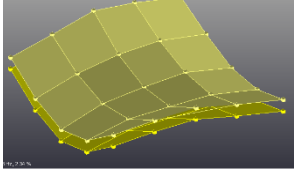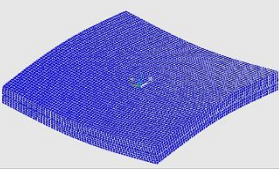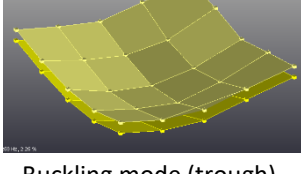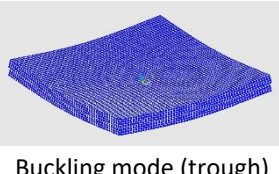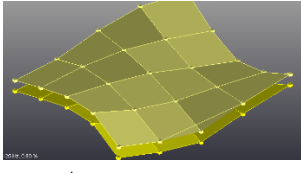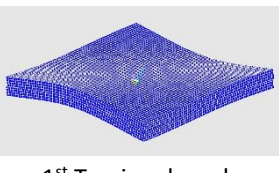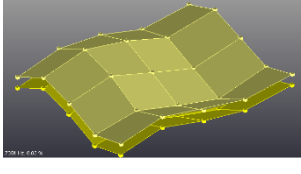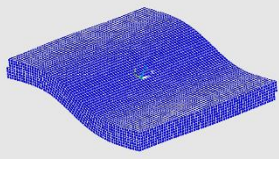
Figure 5-30: Test 05. MAC number representation for each mode-shape. The diagonal red blocks represent consistency (100%) for each mode-shape. The light blue blocks, show 90% consistency of the second mode-shape.

To perform the FE-modal analysis for Test 05, the FE model was developed in a similar fashion as per Test 03, therefore, no details will be reported here. However, this time the effects of subgrade (support condition) were modelled instead of ETHAFOAM 220.

The natural frequencies and mode shapes obtained from the FE-simulation are compared with experimentally computed modal parameters (Table 5-12).

Table 5-12: Test 05. Two slabs, 'fully-debonded' on subgrade**.** Experimentally and Numerically obtained Modal parameters. A comparison.

Mode Nos	EXP Mode Shapes	FEA Mode Shapes	EXP Nat Freq (Hz)	FEA Nat Freq (Hz)	Error (%)
1	Diagonal Bending mode	Diagonal Bending mode	302.80	300.92	0.6
2	1st Bending mode (saddle)	1st Bending mode (saddle)	413.03	442.74	-7.2
3	Buckling mode (trough)	Buckling mode (trough)	511.81	497.62	2.7
4	1st Torsional mode	1st Torsional mode	733.76	746.47	-1.7
5	2nd Bending mode	2nd Bending mode	1214.74	1264.60	-4.1

A good correlation was achieved between the experimentally and numerically acquired modal parameters with an average error of approximately 3% with respect to experimental results (Table 5-12). Though, the debonding was not shown clearly in the

experimentally obtained mode-shapes, the mode-shapes obtained from the numerical model showed clear tendencies of debonding. This was anticipated, since the nodes on the lower slab were not excited one by one as they were excited in the previous case (Test 02). Moreover, the nodes at the soffit of the lower slab acted as *'slave nodes'* and were controlled by their *'master nodes'*, i.e. nodes on the top. This demonstrates that the FE-modal analysis substitutes the experimental modal analysis, and can be used in conjunction with the latter to interpret or evaluate a complex delamination condition.

5.3.2.4 Test 06 (Experimental + Numerical). Two-slabs stacked system, fully-bonded, supported on subgrade

After carrying out number of impact hammer tests on double slabs simulating fully debonded conditions, it was decided to go with the fully bonded idea, where two similar slabs were bonded together and supported on the subgrade (Figure 5-31).

Figure 5-31: Test 06. Two slabs, 'fully-bonded' supported on subgrade.

The aim of the test was to report on the differences between a '*Fully-debonded*' and a '*Perfectly-bonded*' set of slabs.
In addition, this should also act as a 'benchmark', '*controlled specimen-III*' for the similar tests to follow (two-slabs system with defects).

In order to proceed, a similar sized slab with same properties, was cast on the pre-cast slab and a 28-days curing process was followed, to achieve the highest compressive strength. After the curing process, the fully bonded slabs were rested on the subgrade and the test was carried out in the same fashion, as discussed earlier (Section 5.3.1.1).

The DSP parameters selected for this test are represented as: Bandwidth: 2048Hz, Spectral Lines: 1024, Acquisition Time: 0.5s.

The MAC number estimated for the mode-shapes obtained is represented Figure 5-32. A 100% consistency in the mode-shapes were seen, where the MAC number estimated for all the mode-shapes came out to be 1.
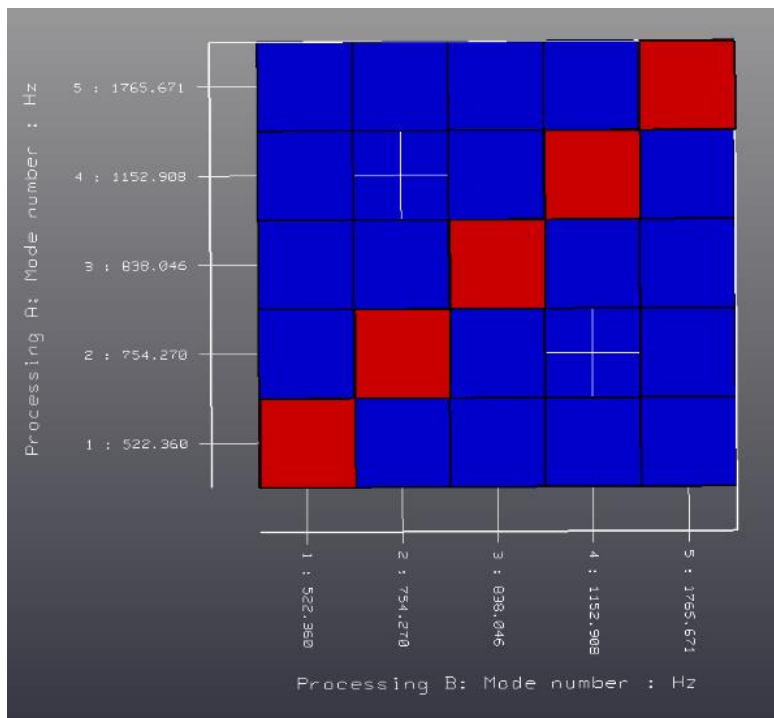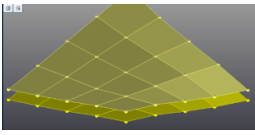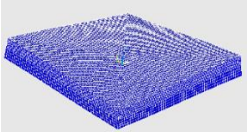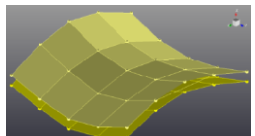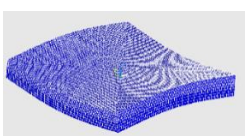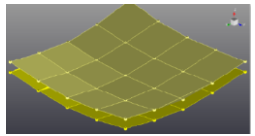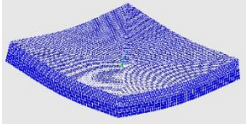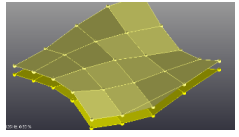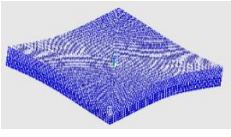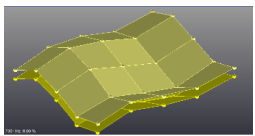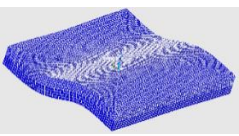

Figure 5-32: Test 06. MAC number representation for each mode-shape. The diagonal red blocks represent 100% consistency for each mode-shape.

To perform the FE-modal analysis for Test 06, the FE model was developed in a similar manner as discussed in previous test. However, at the interface of the two slabs, an '*always bonded*' condition was employed, which made the two slabs glued to each other and no sliding was possible, leading to infinite static friction.

The natural frequencies and mode shapes obtained from the FE-simulation are compared with experimentally computed modal parameters, (Table 5-13).

Table 5-13: Test 06. Two slabs, 'fully-bonded' on subgrade. Experimentally and Numerically obtained Modal parameters. A comparison.

Mode Nos	EXP Mode-Shapes	FEA Mode-Shapes	EXP Nat Freq (Hz)	FEA Nat Freq (Hz)	Error (%)
1	Diagonal Bending mode	Diagonal Bending mode	522.36	522.02	0.2
2	1st Bending mode (saddle)	1st Bending mode (saddle)	754.27	753.50	-.01
3	Buckling mode (trough)	Buckling mode (trough)	838.05	850.13	-2.2
4	1st Torsional mode	1st Torsional mode	1152.91	1199.0	-5.3
5	2nd Bending mode	2nd Bending mode	1765.67	1927.70	-9.6

A good correlation was observed between the experimentally and numerically, acquired modal parameters (Natural frequencies + Mode shapes) with an average error of approx. 3% with respect to experimental results. All natural frequencies were noted to be increased significantly, compared to the corresponding ones in '*fully-debonded*' two-slabs stacked systems. However, the mode-shapes showed the same pattern and order

but that was expected. This was due to lack of accessibility of exciting nodes at the soffit of the lower slab as discussed in the previous test (Test 05).

5.3.2.5 Test 07 (Experimental + Numerical). Two-slabs stacked system with 3 flaws (delaminations) supported on subgrade

The same two-slabs stacked system implanted with 3 delaminations (voids) at their interface, and tailored to fit IRT (Ch 05-Test 02) was tested with IHT, by resting them on the subgrade (support condition) as shown in Figure 5-33.

Figure 5-33: Test 07. Two slabs with '3 Delaminations' supported on Subgrade.

The aim of the test was to note any possible differences between the modal parameters of the 'Perfectly-bonded' two-slabs stacked system (Test 06) with those of the 'Flawed'. This would be used later on to develop the flaw-bond detection method.

The nodes (1-25) were numbered and test was carried out. The DSP parameters selected for this test are represented as: Bandwidth: 2048Hz, Spectral Lines: 1024, Acquisition Time: 0.5s.

The MAC number estimated for the mode shapes is represented below. It was observed that all the mode-shapes showed 100% consistency with the MAC number of 1 (Figure 5-34).
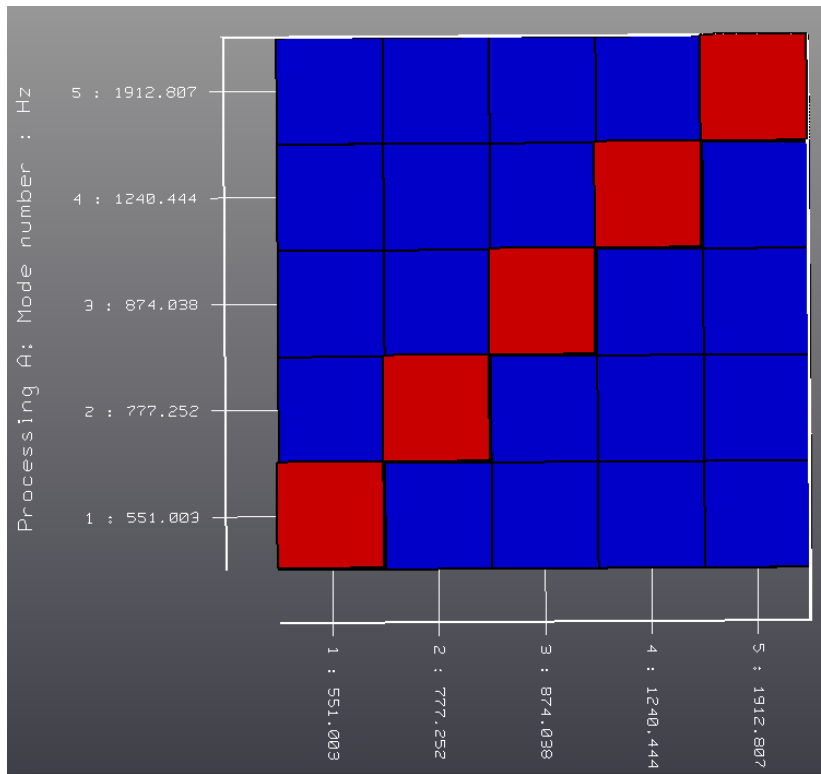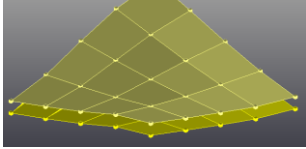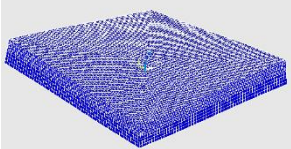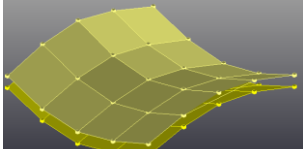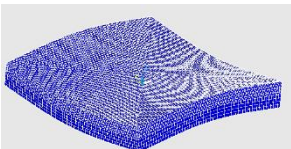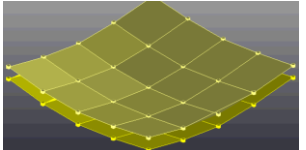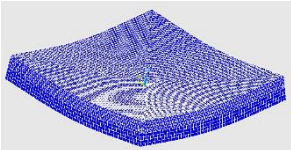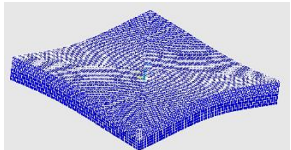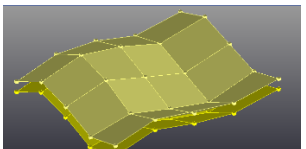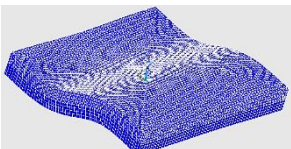

Figure 5-34: Test 07. MAC number representation for each mode-shape. The diagonal red blocks represent 100% consistency for each mode-shape.

To perform the FE-modal analysis for Test 07, the FE-model developed earlier for 'thermal analysis' (Section 4.7), was modified to suit the 'FE-modal analysis'. The modification was done by employing the 'support conditions' and the 'elements' suited for 'FE-modal anal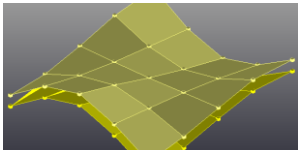ysis'. The rest of the procedure and the details were similar to the Test 06, therefore no details will be reported here.

The natural frequencies and mode shapes obtained from the FE-simulation are compared with experimentally computed modal parameters, (Table 5-14).

Table 5-14: Test 07. Two slabs with '3 Delaminations' on subgrade**.** Experimentally and Numerically obtained Modal parameters. A comparison.

Mode Nos	EXP Mode Shapes	FEA Mode Shapes	EXP Nat Freq (Hz)	FEA Nat Freq (Hz)	Error (%)
1	Diagonal Bending mode	Diagonal Bending mode	551.00	537.28	2.5
2	1st Bending mode (saddle)	1st Bending mode (saddle)	777.25	776.55	.09
3	Buckling mode (trough)	Buckling mode (trough)	874.04	876.34	-0.26
4	1st Torsional mode	1st Torsional mode	1240.44	1236.50	0.32
5	2nd Bending mode	2nd Bending mode	1912.81	1988.60	-3.9

A very good correlation between experimentally and numerically acquired modal parameters was achieved with an average error of less than 2% with respect to experimental results (Table 5-14). Hence, the developed FE-model is updated and can be used, later, for further evaluation or analysis purposes. It was also observed that the

natural frequencies were increased for all mode-shapes when compared to the *'control specimen-III'*. However, the order and pattern of the mode-shapes remained similar.

5.3.2.6 Results Discussion-Essential Tests (04-07)

All the concrete slab systems tested, while resting on subgrade (Test 04-07), showed variations in their modal parameters. They are now going to be compared in order to base our evaluations and interpretations for slab systems with designed defects (voids/debonding).

1. Test 03 Vs Test 04

A first comparison is made between the acquired natural frequencies (Hz) of a single 'robust' slab, *'controlled specimen-I'* and a single 'flawed' slab with 6 voids (Figure 5-35).

MODE SHAPES	Diagonal Bending mode	1st Bending mode	Buckling mode	1st Torsional mode	2nd Bending mode
Controlled Specimen-I	288.99	420.43	488.06	710.5	1195.71
Single Slab-6 Voids	343.24	451.55	500.01	754.97	1249.47

Figure 5-35: Tests 03+04. Experimental Natural frequencies (and corresponding mode-shapes). Comparison between Single 'robust' slab (Controlled Specimen-I) and Single slab with '6 Voids' on subgrade.

It was observed that the natural frequencies (Hz) for all corresponding modes of vibration in a slab with '*6 voids*' showed on an average of 7-8% rise, compared to '*controlled specimen-I*' (Figure 5-35). The difference in their natural frequencies

verifies the presence of voids, which were initially detected by the IRT (Ch 05, Test - 01).

The mode-shapes obtained from both tests (Test 03-04) showed similar pattern, which was expected (Table 5-10).
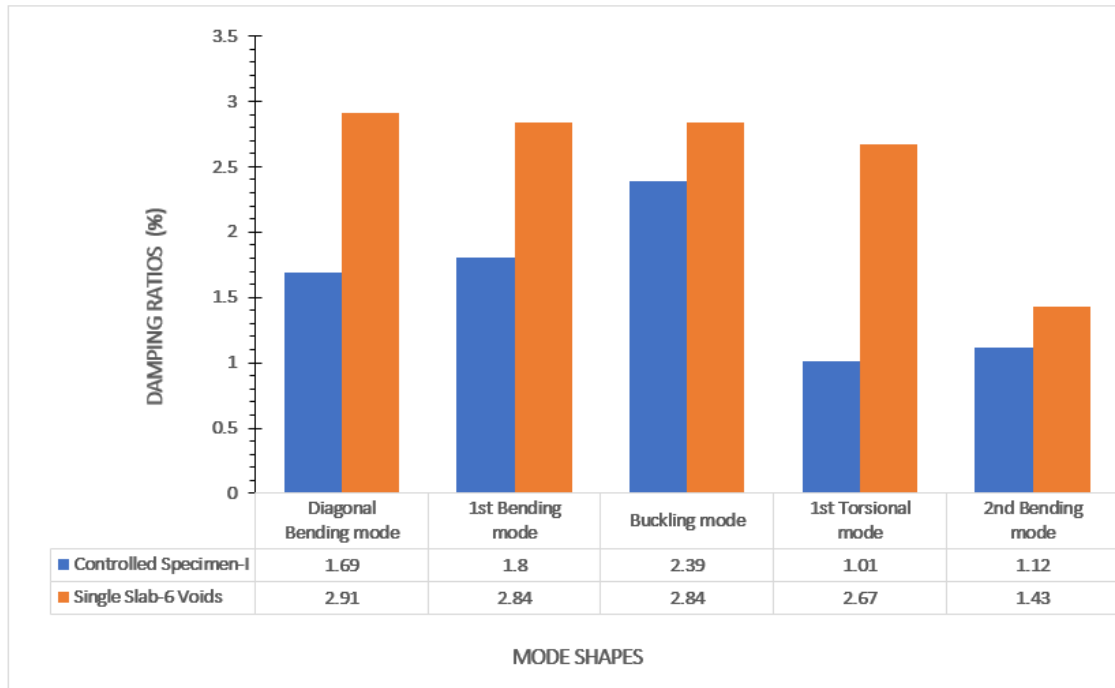
Figure 5-36: Tests 03+04. Experimental Damping ratios. Comparison between Single 'robust' slab (Controlled Specimen-I) and Single slab with '6 Voids' on subgrade.

By comparing the damping ratios, it was observed that a single slab with '*6 voids*' showed high damping ratios for all modes of vibrations, by an average of approximately 35.5% (Figure 5-36). This indicated that due to the presence of defects (voids), the damping ratios were increased. This was a good sign of using damping ratio as an indicator, for the flaw detection. However, more comparisons are still required, in order to monitor the consistency of this parameter, if it can be utilised as a reliable damage indicator.

2. **Test 05 Vs Test 06**

A second comparison is made between the acquired natural frequencies (Hz) of two-slabs stacked system, 'fully-debonded', '*controlled specimen-II*' (Test 05) and two-slabs stacked system, 'perfectly- bonded', (Test 06), and is illustrated in Figure 5-37.
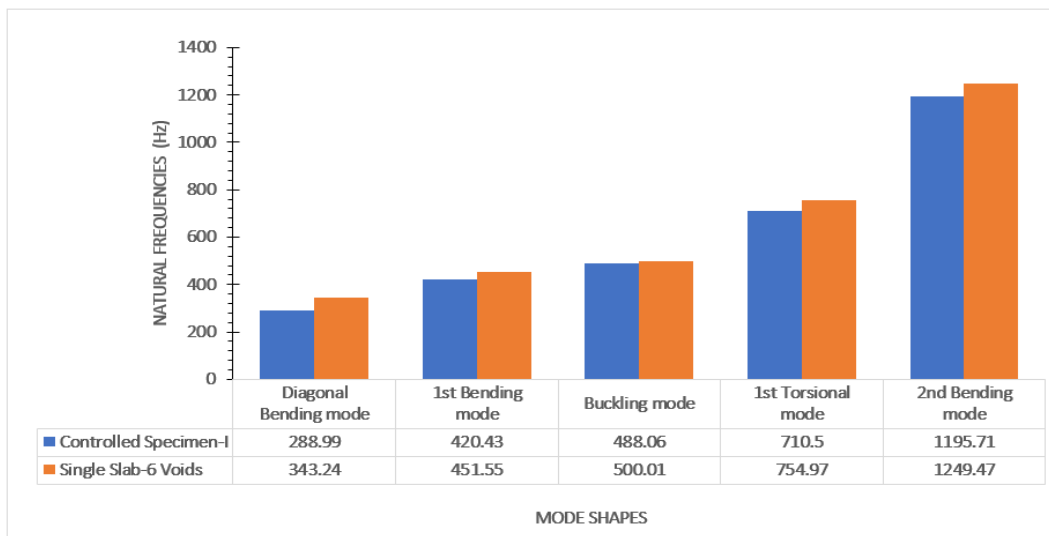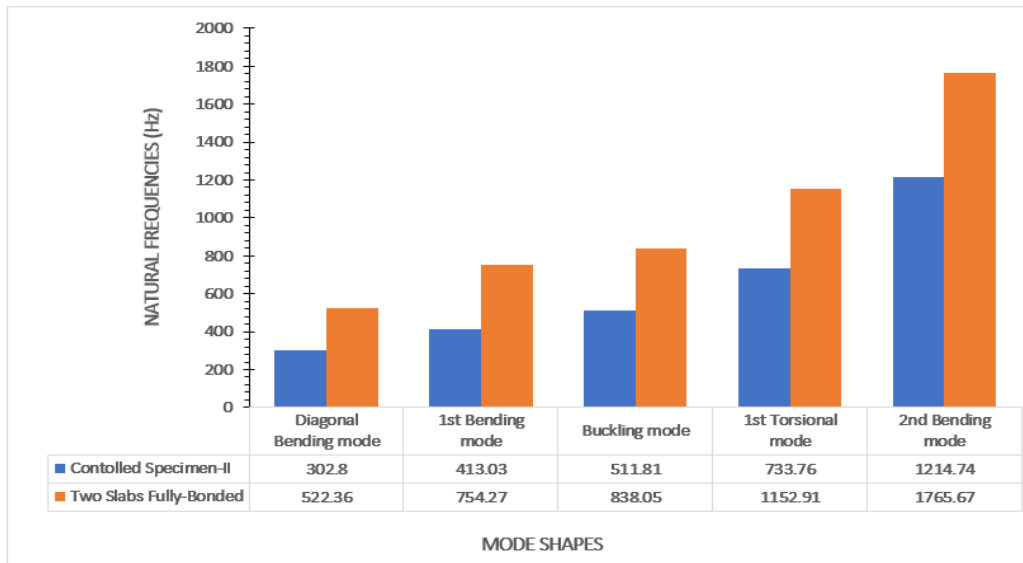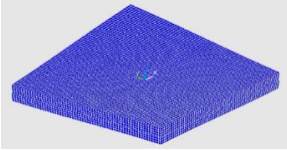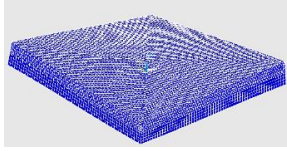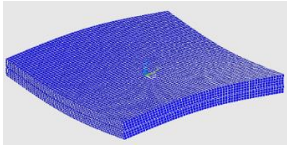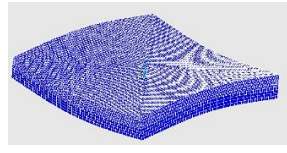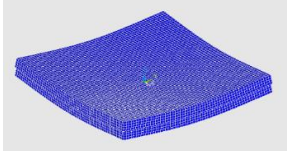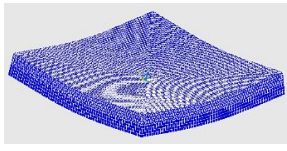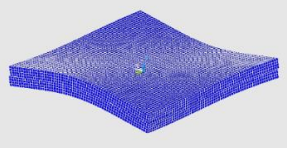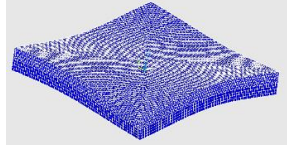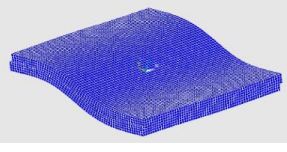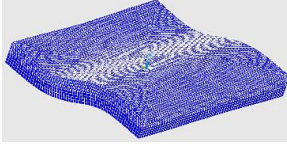

Figure 5-37: Tests 05+06. Experimental Natural frequencies (and corresponding mode-shapes). Comparison between Two slabs 'fully-debonded' (Controlled Specimen-II) and Two slabs 'fully-bonded' on subgrade.

It was observed that the natural frequencies for all corresponding mode-shapes in 'fully-bonded' slabs showed an average rise of 39%, compared to 'controlled specimen-II' (Figure 5-37). This difference was huge to identify the apparently looking two similar slabs system, however one is 'perfectly-bonded' and the other is 'fully-debonded'. This also endorsed the observation that debonding, decreases stiffness, and consequently decrease the natural frequencies of the structure.

The mode-shapes acquired experimentally from both tests (Test 06-07) showed similar patterns. As anticipated, the signs of separations in the 'fully-debonded' condition (*controlled specimen-II*), were not shown, since, the nodes at the soffit of the lower slab were not excited, and they acted as *'slave nodes'*, controlled by their *'master nodes'*, i.e.

nodes on the top. However, this limitation was cope up with the updated FE-model that showed slight but significant separation between the two 'full-debonded' slabs (Table 5-15).

Table 5-15: Test 05+06. FEA Mode shapes. Comparison between Two slabs 'fully-debonded' (*Controlled Specimen-II*) and Two slabs 'fully-bonded' on subgrade.

Mode Nos.	Controlled Specimen_II Mode-Shapes	Two-Slabs_Fully bonded Mode Shapes
1	Diagonal Bending mode	Diagonal Bending mode
2	1st Bending mode (saddle)	1st Bending mode (saddle)
3	Buckling mode (trough)	Buckling mode (trough)
4	1st Torsional mode	1st Torsional mode
5	2nd Bending mode	2nd Bending mode

Hence, it was observed that all the FE-acquired mode-shapes from the 'fully-debonded' slabs (*Controlled specimen-II*) showed signs of separation at their interfaces (though not exaggerated). This was encouraging, as these updated FE-models could be used instead, to differentiate the *'fully-debonded'* slabs from the '*perfectly-bonded*' slabs condition.

	Diagonal Bending mode	1st Bending mode	Buckling mode	1st Torsional mode	2nd Bending mode
Controlled Specimen-II	1.26	2.34	2.25	0.9	0.83
Two Slabs Fully-Bonded	2.38	1.34	1.8	1.97	1.15

Figure 5-38: Tests 05+06. Experimental Damping ratios. Comparison between Two slabs 'fully-debonded' (Controlled Specimen-II) and Two slabs 'fully-bonded' on subgrade.

By comparing the damping ratios, it was noticed that the 'fully-bonded' slabs, showed about 43% and 22% lower values for the 2nd and 3rd modes respectively. However, the rest of the modes, showed higher values on an average of 43%, compared to *'controlled-specimen-II'* (Figure 5-38). No conclusive trend was observed, this time.

3. Test 06 Vs Test 07

A third comparison is made between the acquired natural frequencies (Hz) obtained from two-slabs stacked system, 'fully-bonded', '*controlled specimen-III*' (Test 06), and two-slabs stacked system with '3 delaminations' (voids), Test 07 (Figure 5-39).

	Diagonal Bedning mode	1st Bending mode	Buckling mode	1st Torsional mode	2nd Bending mode
■ Controlled Specimen-III	522.36	754.27	838.05	1152.91	1765.67
■ Two Slabs-3 Delaminations	551	777.25	874.04	1240.44	1912.8
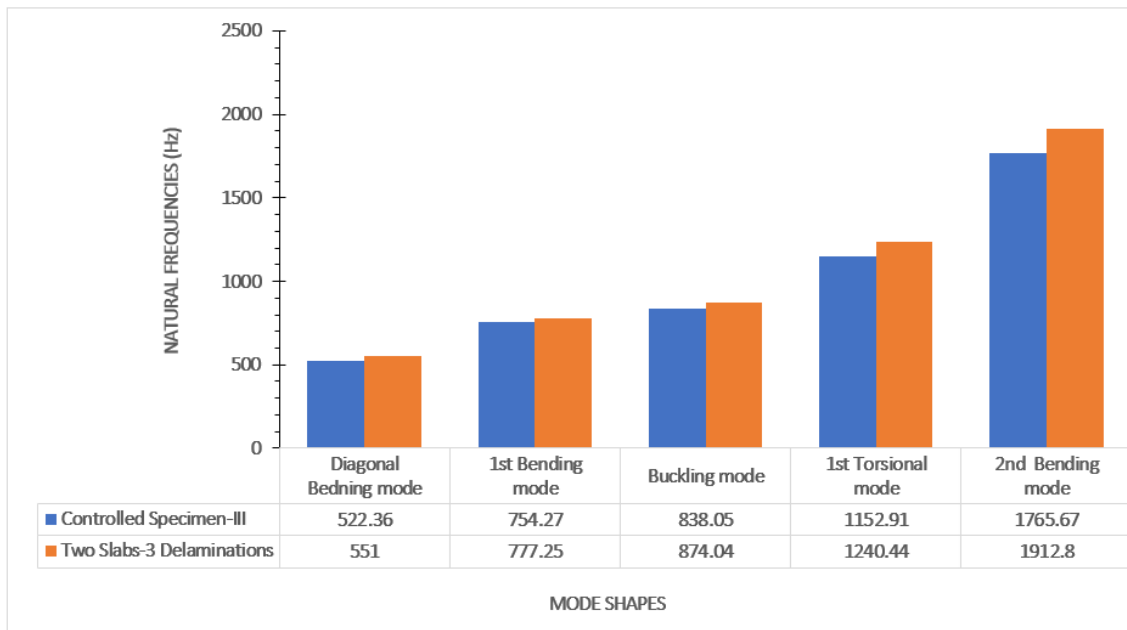
MODE SHAPES

Figure 5-39: Tests 06+07. Experimental Natural frequencies (and corresponding mode-shapes). Comparison between Two slabs 'fully-bonded' (Controlled Specimen-III) and Two slabs with '3 Delaminations' on subgrade.

It was observed that the natural frequencies for all corresponding mode shapes in 'flawed' slabs with 3 delaminations (voids), showed an average rise of 5% (Figure 5-39). These variations were significant enough to identify the 'flawed' slabs (3 delaminations) from the 'perfectly-bonded' slabs, that looked similar apparently. It is important to mention here that the delaminations are not merely due to debonding. In fact, since, their thicknesses (gaps) are increased, they tend to behave more like a void, and therefore, this reinforces compatibility between this research and real-life delamination.

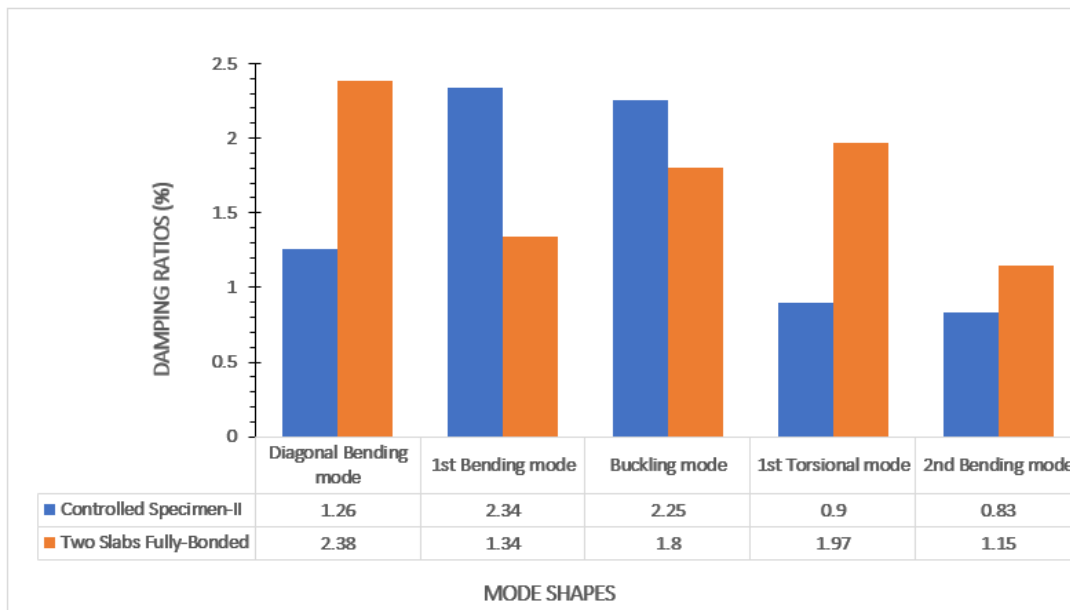The mode-shapes, obtained from both tests (Test 06-07), showed same pattern, which was already anticipated (Table 5-13).
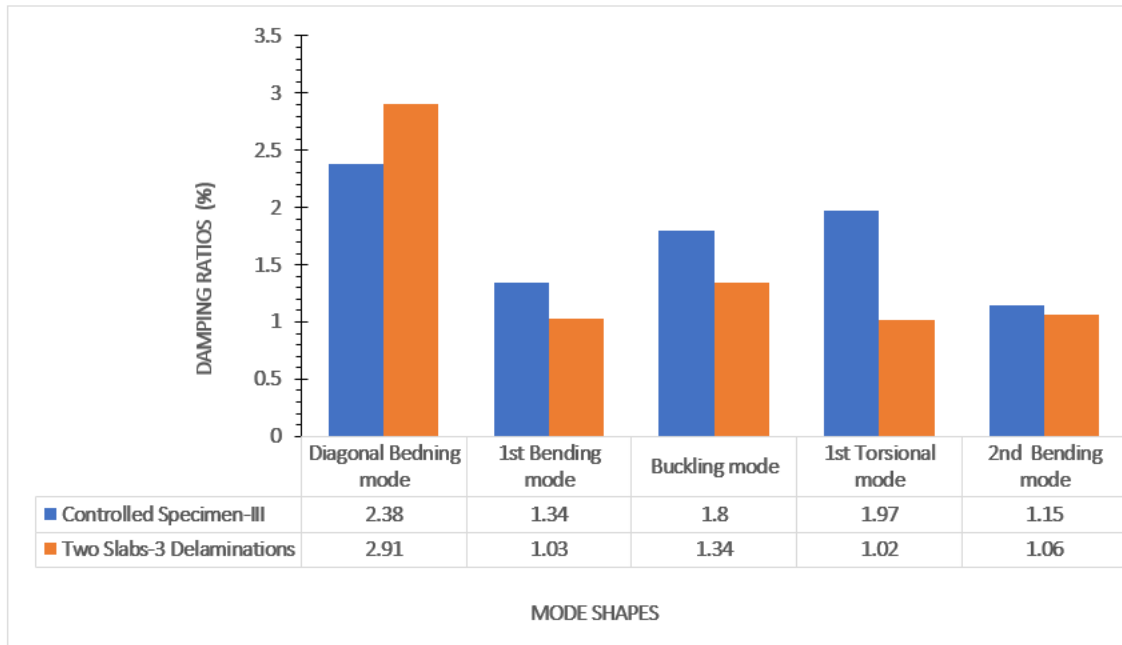
Figure 5-40: Tests 06+07. Experimental Damping ratios. Comparison between Two slabs 'fully-bonded' (Controlled Specimen-III) and Two slabs with '3 Delaminations' on subgrade.

By comparing damping ratios, it was noticed that the two 'flawed' (3 delaminations) slabs system showed relatively lower values, apart from the 1st mode of vibrations (Figure 5-40). This was unlike the trend as observed earlier in the single slab system, where the single 'flawed' (6 voids) slab showed higher values of damping ratios compared to the ones obtained from a single 'robust' slab (Figure 5-36). Hence, again, no definite trend was observed for the damping ratios in the two-slabs system. This reinforces the findings from Razak and Choi (2001), that the trend for damping ratios for the damaged structures is rather mode dependent, therefore, it is still inconclusive to find a particular behaviour from this parameter, and utilise it as a reliable damage indicator with confidence like the other modal parameters (natural frequencies and mode-shapes).

4. Global Summary (Test 03 Vs Test 05 Vs Test 06 Vs Test 07)

In order to have an overall picture of the differences observed between the acquired natural frequencies of all slab(s) system, it was decided to plot them altogether in one synoptic comparison graph (Figure 5-41).

MODE SHAPES	Diagonal Bending mode	1st Bending mode	Buckling mode	1st Torsional mode	2nd Bending mode
One Slab	288.99	420.43	488.06	710.5	1195.71
Two Slabs-Fully-Debonded	302.8	413.03	511.81	733.76	1214.74
Two Slabs Fully-Bonded	522.36	754.27	838.05	1152.91	1765.67
Two Slabs-3 Delaminations	551	777.25	874.04	1240.44	1912.8

Figure 5-41: Tests (03+05+06+07). Experimental Natural frequencies, Comparison between a Single 'robust' slab (Test 3), Two slabs 'fully-debonded' (Test 05), Two slabs 'fully-bonded' (Test 06) and Two slabs with '3 delaminations' (Test 07).
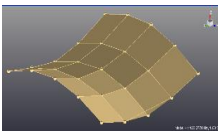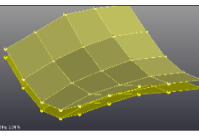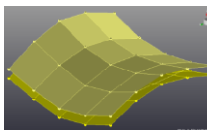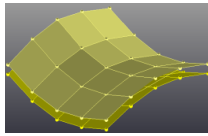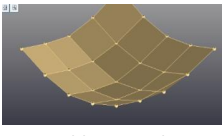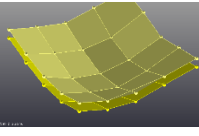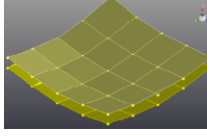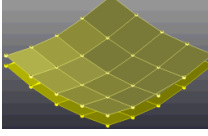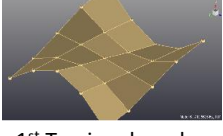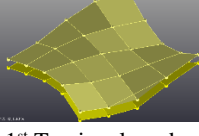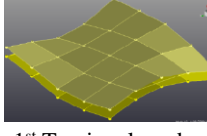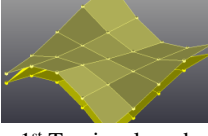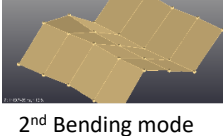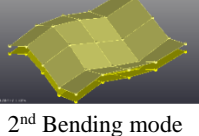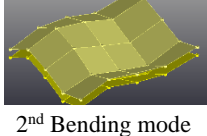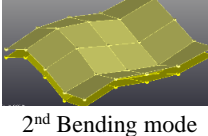
It was observed that two slabs system 'fully-debonded' (Test 05) showed approximately 2-3% higher natural frequencies (Hz) compared to a single 'robust' slab system (Test 03) for all corresponding mode-shapes. However, the 2nd mode of vibration (1st bending mode) showed slightly lower natural frequency i.e. by 1.6% (Figure 5-41).

Two slabs system 'Fully-bonded' (Test 06) on the other hand showed about 35-40% higher natural frequencies (Hz) compared to a single 'robust' slab system (Test 03). This enormous increase in natural frequencies (35-40%) was because of the high bending rigidity of the 'fully-bonded' slabs (Figure 5-41).

The two slabs system with '3 delaminations' (Test 07), showed natural frequencies (Hz) approximately 42-43% high compared to a single 'robust' slab system (Test 03) and 40-42% high, when compared to two slabs 'fully-debonded' system (Test 05).

Hence, from this synoptic comparison it can be summarised that, the slabs with voids showed higher natural frequencies, compared to their *controlled specimens*. Whereas, fully-debonded slabs showed lower natural frequency compared to the counterpart.

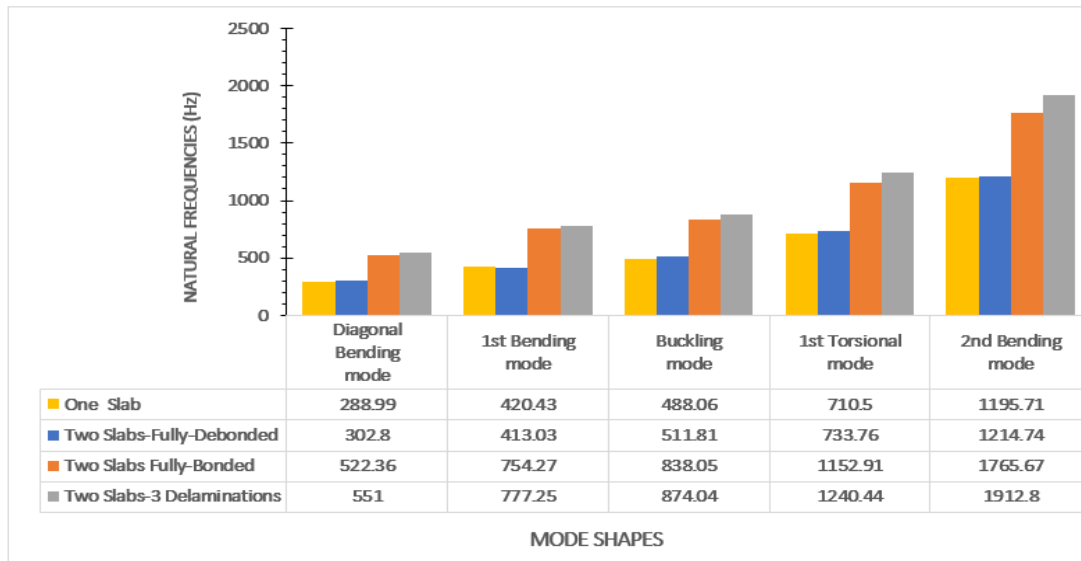Table 5-16: Tests (03+05+06+07). Experimental Mode shapes, Comparison between a Single 'robust' slab (Test 3), Two slabs 'fully-debonded' (Test 05), Two slabs 'fully-bonded' (Test 06) and Two slabs with '3 delaminations' (Test 07).
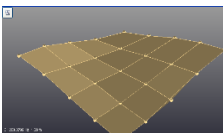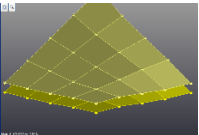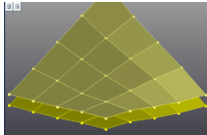
Mode Nos	Single Slab 'robust'	Two Slabs 'fully-debonded'	Two Slabs 'fully-bonded'	Two Slabs '3 delaminations'
1	Diagonal Bending mode	Diagonal Bending mode	Diagonal Bending mode	Diagonal Bending mode
2	1st Bending mode	1st Bending mode	1st Bending mode	1st Bending mode
3	Buckling mode	Buckling mode	Buckling mode	Buckling mode
4	1st Torsional mode	1st Torsional mode	1st Torsional mode	1st Torsional mode
5	2nd Bending mode	2nd Bending mode	2nd Bending mode	2nd Bending mode

It was observed that all the corresponding mode-shapes showed same pattern as expected (Table 5-16). However, in two slabs system with 'fully-debonded' condition, the FE-updated model can be used to show sign of separations (Table 5-15) instead of experimentally acquired mode-shapes, which were limited due to the reasons mentioned earlier.

	Diagonal Bending mode	1st Bending mode	Buckling mode	1st Torsional mode	2nd Bending mode
One Slab	1.69	1.8	2.39	1.01	1.12
Two Slabs Fully-Debonded	1.26	2.34	2.25	0.9	0.83
Two Slabs Fully-Bonded	2.38	1.34	1.8	1.97	1.15
Two Slabs-3 Delaminations	2.91	1.03	1.34	1.02	1.06
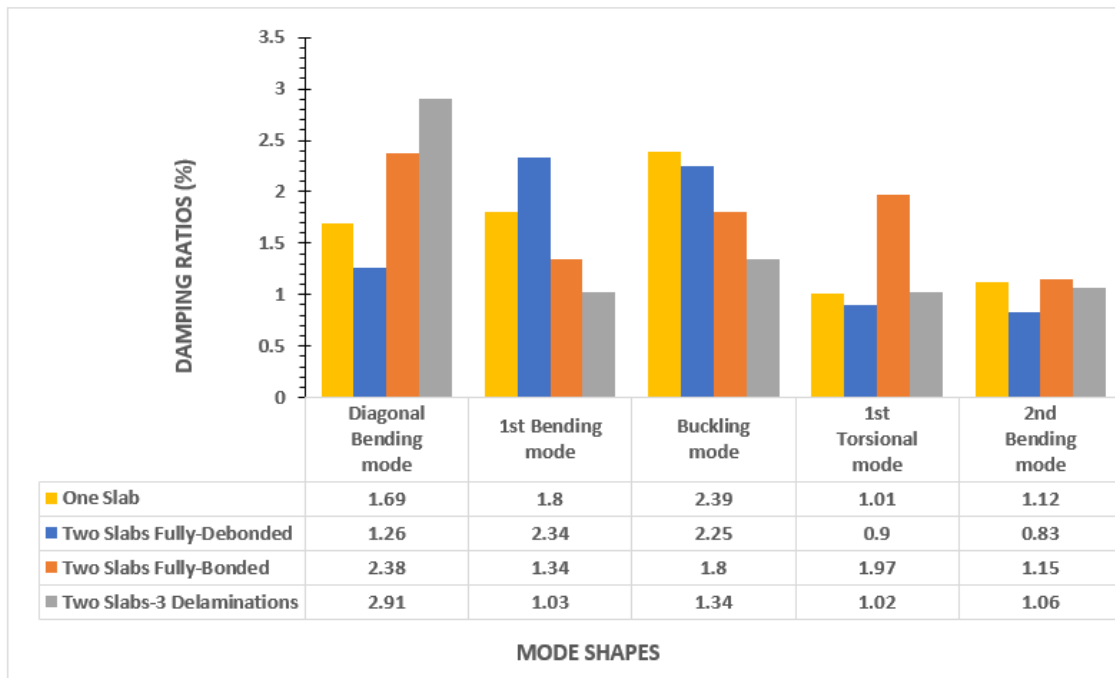
Figure 5-42: Tests (03+05+06+07). Experimental Damping ratios, Comparison between a Single 'robust' slab (Test 3), Two slabs 'fully-debonded' (Test 05), Two slabs 'fully-bonded' (Test 06) and Two slabs with '3 delaminations' (Test 07).
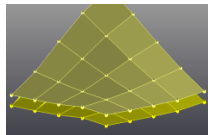
By comparing damping ratios (Figure 5-42), it was observed that for the 1st mode, the 'two slabs system with 3 delaminations showed the highest damping ratio (2.91%), whereas for the 2nd mode, two slabs system 'fully-debonded' showed the highest damping ratio (2.34%). For the 3rd mode of vibrations, a single slab system 'robust' showed the highest damping ratio (2.39%), and finally for the last two modes of vibrations, two slabs system 'fully-bonded' showed the highest damping ratios (1.97 % and 1.15% respectively).

Hence, from this comparison, it can be summarised that damping ratios were not showing any particular trend, rather their behaviour was mode-dependent, and therefore, necessitating further investigation, in order to utilise them in a definite manner, for identifying various bonding/debonding conditions.

The following can be deducted in summary:

1. The experimental modal analysis (EMA) and numerical modal analysis (FEA), showed reasonable correlation with an overall average error less than 3% in their acquired modal parameters (natural frequencies and damping ratios). Hence, the updated-FE-model can be used for compensating the experimental short comings.

2. *'Fully-debonded'* two-slabs stacked system (Test 05) showed 2-3% high natural frequencies compared to a single *'robust'* slab (Test 03).

3. A single slab with *'6 voids'* showed on an average of 7-8% rise in natural frequencies in comparison to a single *'robust'* slab (*controlled specimen-I*).

4. A single slab with '*6 voids'* showed high damping ratios of an overall average of 35.5% compared to a single *'robust'* slab (*controlled specimen-I*). However, the damping ratios for the two-slabs systems (Test 05-07) were not showing any conclusive trend.

5. *'Fully-bonded'* two-slabs stacked systems (Test 06), showed approximately 39% higher natural frequencies in comparison to '*fully-debonded'* two slab stacked system (control specimen-II). Similarly, the former also demonstrated 35-40% high natural frequencies when compared to a single '*robust*' slab (Test 03).

6. Two-slabs stacked system with '*3 delaminations'* (voids), showed 40-42% high natural frequencies compared to '*fully-debonded*' two-slabs stacked system (Test 05) and showed around 5% high natural frequencies, when compared to '*fully-bonded*' two-slabs stacked system (Test 06).

7. Mode-shapes of all the slab(s) systems (robust/flawed), showed similar pattern and order. From the experimentally acquired mode-shapes, the difference between '*fully-debonded*' two-slabs stacked system (Test 05) and '*fully-bonded*'

two-slabs stacked system (Test 06) was not noticeable. However, by using the alternate *FE-models*, the differences between their mode-shapes was visible, as the former was showing signs of debonding.

Following are the remarks, based on the above deductions:

1. 'Robust' slab(s) and 'flawed' slab(s) can be identified based on the variations of their modal parameters.
2. Natural frequencies and mode-shapes were observed to be more reliable indicators, to evaluate the flaws compared to damping ratios.
3. Though the damping ratios showed the variations between the 'robust' and 'flawed' concrete slab(s) systems, however a conclusive trend was not observed.
4. A clear demonstration of separation in 'fully-debonded' two-slabs stacked system (Test 05) was not observed on the subgrade support condition, as they were observed on the ETHAFOAM 220 support block (Test 02). This was anticipated, since the nodes on the lower slab were not excited one by one as they were excited in the previous case (Test 02). Moreover, the nodes at the soffit of the lower slab acted as 'slave nodes' and were controlled by their 'master nodes', i.e. nodes on the top. However, by using an updated FE-model, the signs of separation were noticeable, therefore, the FEA was compensating here the experimental tests with reasonable accuracy.
5. To evaluate each defect independently, it was required to carry out IHT on each 'defected' region separately but, in this way more slabs were required to be cast, where slab(s) each having only one defect at a time. However, by using a tuned or an updated FE-model, these lengthy and costly laboratory based tests were barred and the calibrated FE-models were deployed for further evaluations of multi-defects (voids/delaminations) in the concrete slab(s) system.
6. This combined modal analyses (EXP+FEA) verifies the presence of those defects (voids/delaminations) that were 'uncertain' during the IRT tests. However, the integrated-assessments (IRT+IHT) will be presented in the next chapter.

5.4 Summary

This chapter endeavoured to discuss fundamentals of *'Modal-Analysis'* and it's use, as a NDT&E technique for detecting and assessing 'flaws' in designed concrete slabs.

After giving a brief introduction to 'Experimental' and 'Finite Element' Modal Analyses and FE-model updating, the laboratory scaled tests (Preliminary and Essential) were outlined. Processing and analyses of Experimental and Numerical Modal Analyses were carried out for each test and the comparisons were made between all defined set of tests. Each set comprised of a 'robust' and 'flawed' slab(s) system, where the former was set as a *'controlled specimen'* or *'benchmark'* and the latter was compared to it and the variations in their modal parameters were recorded. Furthermore, numerical procedures (FEA) were combined with experimental tests, in order to have a cross-check with their corresponding results and to update the developed FE models. This FE-model tuning procedure, added more reliability to the IHT method, and were also utilised, at certain stages, as a compensation to the limitation of the experimental modal analysis.

Finally, inferences and remarks were made, and it was reported that the modal parameters, 'Natural frequencies' and 'Mode-shapes', can be used to identify and evaluate the flaws in the concrete slab(s) systems. Moreover, it was noted that with the aid of an updated-FE model, one can predict the variations in dynamic behaviour and can evaluate the defect (voids/delaminations) in concrete slab(s) system with reasonable accuracy and reliability.

Chapter 6 - Integrating Infrared Thermography and Impact Hammer Tests

6.1 Introduction

In the preceding chapters Infrared Thermography (IRT) and Impact Hammer Testing (IHT) were deployed independently, and tested on a number of concrete slabs with a variety of artificial flaws. Efforts were concentrated in improving each method, for detecting and evaluating the sub-surface defects, by studying and interpreting every possible output from laboratory tests. In parallel, the finite element (FE) method was used to assist with the above. Problems/limitations were also addressed, while steps were taken to minimise them. Some promising results were reported in Chapter 4 and 5.

It is now time to integrate the two (improved) methods into one, and develop a specific methodology and a detailed procedure that can be the birth (basis) of a new NDT&E technique, tailor-made for the detection and assessment of voids/delaminations beneath the top thin course in present concrete pavement construction, as illustrated in Figure 6-1.
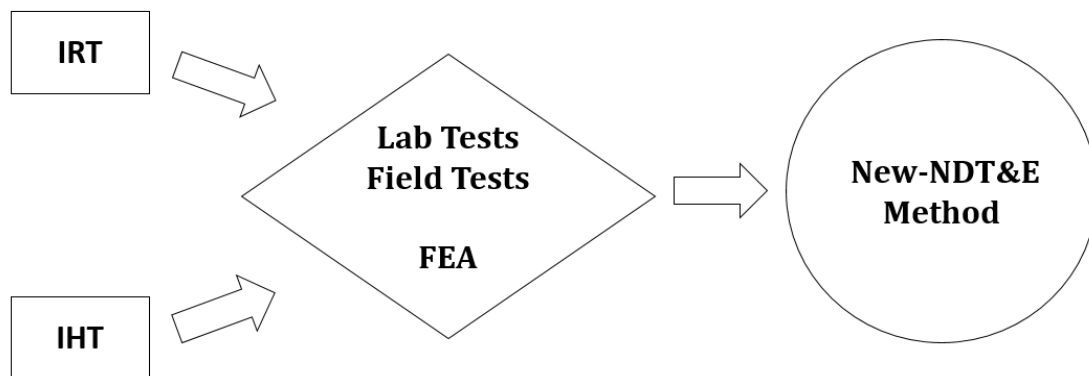
$$(IRT \; \cup \; IHT) \cap \{ FEA, Lab - Tests, Field\ Tests \} = New\ NDT \& E$$

Figure 6-1: Integrating IRT & IHT techniques.

6.2   "New"-NDT&E Method

It is expected that as per most road surveying procedures, the new NDT&E technique will be operational from a specially adapted road-testing vehicle, preferably a purposely designed light-weight lorry, or a vehicle similar to the one used to accommodate the Deflectograph, or the Deflectometer.

In brief, this test-vehicle, *The Flaw-Bond Detect-o-meter (FBD)*, will carry all the basic equipment required for the pavement survey plus two trained technicians (a driver and a computer operator). The vehicle will be equipped with two high resolution infrared thermographic (IRT) cameras mounted at the front (Figure 6-2), capable of continuously scanning the road surface and transmitting information to the on-board computer. A machine, similar to the light version of the Falling Weight Deflectometer will be providing the input signal (impact) on the road surface from inside the vehicle, and a set of accelerometers, or velocity transducers, mounted on two aluminium bars will be lowered on the ground to pick the signal and return it to the computer as illustrated in Figure 6-2.

The vehicle, equipped with safety hardware, will be moving at a relatively low speed, approximately 20kph (12mph approx.), when first indications dictate that there are no faults with the particular stretch of road. It should slow down to 5-10kph (3-6mph), when the IR Thermography test is in operation and the (possible) defects are being revealed. Their position will be located via an accurate GPS tracker. A schematic of the complete setup is shown in Figure 6-2.
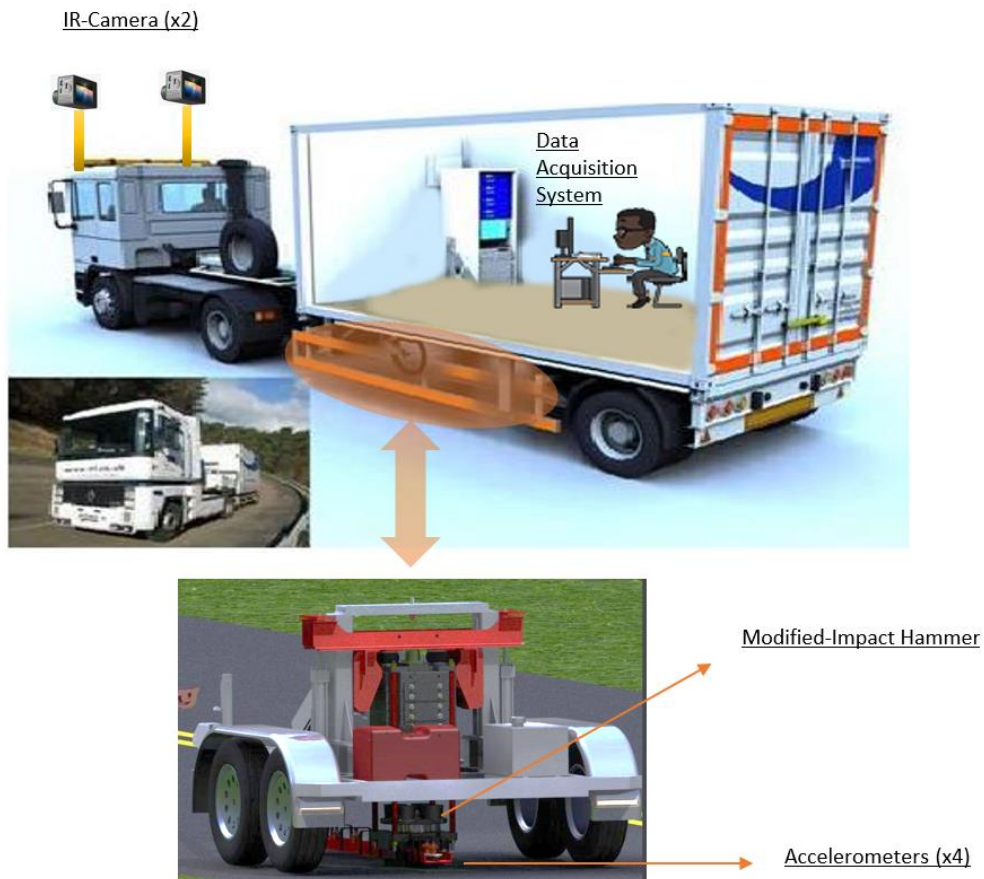
Figure 6-2: Researcher's vision of a Flaw-Bond Detect-o-meter test-vehicle, comprising: Infrared Cameras (x2), "Impact hammers assembly", Data Acquisition System (DAS), Driver and trained Operator.

THE PROCEDURE AT A GLANCE (Preliminary Survey):

As it has been implied earlier, a preliminary survey to familiarise with the site, note any irregularities and create a good testing plan, is highly recommended.

A good test-plan will include all basic information such as: Road stretch to be tested (length-km), lane (near-side, middle-lane, etc), bridges, drainage, various obstacles, approx. traffic volume, etc. This should allow the operator to build a draft visual image (field notes/sketches), similar to the one used in land surveys, of the road to be tested, including any obvious (by naked eye) defects etc, hence, produce the first digital road information map.

Once the preliminary survey is completed and a good test-plan is drafted, it is time to carry out the main survey.

THE PROCEDURE AT A GLANCE (Phase 01-Infrared Thermography Tests):

The main survey will start with the '*Passive Infrared Thermography'* test. It has been shown earlier in Chapter 4, that the best time of the day to carry out thermographic tests is daytime, preferably when the solar intensity is at its peak. This was manifested in a number of experiments carried out outside the Civil Engineering Laboratories of the University. Essentially, it was concluded that the (image) quality of defects (voids, delaminations) detected in a number of thermograms were significantly sharper and clearer during the heating session (daytime), compared to the cooling session (night-time).

In general, it was established that a higher thermal gradient is required to identify clearly, the sub-surface defects (voids/ delaminations) in the recorded thermograms. It was noticed that when the sun is at its Zenith, the solar intensity is high enough to cause high thermal gradients. In addition, due to the "vertical" direction (Zenith) of the sunrays relative to the earth, any shadows that may be casted by the surrounding bodies (trees, buildings) are minimal. This is an advantage as it should minimise the effects of non-uniform heating, otherwise caused by obstacles, such as, trees and shadows of surrounding structures.

It was also observed during the same tests that optimum results were achieved if the wind speed is less than 10kph (6mph). It was found that wind speeds above 16kph (10mph) affected the surface temperature (increasing the rate of heat convection and creating an unstable thermal gradient) of the target specimen, and therefore, reduced the ability of the infrared camera to detect the fault.

Keeping all the above and several safety precautions in file, the test-vehicle starts moving along the specified road with the (two) IR-cameras scanning the lane in front.

The driver and the operator are aware (from earlier visual tests stored in their computer) that the first road defects are approaching and slow the vehicle down to approx. 5kph (3mph). The Cameras are now scanning the road and the first information is recorded in the on-board computer. However, data are still "raw", and therefore, no decision has been made yet. This information is transferred via Bluetooth to a central, more powerful computer with processing capabilities and decision-making software. The test-vehicle (FBD) continues the survey, and information is continuously fed from the on-board computer to the central computer in the form of 'bundles of data' with accurate GPS references. An illustration of the above is shown in Figure 6-3.
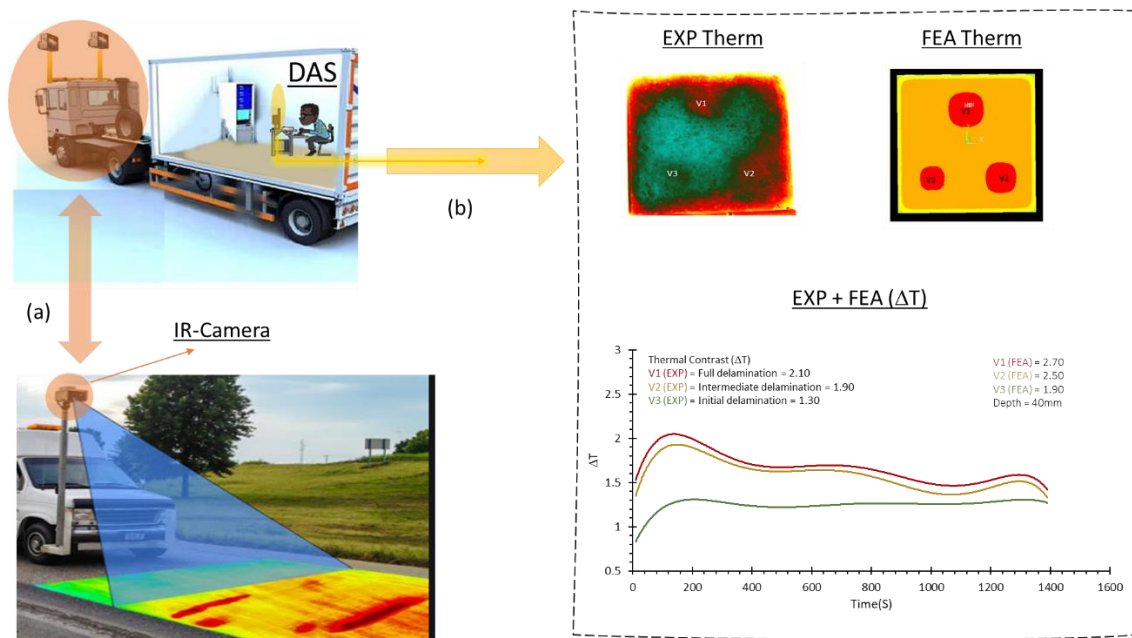
Figure 6-3: IRT-Test. (a) FBD is scanning the road ahead. (b) Info of defects detected is passed to central computer for processing via the on-board computer.

The central computer should decide if the specific problematic zone is classified as Green, Amber or Red zone. This classification is based on a three-way system similar to that of traffic lights. However, in this case each colour would specify the severity, or pliancy of the defect. Red colour would be used to represent a severely damaged area, most probably requiring immediate attention. On the opposite side, a green colour would specify a no-defect (sound) area, or a robust region, or at least an area of no

concern. Finally, an amber colour would specify uncertain conditions or a condition between a severely damaged bond and a robust region, a bond that has started to develop a fault but not necessarily requiring immediate attention.

Hence, based on the above classification, if the problem is classified as Green, the computer decides that no action is necessary. If the problem is classified as a Red, the computer decides a specific course of repairing action depending on the location, the size, the (existing) materials present, etc. It could even, provide an indication of the repair cost involved. However, if the problem is classified as Amber, this is an indication that no decision can be made by the IRT method, due to unclear detection of the defects in the obtained thermograms and their low thermal contrast values (minimum of $0.5^{o}C$ temperature difference as per ASTM D4788-03:2013). Finite element analysis might be used to provide an insight, or facilitate the decision making. However, if the latter is not reached, the central computer moves this information together with other, similar cases in a special database (matrix) and the first part, the IRT road test is terminated here.

THE PROCEDURE AT A GLANCE (Phase 02-Impact Hammer or Shaker Tests):

The central computer passes all (Amber) cases stored in the matrix back to the operations vehicle, and instructs the driver to go back to designated (Amber) areas by the GPS, to carry out the second phase, the impact tests, using the light version of the Falling Weight Deflectometer.

The latter should be fully controlled by the on-board computer, through its designated (interface) software. The operator does not have to step out of the vehicle. In fact, he should be able to control the whole test, from inside as illustrated earlier (Figure 6-2).

The procedure should be as follows: When the vehicle is stationary above the area of defects, the operator lowers the accelerometers (or velocity transducers) on the road surface. He then releases the weight to impact the road. The accelerometers pick the

signal and transmit it to the computer either remotely or via wires. Releasing and rewinding the weights can be automatic (servo motor). The accelerometers are now retracted, and the vehicle moves to the next location for more impact tests. It is worth mentioning here that the excitation signal could be either a random signal or a sine excitation. Both are relatively easy to produce.

Meanwhile, the FRFs obtained are passed to central computer via Bluetooth and the modal parameters are extracted. As "finetuning" is always necessary it is almost certain that this procedure will always be assisted by finite element analysis as a prediction tool. Therefore, the second test can provide all the information missed by the IRT and assist in making a decision (Green or Red). An illustration is shown in Figure 6-4.
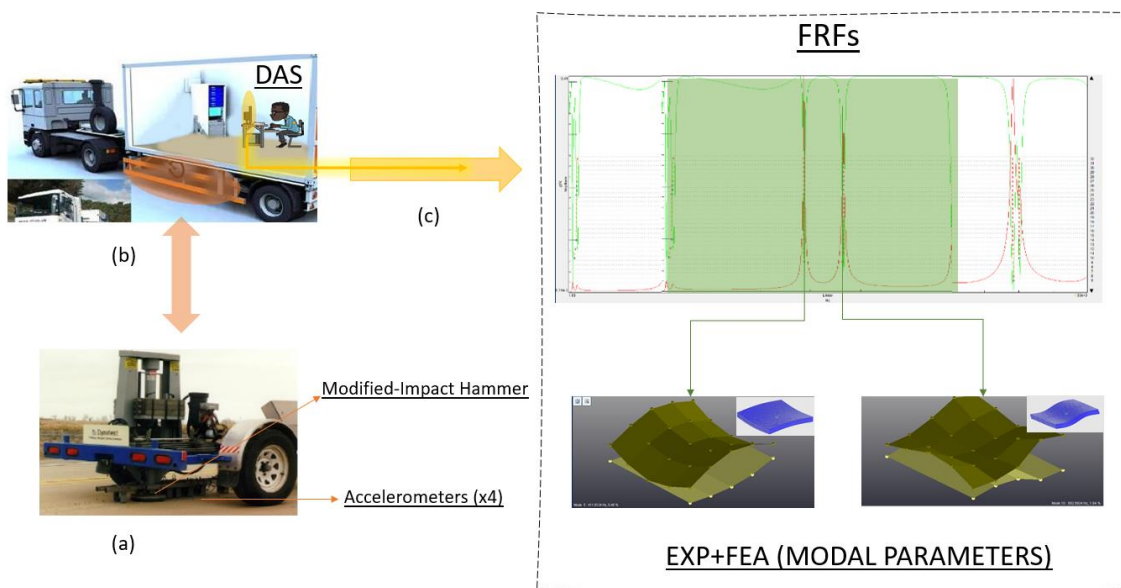
Figure 6-4: IHT-Test. (a): FBD is stationary above the area of defects (Amber). (b): Modified-Impact hammer housed within the vehicle impacts the road. (c): Information is passed from the on-board to central computer for processing.

Hence, with the help of the second test, the problem can now be re-classified either Green or Red, and can be stored in the right matrix in the main computer and dealt accordingly. However, in the unlikely case that no decision can be made even after the second test, then the potential-flaw shall be considered Red.

This was a general methodology and procedure of the proposed New-NDT&E method. The schematic below in Figure 6-5 shows a pictorial representation of this combined (new) method.
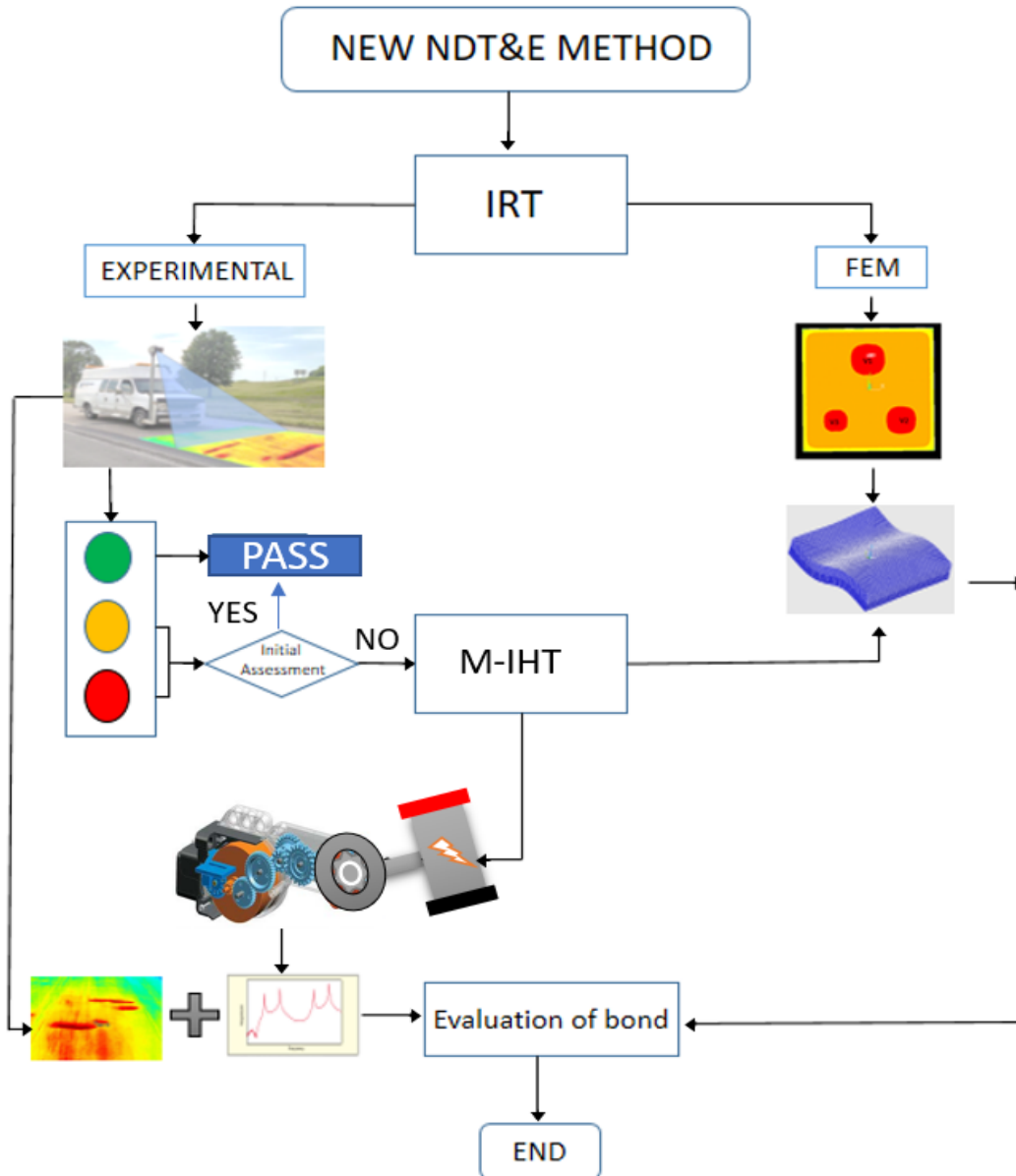
Figure 6-5: A pictorial representation of the new IRT+IHT method.

6.3 Summary

The development of a *new-NDT&E* method was discussed comprehensively, based on the integration of *IRT & IHT* along with the aid of FEA. A number of modifications were proposed for each technique, in order to make it feasible for actual road surveying. A *Red, Amber* and *Green* zone system was used to classify each defect. A schematic is provided at the end to illustrate the whole idea of integration of the IRT+IHT methods into one.

Chapter 7 - Conclusions and Recommendations

7.1 Introduction

Delamination as a recurring problem can spread fast, and even the initially sound areas may be rapidly effected, leading to further damage, in a short time. Therefore, early detection and evaluation will help in repairing the damage section before it spreads out. In parallel, timely evaluation will help in prioritising budgets, especially during current times, when there is already a maintenance backlog of over10 years (ALARM 2019). It is perhaps worth mentioning that no method has been accepted/adopted universally as yet, for the accurate detection and assessment (qualitative + quantitative) of the flaw-bond developing under the top thin road layer.

The two NDT&E techniques, Infrared-Thermography (IRT)' and 'Impact Hammer Test (IHT)' were scrutinised in this pilot study, as part of the first objective. The aim was to improve and "merge" these two otherwise well-established for different intend "incompatible" methods, and devise a "*new*" NDT&E procedure for the detection and evaluation of the flaw-bond under the top thin layer in rigid pavements (roads, airfields and bridge decks). This has not been attempted before, given the inherited incompatibilities of the aforementioned methods.

Hence, both NDT&E techniques were investigated in-depth, by carrying out a number of lab-scaled tests, accompanied by corresponding numerical studies on specially designed and constructed concrete specimens (solid and flawed). Some tests were carried out outside the laboratory in an effort to take advantage of the real environmental conditions and calibrate the numerical models with them.

The concrete specimens designed to contain voids/delaminations were tested and assessed qualitatively and quantitatively by the IRT and IHT methods. Finally, both the NDT&E techniques were joined together with some help from the finite element

analysis and the 'New-NDT&E method' emerged. In the absence of a full-scale validation (reasons explained earlier), a proposed implementation scenario is going to be presented at the end of this chapter, to help explain the procedures developed, and give a touch of reality in the method.

7.2 Key-Findings

To assist and comply with the tests procedure, the new method was divided into three main phases. Each phase was associated with a particular objective. The key findings in each phase are reported below.

<u>Phase-I, InfraRed Thermography (IRT)</u>

InfraRed Thermography (IRT) was examined and preliminary IRT tests (pre-IRT), followed by essential IRT tests were carried out outside the Civ. Eng. laboratories in a sunny (hazy sun) day with a surrounding ambient temperature range between 29-31ºC and a maximum wind speed of 8-10kph (5-6mph). Both tests were augmented with numerical models.

The IRT method was first employed on a Single, 40mm thick slab incorporating six subsurface voids (pre-IRT) of 3mm and 5mm thicknesses and at 10mm, 20mm and 30mm depths. These were evaluated qualitatively and quantitatively. It was concluded that:

1. A good correlation was achieved between experimentally obtained temperature distribution profiles and numerically simulated temperature profiles of the same parameter, with an average error below 2% for all voids. However, the thermal contrast (ΔT) values estimated for each void (Equation 4.16), showed slight discrepancies on an average of 10%. The highest ΔT value was found to be for shallow-thick (10.5mm) voids, such as:

$\Delta T_{(EXP)} = 2.33$ @ 220s and $\Delta T_{(FEA)} = 2.26$ @ 250s.

Whereas the least value was allocated to deep-thin (30.3mm) voids:

$\Delta T_{(EXP)} = 1.29$ @ 180s and $\Delta T_{(FEA)} = 1.01$ @ 180s.

These unique ΔT (peak) values, in conjunction with their corresponding time of occurrences, were useful in providing some information of the position of the void relative to the surface, although, the latter should be known and constant under normal circumstances.

2. The 300 seconds required for the voids to first appear in the computer screen (thermogram hot spots) and contribute to the assessment is a **crucial time** for the best possible quality of void detection by the IRT camera. This includes processing time by the *Research Max IR* software. However, with time, the visual appearance of deeper voids got much sharper.

3. Brief tests indicated that the combination of higher specifications (more powerful) computer and IR-camera can reduce the above time (although not dramatically), and improve the overall time taken for the procedure to produce more accurate results faster.

4. It is, of course, very encouraging that the FE models predicted the same time of 300 seconds for the shallow (10mm) and mid-depth (20mm) voids, for a variety of reasons. Also, as this "*time delay*" is now confirmed, it reinforces the need for segregation between initial detection of voids by the on-board computer, and final assessment by the central computer. In other words, an "instantaneous" detection-evaluation-decision is not realistic.

5. The 600 seconds taken for the deeper voids (30mm from the surface) to appear in the FE-thermal image, is in need of further investigation (although, it was noticed that the FEA software was unable to detect the minute temperature difference, occurred initially, until the thermal contrast became significant). First it was established that the 2 times the initial time taken, is related to the depth of the void as well as other parameters. This was investigated furthermore. It was found that the relationship between the depth of void and the time taken for its image to appear sharp in the screen is not linear. It was also realised that it was not possible to fit any curve with confidence as only three different depths could

be accommodated within the overall thickness (40mm) of the slabs used. However, this does not impair this method because the depth (position) of the void relative to the surface should be constant, usually 40mm throughout.

6. In general, and after a comparison between voids at 10mm, 20mm and 30mm depth, it was established that the depth of a void is more easily detectable than its thickness on the obtained thermograms. In other words, all shallow voids showed higher ΔT values, irrespective of their thicknesses, compared to the deeper voids. That is, the shallower the voids (10mm) in the slab, the sharper and clearer their IRT image too.

7. Also, thick voids (5mm) showed higher thermal contrasts (ΔT) compared to their corresponding thin voids (3mm) at the same depth.

8. Thin voids (3mm) took longer to reach their peak values of ΔT compared to corresponding thick voids (5mm).

9. Finally, it was found that deep voids (30mm below surface) took lesser time to reach their peak values of ΔT than voids at mid-depth (20mm) and the latter took even lesser than the shallow voids (10mm). That is shallow voids took the longest time to reach peak. This phenomenon was observed for both thick and thin voids, and is summarised below by reversing the statement (reverse engineering) in order to be used in the NDT&E method.

Given:

Two voids V1 & V2 in a pavement system:

such as: $\Delta T_{V1} > \Delta T_{V2}$, and thermogram formation (peak) times t_1 & t_2

Then:

$$\begin{cases} if: t_1 > t_2, \Rightarrow V1 \text{ is nearer to surface (shallower) than V2} \\ if: t_1 < t_2, \Rightarrow V1, V2 \text{ are at the same depth and V1 is thicker (more damaged) than V2} \end{cases}$$

The above can be attributed to the general rule that high temperature gradient will always be present at the beginning of the heating process, and therefore, during this

period the heat transfer rate is high and reduces with time, as thermal equilibrium is reached.

Hence, if the defects are close to the surface, the heat transfer rate will be higher, following Fourier's law of conduction (heat transfer rate is inversely proportional to thickness – in this case the defect). Heat will start concentrating over the surface above the void, causing high rise in temperature and finally a steep increase in ΔT.

In contrast, the heat transfer rate will be low and heat over the deeper voids will find the time to disperse due to the increased depth. This will result in lower temperature rise and the corresponding increase in ΔT will not be steep.

Finally, when both defects are at the same depth (classic case of top road layer delamination) the heat transfer rate from the top to the defects will be approximately similar. However, since one is more damaged (thick) than the other (thin), it will accumulate more heat. The rate of heat accumulated will be higher in the thick, more damaged case, resulting in relatively steeper rise of ΔT, and taking less time to reach its peak compared to the thin defect. In essence, this is where the IRT method relies to detect and evaluate voids (delaminations).

It was also noticed that depths and thicknesses of a void were "*compensating each other*" in using timings of the peak ΔT values. In other words, the occurrence of their peak values was determined by the combination of thicknesses and depth (variation of two parameters at the same time) of the void. Measuring from the surface:

Increasing the thickness (bad defect), or decreasing the position (shallow defect) of a void, resulted in a **steep rise of ΔT**. Whereas, decreasing the thickness, or increasing the depth of a void resulted in a **gradual rise of ΔT**. This can introduce complications in the detection and evaluation procedures in-terms of accuracy and confidence. The difference of thermal contrast (ΔT) values between thick and thin voids, when compared

via their depths, reduced significantly as the depth was increased. Beyond the 30mm depth it became difficult to differentiate between thick (5mm) and thin (3mm) voids. This is perhaps a downside of the IRT technique, and further information, or more sophisticated equipment may be necessary to compensate for the problem. At present, and in such circumstances, seeking clarification from the corresponding FE-models may be the answer but failing that, the IHT test should be taking over for further assessments/evaluations.

Similar patterns of thermal contrasts (ΔT) were observed in all voids; a steep rise, a peak, a gradual drop and a steady-state region. However, the values of peaks and the time taken to reach these peaks were different from void to void. This is promising and can be used as the basis for a detection and evaluation procedure. It is important to mention that sometimes the specimen does not have a uniform temperature. After exposing it to a heat source, this non-uniformity delays the pattern (thermal contrasts) to be developed. Therefore, sometimes it takes longer to observe an established pattern, as initially there is a random thermal contrasts profile forming.

The second group of tests was conducted on 'Two-slabs stacked system", containing 3-delaminations at their interface' (constant depth). This time thicknesses (voids) of 1mm, 2.5mm and 5mm, were considered in order to replicate the "*evolution*" of delaminations (initial, intermediate, severe).

It was observed with gratification that all three delaminations were detected in the recorded thermograms, despite of their small thicknesses and increased depth of 40mm. All delaminations were revealed at 710 seconds (approx. 12mins.) in the captured thermograms. However, the '*initial*' delamination, was not as *sharp* as the '*intermediate*' and '*severe*' in the captured thermogram. This shows that IRT struggles, when dealing with very thin (1mm), or an early stage delamination detection. It is noted that the same kind of problem (limitation) was also noticed earlier, in Test 01, while detecting and evaluating the deep-thin void (30mm, 3mm).

In parallel, the corresponding FE-thermal image, showed the 'severe' delamination at 710s. The other two (intermediate and initial) were revealed at 750s. A good correlation with an average error of approximately less than 2%, was achieved for all delaminations between the experimental and numerical results (temperature profiles). Whereas, the ΔT values estimated, showed slightly higher %error, on an average below 15%, however, it is still an acceptable range in transient analysis.

Summarising, the severe (5mm thick) delamination, revealed the highest estimated thermal contrast value of $\Delta T_{(EXP)} = 2.10$ @ 120s and $\Delta T_{(FEA)} = 2.70$ @ 100s.

The initial or "*just starting*" (1mm thick) delamination, showed the least thermal contrast peak value; $\Delta T_{(EXP)} = 1.30$ @ 200s and $\Delta T_{(FEA)} = 1.90$ @ 140s.

It was also noticed from the ΔT histories developed, that '*initial*' delamination took the longest time (200s) to reach its peak value and '*severe*' delamination took the least time (120s) to reach its peak ΔT. This trend endorsed the one obtained earlier in Test 01, where thin voids were taking longer to reach their peaks (ΔT) compared to thick voids at similar depths. Almost the same trend of ΔT was observed for each delamination, 'a sudden rise', a peak, 'a gradual drop' and a 'steady-state' to the end. This was again quite similar to the pattern observed for voids in Test 01.

It was concluded that the quality of defects (image of voids/delaminations) detected in a number of thermograms were significantly sharper and clearer during the heating session (day-time), compared to the cooling session (night-time). In general, it was established that a higher thermal gradient is required to identify clearly the sub-surface defects (voids/delaminations) in the recorded thermograms.

It was observed during the same tests that optimum results were achieved, if the wind speed was less than 10kph (6mph approx.). It was found that wind speeds above 16kph (10mph) affected the surface temperature (increasing the rate of heat convection and

creating an unstable thermal gradient) of the target specimen, and therefore, reduced the ability of the infrared camera to detect the fault.

Furthermore, it was found that the best time recommended to carry out IRT-tests is noon-time, since, the solar intensity is also high and possibility of detecting sub-surface defects (voids/delaminations) is maximum. In addition, due to the position of the sun (zenith) at this time of the day, the casting of shadows from the surrounding objects (buildings trees etc.) on the specimen are minimised. This reduces further the possibility of non-uniform heating. Finally, the best time to assess the condition of the voids was the time taken by ΔT to reach peak.

In addition, it was found that the use of 'Standard thermal contrast' in Passive thermography helped in analysing the results more efficiently, especially at the quantification process of the defects. This technique is generally applied in Active thermography, a quantitative technique, unlike passive thermography, which is mostly qualitative. Nevertheless, by utilising the 'standard thermal contrast' in passive thermography, helped improving the efficiency of the whole method, where all the defects (voids/delaminations) could be evaluated within 100-300s (2-5 mins approx.) by their unique ΔT peak values.

Moreover, with the inclusion of FEA, the overall reliability of the method was enhanced and founded, and therefore, satisfying the second objective of this research.

Phase-II, Impact Hammer Testing (IHT)

Results from the Impact Hammer Test (IHT) were associated with the third objective. A couple of preliminary tests, followed by a larger number of essential tests, were conducted on a range of concrete slabs, while initially "*suspended*" by ETHAFOAM-220 block, and later supported by a specifically built 'Subgrade'. These tests were also augmented by the updated FE-models.

The aim of the preliminary IH-tests, was to determine the dynamic behaviour of the 'Single *robust* concrete slab' and the Two-slabs stacked system with no bond (fully-debonded conditions), and use them later as a control specimen.

From the initial comparison, it was observed that the 'Two slabs, the fully-debonded system' showed an average 3% higher natural frequencies for *diagonal* bending and 1st *torsional* mode, compared to single '*robust*' slab system for similar mode shapes. However, the latter showed about 1% higher value (natural frequency) in the 1st bending mode, 8% in *buckling* mode and about 15% higher in 2nd bending mode compared to the former. At this stage there was not obvious or reasonable trend observed between the two from their natural frequencies, however, the Mode Shapes of two fully-debonded slabs system, showed separation, as illustrated by the (exaggerated) mode-shape animations, in the experimental modal analysis and were verified by the finite element analysis.

In addition, the predicted damping ratios of the two fully-debonded slabs showed 29% (approx.) higher values compared to single 'robust' slab for all similar mode shapes except for the buckling mode. This should be expected as, in general, the higher the mass non-participating in the motion, the higher the damping present (double slab system acts as a damper compared to the single slab system when the two slabs do not vibrate in unison). However, mode 3 produced an approximately equal damping between single and double slabs. This indicates that mode 3, a purely buckling mode, is very tuneful, and that the two-slab system does vibrate in unison.

The essential tests were carried out on a range of Single and Two-slabs stacked systems. However, this time, a 'Subgrade' layer was introduced approximating realistic support conditions, hence, each slab system was placed and tested on the subgrade. The aim of these tests was to determine the variations in the dynamic properties of each slabs system associated with the voids, or a particular debonded condition. From the results of experimental and numerical (FE) modal analysis, a good correlation with an overall

average error less than 3% was achieved. Hence, the updated FE-models can be used on their own, replacing similar experimental conditions.

It was observed that a single slab with *'6 voids'* showed an average of 7-8% rise in natural frequencies in comparison with a single *'robust'*, no-voids slab (controlled specimen-I). The same voided slab showed 35.5% higher damping ratios compared to the robust slab.

In contrast, the damping ratios for the two-slabs stacked systems did not show any conclusive trend. It was observed that their behaviour was rather mode-dependent, and therefore, needs further investigation, in order to utilise them in a conclusive manner, for identifying various bonding/debonding conditions.

A two-slabs stacked system *'fully-bonded'* showed an average rise of 39% compared to the two-slabs stacked system *'fully-debonded'*. This difference was significant to differentiate the apparently looking two similar slabs system, however, one is perfectly bonded and the other is zero bonded.

The Two-slabs stacked system incorporating *'3 delaminations'* (voids), demonstrated 5% higher natural frequencies, when compared to the '*fully-bonded'*, sound, two-slabs stacked system (control specimen – no delaminations).

Mode-shapes, although difficult to recognise, played a vital role in the comparison. Efforts were directed in comparing similar mode shapes, although, it is understood that it may be possible for the amount and size of delamination to change the mode of vibration of a system. From the experimentally acquired mode-shapes, the difference between the fully-debonded two-slabs stacked system (Test 05) and the fully-bonded two-slabs stacked system (Test 06) was not obvious. However, by taking advantage of the alternative *FE-models*, the differences between their mode-shapes was visible. The former was showing signs of debonding.

It is apparent that Robust slabs and Flawed slabs can be identified based on the variations of their modal parameters. Natural frequencies and mode-shapes were observed to be more reliable indicators to evaluate the flaws compared to damping ratios. Although the latter showed variations between robust and flawed concrete slab systems, a conclusive trend was not reached.

Phase-III, Combined IRT+IHT – ''New''NDT&E Method

The improved versions of two aforementioned, and initially non-compatible NDT&E techniques were integrated into one, and a set of new guidelines were put forward paving the way for the implementation of a '*New-NDT&E method*' assessing rigid pavement systems. This was related to the last objective of this research study. It was envisioned that these two techniques, if modified and enhanced appropriately, could be a way forward to answer the problem of accurate detection and assessment of thin overlay delaminations.

A test-vehicle, the *Flow-Bond Detect-o-meter (FBD)*, equipped with all the essentials (Infrared Cameras *(*x2*)*, Modified-Impact hammer device, Data Acquisition System *(*DAS*))* and two trained operators was proposed.

It was demonstrated how the improved version of IRT and IHT could be used to detect and evaluate/classify delamination. A special '*three*-way' system analogous to traffic lights (Green, Amber, Red) was proposed. Each colour signified the severity of delamination. It was also illustrated that FEA can be a useful prediction tool to supplement the IRT method, if the data collected from the site were not conclusive (Amber). It is accepted that the introduction of IHT would slow down the evaluation procedure but this should not always be present, and it is the *price-to-pay* to increase reliability.

7.3 Principal Limitations and Future Recommendations

It is apparent that the choice of thermal imaging camera is very important and has a knock-on effect at the quality of data collected.

The thermal imager used in this research also known as 'uncooled microbolometer', is generally suitable for static building surveys. They have relatively low frame rates, unprecise triggering and more integration time, they are unsuitable for the pavement surveys, while the vehicle is moving at a certain speed (15-20kph).

In contrast, there are advanced high speed thermal imaging cameras available, with higher frame rates (100Hz), also known as 'cooled-microbolometers'. In general, they are extremely expensive (£150k-200k) than the former and obviously more efficient. These cameras have global shutters compared to roller shutter (former case), which improves the image blurring and quality of the thermal image due to shaking, common in pavement surveys.

The latter can easily perform spectral filtering, capturing minor details, otherwise left out by the 'uncooled microbolometer'.

Moreover, these high-speed cameras are more sensitive to thermal changes, and therefore, can detect fine thermal anomalies and for longer duration, compared to their counterparts. Hence, they provide better details of the target. This might help in distinguishing the early stage of a delamination (less than 1mm thick), better than the former. Hence, the verdict here is: The higher the specs, the more expensive the camera, the more accurate the detection.

A second limitation (also mentioned earlier) is the dependency of the infrared radiation detection technique on environmental conditions. Optimum results were observed, when the wind speed was lower than 10kph (6mph), during noon time, minimising the

possibilities of the shadow casting due to surrounding objects (trees, buildings etc.), hence, avoiding non-uniform heating of the specimen. In addition, IRT cannot be carried out during rainy or snowy day, although still possible on a hazy-day.

A third limitation is associated with the speed (overall time-taken) of the method when the m-IHT method is recalled. This applies to all Amber regions, as explained earlier, and will necessitate for the operations vehicle, to revisit the particular Amber site, and carry out (complementary) impact tests in a stationary mode. This, of course, delays the overall procedure. It is however anticipated that this would not always be the case, and in return accuracy is the reward.

Despite of promising results obtained from the lab-scaled tests conducted, optimisation (micro-modifications, fine-tuning) of the new method would still be appropriate before implementing it into full size field tests. A set of new guidelines were already developed in the previous chapter, demonstrating the application of the whole method on real pavements.

The following are recommendations for more research.

- A large size shaker to replace the hammer, modified in such a way as to allow full operation of the m-IHT method from inside the vehicle is highly recommended. The test procedure should be similar to the light version of the Falling Weight Deflectometer (FWD). There should be no need for a grid, as frequencies obtained will not be based on a free vibration approach, but rely on the correlation between input (excitation) and output (response) signals.
- After carrying out the successful site trial tests, efforts can be extended and directed towards the real time pavement surveys. It is envisioned to devise a cost-effective programme by developing an expert software (NDT&E-Intelligent Management System), to integrate the data gathered from IRT and IHT, and their interpretation.

- The system should incorporate a test programme for fast and efficient quantitative and qualitative detection of delaminations, and should identify long or short-term maintenance needs. Essentially, a pre-calibrated, automated intelligent system is proposed, designed to make decisions, as to whether the particular site is sound or in need of repair, evaluate the amount of damage, if any, and even suggest typical methods of repair and costs based on the proposed *'three-way system'*. The System will allow future input of a series of other data related, for example, to pavement serviceability variables, to yield a basis from which to develop a number of management information expert system formats.

- As it was observed that the thickness and the depth of a defect were compensating each other in the determination of thermal contrast values. However, what-if the depth varies too or it is unknown, and one cannot decide, if the thickness is responsible for the thermograms obtained or the depth. This would need further research to investigate the combined effects of these two parameters (perhaps sensitivity analysis) on the unique thermal contrast values and thermograms display.

7.4   Proposed Implementation Scenario

To demonstrate the complexities one would encounter if real tests were performed on a stretch of road. A proposed implementation scenario like the below can be useful to help the investigators understand, how the complexities of real-life influence decisions but also to detect and unwrap any glitches (bags) that the method may hide.

It has been stressed that, early stage detection of delaminations is crucial. However, the latter are the hardest to detect, and therefore, the consequences are twofold: First, if the particular defect goes undetected, it will progress to a pot-hole, which is exactly what the research is trying to eliminate. Second, it can become hazardous to traffic, and therefore, require urgent repairs as an emergency case, and mounting costs.

Hence, to deal with the detection and full-evaluation (qualitative + quantitative) of this specific flaw, *delamination*, particularly when it is in its early stages, this 'New-NDT&E method' developed and proposed earlier (Chapter 06) will be deployed to demonstrate its real-time applications. For this purpose, a virtual scenario is created, that will reveal, how one NDT technique supplements the other and provides a full-evaluation of the sub-surface delaminations.

It is reminded that the sub-surface flaws (voids/delaminations) picked from the lab-tests for this virtual scenario, were deliberately designed with simple geometrical shapes. This might not be the case in the real-tests, but will set bases for the' *'detect-assess-decide'* programme.

Two particular slab systems: *'Single slab with 6 flaws (voids)'* and '*Two-slabs stacked system with 3 delaminations',* that were tested initially via IRT (Chapter 4) and IHT (Chapter 5), are chosen as representative examples for this proposed implementation scenario. The single slab with 6 voids is chosen, since, it can be used to give a good representation of how the delaminations can be classified based on their visual appearance (thermograms) and on their thermal contrast values. It can also be exploited for the uncertain and unclassified delaminations and the insufficient evidence for a tangible decision.

The two-slabs system was chosen because it displays certain similarities with any layered road (pavement) system, where various stages of delaminations (*Initial, Intermediate* and *Severe*) exist between the thin overlay and the base. It is worth remembering that in full-size real pavement systems, the depth to delaminations is constant (usually 40mm), between the top, thin layer and the base.

Proposed Method/Solution

A hypothetical scenario based on the real ambient conditions can be envisioned, that on a good sunny day at a temperature range of $22^{\circ}C – 25^{\circ}C$ and a wind speed of 10kph (6mph), a road survey is planned to be conducted at around noon time.

A hypothetical bridge deck has been chosen for the survey, as part of a predictive maintenance. Prior to the main tests, a preliminary survey has been conducted, and a few notes should be made regarding, for example, any surface irregularities, debris, drainage, safety barriers, etc.

The specially adapted test vehicle, the FBD (Flaw Bond Detect-o-meter) mentioned earlier, is brought on site (the bridge). The FBD should be equipped with all the essential equipment, including IR-cameras, modified-Impact hammer machine, computer and a data logger, and two operators, one steering the vehicle and the other operating the computer as illustrated, in Figure 6-2 (Ch 06, Pg:259). The entire procedure should be fully controlled via the on-board computer.

IRT-Test: The FBD is brought to one end of the bridge surface to be tested. Final checks are made before the start of the survey and the position and angles of the mounted IR-cameras adjusted. The initial settings of the camera, emissivity value, ambient temperature, relative humidity, the estimated distance between the lens and the road surface, should be fed via an interface software, '*Research-Max-IR*' (FLIR Systems Inc. 2016). The GPS system is also synchronized with the IR-camera recordings, in order to track the location of the defects.

Following operator's instructions the driver steers the vehicle at a low speed of 20kph (12mph). The cameras are switched ON, and the first scanned images of the bridge-deck arrive in the computer; the operator observing the thermograms in his screen. If the first thermograms show nothing but a constant dark colour, this is an indication that the top

layer of the road is well bonded to the base, and no delamination is present. Therefore, this road surface is classified as Green

As soon as the first indications (bright spots, or patches, or areas) of a fault arrive on the computer screen, the operator should instruct the driver to slow down the vehicle, to approximately 5-10kph (3-6mph).

The first potential defects are now shown in the computer screen. The driver slows down on the operator's call and the defect is captured in the thermograms. The test-vehicle keeps moving slowly and more potential defects start showing in the computer screen. A scan of the first half of a 2km long bridge deck is completed, and the following potential defects are observed in the recorded thermograms (Figure 7-1).
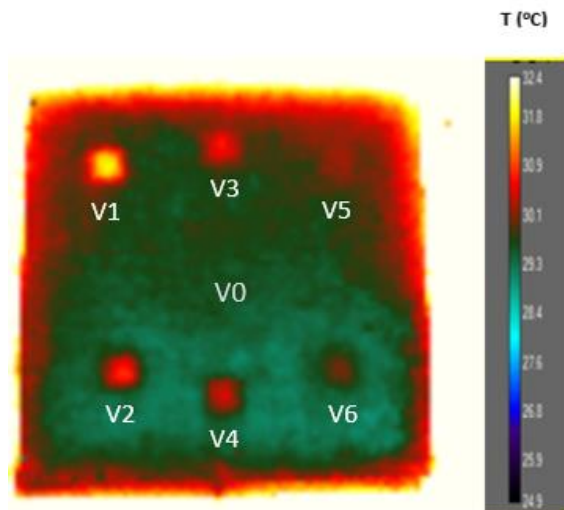
Figure 7-1: 6-potential defects are observed via IRT in the stretch of 1km scanned length of a total 2km long bridge deck.

The absolute temperature difference and thermal contrast (ΔT) values are estimated for each detected defect with respect to a reference (sound) region or '*fully-bonded*' region which is represented by V0 and is classed as '*Green*' (Figure 7-1*)*.

A summary of the "results" obtained for the detected defects is presented in Table 7-1.

Table 7-1: Test 01 (Ch 4). Thermal contrast obtained by the IRT test (EXP+FEA). 'Single concrete slab system incorporating '6-Voids''.
Note: ΔT = thermal contrast (dimensionless)

Defects	EXP-Abs Temp Diff (°C)	EXP-ΔT Peak value	FEA-Abs Temp Diff (°C)	FEA-ΔT Peak value	Preliminary assessment	Delaminations Classifications
V0 (Reference)	NA	NA	NA	NA	Fully-bonded	Green
V1	5.8	2.33	4.8	2.26	Clear detection-classification, no need for further assessments	Red
V2	2.8	1.60	2.9	1.80	Clear detection-classification, no need for further assessments	Red
V3	1	1.45	2	1.11	Clear detection-classification, no need for further assessments	Red
V4	0.6	1.35	1.8	1.09	Clear detection-classification, no need for further assessments	Red
V5	0.4	1.30	0.8	1.06	Unclear. Further assessment necessary	Amber
V6	0.2	1.29	0.4	1.01	Unclear. Further assessment necessary	Amber

It is important to remember that as the thickness of the layer is constant, the depth of these defects is not a variance. Therefore, only the thicknesses (*degree of delamination*)

of the defects will define their characteristics. This, somehow, simplifies the whole detection procedure.

The first four defects, captured in the thermograms are represented by V1, V2, V3 and V4 (Figure 7-1). First, by looking at their thermograms, the defects are clearly recognized. Their absolute temperature differences are also taken into an account in addition to their visual assessments. It is noticed that all these defects showed high absolute temperature differences i.e. V1 = 5.8 ^{o}C (ΔT = 2.33); V2 = 2.8 ^{o}C (ΔT = 1.60); V3 = 1 ^{o}C (ΔT = 1.45) and V4 = 0.6 ^{o}C (ΔT= 1.35) compared to the (reference) adjacent sound region, V0 (Table 7-1). These differences are more than 0.5^{o}C, which, according to ASTM D4788-03:2013 is the least difference to be classed as delamination. Whereas, V5 and V6, showed an absolute temperature difference of 0.4 ^{o}C (or 1.30 ΔT) and 0.2 ^{o}C (or 1.29 ΔT) respectively (Table 7-1), which is less than 0.5^{o}C (ASTM D4788-03:2013). However, by looking at their thermograms (Figure 7-1), the defects are fairly visible and therefore, they cannot be neglected.

Based on the above criterion (ΔT values + thermograms display), the central computer would classify V1-V4 as Red, indicating severe delaminations, thus requiring immediate action. Whereas, for V5 and V6, FEA should be sought for assistance, as there is uncertainty observed in the test results (ΔT + thermograms), and the decision alone based on test results is not possible. In the particular case that FEA, in combination with the IRT tests, cannot provide a decision, the particular defects, V5 and V6, will be collected in the special database of the central computer to be tested again later on with the IHT method.

A synoptic demonstration of the IRT-survey for the first half (1km) of a bridge deck is illustrated in Figure 7-2.
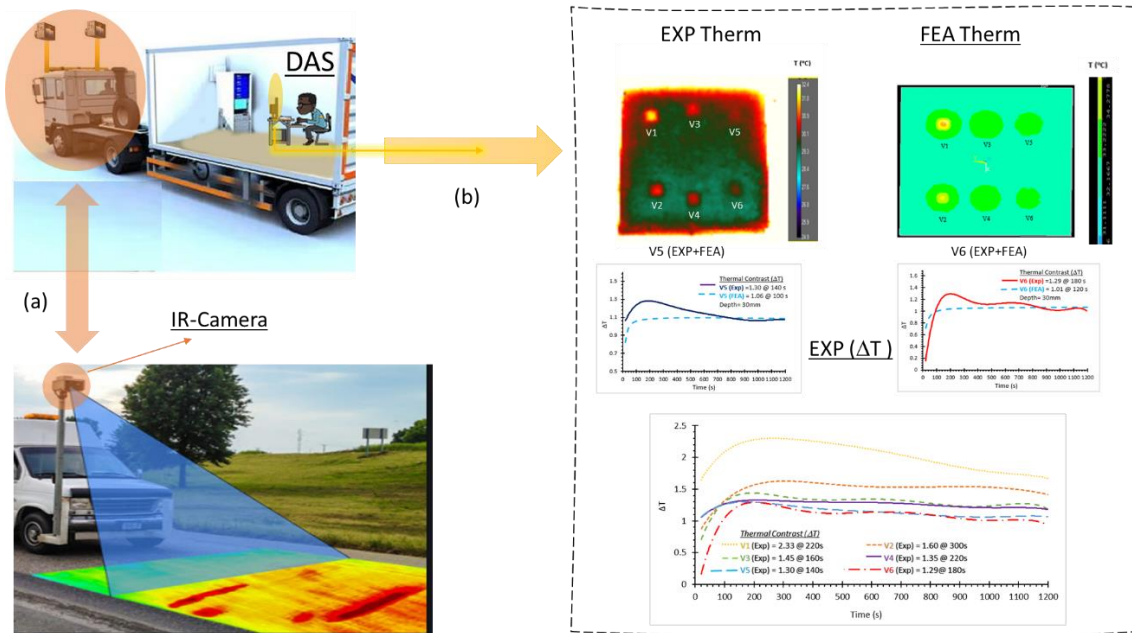
Figure 7-2: IRT-Test. (a) FBD is scanning the bridge deck. (b) Info of defects (V1-V6) detected is passed to central computer for processing via the on-board computer. V5,V6 needed further aid from FEA.

The test-vehicle keeps on moving and scanning the remaining 1km of the bridge deck. Another 3 potential defects are detected and are shown in the operator's screen (Figure 7-3).
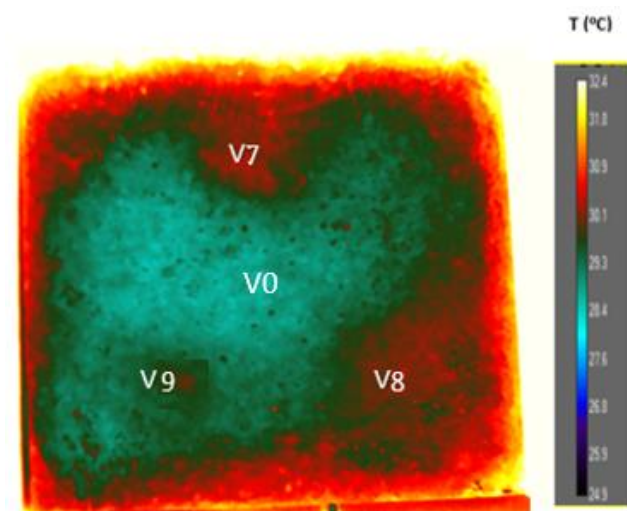

Figure 7-3: 3-potential defects are observed in the stretch of remaining 1km scanned length of a 2km long bridge deck.

Once again, no decision is made, and their thermal contrast values and absolute temperature differences are estimated with respect to a reference *fully-bonded* (sound) region, represented by V0 and classified as '*Green*' (3-potential defects are observed in the stretch of remaining 1km scanned length of a 2km long bridge deck.).

A summary of the results obtained for the detected defects is illustrated in (Table 7-2).

Table 7-2: Test 02 (Ch 4). Thermal contrast obtained by the IRT test (EXP+FEA). 'Two-slabs stacked system incorporating '3-delaminations'.
Note: ΔT = thermal contrast (dimensionless)

Defects	EXP-Abs Temp Diff (°C)	EXP-ΔT Peak value	FEA-Abs Temp Diff (°C)	FEA-ΔT Peak value	Preliminary assessment	Delaminations Classifications
V0 (Reference)	NA	NA	NA	NA	Fully-bonded	Green
V7	2.4	2.10	2.6	2.70	Clear detection-classification, no need for further assessments	Red
V8	2	1.90	2.1	2.50	Clear detection-classification, no need for further assessments	Red
V9	1	1.30	1.8	1.90	Unclear. Further assessment necessary	Amber

Two defects (V7, V8) are clearly indicated in the captured thermograms (Figure 7-3), their absolute temperature difference being 2.4 ºC ($\Delta T = 2.10$) and 2 ºC ($\Delta T = 1.90$) in contrast with the sound region (Figure 7-3), which, in accordance with the ASTM D4788-03:2013 recommendations is classified as delaminations. The thermogram of the third defect, V9, is not as evident as V7 or V8 (Figure 7-3), but, it shows an absolute temperature difference of 1 ºC ($\Delta T = 1.30$) with respect to the robust surrounding region, V0 (Table 7-2).

The central computer would make the decision based on the combined ΔT values + thermograms display, for each defect. Hence, based on the readings (ΔT + thermograms), V7, V8 would be classified as 'Red', indicating severe delamination and possibly needing immediate action.

FEA should be called for assistance again for V9, due to ambiguities in the captured thermograms display. By analysing the FEA produced thermal images, V9 is clearly rated as a defect.

However, discrepancies are observed in the ΔT values with respect to test results. This means, the FEA has provided a partial assistance, but the uncertainty is still present. Based on that, the computer would classify V9, as '*Amber*' and would store this information in that special database (matrix) for the time being.

IH-Test: The first phase of survey via IRT test is terminated here. The central computer passes all (Amber) cases stored in the matrix back to the operations vehicle and instructs the driver to go back to designated by the GPS, V5, V6, V9, (Amber) areas to carry out the IHT tests. Hence, the test-vehicle, FBD traces back those spots (V5, V6 V9), with the help of GPS, and begins testing.
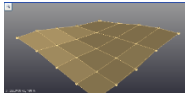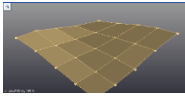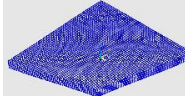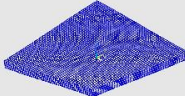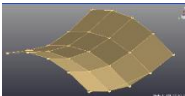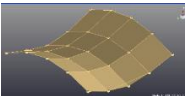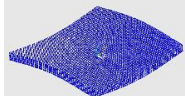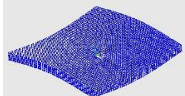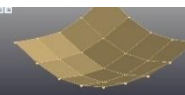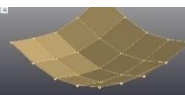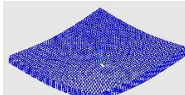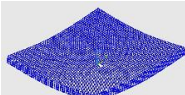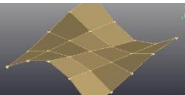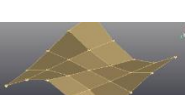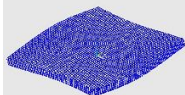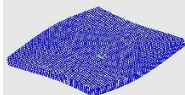
After reaching the first spot to be tested i.e. V5, the test-vehicle (FBD) stops above the area of the defect (Figure 6-4). A 8-Channel data-logger is connected to 4-
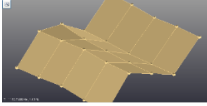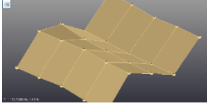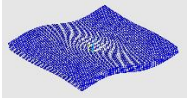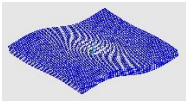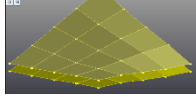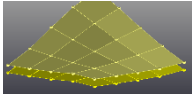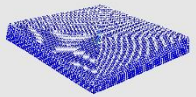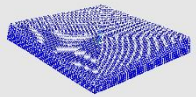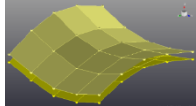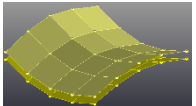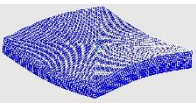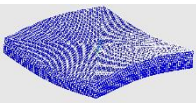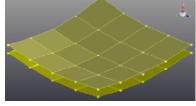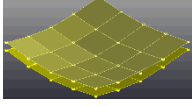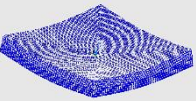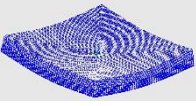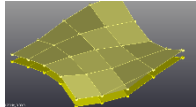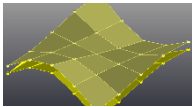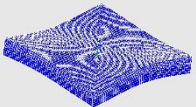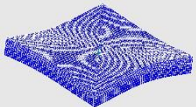
accelerometers and a modified-impact hammer via a special interface software. The operator lowers the 4-accelerometers (attached to an aluminium frame) from the vehicle. The accelerometers are positioned around the spot to be tested and the modified-impact hammer is released by the operator (via a designated computer programme). Initially, a few trial hits are carried out prior to the main recordings and the readings from the accelerometers are checked. This is done in order to make sure that the excitation energy is compatible with the frequency bandwidth, chosen for the test. A FEA model is also sought for assistance.
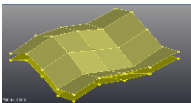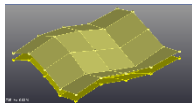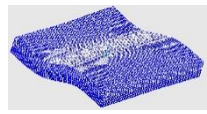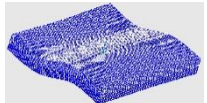
After finalising the right bandwidth and the PSD parameters (bandwidth, resolution and acquisition time), the main tests are conducted. Each time, the operator releases the weight to impact the road (with the help of a servo motor), the accelerometers record the signals and transmit them to the computer. It is stressed again that excitation is achieved by a modified hammer or a shaker. FRFs are estimated and the modal parameters are extracted. In parallel, the FE-model is also continuously updated, and the results are matched to the experimentally obtained modal parameters (Natural frequencies and Mode-shapes). The accelerometers are then retracted and the test-vehicle, FBD, moves to next spots (V6, V9). The same procedure is followed.

Finally, data are collected for all the 'Amber' spots (V5, V6 and V9). The FE-models are continuously updated and the results (natural frequencies and mode shapes) are compared. As part of the calibration procedure, an adjacent robust (sound) region is set as a 'reference' (benchmark), value. A summary of the results obtained for all 'Amber' regions is shown below (Table 7-3).

Table 7-3: Natural frequencies and mode shapes estimated (EXP+FEA) for disputed voids V5, V6, and V9. Note: f = Natural frequency (Hz)

Mode Nos.	Exp Reference Mode-Shape f= (Hz)	Exp Amber Zone Mode-Shape f= (Hz)	FEA Reference Mode-Shape f= (Hz)	FEA Amber Zone Mode-Shape f= (Hz)	Assessments (EXP results)
1.	Diagonal bending f= 288.99	Diagonal bending f= 343.24	Diagonal bending f= 289.67	Diagonal bending f= 313.08	16% rise in Natural frequency for Diagonal-bending mode compared to calibrated-Ref.
2.	1st bending mode (saddle) f= 420.43	1st bending mode (saddle) f= 451.55	1st bending mode (saddle) f= 422.35	1st bending mode (saddle) f= 451.05	6.9% rise in Natural frequency for 1st Bending mode compared to calibrated-Ref.
3.	Buckling mode (trough) f= 488.06	Buckling mode (trough) f= 500.01	Buckling mode (trough) f= 474.27	Buckling mode (trough) f= 509.93	2.4% rise in Natural frequency for Buckling-mode compared to calibrated-Ref.
4.	1st Torsional mode f= 710.50	1st Torsional mode f= 754.97	1st Torsional mode f= 708.59	1st Torsional mode f= 765.40	5.9% rise in Natural frequency for 1st Torsional mode compared to calibrated-Ref.

5.	2nd bending mode *f*= 1195.71	2nd bending mode *f*= 1249.47	2nd bending mode *f*= 1194.50	2nd bending mode *f*= 1280.80	4.3% rise in Natural frequency for 2nd bending mode compared to calibrated-Ref.
1.	Diagonal bending *f*= 522.36	Diagonal bending *f*= 551.00	Diagonal bending *f*= 522.02	Diagonal bending *f*= 537.28	5.2% rise in Natural frequency for Diagonal-bending mode compared to calibrated-Ref.
2.	1st bending mode (saddle) *f*= 754.27	1st bending mode (saddle) *f*= 777.25	1st bending mode (saddle) *f*= 753.50	1st bending mode (saddle) *f*= 776.55	3.0% rise in Natural frequency for 1st Bending mode compared to calibrated-Ref.
3.	Buckling mode (trough) *f*= 838.05	Buckling mode (trough) *f*= 874.04	Buckling mode (trough) *f*= 850.13	Buckling mode (trough) *f*= 876.34	4.1% rise in Natural frequency for Buckling-mode compared to calibrated-Ref.
4.	1st Torsional mode *f*= 1152.91	1st Torsional mode *f*= 1240.44	1st Torsional mode *f*= 1199.0	1st Torsional mode *f*= 1236.50	7.1% rise in Natural frequency for 1st Torsional mode compared to calibrated-Ref.

5.	2nd bending mode f= 1765.67	2nd bending mode f= 1912.81	2nd bending mode f= 1927.70	2nd bending mode f= 1988.60	7.7% rise in Natural frequency for 2nd bending mode compared to calibrated-Ref.

Based on the modal parameters, comparisons between the set '*reference*' and the uncertain, '*Amber*' regions, it is observed that '*V5, V6*' showed higher natural frequencies on an average of 7%, whereas '*V9*' showed on an average of 5% higher natural frequencies for all the corresponding mode-shapes, when compared to the set '*reference*' (Table 7-3). The corresponding FE-model also produced similar results as estimated in experimental modal analysis to an accuracy of approx. 98%.

The rise of natural frequencies (Hz) of V5, V6 by 7% and V9 by 5%, are significant enough to classify them as defects (delaminations/voids). The central computer would make the final decision and would re-classify and turn these regions (V5, V6, V9) from Amber to Red. As they do not appear to be as severe as V1, V2, V3, V4, V7 and V8, they can be classed as an '*Initial*' or '*Intermediate delamination*' requiring no immediate attention. They could however, be prioritised, for future re-monitoring or repair.

The IH-Tests are now finished, and the road-survey is terminated here.

It is important to mention that it is not always the case that an *Amber* region will be classified as Red after carrying out IH-Tests. For instance, if there was some oil/water spattered on the road, this may appear as a slight/small ΔT and might look like a defect in the captured thermograms, and therefore, initially classed as Amber during the first phase of survey via IRT.

After carrying out the IH-tests, this would be classed as Green, i.e. no-defect or robust region, hence, clearing the uncertainty, observed in the first phase. Nevertheless, if the uncertainty is still present even after the second phase of tests via IHT, the defects would be classed Red by the system so that they can be monitored on regular bases.

The Integration of the two methods is illustrated below in Figure 7-4.
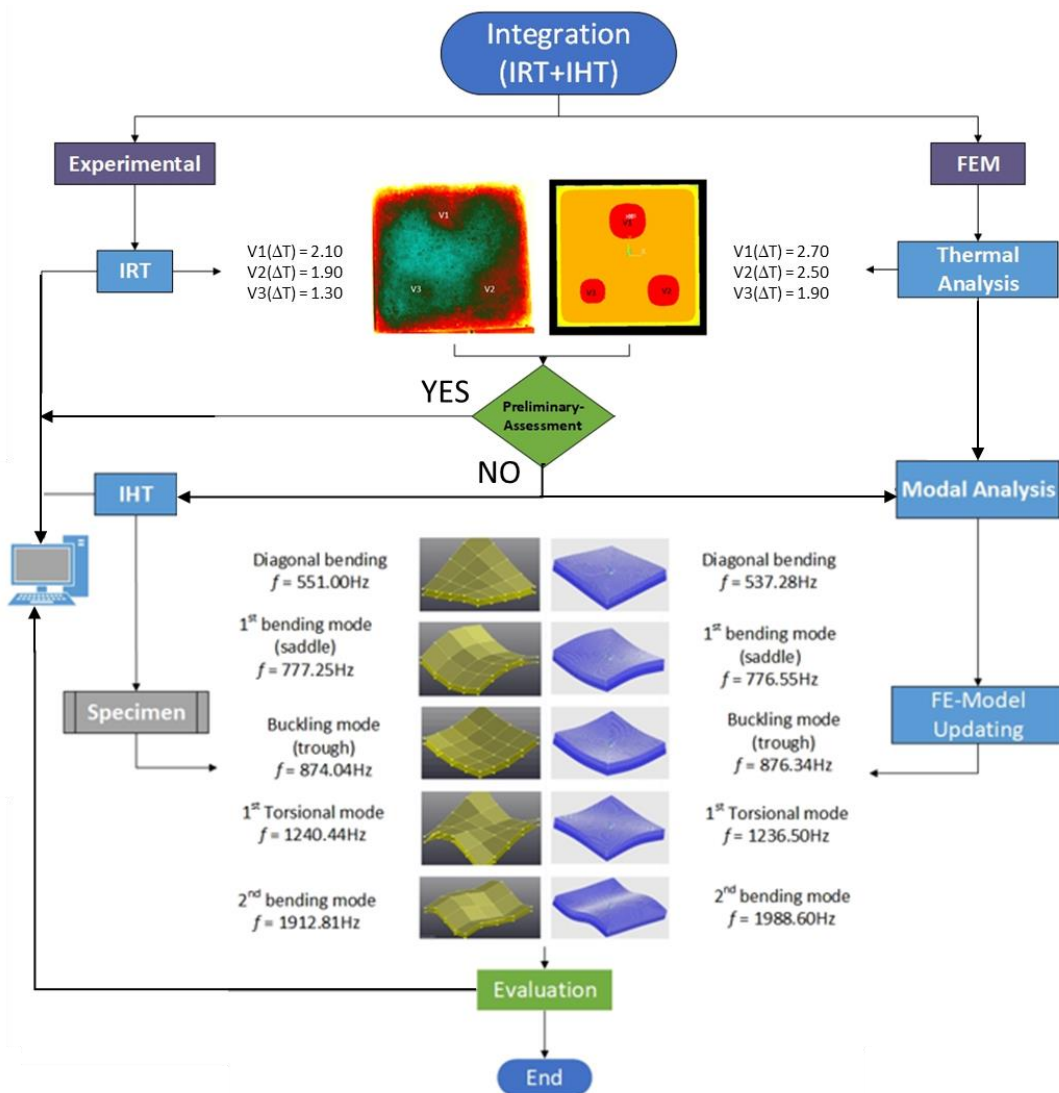
Figure 7-4: Proposed Implementation Scenario (Virtual). Synoptic outline of the two integrated NDT&E techniques, IRT+IHT.

Although, it is accepted that the above virtual scenario is speculative (semi-hypothetical), it can serve as an example, to introduce the integrated procedure, make it more comprehensible, reveal any flaws and demonstrate that the methodology suggested is realistic.

It is understood that a real case study would necessitate full size tests on a predefined road (bridge) stretch, and it should act as **validation** to the method proposed. However, this would also necessitate significant extra resources, such as the test vehicle, staffing, electronics equipment, machinery etc. This could only be achieved by negotiating external funding, and probably obtaining the permission and support of a number of organisations, such as Highways England, local (council) authorities, etc. It was therefore outside the scope of this research.

REFERENCES

Abdel-Qader, I., Yohali, S., Abudayyeh, O., and Yehia, S. (2008) 'Segmentation of Thermal Images for Non-Destructive Evaluation of Bridge Decks'. *NDT and E International* 41 (5), 395–405

Abramo, D.C. (2011) *Impact-Echo Modeling and Imaging Techniques*. Northeastern University Boston, Massachusetts

Adams, R.D., Cawley, P., Pye, C.J., and Stone, B.J. (1978) 'A Vibration Technique for Non-Destructively Assessing the Integrity of Structures.' *Journal of mechanical engineering science* 20 (2), 93–100

Adeli, H. (2001) 'Neural Networks in Civil Engineering: 1989-2000.' *Computer-Aided Civil and Infrastructure Engineering* 16 (2), 126–142

Agilent Technologies (2000) The Fundamentals of Modal Testing. Application Note 243-3. USA

Al-Qaisia, A. and Meneghetti, U. (1997) 'Crack Detection in Plates by Sensitivity Analysis.' in *Proc. of the 15th International Modal Analysis Conference*. held 1997 at Orlando, FL.

ALARM (2019) *Each Year the Asphalt Industry Alliance (AIA) Commissions an Independent Survey of Local Authority Highway Departments in About the ALARM Survey* [online] Bristol. available from <www.roadusers.org.uk>

Allemang, R.J. (2003) 'The Modal Assurance Criterion – Twenty Years of Use and Abuse.' *Sound and vibration* 37 (8), 14–21

Allemang, R.J. and Brown, D.L. (1983) 'Correlation Coefficient for Modal Vector Analysis'. in *1st International Modal Analysis Conference, Society for Experimental Mechanics, Inc.* held 1983. 690–695

Al Hakim, B., Armitage, R., and Thom, N.H. (1998) 'Pavement Assessment Including Bonding Condition: Case Studies.' in *Proceedings, 5th International Conference on Bearing Capacity of Roads and Airfields*. held 1998 at Norway. University of Trondheim, Trondheim, 439–448

Al Hakim, B., Cheung, L.W., and Armitage, R. (2000) 'Use of FWD Data for Prediction of Bonding between Pavement Layers.' *Int. J. Pav. Eng.* 1 (1), 49–59

Al Hakim, B., Al Nageim, H., Pountney, D., and Lesley, L. (1997) 'The Development of an Improved Pavement Backcalculation'. in *Proceedings, 1st International Conference on Rehabilitation and Development of Civil Engineering Infrastructure Systems*. held 1997 at Lebanon

Altunışık, A.C., Okur, F.Y., and Kahya, V. (2017) 'Modal Parameter Identi Fi Cation and Vibration Based Damage Detection of a Multiple Cracked Cantilever Beam'. *Engineering failure analysis* 79 (April), 154–170

Altunışık, A.C., Okur, F.Y., Karaca, S., and Kahya, V. (2019) 'Vibration-Based Damage Detection in Beam Structures with Multiple Cracks : Modal Curvature vs . Modal Flexibility Methods'. *Nondestructive Testing and Evaluation* [online] 34 (1), 33–53. available from <https://doi.org/10.1080/10589759.2018.1518445>

ANSYS (2018) 'ANSYS Mechanical APDL Element Reference'. in *Knowledge Creation Diffusion Utilization*. (14). ANSYS, Inc. Release 18.1 Southpointe November 2018 275 Technology Drive Canonsburg, 1416

Armitage, R., Kruntcheva, M.R., and Willett, M.R. (2000) *Trials of the Portable Seismic Pavement Analyzer (PSPA)*. Nottingham

ARNDT, R., Maierhofer, C., and Röllig, Mathias (2006) 'Quantitative Pulse-Phase-Thermography for Masonry and Concrete Structures'. *European Conference on NDT* 1–8

American Society for Testing and Materials (2013) *Standard Test Method for Detecting Delaminations in Bridge Decks Using Infrared Thermography*. *ASTM D4788-03:2013*. West Conshohocken: American Society for Testing and Materials

American Society for Testing and Materials (2000) *Standard Practice for Measuring Delaminations in Concrete Bridge Decks by Sounding*. ASTM D4580-86:2000. vol. 86. West Conshohocken: American Society for Testing and Materials

Avdelidis, N.P., Moropoulou, A., and E.T. Delegou (2003) 'Applications of Thermography in Assessment of Masonry, Airport Pavement and Composite Material.' *Insight-Non-Destructive Testing and Condition Monitoring.* 45 (12), 836–841

Avitabile, P. (2001) 'A Simple Non-Mathematical Presentation'. *Modal Analysis* 35 (1), 1–15

Azari, H., Nazarian, S., and Yuan, D. (2014) 'Assessing Sensitivity of Impact Echo and Ultrasonic Surface Waves Methods for Nondestructive Evaluation of Concrete Structures'. *Computers and Chemical Engineering* [online] 71, 384–391. available from <http://dx.doi.org/10.1016/j.conbuildmat.2014.08.056>

Bakhary, N. (2008) *Structural Condition Monitoring and Damage Identification With Artificial Neural Network*. The university of Western Australia.

Balis, C.L., Castellani, A., and Coppotelli, G. (1995) 'Generalization Of Non Destructive Damage Evaluation Using Modal Parameters.' in *Roc. of the 13th International Modal Analysis Conference*. held 1995. 428–431

Bangade, Y. V., and Kulkarni, V. V. (2017) 'Experimental & Numerical Analysis of Composites with Delaminations'. *International Research Journal of Engineering and Technology (IRJET)* 4 (8), 2382–2386

Baright, M.D. (1999) *Inspection of Concrete Bridge Decks With Asphalt Overlays. Â Comparison of Nondestructive Evaluation Methods*. 18, 2137–2144

British Standards Institution (1999) *Thermal Performance of Buildings - Qualitative Detection of Thermal Irregularities in Building Envelopes - Infrared Method*. BS EN 13187:1999. London: British Standards Institution

Bukowski, M.E., Tucker, R.L., and Fowler, D.W. (1983) *Detection of Voids Underneath Concrete Pavements Using Infrared Thermography*. (2)

Cannas, B., Carcangiu, S., Concu, G., and Trulli, N. (2012) 'Modeling of Active Infrared Thermography for Defect Detection in Concrete Structures.' in *In: COMSOL Conference 7*. held 2012

Carden, E.P., and Fanning, P. (2004) 'Vibration Based Condition Monitoring: A Review.' *Structural Health Monitoring* 3, 355–377

Carino, N.J. (2001) 'The Impact-Echo Method: An Overview'. *2001 Structures Congress & Exposition* [online] 18. available from <http://fire.nist.gov/bfrlpubs/build01/PDF/b01005.pdf>

Carino, N.J., Sansalone, M.J., and Hsu, N.N. (1986) 'A Point Sourcepoint Receiver, Pulse-Echo Technique for Flaw Detection in Concrete.' *ACI* 83, 199–208

Cawley, P., and Adams, R.D. (1979) 'The Location of Defects in Structures from Measurements of Natural Frequencies'. *The Journal of Strain Analysis for Engineering Design* 14 (2), 49–57

Celaya, Manuel (2011) *Evaluation of Nondestructive Technologies to Assess Presence and Extent of Delamination of Hot Mix Asphalt Airfield Pavements*.

Chatterjee, K., Tuli, S., Pickering, S.G., and Almond, D.P. (2011) 'A Comparison of the Pulsed, Lock-in and Frequency Modulated Thermography Nondestructive Evaluation Techniques'. *NDT and E International* [online] 44 (7), 655–667. available from <http://dx.doi.org/10.1016/j.ndteint.2011.06.008>

Chaudhary, M.T.A. (2013) 'Effectiveness of Impact Echo Testing in Detecting Flaws in Prestressed Concrete Slabs'. *Construction and Building Materials* [online] 47, 753–759. available from <http://dx.doi.org/10.1016/j.conbuildmat.2013.05.021>

Chown, G., and Burn, K. (1983) 'Thermographic Identification of Building Enclosure Defects and Defiencies.' *Canadian Building Digest*

Civil Engg Dictionary (2014) *Civil Engg Dictionary* [online] available from <http://www.aboutcivil.org/types-of-pavements.html> [15 March 2017]

Clark, M., McCann, D., and Forde, M.. (2003) 'Application of Infrared Thermography to the Non-Destructive Testing of Concrete and Masonry Bridges'. *NDT & E International* 36 (4), 265–275

Cotič, P., Kolarič, D., Bosiljkov, V.B., Bosiljkov, V., and Jagličić, Z. (2015) 'Determination of the Applicability and Limits of Void and Delamination Detection in Concrete Structures Using Infrared Thermography.' *NDT E Int.* 74, 87–93

Curadelli, R.O., Riera, J.D., Ambrosini, D., and Amani, M.G. (2008) 'Damage Detection by Means of Structural Damping Identification'. *Engineering Structures* [online] 30 (12), 3497–3504. available from <http://dx.doi.org/10.1016/j.engstruct.2008.05.024>

Dackermann, U. (2010) 'Vibration-Based Damage Identification Methods for Civil Engineering Structures Using Artificial Neural Networks'. University of Technology Sydney

Davis, A.G., Hertlein, B.H., Lim, Malcolm K., and Michols, K. (1996) 'Impact-Echo and Impulse Response Stress Wave Methods: Advantages and Limitations for the Evaluation of Highway Pavement Concrete Overlays'. in *Conference on Nondestructive Evaluation of Bridges and Highways* [online] held 1996. SPIE, 88–96. available from <http://dx.doi.org/10.1117/12.259127>

Delatte, N. (2008) *Concrete Pavement Design, Construction, and Performance* [online] Milton, Vale of white horse: Taylor and Francis. available from www.eBookstore.tandf.co.uk

Delatte, Jr., N.J., Fowler, D.W., McCullough, B.F., and Gräter, S.F. (1998) 'Investigating Performance of Bonded Concrete Overlays'. *Journal of Performance of Constructed Facilities*

Desta, Belayneh. (2014). Hydraulic Fracture Test to Determine Aggregate Freeze-Thaw Durability. 10.5703/1288284315515.

Diaz, J.J. del C., Nieto, P.J.G., Rodriguez, A.M., Luengas, A.L.M., and Biempica, C.B. (2006) *Non-Linear Thermal Analysis of Light Concrete Hollow Brick Walls by the Finite Element Method and Experimental Validation*. 26, 777–786

Doebling, S.W., Farrar, C.R., and Goodman, R.S. (1997) 'Effects of Measurement Statistics on the Detection of Damage in the Alamosa Canyon Bridge.' in *Proceedings 15th International Modal Analysis Conference*. held 1997 at Orlando, FL. 919–929

Doebling, S.W., Farrar, C.R., and Prime, M.B. (1998) 'A Summary Review of Vibration-Based Damage Identification Methods'. *Shock and Vibration Digest* 30 (2), 91–105

Doebling, S.W., Farrar, C.R., Prime, M.B., and Shevitz, D.W. (1996) *Damage Identification and Health Monitoring of Structural and Mechanical Systems from Changes in Their Vibration Characteristics: A Literature Review*.

Dow, C.C. (2001) *ETHAFOAM 220 Anti-Static*. USA

Elhakim, A.F., Elbaz, K., and Amer, M.I. (2014) 'The Use of Light Weight Deflectometer for in Situ Evaluation of Sand Degree of Compaction'. *HBRC Journal* [online] 10 (3), 298–307. available from <http://dx.doi.org/10.1016/j.hbrcj.2013.12.003>

Engineering ToolBox (2001) *Engineering ToolBox* [online] available from <https://www.engineeringtoolbox.com/> [3 August 2019]

Evans, R.D., Frost, M.W., Stonecliffe-Jones, M., and Dixon, N. (2008) 'A Review of Pavement Assessment Using Ground Penetrating Radar (GPR)'. *12th International Conference on Ground Penetrating Radar* [online] available from <https://dspace.lboro.ac.uk/2134/3590>

Ewins, D.J. (2000) *Modal Testing : Theory, Practice and Application*. 2nd edn. ed. by Roberts, P.J.B. Hertfordshire: Research Studies Pess Ltd.

Fan, W., and Qiao, P. (2011) 'Vibration-Based Damage Identification Methods: A Review and Comparative Study'. *Structural Health Monitoring* 10 (1), 83–111

Farrar, C.R., and Doebling, S.W. (1997) *An Overview of Modal-Based Damage Identification Methods.* Los Alamos

Farrar, C.R., Doebling, S.W., and Nix, D. (2001) 'Vibration-Based Structural Damage Identification.' *Philosophy transactions royal society* 359, 131–149

FHWA (2003) *Distress Identification Manual for the Long-Term Pavement Performance Program.*

FLIR Systems (2013) 'IR Thermography'. *Flir* 53 (9), 1689–1699

FLIR Systems Inc. (2016) *User ' s Guide*. Wilsonville, Oregon, 100

Foti, D. (2013) 'Dynamic Identification Techniques to Numerically Detect the Structural Damage.' *The open construction and building technology journal* 7, 43–50

Fotsch, D., and Ewins, D.J. (2000) 'Application of MAC in the Frequency Domain'. *Proceedings of the International Modal Analysis Conference - IMAC* 2, 1225–1231

Fox, C.H.J. (1992) 'The Location Of Defects In Structures: A Comparison Of The Use Of Natural Frequency And Mode Shape Data.' in *10th International Modal Analysis Conference*. held 1992. 522–528

Fritzen, C.P. (2005) 'Vibration-Based Structural Health Monitoring - Concepts and Applications'. *Key Engineering Materials* 293–294 (January 2005), 3–18

Fujie, Z., and Scullion, Tom. (2007) *GUIDELINES FOR EVALUATION OF EXISTING PAVEMENTS FOR HMA OVERLAY*. [online] vol. 7. Austin, Texas. available from <http://tti.tamu.edu/documents/0-5123-2.pdf>

Gadelrab, R.M. (1996) 'The Effect of Delamination on the Natural Frequencies of a Laminated Composite Beam.' *J. sound vib.* 197 (3), 283–292

Galbraith, B. (2013) *Infrared Thermography Theory , Technology and Structural Applications Thermography Basics*.

Garbacz, A., Piotrowski, T., Courard, L., and Kwaniewski, L. (2017) 'On the Evaluation of Interface Quality in Concrete Repair System by Means of Impact-Echo Signal Analysis'. *Construction and Building Materials* 134, 311–323

Garesci, F., Catalano, L., and Petrone, F. (2006) 'Experimental Results of a Damage Detection Methodology Using Variations in Modal Parameters.' *Experimental Mechanics* 46, 441–451

Gaussorgues, G. (1994) *Infrared Thermography*. London: Chapman & Hall

Gibbs, K. (2013) *Thermal Data*. Somerset. available from <http://www.schoolphysics.co.uk/data/Thermal data/index.html>

Gomaa, F.R., Nasser, A.A., and Ahmed, S.O. (2014) 'Sensitivity of Modal Parameters to Detect Damage through Theoretical and Experimental Correlation'. *International Journal of Current Engineering and Technology* 4 (1), 172–181

Gomba, S.M. (2004) *Evaluation of Interlayer Bonding in Hot Mix Asphalt Pavements.* Rowan University, Glassboro, New Jersey.

Gopalakrishnan, K., and Papadopoulos, H. (2011) 'Reliable Pavement Backcalculation with Confidence Estimation'. *Scientia Iranica* [online] 18 (6), 1214–1221. available from <http://dx.doi.org/10.1016/j.scient.2011.11.018>

Granju, J.L. (2001) *Debonding of Thin Cement-Based Overlays.* 13 (April), 114–120

Gucunski, N., Antoljak, S., and Maher, A. (2000) 'Seismic Methods in Post-Construction Condition Monitoring of Bridge Decks.' in S, N. and Diehl J (eds.) *Use of Geophysical Methods in Construction.* held 2000. Geo Institute, ASCE, 35–51

Gudmundson, P. (1982) 'Eigenfrequency Changes Of Structures Due To Cracks, Notches, Or Other Geometrical Changes.' *Journal of the Mechanics and Physics of Solids* 30, 339–353

Hain, M., Bartl, J., and Jacko, V. (2009) 'Active Infrared Thermography in Non-Destructive Testing'. *MEASUREMENT 2009, Proceedings of the 7th International Conference* 339–343

Hammons, M.I., Von Quintus, H., Maser, K., and Nazarian, S. (2005) *Detection of Stripping in Hot Mix Asphalt.* Georgia

He, J., and Fu, Z.-F. (2001) *Modal Analysis.* Oxford ; Boston : Butterworth-Heinemann

Hearn, G. and Testa, R.B. (1991) 'No TitleModal Analysis for Damage Detection in Structures.' *Journal of structural engineering* 117, 3042–3063

Heitzman, M., Maser, Kenneth l., Tran, N.H., Brown, R., Bell, H., Holland, S., Ceylan, H., Belli, K., and Hiltunen, D. (2013) *Nondestructive Testing to Identify Delaminations Between HMA Layers, Volume 1 - Summary.* [online] available from <https://www.nap.edu/catalog/22768>

Hiasa, S. (2016) *Investigation of Infrared Thermography for Subsurface Damage Detection of Concrete Structures.* [online] University of Central Florida. available from <https://stars.library.ucf.edu/etd/5063/>

Hiasa, S., Birgul, R., and Catbas, F.N. (2017a) 'Effect of Defect Size on Subsurface Defect Detectability and Defect Depth Estimation for Concrete Structures by Infrared Thermography.' *J. Nondestruct Eval.* [online] 3 (2), 54–67. available from <http://repositorio.unan.edu.ni/2986/1/5624.pdf>

Hiasa, S., Birgul, R., and Catbas, F.N. (2017b) 'Investigation of Effective Utilization of Infrared Thermography (IRT) through Advanced Finite Element Modeling.' *Constr. Build. Mater.*

Hiasa, S., Catbas, F.N., Matsumoto, M., and Mitani, K. (2016) 'Monitoring Concrete Bridge Decks Using Infrared Thermography with High Speed Vehicles'. *Structural Monitoring and Maintenance* 3 (3), 277–296

Highways Agency (2012) *Maintaining England ' s Motorways and Trunk Roads*. London

Hoegh, K. (2012) 'Evaluation of an Ultrasonic Technique for Detecting'. *Transportation Research Board 91st Annual Meeting* (January), 22–26

Hoegh, K., Khazanovich, L., and Yu, H.T. (2011) 'Ultrasonic Tomography Technique for Evaluation Concrete Pavements'. *Transportation Research Record: Journal of the Transportation Research Board* (2232), 85–94

Holman, J.P. (2010) *Heat Transfer*. 10th edn. ed. by Holman, J.P. and Lloyd, J. Michigan: McGraw-Hill, Inc, New York

Huang, L., Agrawal, H., and Borowski, V. (1997) 'Durability Analysis of a Vehicle Body Structure Using Modal Transient Methods'. in *Proceedings of the 15th International Modal Analysis Conference*. held 1997. 407–414

Huang, Y. (2006) 'Automatic Inspection of Pavement Cracking Distress'. *Journal of Electronic Imaging* [online] 15 (1), 13017. available from http://electronicimaging.spiedigitallibrary.org/article.aspx?doi=10.1117/1.2177650

Huang, Y.H. (2004) *Pavement Analysis and Design*. 2nd edn. Upper Saddle River, New Jersey: Prentice Hall

Huang, Q., Gardoniand, P., and Hurlebaus, S. (2012) 'A Probabilistic Damage Detection Approach Using Vibration-Based Nondestructive Testing.' *Structural safety* 38, 11–21

Huh, J., Tran, Q.H., Lee, J., Han, D., Ahn, J., and Yim, S. (2016) 'Experimental Study on Detection of Deterioration in Concrete Using Infrared Thermography Technique.' *Adv. Mater. Sci. Eng.* Article ID

IAEA, (2002) 'Guidebook on Non-Destructive Testing of Concrete Structures'. *Training Course Series* [online] 17 (17), 231. available from <http://200.10.161.33/cirsoc/pdf/ensayos/tcs-17_web.pdf>

Iliopoulos, A., Shirzadeh, R., Weijtjens, W., Guillaume, P., Hemelrijck, D. Van, and
 Devriendt, C. (2016) 'A Modal Decomposition and Expansion Approach for
 Prediction of Dynamic Responses on a Monopile Offshore Wind Turbine Using a
 Limited Number of Vibration Sensors'. *Mechanical Systems and Signal
 Processing* [online] 68–69, 84–104. available from
 <http://dx.doi.org/10.1016/j.ymssp.2015.07.016>

Jassim, Z.A., Ali, N.N.B., Mustaphac, F., and Abdul Jalil, N.A. (2013) 'A Review on
 the Vibration Analysis for a Damage Occurrence of a Cantilever Beam.'
 Engineering failure analysis 31, 442–461

Jeuffroy, G., and Sauterey, R. (1996) *Concrete Definition and General Characteristics*.
 ed. by Jeuffroy, G. and Sauterey, R. USA: A.A. Balkema

Kam, T.Y., and Lee, T.Y. (1992) 'Detection Of Cracks In Structures Using Modal Test
 Data.' *Engineering Fracture Mechanics* 42 (2), 381–387

Karadelis, J.N. (2009) 'Concrete Grandstands. Part II. Numerical Modelling.'
 *Proceedings of the Institution of Civil Engineers, Engineering and Computational
 Mechanics Journal* 162 (EM1)

Karadelis, J.N. (2012) 'Reliability Pointers for Modal Parameter Identification of
 Grandstand Terraces'. *Journal of Civil Engineering Research* [online] 2 (6), 84–
 99. available from <http://article.sapub.org/10.5923.j.jce.20120206.05.html>

Karadelis, J.N., and Hughes, B.P. (1998) 'Computation of Rigid Pavement Stiffnesses
 Using Surface Deflections from the Falling Weight Deflectometer.' in
 *Proceedings, Concrete Communication Concrete Communication Conference 98,
 The 8th BCA Annual Conference on Higher Education and Concrete Industry*. held
 1998 at Southhampton. 87–101

Kashif Ur Rehman, S., Ibrahim, Z., Memon, S.A., and Jameel, M. (2016) 'Nondestructive Test Methods for Concrete Bridges: A Review'. *Construction and Building Materials* [online] 107, 58–86. available from <http://dx.doi.org/10.1016/j.conbuildmat.2015.12.011>

Kwak, Hyo-Gyoung., Filippou, F.C. (1990). 'Finite Element Analysis of Reinforced Concrete Structures under Monotonic Loads', *Structural Engineering Mechanics and Materials,* PhD Thesis, Dept of Civil Engineering University of California, Berkeley, California, Report No. UCB/SEMM-90/14

Kennedy, C.K. (1978) 'The Development of Slip-Planes in Rolled Asphalt Surfacings'. *Transport and Road Research Labortary* 35

Kennedy, C.K. and Lister, N.. (1979) 'Experimental Studies of Slippage'. in *The Performance of Rolled Asphalt Road Surfacings Conference, London.* held 1979. ICE Publishing, 31–56

Khan, F., Bolhassani, M., Kontsos, A., Hamid, A., and Bartoli, I. (2015) 'Modeling and Experimental Implementation of Infrared Thermography on Concrete Masonry Structures.' *Infrared Phys. Technol.* 69, 228–237

Khweir, K., Fordyce, D., and Khweir, K. (2003) 'Influence of Layer Bonding on the Prediction of Pavement Life.' *ICE J. Trans* 156 (TR2), 73–83

Kim, H.Y.. and Hwang, W. (2002) 'Effect of Debonding on Natural Frequencies and Frequency Response of Honeycomb Sandwich Beams.' *Composite structures* 55, 51–62

Kim, J.H., Jeon, H.S., and Lee, C.W. (1992) 'Application Of The Modal Assurance Criteria For Detecting And Locating Structural Faults.' in *10th International Modal Analysis Conference*. held 1992. 536–540

Krishnapillai, M., Jones, R., Marshall, I.H., Bannister, M., and Rajic, N. (2006) 'NDTE Using Pulse Thermography: Numerical Modeling of Composite Subsurface Defects.' *Compos. Struct.* 75, 241–249

Kruntcheva, M.R., Collop, A.C., and Thom, N.H. (2005) 'Effect of Bond Condition on Flexible Pavement Performance.' *Journal of Transportation Engineering* 131 (11), 880–888

Kylili, A., Fokaides, P.A., Christou, P., and Kalogirou, S.A. (2014) 'Infrared Thermography (IRT) Applications for Building Diagnostics: A Review'. *Applied Energy* [online] 134, 531–549. available from <http://dx.doi.org/10.1016/j.apenergy.2014.08.005>

Lafarge Tarmac Limited (2015) *LOW THERMAL CONDUCTIVITY CONCRETE*. Solihull, West Midlands, B37 7BQ, 30. available from <https://www.tarmac.com/media/492800/low-thermal-conductivity-concrete-solution-guide.pdf>

Lee, L.S., Vistasp Karbhari, M., and Charles, S. (2004) *Investigation of Integrity and Effectiveness of RC Bridge Deck Rehabilitation with CFRP Composites* [online] California. available from <https://pdfs.semanticscholar.org/55f3/1433f849fc8273f5c5b8fb12b2a70fd772e2.pdf>

Lenz, P.E.. and Russel, W. (2011) *Pavement Design Guide Manual*. Texas: Texas Department of Transportation. available from <http://onlinemanuals.txdot.gov/txdotmanuals/pdm/index.htm.>

Lepert, P., Poilane, J.P., and Villard-Bats, M. (1992) 'Evaluation of Various Field Measurement Techniques for the Assessment of Pavement Interface Condition.' in *7th International Conference on Asphalt Pavements*. held 1992. 224–237

Liang, R.Y., Hu, J.L., and Choy, F. (1992) 'Theoretical-Study of Crack-Induced Eigenfrequency Changes on Beam Structures.' *Journal of Engineering Mechanics-ASCE* 118, 384–396

Lin, J.M.. and Sansalone, M.J. (1996) 'Impact-Echo Studies of Interfacial Bond Quality in Concrete'. *ACI Materials Journal* 93, 223–232

Lin, J.M., Sansalone, M.J., and Poston, R. (1996) 'Impact-Echo Studies of Interfacial Bond Quality in Concrete'. *ACI Materials Journal* 93, 318–326

LMS (2017) *LMS Test . Lab Solutions Guide*.

Lowe, S. (2008) 'A Primer on Infra-Red Thermography'. *Thermalcities* [online] 16–19. available from <http://thermalcities.com/HOWITWORKS.htm>

Maia, N.M.M. and Silva, J.K.M. e (1997) Theoretical and Experimental Modal Analysis. Taunton : Research Studies Press ; New York ; Chichester : Wiley

Maierhofer, C., Arndt, R., Röllig, M., Rieck, C., Walther, A., Scheel, H., and Hillemeier, B. (2006) 'Application of Impulse-Thermography for Non-Destructive Assessment of Concrete Structures'. *Cement and Concrete Composites* 28 (4), 393–401

Maierhofer, C., Brink, A., Röllig, M., and Wiggenhauser, H. (2005) 'Quantitative Impulse-Thermography as Non-Destructive Testing Method in Civil Engineering - Experimental Results and Numerical Simulations'. *Construction and Building Materials* 19 (10), 731–737

Maintenance Technical Advisory Guide (2003) *Common Distresses on Flexible Pavements Fundamentals of Pavements* [online] available from <http://www.dot.ca.gov/hq/maint/MTAG-CommonFlexiblePavementDistresses.pdf>

Maldague, X. (2000) 'Applications of Infrared Thermography'. *Trends in Optical Nondestructive Testing* 591–609

Marinetti, S., Plotnikov, Y. a., Winfree, W.P., and Braggiotti, A. (1999) *Pulse Phase Thermography for Defect Detection and Visualization*. [online] 230–238. available from <http://proceedings.spiedigitallibrary.org/proceeding.aspx?articleid=975329>

Mathew, T. and Rao, K. (2007) 'Introduction to Pavement Design'. in *Introduction to Transportation Engineering* [online] National Programme on Technology Enhanced Learning (NPTEL), 19.1-19.7. available from <http://nptel.ac.in/courses/105101087/downloads/Lec-19.pdf>

Mazzeo, B.A., Patil, A.N., and Guthrie, W.S. (2012) 'Acoustic Impact-Echo Investigation of Concrete Delaminations Using Liquid Droplet Excitation'. *NDT and E International* [online] 51, 41–44. available from <http://dx.doi.org/10.1016/j.ndteint.2012.05.007>

Meola, C. (2013) 'Infrared Thermography in the Architectural Field'. *The Scientific World Journal* 2013

Miller, J.S., Bellinger, W.Y., and FHWA (2003) 'Distress Identification Manual for the Long-Term Pavement Performance Program'. *Publication of US Department of Transport, Federal Highway Administration* (June), 129

Mindess, S., Young, J.., and Darwin, D. (2003) *Concrete*. 2nd edn. Upper Saddle River, New Jersey: Pearson Education

Mishra, S.B., and Alok, S. (2017) *Handbook of Research Methodology*. 1st edn. Educreation

Modena, C., Sonda, D., and Zonta, D. (1999) 'Damage Localization in Reinforced Concrete Structures by Using Damping Measurements.' *Key engineering materials* 167, 132–141

Mohan, V., Parivallal, S., Kesavan, K., Arunsundaram, B., Ahmed, A.K.F., and Ravisankar, K. (2014) 'Studies on Damage Detection Using Frequency Change Correlation Approach for Health Assessment'. *Procedia Engineering* [online] 86, 503–510. available from <http://dx.doi.org/10.1016/j.proeng.2014.11.074>

Moorthy, R.I.K., Kakodkar, A., Srirangarajan, H.R., and Suryanarayan, S. (1993) 'An Assessment of the Newmark Method for Solving Chaotic Vibrations of Impacting Oscillators'. *Computers & Structures* [online] 49 (4), 597–603. available from <http://www.sciencedirect.com/science/article/pii/004579499390064K>

Morassi, A. (1993) 'Crack-Induced Changes in Eigenparameters of Beam Structures.' *Journal of Engineering Mechanics-ASCE* 119, 1798–1803

Moropoulou, A., Avdelidis, N.., Koui, M., and Kakaras, K. (2001) 'An Application of Thermography for Detection of Delaminations in Airport Pavements'. *Int'l Journal for NDT & E* 34, 329–335

Narkis, Y. (1994) 'Identification Of Crack Location In Vibrating Simply Supported Beams.' *Journal of Sound and Vibration* 172, 549–558

NASA LaRC (2018) *NASA Prediction Of Worldwide Energy Resources* [online] available from <https://power.larc.nasa.gov/> [5 July 2018]

Nawy, E.G.. and Ukadike, M.. (1983) 'Shear Transfer in Concrete and Polymer Modified Concrete Members Subjected to Shearing Loads.' *Journal of Testing and Evaluation, JTEVA* 89–98

Nazarian, S., Celaya, C., Mejía, D., Ertem, S., Rao, C., Von Quintus, F., and Shokouhi, P. (2010) *Evaluation of NDT Technologies to Assess Presence and Extent of Delamination of HMA Airfield Pavements. Final Report for AAPTP Research Project 06-04.* Texas

Ndambi, J.M., Vantomme, J., and Harri, K. (2002) 'Damage Assessment in Reinforced Concrete Beams Using Eigenfrequencies and Mode Shape Derivatives.' *Engineering structures* 24 (4), 501–515

Nicholas, J.H.. (1979) *Working Party on the Slippage of Rolled-Asphalt Wearing Course.* Crowthorne

Nicholls, C. (1998) *Asphalt Surfacings.* ed. by Nicholls, C. London and NewYork

NRMCA (2000) *CIP 20 - Delamination of Troweled Concrete Surfaces.* National Ready Mixed Concrete Association, 3–4

Osegueda, R., Dsouza, P.D., and Qiang, Y. (1992) 'Damage Evaluation Of Offshore Structures Using Resonant Frequency Shifts.' *Serviceability of Petroleum, Process, and Power Equipment, ASME PVP239/MPC33* 31–37

Owen, J., and Pearson, R. (2004) 'The Use of Dynamic Data for the Structural Health Monitoring of Bridges.' in *Proceedings of 1st FIG International Symposium on*

Engineering Surveys for Construction Works and Structural Engineering. held 2004 at Nottingham, United Kingdom

Özen, F.S., Celaya, M, Nazarian, S., and Saltan, M. (2013) 'Feasibility of Detecting Debonding of Hot Mix Asphalt Layer With Sonic / Seismic and Impulse Methods'. *Nondestructive Testing of Materials and Structures* (June 2012), 877–881

Pandey, A.K., and Biswas, M. (1994) 'Damage Detection in Structures Using Changes in Flexibility.' *Journal of sound and vibration* 169 (1), 3–17

Pandey, P.C., and Barai, S.V. (1994) 'Sensitivity-Based Weighted-Average in Structural Damage Assessment.' *Journal of performance of constructed facilities* 8 (4), 243–263

Paolozzi, A., and Peroni, I. (1990) 'Detection of Debonding Damage in a Composite Plate through Natural Frequency Variations.' *Journal of reinforced plastics and composites* 9, 369–389

Pastor, M., Binda, M., and Harčarik, T. (2012) 'Modal Assurance Criterion'. *Procedia Engineering* 48, 543–548

Patel, N.B. (2010) *Factors That Influence the Performance of Interface Shear Strength of Pavement*. Louisiana State University and Agricultural and Mechanical College

Paul, R.F., Matthew, W.F., and John, P.L. (2007) 'A Review of the Lightweight Deflectometer (Lwd) for Routine Insitu Assessment of Pavement Material Stiffness'. *Transportation Research Record* 44 (07), 1–15

PCB (2011) 'Test & Measurement Sensors & Instrumentation Test & Measurement Sensors & Instrumentation'. Pcb Piezotronics Mts Systems Corporation

Peattie, K. (1980) 'The Performance of Rolled Asphalt Road Surfacings." The Incidence and Investigation of Slippage Failures'. *The performance of rolled asphalt road surfacings." The incidence and investigation of slippage failures - See more at:* [online] 3–15. available from <http://ascelibrary.org/doi/full/10.1061/(ASCE)0899-1561(2006)18%3A3(467)?src=recsys#sthash.0AA5nCWj.dpuf>

Peattie, K.R. (1979) 'The Incidence and Investigation of Slippage Failures'. in *The Performance of Rolled Asphalt Road Surfacings.* [online] held 1979. ICE Publishing, 3–15. available from <http://ascelibrary.org/doi/full/10.1061/(ASCE)0899-1561(2006)18%3A3(467)?src=recsys#sthash.0AA5nCWj.dpuf>

Pell, P. (1980) 'The Performance of Rolled Asphalt Road Surfacings. Discussion on Slippage of Rolled Asphalt Wearing Courses'. *The Institution of Civil Engineers* 64–65

Petterson, B., and Axen, B. (1980) 'Thermography; Testing of the Thermal Insulation and Airtightness of Buildings.' in *Swedish Council for Building Research, Spangbergs Tryckerier AB.* held 1980 at stockholm

Poston, R.W., Whitlock, A.R., and Kesner, K.E. (1995) 'Condition Assessment Using Nondestructive Evaluation'. *Concr Int. Am Concr Inst* 36–42

Raab, C. (2010) *Development of a Framework for Standardisation of Interlayer Bond of Asphalt Pavements.* Carleton University, Ottawa, Canada

Raab, C., and Partl, M.N. (2004) 'Interlayer Shear Performance: Experience with Different Pavement Structures.' in *Proceedings of the 3rd Eurasphalt & Eurobitume Congress.* held 2004 at Vienna. 535–545

Raja, B.N.K., Miramini, S., Duffield, C., Sofi, M., Mendis, P., and Zhang, Lihai. (2020) 'The Influence of Ambient Environmental Conditions in Detecting Bridge Concrete Deck Delamination Using Infrared Thermography (IRT).' *International association for structural control and monitoring*

Razak, H.A. and Choi, F.C. (2001) 'The Effect of Corrosion on the Natural Frequency and Modal Damping of Reinforced Concrete Beams'. *Engineering Structures* 23, 1126–1133

Rens, K., Nogueira, C.., and Transue, D.. (2005) 'Bridge Management and Non-Destructuve Evaluation'. *Journal of Performance of Constructued Facilities, ASCE* 19, 3–16

Restrepo, G.A.D., and Loaiza, C.H. (2013) 'New 3D Finite Difference Method for Thermal Contrast Enhancement in Slabs Pulsed Thermography Inspection.' *J. Nondestruct. Eval.* 33 (1), 62–73

Richardson, M.H., and Mannan, M.A. (1992) 'Remote Detection And Location Of Structural Faults Using Modal Parameters.' in *Proc. of the 10th International Modal Analysis Conference*. held 1992. 502–507

Rizos, P.F., Aspragathos, N., and Dimarogonas, A.D. (1990) 'Identification Of Crack Location And Magnitude In A Cantilever From The Vibration Modes.' *Journal of Sound and Vibration* 138 (3), 381–388

Rmelie, E., and Scullion, T. (1997) . '. Detecting Stripping in as- Phalt Concrete Layers Using Ground Penetrating Radar.' *Journal of the Trans- portation Research Board.* 1568 (1), 165–174

Rocha, J.H.A., Póvoas, Y.V., and Santos, C.F. (2019) 'Detection of Delaminations in Sunlight-Unexposed Concrete Elements of Bridges Using Infrared Thermography.' *J Nondestruct Eval.* 38 (8)

Rollings, R.. (2001) 'Concrete Pavement Design: Its More than a Thickness Design Chart'. in *7th International Conference on Concrete Pavements.* held 2001 at Orlando. International Society for Concrete Pavements, 281–295

Ručevskis, S., Wesolowski, M., and Čate, A. (2009) 'Vibration-Based Damage Identification in Laminated Composite Beams.' *Construction science* 10 (ISSN 14077329), 100–113

Rumbayan, R., and Washer, G.A. (2014) 'Modeling of Environmental Effects on Thermal Detection of Subsurface Damage in Concrete.' *Res. Nondestruct. Eval.* 25, 235–252

Rytter, A. (1993) *Vibration Based Inspection of Civil Engineering Structures.* Aalborg University, Denmark

Saarenketo, T., and Scullion, Tom (2000) 'Road Evaluation with Ground Penetrating Radar'. *Journal of Applied Geophysics* 43 (2–4), 119–138

Saitoh, M., and Takei, B.T. (1996) 'Damage Estimation and Identification of Structural Faults Using Modal Parameters.' in *14th International Modal Analysis Conference.* held 1996 at Dearborn, MI.

Salawu, O.S. (1997) 'Detection of Structural Damage Through Changes in Frequency: A Review.' *Engineering Structures* 19, 718–723

Salawu, O.S., and Williams, C. (1995) 'Bridge Assessment Using Forced-Vibration Testing'. *Journal of structural engineering* 121 (2), 161–173

Sanayei, M. and Sipple, J.D. (2014) 'Finite Element Model Calibration of a Full Scale Bridge Using Measured Frequency Response Functions'. 4th International Conference on Bridges (January), 1–8

Sanders, D., Kim, Y.I., and Stubbs, R.N. (1992) 'Nondestructive Evaluation Of Damage In Composite Structures Using Modal Parameters.' *Experimental Mechanics* 32, 240–251

Sangiorgi, C., Collop, A., C., and Thom, N., H. (2003) 'A Nondestructive Impulse Hammer for Evaluating the Bond between Asphalt Layers in a Road Pavement.' in *Non-Destructive Testing in Civil Engineering, International Symposium, Liverpool, UK.* held 2003

Sansalone, M.J., and Carino, N.J. (1986) *Impact-Echo: A Method for Flaw Detection in Concrete Using Transient Stress Waves*. Gaithersburg, MD, USA

Saravanos, A.D., and Hopkins, D. (1995) 'Effects of Delaminations on the Damped Dynamic Characteristics of Composites.' *Journal of Sound and Vibration* 192, 977–993

Saucier, F., and Pigeon, M. (1991) 'Durability of New-to-Old Concrete Bondings'. in *ACI Int. Conf. On Evaluation and Rehabilitation of Concrete Structures and Innovation in Design,*. held 1991 at Detroit. 689–706

Schwarz, B.J. and Richardson, M.H. (1999) 'Experimental Modal Analysis'. Vibrant Technology October, 1–12

Scott, M., Rezaizadeh, A., Delahaza, A., Santos, C., Moore, M., Graybeal, B., and Washer, G. (2003) 'A Comparison of Nondestructive Evaluation Methods for Bridge Deck Assessment'. *Int'l Journal for NDT & E* 36, 245–255

See, J.E. (2012) 'Visual Inspection: A Review of the Literature'. *Sandia Report* (October), 77

Shahin, M.Y., Kirchner, K., Blackmon, E.W., and Tomita, H. (1986) '"Effect of Layer Slippage on Performance of Asphalt-Concrete Pavements'. *Journal of the Transportation Research Board* 79–85

Shepard, S.M. (1997) *Contributed Papers Introduction to Active Thermography for Non- Destructive Evaluation*. 44 (4), 236–239

Sherif, A.G., and Dilger, W.H. (2006). "Analysis and deflections of reinforced concrete flat slabs", *Canadian Journal of Civil Engineering*, 25 (3), 451-466

Shi, Z., Law, S., and Zhang, L. (2000) 'Localization by Directly Using Incomplete Mode Shapes.' *J. Eng. Mech.* 126 (6), 656–660

Skjaerbaek, P.S., Nielsen, S.R.K., and Cakmak, A.S. (1996) 'Assessment Of Damage In Seismically Excited RC-Structures From A Single Measured Response.' in *Proc. of the 14th International Modal Analysis Conference*. held 1996. 105–111

Slastan, J., and Pietrzko, S. (1993) 'Changes of RC Beam Modal Parameters Due to Cracks.' in *11th International Modal Analysis Conference*. held 1993. 70–76

Sohn, H., Farrar, C.R., Hunter, N., and Worden, K. (2003) *A Review of Structural Health Monitoring Literature: 1996–2001.*

Solla, M., Lagüela, S., González-Jorge, H., and Arias, P. (2014) 'Approach to Identify Cracking in Asphalt Pavement Using GPR and Infrared Thermographic Methods: Preliminary Findings'. *NDT and E International* [online] 62, 55–65. available from <http://dx.doi.org/10.1016/j.ndteint.2013.11.006>

Soltis, L.A., Wang, X., Ross, R.J., and Hunt, M.O. (2002) 'VIBRATION TESTING OF TIMBER FLOOR SYSTEMS.' *Forest Products Journal* 52 (10), 75–81

Srinivasan, M.G., and Kot, C.A. (1992) 'Effects Of Damage On The Modal Parameters Of A Cylindrical Shell.' in *10th International Modal Analysis Conference*. held 1992. 529–535

Stimolo, M., Dübendorf, E., Strassenbau, A.A., Dübendorf, and Schweiz (2003) 'Passive Infrared Thermography as Inspection and Observation Tool in Bridge and Road Construction.' in *Proceedings of the International Symposium on Nondestructive Testing in Civil Engineering*. held 2003 at Berlin, Germany

Storck, H., Sumali, H., and Pu, Y. (2001) 'Experimental Modal Analysis of Automotive Exhaust Structures'. *Advanced Engine, Powerplant, and Component Design-SP-1620* [online] (0148–7191), 10. available from <https://www.sae.org/publications/technical-papers/content/2001-01-0662/>

Stubbs, N., and Osegueda, R. (1990a) 'Global Damage Detection In Solids–Experimental Verification.' *Modal Analysis: The International Journal of Analytical and Experimental Modal Analysis* 5, 81–97

Stubbs, N., and Osegueda, R. (1990b) 'Global Non-Destructive Damage Evaluation In Solids.' *Modal Analysis: The International Journal of Analytical and Experimental Modal Analysis* 5, 67–79

Sultan, A.A., and Washer, Glen A. (2018) 'Reliability Analysis of Ground-Penetrating Radar for the Detection of Subsurface Delamination'. *Journal of Bridge Engineering* 23 (2), 20

Sultan, R., Guirguis, S., Younes, M., and El-Soaly, E. (2012) 'Delamination Detection of Composite Laminates Using Natural Frequency Vibration Method.' *International journal of mechanical engineering and robotics research* 1 (2), 286–296

Tawfiq, J., Armaghani, K., and Sobanjo, J. (2002) 'Rational Method for Selecting Seismic Waves for Pavement Evaluation, Journal of Transportation Engineering, ASCE'. *Journal of Transportation Engineering, ASCE* 550–558

The Constructor-Civil Engineering Home (2015) *Types of Pavement- Flexible Pavements and Rigid Pavements* [online] available from <https://theconstructor.org/transportation/types-of-pavement-flexible-and-rigid-pavement/9570/> [13 March 2017]

The Construction-Civil Engineering Home (2015) *Rigid Pavment Composition and Structure* [online] available from <https://theconstructor.org/transportation/rigid-pavement-composition-and-structure/5495/> [7 May 2017]

The Constructor-Civil Engineering Home (2015) *Types of Pavement- Flexible Pavements and Rigid Pavements* [online] available from <https://theconstructor.org/transportation/types-of-pavement-flexible-and-rigid-pavement/9570/> [13 March 2017]

Tsubokawa, Y., Mizukami, J., Esaki, T., and Hayano, K. (2007) 'Study on Infrared Thermographic Inspection of De-Bonded Layer of Airport Flexible Pavement.' in *FAA Worldwide Airport Technology Transfer Conference.* held 2007 at Atlantic City, New Jersey. 3–10

Uzan, J., Livneh, M., and Eshed, Y. (1978) 'Investigation of Adhesion Properties between Asphaltic-Concrete Layers'. *AAPT*

Vavilov, V.P. (2007) 'Pulsed Thermal NDT of Materials:Back to the Basics.' *Nondestruct. Test. Eval. 22*

Vavilov, V.P., Burleigh, D.D., and Klimov, A.G. (2002) 'Advanced Modeling of Thermal NDT Problems: From Buried Landmines to Defects in Composites.' *In: Maldague, X.P., Rozlosnik, A.E. (eds.) Thermosense XXIV, SPIE, Orlando* 507–521

Vavilov, V.P., and Maldague, X. (1994) 'Optimisation of Heating Protocol in Thermal NDT, Short and Long Heating Pulses.' *Res Non-Destruct Evaluat* 6, 1–17

Venter, G. (2016) 'Thermography on Composite Materials'. *R & D Journal of the South African Institution of Mechanical Engineering* 32 (September), 35–43

Villemure, I., Ventura, C.E., and Sexsmith, R.G. (1996) 'Impact and Ambient Vibration Testing to Assess Structural Damage in Reinforced Concrete Beams.' in *Proc. of the 14th International Modal Analysis Conference*. held 1996 at Dearborn, MI.

Virginia Department of Transportation (2012) *A Guide to Evaluating Pavement Distress through the Use of Digital Images, Version 2.6.* (November)

Walraven, J.C. (2007) *Strengthening and Bond between New and Old Concrete – Overlay Design Concept. Group Concrete Structures*, Delft University of Technology

Wang, W., and Zhang, A. (1987) 'Sensitivity Analysis in Fault Vibration Diagnosis of Structures.' in *Proc. of 5th International Modal Analysis Conference*. held 1987. 496–501

Wang, Y. (2010) *A Non-Destructive Damage Detection Method for Reinforced Concrete Structures Based on Modal Strain Energy* [online] University of technology, Sydney. available from <http://epress.lib.uts.edu.au/dspace/handle/2100/1154>

Wang, Z., Lin, R.M., and Lim, M.K. (1997) 'Structural Damage Detection Using Measured FRF Data.' *Computer Methods in Applied Mechanics and Engineering* 147, 187–197

Washer, G., Fenwick, R., Nelson, S., and Rumbayan, R. (2013) 'Guidelines for the Thermographic Inspection of Concrete Bridge Components in Shaded Conditions.' *Transp. Res. Rec. J. Transp. Res. Board.* 2360, 13–20

Watase, A., Birgul, Recep;, Hiasa, Shuhei;, Matsumoto, Masato;, Mitani, Koji;, and Catbas, N. (2015) 'Practical Identification of Favorable Time Windows for Infrared Thermography for Concrete Bridge Evaluation'. *Constructions and Building Materials* [online] 101 (1), 1016–1030. available from <https://www.sciencedirect.com/science/article/abs/pii/S0950061815305808>

WebFinance Inc (2017) *Dictionary of Constructio* [online] available from <http://www.dictionaryofconstruction.com/definition/rigid-pavement.html> [6 May 2017]

Weil, G., and Haefner, L.. (1989) 'Toward an Integrated Non-Destructive Pavement Testing Management Information System Using Infrared Thermography'. *Transportation Research Record* 1215, 124–131

Weil, G., and Rowe, T.. (1998) 'Non-Destructive Testing and Repair of the Concrete Roof Shell at the Seattle Kingdome'. *Int'l Journal for NDT & E* 31, 389–400

West, T. (2012) *The Ultimate Infrared Handbook for R & D Professionals* [online] available from <http://www1.flir.com/e/5392/research-development-guidebook/x7hz7/869543448>

West, W.M. (1984) 'Illustration Of The Use Of Modal Assurance Criterion To Detect Structural Changes In An Orbiter Test Specimen.' in *Proc. Air Force Conference on Aircraft Structural Integrity*. held 1984. 1–6

Wild, W. (2007) 'Application of Infrared Thermography in Civil Engineering'. *Proc. Estonian Acad. Sci. Eng* 13 (4), 436–444

Yehia, S., Osama, A., Saleh, N., and Ikhlas, A. (2007) 'Detection of Common Defects in Concrete Bridge Decks Using Nondestructive Evaluation Techniques.' *Journal of Bridge Engineering* 12 (2), 215–225

Yoder, E.. and Witczak, M.. (1975) *Principles of Pavement Design*. 2nd edn. New York: John Wiley & Sons

Yu, H.T., Smith, K.D., Darter, M.I., Jiang, J., and Khazanovich, L. (1998) *Performance of Concrete Pavements*. McLean VA

Yuen, M.M.F. (1985) 'A Numerical Study Of The Eigenparameters Of A Damaged Cantilever.' *Journal of Sound and Vibration* 103, 301–310

Zhang, J.K., Yan, W., and Cui, D.M. (2016) 'Concrete Condition Assessment Using Impact-Echo Method and Extreme Learning Machines'. *Sensors (Switzerland)* 16 (4), 1–17

APPENDIX A ─ FE-Thermal Images and Exp-Thermograms.
IRT-Test 01. (Section 4.5.1.1)

FEA Frame: 60 @ 60s
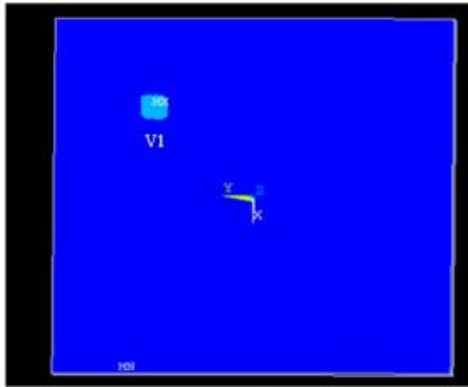
EXP Frame: 60 @ 60s

Temperature (^{0}C)
V1= 29.5
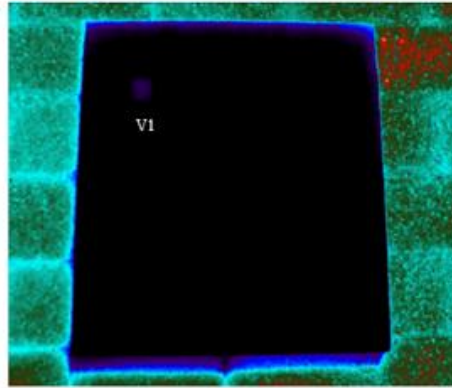
Temperature (^{0}C)
V1= 30.4

FEA Frame: 100 @ 100s
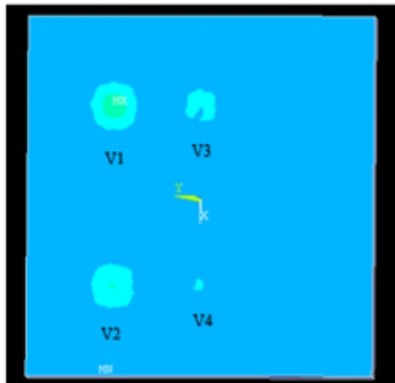
EXP Frame: 100 @ 100s

Temperature (^{0}C)
V1= 30.4
V2= 29.9
V3= 29.4
V4= 29.3
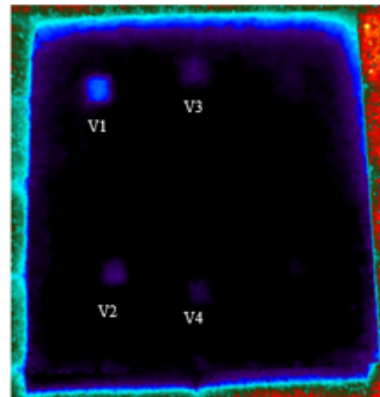
Temperature (^{0}C)
V1= 30.7
V2= 30.2
V3= 30.1
V4= 29.7

FEM Frame : 600 @ 600s
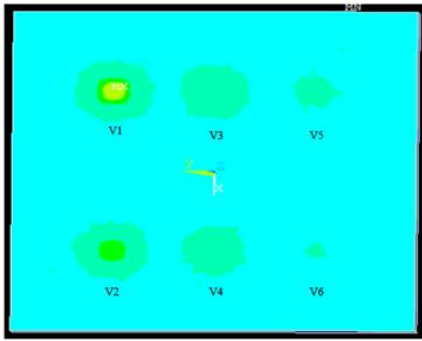
EXP Frame: 600 @ 600s

Temperature (⁰C)
V1= 36.2
V2= 34.5
V3= 32.8
V4= 32.5
V5= 32.2
V6= 32.1
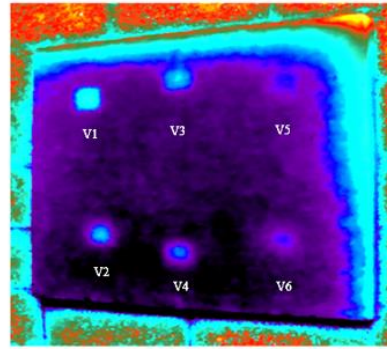
Temperature (⁰C)
V1= 34.2
V2= 33.3
V3= 32.6
V4= 32.5
V5= 32.2
V6= 32.0

FEA Frame: 1200 @ 1200s

EXP Frame: 1200 @ 1200s
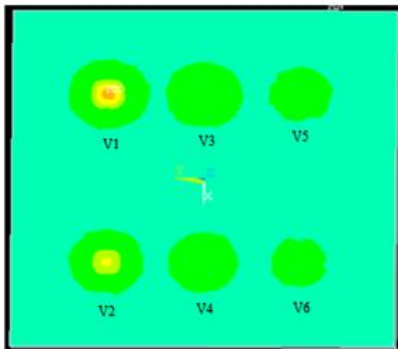
Temperature (⁰C)
V1= 38.1
V2= 36.3
V3= 34.6
V5= 33.9
V6= 33.5
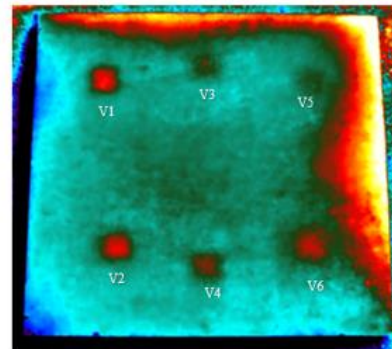
Temperature (⁰C)
V1= 38.4
V2= 36.3
V3= 35.0
V5= 34.3
V6= 33.8

APPENDIX B ─ FE-Thermal Images and Exp-Thermograms.
IRT-Test 02. (Section 4.7.1)

FEA Frame: 710 @ 710s
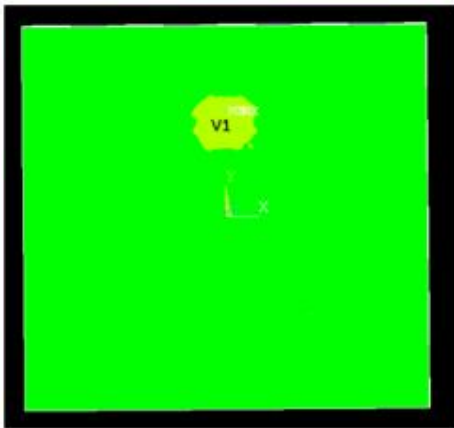
Temperature (^0C)
V1= 34.42

EXP Frame: 710 @ 710s
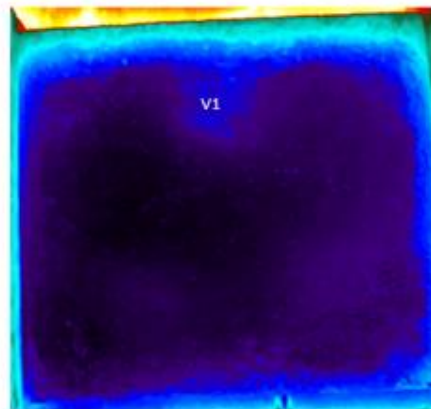
Temperature (^0C)
V1= 34.11

FEA Frame: 750 @ 750s
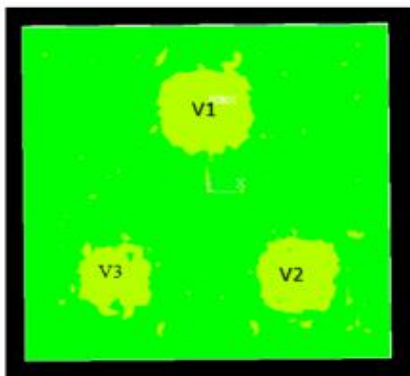
Temperature (^0C)
V1= 34.55
V2= 34.38
V3= 33.75

EXP Frame: 750 @ 750s
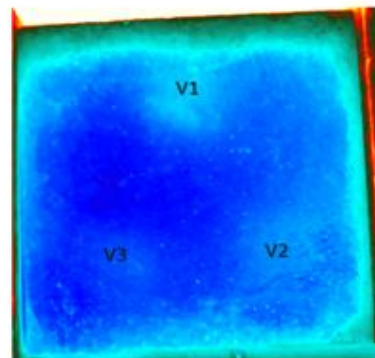
Temperature (^0C)
V1= 34.30
V2= 34.10
V3= 33.12

FEA Frame: 1050 @ 1050s

EXP Frame: 1050 @ 1050s
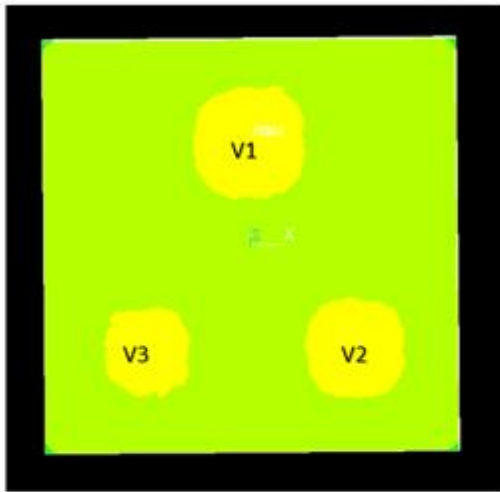
Temperature (^{0}C)
V1= 35.55
V2= 35.23
V3= 34.62
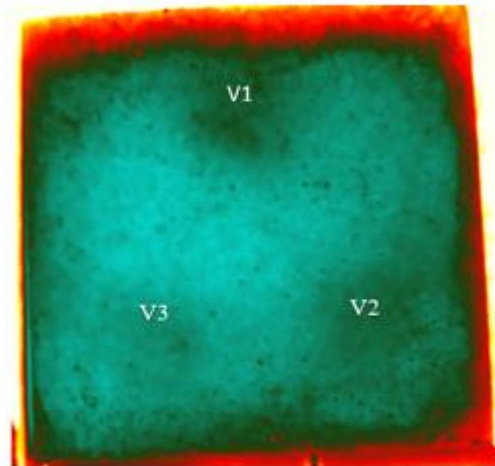
Temperature (^{0}C)
V1= 35.50
V2= 35.15
V3= 34.50

FEA Frame : 1390 @ 1390s

EXP Frame: 1390 @ 1390s
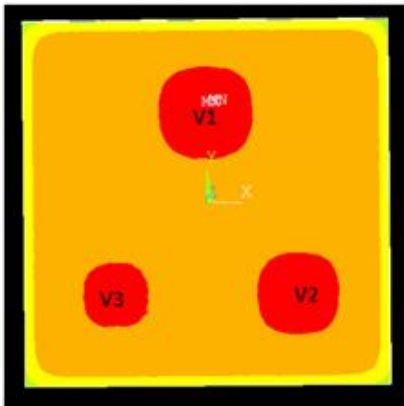
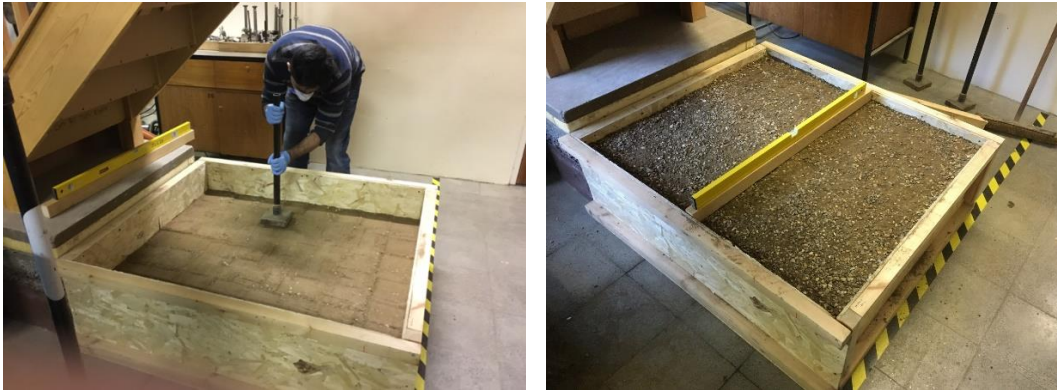| Temperature (^{0}C) |
| --- |
| V1= 36.57 |
| V2= 36.07 |
| V3= 35.79 |
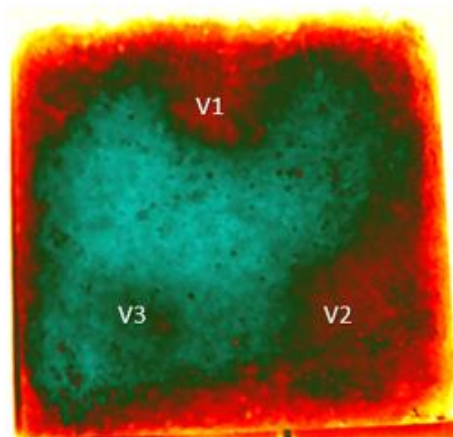
Temperature (^{0}C)
V1= 36.35
V2= 36.00
V3= 35.35

APPENDIX C ─ Active Thermography Trial Test (Section 4.3)
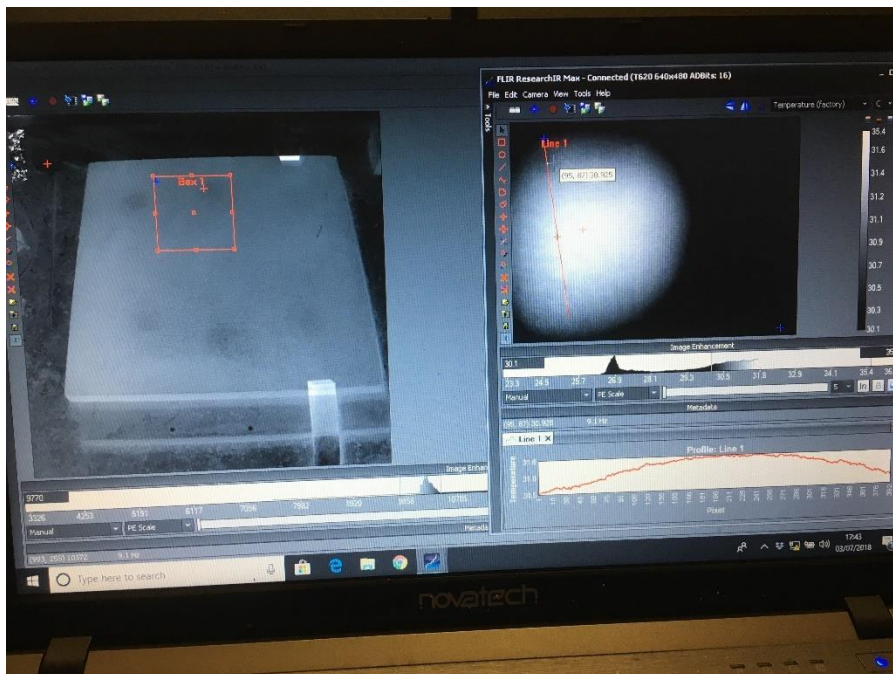
APPENDIX D ─ Preparation of Sandpit (Section 5.3.2)

Sand Pit Preparation

- Sand pit **(1200x1070x350mm)** is prepared with the compaction level of **58** blows (via heavy plate 4.4kg) as per **BS: 1377-4**.

- Three layers each layer of around 10cm was compacted and then the next layer was placed upon it.

- A total mixture of 900 kg mass was used with the percentage of **54.13%** sharp sand by mass, **43.35%** aggregate (10mm) by mass and **2.52%** dry cement by mass.

- A big mixture with the capacity of **100L** was used several times (9 times approx.) for mixing around 1ton **(900kg)** sand-aggregate-cement mixture.

- Three mixtures, altogether **300kg** was used for each layer. Each layer was levelled first with the wooden block and measured via spirit level (bubble meter) and then was compacted with 58 blows compaction level. Finally the spirit level was used again to measure the level of the sand pit as shown in figures. The mixture is dry so far, no water spray has been done yet and is left to the air moisture.